Fabrication of Large Area Two-Dimensional PtX₂ (X=S, Se) Heterostructures for Broadband Photodetector Studies

Doctoral Thesis

by

Gaurav Bassi

(2019PHZ0005)



DEPARTMENT OF PHYSICS INDIAN INSTITUTE OF TECHNOLOGY ROPAR

March 2025

Fabrication of Large Area Two-Dimensional PtX₂ (X=S, Se) Heterostructures for Broadband Photodetector Studies

A Thesis Submitted

In Partial Fulfilment of the Requirements for the Degree of

DOCTOR OF PHILOSOPHY

by

Gaurav Bassi

(2019PHZ0005)



DEPARTMENT OF PHYSICS

INDIAN INSTITUTE OF TECHNOLOGY ROPAR

March 2025

Gaurav Bassi: Fabrication of Large Area Two-Dimensional PtX_2 (X=S, Se) Heterostructures for Broadband Photodetector Studies

Copyright © 2025, Indian Institute of Technology Ropar

All Rights Reserved

DEDICATED

TO

MY PARENTS

(Mrs. Bandana & Mr. Shiv Kumar)

&

Grand Parents

(Late Dr. Kewal Krishan Bassi & Late. Shrishta Devi)

Declaration of Originality

I hereby declare that the work which is being presented in the thesis entitled "Fabrication of Large Area Two-Dimensional PtX2 (X=S, Se) Heterostructures for Broadband Photodetector Studies" has been solely authored by me. It presents the result of my own independent investigation/research conducted during the time period from January 2020 to March 2025 under the supervision of Prof. Mukesh Kumar, Department of Physics, Indian Institute of Technology Ropar. To the best of my knowledge, it is an original work, both in terms of research content and narrative, and has not been submitted or accepted elsewhere, in part or in full, for the award of any degree, diploma, fellowship, associateship, or similar title of any university or institution. Further, due credit has been attributed to the relevant state-ofthe-art and collaborations (if any) with appropriate citations and acknowledgments, in line with established ethical norms and practices. I also declare that any idea/data/fact/source stated in my thesis has not been fabricated/ falsified/ misrepresented. All the principles of academic honesty and integrity have been followed. I fully understand that if the thesis is found to be unoriginal, fabricated, or plagiarized, the Institute reserves the right to withdraw the thesis from its archive and revoke the associated Degree conferred. Additionally, the Institute also reserves the right to appraise all concerned sections of society of the matter for their information and necessary action (if any). If accepted, I hereby consent for my thesis to be available online in the Institute's Open Access repository, inter-library loan, and the title & abstract to be made available to outside organizations.

Signature:

Name: Gaurav Bassi

Gamar Bami

Entry Number: 2019PHZ0005

Department: Physics

Indian Institute of Technology Ropar

Rupnagar, Punjab 140001

Date: March 20, 2025

Certificate

This is to certify that the thesis entitled "Fabrication of Large Area Two-Dimensional PtX₂ (X=S, Se) Heterostructures for Broadband Photodetector Studies" submitted by Gaurav Bassi (2019PHZ0005) for the award of the degree of Doctor of Philosophy at Indian Institute of Technology Ropar, is a record of bonafide research work carried out under my guidance and supervision. To the best of my knowledge and belief, the work presented in this thesis is original and has not been submitted, either in part or full, for the award of any other degree, diploma, fellowship, associateship or similar title of any university or institution.

In my opinion, the thesis has reached the standard of fulfilling the requirements of the regulations relating to the Degree.

Signature:

Prof. Mukesh Kumar

Department of Physics

Indian Institute of Technology Ropar

Rupnagar, Punjab 140001

Date: March 20, 2025



Acknowledgment

My PhD journey has been filled with numerous challenges and triumphs, making it essential to express my heartfelt gratitude to those who have supported me throughout this endeavor. First and foremost, I extend my deepest gratitude to my PhD mentor and supervisor, Prof. Mukesh Kumar, Department of Physics, Indian Institute of Technology Ropar, for his unwavering guidance, support, and motivation. His encouragement has been instrumental in shaping my research and pushing me beyond my comfort zone to achieve greater heights. His insightful discussions, constructive feedback, and commitment to excellence have significantly contributed to the success of this work. I sincerely appreciate his prompt review of manuscripts and his constant pursuit of high-impact research, which has greatly enhanced my potential. His ability to maintain a perfect balance between personal and professional life is truly admirable, and I consider myself fortunate to have worked under his esteemed guidance.

I would also like to extend my sincere gratitude to my Doctoral Scrutiny Committee (DSC) members Dr. Subhendu Sarkar, Prof. Rajesh V. Nair, Prof. C. M. Nagaraja, and Chairperson Dr. Asoka Biswas, for their valuable time, insightful discussions, and constructive feedback, which have significantly contributed to the refinement of my research.

Furthermore, I sincerely acknowledge my collaborators, Dr. Pradeep Kumar and his group from IIT Mandi, Prof. Mahesh Kumar and his team from IIT Jodhpur, and Dr. S. Sarkar and his group from IIT Ropar for their generous support and for providing access to various characterization facilities.

I would like to express my profound gratitude to the members of Functional & Renewable Energy Materials Laboratory (FREM Lab). The support and encouragement from both current members and alumni have been invaluable throughout this journey. I extend my heartfelt thanks to Dr. Naveen Kumar, Dr. Kanika Arora, Dr. Abhay V. Agarwal, Dr. Kulwinder Kaur, Dr. Nisika, Dr. Riya Wadhwa, and Dr. Damanpreet Kaur for their constant guidance and support. Their insights and encouragement have played a crucial role in my academic and research endeavors. I also cherish the wonderful memories of our gatherings outside the lab. I also sincerely grateful to Dr. Riya Wadhwa for her patience and willingness to engage in discussions, and for bearing with my endless questions. Her assistance with lab equipment training and paper writing has been invaluable, and I find it difficult to express my gratitude in words. I am also thankful to Mrs. Puja for her generous nature and insightful troubleshooting

discussions in the lab. Additionally, I would like to acknowledge my fellow lab members Shivani Dahiya, Rohit Dahiya, Vinit, Priya, Moumita, Shiksha, and Jiya for their support and assistance in various lab activities.

Beyond the lab, I am immensely grateful to my close friends Amanjot, Sanjeet Singh Kaintura, Subham Kumar, Abhishek Kumar, Aatish, Naresh Kumar, Aswathi, and all my batchmates for their motivation and companionship throughout this PhD journey. The daily post-dinner walks with Amanjot, filled with lively conversations and gossip, provided a refreshing break from the exhausted days. The countless "chai par charcha" sessions with Naresh will always be cherished. I also fondly remember many wonderful friends I met while attending conferences. Their presence made those experiences truly special and fostering lifelong bonds that I deeply value.

I am sincerely thankful to the Ministry of Human Resource & Development (MHRD) for providing the fellowship during my PhD tenure. I also extend my gratitude to the faculty and staff of the Department of Physics for their assistance during my teaching assistant (TA) duties. Special thanks to Mr. Anshu Vaid, Mr. Rahul, and other staff members of the Department of Physics for ensuring smooth process of documents. I am also grateful to the Central Research Facility (CRF) at IIT Ropar for providing access to various characterization facilities, including XPS, AFM, Raman, PL, FESEM, and TEM. Furthermore, I sincerely appreciate the support of all CRF operators/staffs, Mr. Amit Kaushal, Mr. Damninder Singh, Mr. Harsimranjit Singh, Mr. Manu Rana, Mr. Abhishek, and Mr. Manish for their assistance throughout this journey.

Above all, I am deeply indebted to my parents for their unwavering love and support. Their emotional encouragement has been a source of immense strength, instilling positivity and motivation to achieve greater heights. Additionally, I extend my heartfelt gratitude to my uncle and aunty for their continuous love and support throughout this journey.

Lastly, I thank God for blessings and for giving me the strength and perseverance to navigate this journey.

.

Lay Summary

Photodetectors are optoelectronic devices that convert light signals into electrical signals and are used to detect a range of the electromagnetic spectrum. This thesis aims to develop PtX₂ (X=S, Se) heterostructure-based broadband photodetectors with high performance in the nearinfrared (NIR) region. Broadband photodetectors have multiple applications in optical communication, defence security, environmental monitoring, and medical imaging. Two-dimensional (2D) materials, especially group-10 transition metal dichalcogenides (TMDC), PtX₂ are highlighted for their distinct properties including narrow band gap range, high carrier mobility, and ambient stability, required to fabricate high-performance broadband photodetectors. The thesis starts with a discussion on large area and controlled growth of PtS₂ film by thermally assisted conversion (TAC) method. The fabrication of various PtX₂ heterostructure like PtS₂/MoS₂, PtS₂/Ga₂O₃, and PtSe₂/MoS₂ and their photodetector study are described. All these heterostructure devices show broadband response and have the best performance in the NIR region. Moreover, a detailed interface study of the heterojunction including their band alignment and carrier transport mechanism is discussed.

Abstract

Over the last few decades, two-dimensional (2D) materials, especially transitional metal dichalcogenides (TMDCs) have procured a huge attraction for their wide range of intriguing properties. The thickness-dependent band gap, high absorption coefficient, and high on-off ratio of TMDC based devices make them potential candidates in the optoelectronics field to develop photodetectors, phototransistors, and solar cells. Photodetectors are optoelectronic devices that convert light signals into electrical signals. In recent years, for photodetector applications, group-10 TMDCs, especially PtS₂ and PtSe₂ have become a spotlight for their narrow band gap (0-1.6 eV) and high carrier mobility. Despite these properties, the controlled growth of PtS₂ on various substrates and high-performance PtX₂ (X=S, Se) based broadband photodetectors with best response in near-infrared region (NIR) are less explored.

In present thesis work, we try to solve these challenges. In the first work, a large area and controlled growth of PtS₂ films is achieved via thermally assisted conversion (TAC) method. The main issue during the growth of PtS₂ by TAC method is the formation of an intermediate PtS phase due to its more stability. The present study shows that by optimizing the growth parameters such as Pt film thickness, sulfur amount, and carrier gas flow rate, a controlled growth of PtS₂ and PtS to PtS₂ conversion can be obtained. A detailed Raman and X-ray photoelectron spectroscopy (XPS) further revealed that PtS₂ is dominantly to form for thinner Pt film, sulfurized under sulfur-rich vapors at a moderate gas flow rate. Furthermore, the PtS₂ growth is highly reproducible and can be grown on different substrates such as SiO₂/Si, Sapphire, Si, and mica, and their photodetector performance is also checked.

In the second part of the thesis, different PtS₂ heterostructures (PtS₂/MoS₂, PtS_{2-x}/Ga₂O₃) are fabricated and their broadband photodetector performance are discussed. A detailed interface study of heterojunction, including their band alignment, valence band offset (VBO), and conduction band offset (CBO) is calculated. The PtS₂/MoS₂ heterostructure is fabricated by directly growing PtS₂ film on MoS₂-coated substrate by TAC method. The fabricated PtS₂/MoS₂ photodetector gives a broad response in the range of 400-1200 nm (Visible to NIR) with a maximum responsivity of 30.2 AW⁻¹ under 900 nm illumination. The PtS_{2-x}/Ga₂O₃ heterostructure is fabricated by wet transfer of PtS_{2-x} film over Ga₂O₃ film. The fabricated PtS_{2-x}/Ga₂O₃ based photodetector gives a wide response covering ultraviolet (UV)-C to NIR (250-1100 nm) with a maximum responsivity of 38.7 AW⁻¹ under 1100 nm illumination and exhibits a fast millisecond response.

In the last part of the thesis, large PtSe₂/MoS₂ heterostructure fabrication and its photodetector study are explained. The problem of high dark current in bare PtSe₂ owing to narrow and semimetal is resolved by fabricating its heterostructure with MoS₂. Compared to bare PtSe₂, the PtSe₂/MoS₂ heterostructure shows a 10³ order of reduction in dark current and an increase in detectivity of the fabricated photodetector. Moreover, PtSe₂/MoS₂ heterostructure shows a broad detection response covering visible to NIR (400-1200 nm) with maximum detectivity of 9.8×10¹² Jones under 900 nm irradiation. An ultrafast response with a rise/fall time of 103 μs /117 μs is also achieved in the PtSe₂/MoS₂ device which shows its high performance.

In conclusion, we have grown a controlled and large area of PtS₂ film on various substrates by optimizing the critical growth parameters. The different PtX₂ heterostructure (PtS₂/MoS₂, PtS_{2-x}/Ga₂O₃, PtSe₂/MoS₂) fabrication, band alignment study, and their broadband photodetector study have also been carried out. Thus, these results suggest that PtS₂ and PtSe₂ are suitable materials for developing future optoelectronic devices.

Keywords: 2D materials, PtS₂, PtSe₂, MoS₂, Photodetector, TAC, CVD, Sputtering, Heterostructure, Band-alignment

List of Publications

- 1) <u>Gaurav Bassi</u>, Riya Wadhwa, Sonia Deswal, Pradeep Kumar and Mukesh Kumar, "Controlled and tunable growth of ambient stable 2D PtS₂ thin film and its high-performance broadband photodetectors". *Journal of Alloys and Compounds 955 (2023)* 170233
- **2)** <u>Gaurav Bassi</u>, Riya Wadhwa, and Mukesh Kumar "Broadband and high-performance photodetector fabricated using large area and transfer-free 2D–2D PtS₂/MoS₂ heterostructure". *Advanced Optical Materials* 2023, 2301899
- 3) <u>Gaurav Bassi</u>, Damanpreet Kaur, Rohit Dahiya and Mukesh Kumar "2D–3D heterostructure of PtS_{2-x}/Ga₂O₃ and their band alignment studies for high performance and broadband photodetector". *Nanotechnology* 35 (2024) 325706
- **4)** Gaurav Bassi, Rohit Dahiya, Atul G. Chakkar, Pradeep Kumar and Mukesh Kumar "Large area, ultrafast, suppressed dark current and high-performance PtSe₂/MoS₂ van der Waals heterostructure based visible to NIR broadband photodetector". *Applied Surface Science* 681 (2025) 161598
- 5) Arpita Biswas, Ashok Kumar, Amit Kumar, Monika Kwoka, <u>Gaurav Bassi</u>, Mukesh Kumar and Mahesh Kumar "High performance Pt-anchored MoS₂ based chemiresistive ascorbic acid sensor". *Nanotechnology* 35 (2024) 365501
- 6) Damanpreet Kaur, Rohit Dahiya, Vinit Sheokand, <u>Gaurav Bassi</u> and Mukesh Kumar "Ultrafast, self-powered and highly-stable PtS-Ga₂O₃ heterojunction photodetector for broad-spectrum sensing". *Surfaces and Interfaces 61 (2025) 106125*
- 7) Rahul Gond, Suraj Barala, Prajjwal Shukla, <u>Gaurav Bassi</u>, Suresh Kumar, Mukesh Kumar, Mahesh Kumar, Brajesh Rawat, "Fe₂O₃-functionalized MoS₂ nanostructure sensor for high sensitivity and selective SO₂ detection". *ACS Sens. 2025*, *10*, *5*, *3412–3422*
- **8)** Rovins, Suresh Kumar, Ashok Kumar, <u>Gaurav Bassi</u>, Mukesh Kumar and Mahesh Kumar, MoSe₂@MoO₂ hybrid nanostructures decorated with gallium nanoparticles for room temperature hydrogen gas sensor, Nanotechnology (Under Review)

Table of Contents

Declaration of Originalityv
Certificatevi
Acknowledgmentix
Lay Summaryx
Abstractxi
List of Publicationsxiv
List of symbols, and abbreviationsxix
List of Figuresxxi
List of Tablesxxv
Chapter-1: Introduction 1
1.1 Back ground
1.2 Transitional metal dichalcogenides
1.3 PtX_2 (X=S, Se)
1.4 Properties of PtX ₂ (X=S, Se)
1.4.1 Crystal structure
1.4.2 Electronic band structure
1.4.3 Vibration mode (Raman) of PtX ₂
1.5 Synthesis Methods of PtX ₂ (X=S, Se)
1.5.1 Mechanical Exfoliation
1.5.2 Chemical vapor deposition
1.5.3 Thermally assisted conversion
1.6 Applications of PtX ₂ (X=S, Se)
1.7. Photodetectors
1.7.1 Figure of merits of photodetectors
1.7.2. Working mechanism of a photodetector
1.8 History and current Scenario in the field of PtX ₂ based photodetectors (PDs)
1.9 Types of Heterostructure
1.10 Challenges and Motivations
1.11 Objectives of the present thesis work
1.12 Outline of the thesis
References
Chapter 2: Fabrication and characterization techniques23
2.1 Deposition techniques

	2.1.1 Magnetron sputtering	. 23
	2.1.2 Chemical Vapor Deposition	. 24
	2.1.3 Thermally assisted conversion	. 25
	2.2 Characterization techniques	. 26
	2.2.1 Optical characterizations	. 26
	2.2.2 Morphological characterizations	. 27
	2.2.3 Crystal Structure Characterization	. 28
	2.2.4 Chemical composition analysis and band alignment studies	. 28
	2.3 Device fabrication and characterization	. 28
	2.3.1 Device fabrication	. 28
	2.3.2 Photodetector device measurements	. 29
	References	. 31
C	hapter 3: Large area and controlled growth of PtS2 on various substrates	. 33
	3.1 Requirement of large area and controlled growth of PtS ₂ film	. 33
	3.2 Experimental section	. 33
	3.2.1 Synthesis of PtS ₂	. 33
	3.2.2 Characterizations of PtS ₂	. 34
	3.2.3 Photodetector fabrication and measurements	. 34
	3.3 Results and Discussion	. 35
	3.3.1 Effect of Sulfur amount	. 35
	3.3.2 Effect of Pt thickness	. 37
	3.3.3 Effect of gas flow rate	. 37
	3.3.4 XPS data analysis	. 38
	3.4 PtS ₂ grown on different substrates	. 39
	3.5 Proposed growth Mechanism of PtS ₂	. 41
	3.6 PtS ₂ photodetector device performance	. 44
	3.7 Conclusion	. 49
	References	. 50
C	hapter 4: Large area 2D PtS2 heterostructures for broadband photodetection	. 53
	4.1 Requirement of highly sensitive, fast and broadband photodetectors	. 53
	4.2 PtS ₂ /MoS ₂ heterostructure	. 53
	4.2.1 Experiment section	. 54
	4.2.2 Results and discussion	. 56
	4.2.3 Conclusion	. 71
	4.3 PtS _{2-x} /Ga ₂ O ₃ heterostructure	. 72

4.3.1 Experiment section	72
4.3.2 Results and discussion	73
4.3.3 Conclusion	85
References	86
Chapter 5: 2D PtSe ₂ heterostructure for photodetector study	89
5.1 Requirement of PtSe ₂ /MoS ₂ heterostructure	89
5.2 Experimental section	90
5.2.1 Growth of PtSe ₂ film	90
5.2.2. Fabrication of MoS ₂ film and PtSe ₂ /MoS ₂ heterostructure device	90
5.2.3. Device measurement and characterization	91
5.3 Results and discussion	91
5.4 Conclusion	105
References	106
Chapter 6: Summary and Scope for Future Studies	109
6.1 Summary	109
6.1.1 Large area and controlled growth of PtS ₂ on various substrates	109
6.1.2 Large area 2D PtS ₂ heterostructure for broadband photodetection	109
6.1.3 2D PtSe ₂ heterostructure for photodetector study	110
6.2 Scope for future studies	111
Conferences/Workshop Attended	113
Curriculum Vitae	115

List of symbols, and abbreviations

Symbol/ abbreviations	Description
2D	Two-dimensional
TMDCs	Transition metal dichalcogenides
PtS ₂	Platinum disulfide
PtS	Platinum sulfide
MoS ₂	Molybdenum disulfide Platinum diselenide
$\frac{\text{PtSe}_2}{\text{BP}}$	Black phosphorus
h-BN	Hexagonal-Boron nitride
Se	Selenium
S	Sulfur
Ga ₂ O ₃	Gallium oxide
Pt	Platinum
Au	Gold
PD	Photodetector
FET	Field effect transistor
3D	Three-dimensional
Si	Silicon
SiO ₂	Silicon dioxide
Vis	Visible
UV	Ultraviolet
NIR	Near infrared
MIR	Mid infrared
JCPDS	Joint Committee of Power Diffraction Standards
VBM	Valence band maximum
CBM	Conduction band minimum
VBO	Valence band offset
CBO	Conduction band offset
FESEM	Field emission scanning electron microscope
EDX	Energy dispersive X-ray spectroscopy
XPS	X-ray photoelectron spectroscopy
UPS	Ultraviolet photoelectron spectroscopy
AFM	Atomic force microscopy
RMS	Root mean square
XRD	X-ray diffraction

PL	Photoluminescence
GIXRD	Grazing incidence X-ray diffraction
TEM	Transmission electron microscopy
HR-TEM	High resolution-Transmission electron microscopy
ARPES	Angle resolved photoemission spectroscopy
ME	Mechanical exfoliation
PVD	Physical vapor deposition
CVD	Chemical vapor deposition
APCVD	Atmospheric vapor chemical vapor deposition
TAC	Thermally assisted conversion
EBE	Electron beam evaporation
PMMA	Polymethyl methacrylate
E _C	Conduction band
Ev	Valence Band
$E_{\mathbf{f}}$	Fermi level
CT	Charge transfer
ф	Work function
Re	Reynold number
η	Viscosity of gas
ρ	Density of gas
v	Velocity of gas in pipe
M	Diameter of the CVD tube
DFT	Density functional theory
Ar	Argon
H_2	Hydrogen
H_2S	Hydrogen sulfide
SO_2	Sulfur dioxide
С	Speed of light in air
RT	Room temperature
nm	Nanometer
τ	Carrier lifetime
$ au_{tr}$	Carrier transit time
k _B	Boltzmann constant
T	Temperature
I _{light}	Photocurrent
I _{dark}	Dark current
P	Power density

A	Active area
e	Electronic charge
λ	Incident light wavelength
R	Responsivity
D*	Specific detectivity
EQE	External quantum efficiency
IQE	Internal quantum efficiency
S_{s}	Shot noise
S_{tn}	Thermal noise
Rs	Resistance of the device
G	Photo gain
NEP	Noise equivalent power
h	Planck constant
μ	Mobility
L	Channel length
DC	Direct current
RF	Radio frequency
a	Absorption coefficient
α	Power exponent
V	External bias to the device
PCE	Photo conductive effect
PVE	Photo voltaic effect

List of Figures

Figure 1.1 (a) Periodic table showing the elements forming the TMDC compounds with transition metals (group 4-10) and chalcogens. The complete highlighted elements mainly form layered TMDC, whereas partially highlighted (Co, Rh, Ir and Ni) exhibits that selected dichalcogenides form layered structure. (b, c) crystal structure view of atoms along top, side
of single layer TMDC with trigonal prismatic (b) and (c) octahedral coordination [8] 3 Figure 1.2 Crystal structure of PtS ₂ and PtSe ₂ with atoms arrangements under different
direction views [16]
Figure 1.3 Electronic band structure of (a) monolayer (1L) (b) bulk PtS ₂ (c) Band gap
calculated for different thickness PtS ₂ layers by Tuac plot (d) Variation of experimentally and
theoretically (DFT) calculated band gap of PtS_2 with thickness [10]
Figure 1.4 Electronic band structure of (a) Monolayer (1L) and (b) bulk PtSe ₂ (c) Tuac plot
using experimentally band gap calculated for different PtSe ₂ thickness [11]6
Figure 1.5 (a) Layer depended Raman spectra of PtS ₂ under 633 nm laser illumination. (b)
Peak position variation of E_g^1 , A_{1g}^1 and A_{1g}^2 vibrational modes with increasing number of
layers. (c) Layer depended Raman spectra of PtSe ₂ (d) Thickness depended peak position
variation of A _{1g} and E _g vibration modes of PtSe ₂ (e) Schematic showing the Raman vibrational
mode in PtSe ₂ [11, 22]
method (b) Chemical vapor deposition (CVD) method, where Pt and S/Se precursors are used
in powder form and also known as one-step CVD (c) Thermally assisted conversion (TAC)
method or also known as two-step CVD method [22].
Figure 1.7 (a) Schematic of a Photodetector (b) schematic of a response time with rise and fall
time
Figure 1.8 Performance comparison in the current scenario in (a) PtS2 and its heterostructure
$(b)PtSe_2anditsheterostructurebasedphotodetectors(PDs).ThedatainFigureshasbeentaken$
from Ref. [15, 37, 38, 44, 51-70]
Figure 1.9 Different type of heterostructures based on their band alignment
Figure 2.1 (a) Schematic illustrating the Sputtering system (b) Sputtering system employed in
our lab to deposit platinum (Pt) and MoS ₂ thin film
Figure 2.2. (a) Schematic illustrating the common elementary steps occurring in the CVD process (b) CVD equipment used for the growth of PtX ₂ (X=S, Se)
Figure 2.3 The schematic exhibiting the steps used for the growth of PtX_2 (X=S, Se) by TAC
method
Figure 2.4 (a) Schematic demonstrating the light interacted with molecule leads to Raman and
Rayleigh scattering (b) Schematic shows the band diagram of a material under electron
excitation and de-excitation in PL spectroscopy
Figure 2.5 (a) Physical shadow mask used for electrode deposition with different geometry
shapes of (i) interdigitated (ii) strips (iii) lines strips (b) Thermal evaporator system employed
for metal electrode deposition. 29
Figure 2.6 Testing equipment used for photodetector device measurements which consist of
light source, monochromator, probe station, 6430 SMU Keithley and computer
Figure 3.1 (a) 1st step of Pt coated on substrate by magnetron sputtering, and (b) 2nd step of
sulfurization of Pt coated substrate in a tube-in-tube APCVD (c) Temperature profile of Sulfur (S) and Pt coated substrate in APCVD.
(S) and Pt coated substrate in APCVD 35

Figure 3.2 (a) Raman spectra of PtS_x (x=1, 2) thin films synthesized at different sulfur amount
$0.4~g,0.8~g,1.2~g,$ and $1.6~g$ (b) Raman spectra of PtS_x films obtained after sulfurizing different
Pt thickness (c) Raman spectra of PtS2 films prepared at different gas flow rate in APCVD (d)
Raman spectra of PtS2 synthesized from different Pt thickness at 75 sccm carrier gas flow rate.
(e) Thickness of PtS2 film calculated by AFM grown by TAC method with 2.4 nm Pt, 1.2 g
sulfur, and 75 sccm gas flow rate growth parameters (f) band gap value of best grown PtS ₂ thin
film calculated by Tauc plot
Figure 3.3 XPS spectra of Pt 4f and S 2p core level regions of the PtS _x grown on SiO ₂ /Si
substrate at different growth conditions of (a, d) 0.4 g sulfur and 150 sccm gas flow rate, (b, e)
0.8 g sulfur and 75 secm gas flow rate and (c, f) 1.2 g sulfur and 75 secm gas flow rate 38
Figure 3.4 (a) Raman spectra of PtS ₂ film synthesized on different substrates (mica, Si,
Sapphire, and SiO ₂ /Si) (b) AFM surface topography images of PtS ₂ film grown on these
substrates with a scale bar of 1 μm and scan area of 3 μm×3 μm (c) Optical images of the same
PtS ₂ film synthesized on mica, Si, Sapphire, and SiO ₂ /Si with scale bar 100 μm. (d) Uniformity
of PtS ₂ on different substrates (mica, Si, Sapphire, SiO ₂ /Si) is confirmed by performing the
Raman on different positions (near the edges of the samples) of size 1×1 cm ² area
Figure 3.5 Growth mechanism of PtS and PtS ₂ at different growth conditions (b)-(d) Effect of
sulfur amount, (e)-(g) Effect of Pt thickness, (h)-(j) Effect of gas flow
Figure 3.6 (a) Schematic of PtS ₂ photodetector device (b) I-V characteristics of PtS ₂ device
under dark and illumination of different wavelengths (c), (d), (e) and (f) represents the variation
of Responsivity, Detectivity, EQE, and NEP, respectively as a function of wavelength at low
voltage (1V) biasing
Figure 3.7 (a) Time dependent photoresponse of the fabricated PtS ₂ device under broad visible-
NIR range (400-1100 nm) at 1V bias (b) Calculated response time (rise and fall time) of PtS ₂
photodetector at 500 nm (1V bias). (c, d) Raman spectra and responsivity of pristine PtS ₂ and
after 6 months kept in ambient conditions device
Figure 3.8 I-T characteristics of PtS ₂ photodetector grown on different substrates (a) Si/SiO ₂
substrate (b) Sapphire (c) Mica, under illumination of 532 nm at 3V. (d)-(f) Response time of
the fabricated photodetector on Si/SiO ₂ , Sapphire and mica, respectively
Figure 4.1 (a) Schematic of the PtS ₂ thin film synthesis by TAC method (b) Schematics of
PtS ₂ /MoS ₂ heterostructure device fabrication by multiple steps
Figure 4.2 (a) Raman spectra of bare PtS ₂ , MoS ₂ and PtS ₂ /MoS ₂ (b) Optical image of
PtS ₂ /MoS ₂ heterostructure with a scale bar of 10 µm where Raman mapping was performed (c)
A _{1g} peak Raman mapping of MoS ₂ in heterostructure (d) E _g ¹ peak Raman mapping of PtS ₂ in
heterostructure.
Figure 4.3. (a) Thickness of MoS2 and (b) thickness of PtS2 estimated from AFM with inset
showing their actual step
Figure 4.4 (a) Photoluminescence (PL) spectra of bare MoS ₂ and PtS ₂ /MoS ₂ (b) Comparison
plot of absorption spectra of bare PtS ₂ , MoS ₂ , and PtS ₂ /MoS ₂ film grown on quartz substrates.
Band gap calculated of (c) bare MoS ₂ and (d) bare PtS ₂ using Tauc plot
Figure 4.5 (a) Valence band spectra and Mo core level binding energy spectra of bare MoS ₂
(b) Pt 4f core level binding energy spectra and valence band spectra of PtS ₂ (c) Core level
spectra of Pt 4f and Mo 3d of the PtS ₂ /MoS ₂ heterostructure (d) Band alignment (Type-I)
between PtS ₂ and MoS ₂
Figure 4.6 Current-voltage (I-V) characteristics of (a) bare MoS ₂ (b) PtS ₂ /MoS ₂ device with
inset shows their respective device structure (c) Comparison plot of photocurrent of hare MoS2

and PtS ₂ /MoS ₂ device under 900 nm illumination light (d) Comparison temporal response of PtS ₂ /MoS ₂ and MoS ₂ device under 900 nm (3V) illumination (e) I-V characteristics of PtS ₂ under 400-1200 nm light illumination with inset displaying its device structure
diagram of PtS ₂ /MoS ₂ heterojunction after contact under equilibrium (V=0). Energy band gap diagram of PtS ₂ /MoS ₂ heterojunction under illumination (c) V<0 (forward bias with respect to PtS ₂) (d) V>0 (reverse bias with respect to PtS ₂)
photodetector with bare MoS ₂ device at 3V bias with variation with wavelength of 400-1200 nm
Figure 4.9 (a-i) Temporal response of PtS ₂ /MoS ₂ photodetector device under 400 nm-1200 nm light illumination at 3V bias
Figure 4.10 Temporal response of PtS ₂ /MoS ₂ device under the illumination of (a) 532 nm laser (5 mW) (b) 650 nm laser (5 mW) at 2V bias and 5Hz frequency (c), (d) represent the rise and fall time under 532 nm and 650 nm laser illumination, respectively, at 2V bias by considering their one respective cycle
Figure 4.11 (a) Fabrication steps of PtS _{2-x} thin film by TAC method (b) synthesis of Ga ₂ O ₃ film by sputtering (c) PtS _{2-x} /Ga ₂ O ₃ heterostructure schematic (d) PtS _{2-x} /Ga ₂ O ₃ heterostructure image
Figure 4.12 (a) Schematics of PtS _{2-x} /Ga ₂ O ₃ heterostructure (b) Raman spectra of PtS _{2-x} and PtS _{2-x} /Ga ₂ O ₃ thin films performed with 532 nm laser (c) Thickness of PtS _{2-x} thin film transferred on SiO ₂ /Si substrate measured by AFM (d) GIXRD of Ga ₂ O ₃ grown on Si substrate.
Figure 4.13 (a) XPS Pt 4f core level spectra of bare PtS _{2-x} and PtS _{2-x} /Ga ₂ O ₃ heterostructure (b) XPS Ga 3d core level spectra of bare PtS _{2-x} and PtS _{2-x} /Ga ₂ O ₃ heterostructure (c) Valence band maximum (VBM) of bare PtS _{2-x} and bare Ga ₂ O ₃ . The band gap of (d) PtS _{2-x} and (e) Ga ₂ O ₃ calculated using Tauc's plot method. (f) Type-I band alignment between the PtS _{2-x} and Ga ₂ O ₃ .
Figure 4.14 (a) Schematic of the PtS _{2-x} /Ga ₂ O ₃ device with external biasing V (b) Current-Voltage (I-V) characteristics of PtS _{2-x} /Ga ₂ O ₃ device under dark and 250-1100 nm wavelength illumination. I-T comparison of bare Ga ₂ O ₃ and PtS _{2-x} /Ga ₂ O ₃ under (c) 254 nm illumination at 4V (d) 1100 nm illumination at 5V.
Figure 4.15 (a) Variation of (a) Responsivity (b) Detectivity (c) External quantum efficiency (EQE) of PtS _{2-x} /Ga ₂ O ₃ device with wavelength range 250-1100 nm at 5V bias
Figure 4.17 I-T measurement showing the stability of the PtS _{2-x} /Ga ₂ O ₃ device after 5 months under illumination of (a) 254 nm at 4V (b) 600 nm at 5V (c) 1100 nm at 5V covering broad UV-C to near infrared (NIR) region
spectroscopy (LIPS) spectroscopy 84

Figure 4.21 Energy band diagram of PtS_{2-x}/Ga_2O_3 under (a) no bias V=0 (or equilibrium) (b)
Forward bias (V>0) with respect to Ga ₂ O ₃ . (c) Reverse bias (V<0) with respect to Ga ₂ O ₃ 84
Figure 5.1 Schematic showing the multiple steps used for the fabrication of PtSe ₂ /MoS ₂
heterostructure device
Figure 5.2 (a, b) Pt 4f and Se 3d core level XPS spectra of PtSe2 (c) Thickness of PtSe2
calculated by AFM and inset displaying its AFM image with step mark (d, e) XPS spectra of
Mo 3d and S 2p core levels of MoS2 (f) Thickness of MoS2 estimated by AFM with inset
shows the AFM image of step
Figure 5.3 (a) TEM image of PtSe2 showing different grains and polycrystalline nature (b)
HRTEM image of PtSe2 with different grains while the inset shows the interplanar spacing of
the selected planes (c) SAED pattern of PtSe2 film again shows the polycrystalline nature (d)
EDS spectra confirmed the growth of PtSe ₂ with different elements present in it
Figure 5.4 (a) X-ray diffraction (XRD) spectra of PtSe ₂ film grown on SiO ₂ /Si substrate (b)
AFM thickness of PtSe ₂ film transferred over MoS ₂ with inset its AFM image
Figure 5.5 (a) Schematic of PtSe ₂ /MoS ₂ heterostructure (b) Optical image of PtSe ₂ /MoS ₂
exhibiting its large area growth and high uniformity (c) FESEM image of PtSe ₂ /MoS ₂
heterostructure (d) Raman spectra of MoS2, PtSe2 and PtSe2/MoS2 film grown on SiO2/Si
substrates
Figure 5.6. I-V characteristics of (a) bare PtSe ₂ (b) PtSe ₂ /MoS ₂ heterostructure under dark and
400-1200 nm light illumination with inset Figure exhibit their device schematic (c) Dark
current comparison of PtSe ₂ and PtSe ₂ /MoS ₂ device with a ~10 ³ order ratio difference (d)
Detectivity comparison of PtSe ₂ and PtSe ₂ /MoS ₂ device under light illumination of 400-1200
nm at bias of -5V (e) Comparative current-time (I-T) response of PtSe2 and PtSe2/MoS2 devices
under 400 nm irradiation where PtSe ₂ /MoS ₂ demonstrate much more stability than PtSe ₂ (f)
multiple I-T cycles show high stability of the PtSe ₂ /MoS ₂ device measured under 600 nm light
and at -5V bias
Figure 5.7 Calculated (a) Responsivity, Detectivity, and (b) External quantum efficiency of
PtSe ₂ /MoS ₂ device under wide 400-1200 nm wavelength range with -5V biasing. (c)
Absorption spectra of PtSe ₂ , MoS ₂ and PtSe ₂ /MoS ₂ films grown on quartz substrate (d) I-V
plot of PtSe ₂ /MoS ₂ device under dark and power density of 500 nm light with inset shows the
power depended current linear fit graph (e) I-T response of PtSe2/MoS2 device under different
power density of 500 nm illumination (f) Responsivity variation of PtSe ₂ /MoS ₂ device with
different power density of 500 nm light irradiation
Figure 5.8 (a-i) Time-dependent photo response of PtSe ₂ /MoS ₂ device under broad 400-1200
nm wavelength range at -5V bias
Figure 5.9. (a) Schematic of the experiment set-up utilized to detect fast speed (µs) testing of
the PtSe ₂ /MoS ₂ device (b) Temporal response of PtSe ₂ /MoS ₂ device under 532 nm light
illumination at -5V with a chopping frequency of 2.8 KHz. (c) An enlarged single cycle shows
a rise and fall time of PtSe ₂ /MoS ₂ device under 532 nm illumination and 2.8 KHz chopping
frequency
Figure 5.10 (a) Band gap of MoS ₂ evaluated by Tauc plot (b) Valence band maxima (VBM)
of MoS ₂ calculated from ultraviolet photoelectron spectroscopy (UPS) measurements. Work
function of (c) MoS ₂ and (d) PtSe ₂ calculated from UPS measurements
Figure 5.11 Energy band diagram between PtSe ₂ and MoS ₂ under (a) equilibrium condition
and (b) under reverse bias

List of Tables

Table 1.1 The Reported literature of PtS ₂ and PtSe ₂ synthesized by CVD method	9
Table 1.2 The reported literature of PtS ₂ and PtSe ₂ synthesized by TAC method	10
Table 2.1 Incident beam Power density of each wavelength	30
Table 3.1 Comparison of our fabricated PtS2 photodetector performance with other re-	eported
literature based on TMDCs photodetector.	48
Table 4.1 Comparison of PtS ₂ /MoS ₂ photodetector device performance with reported	l MoS ₂
based heterostructures.	71
Table 4.2. Comparison of PtS _{2-x} /Ga ₂ O ₃ device with other Ga ₂ O ₃ heterostructure based re	eported
photodetector in literature.	80
Table 5.1. Performance Comparison of fabricated PtSe ₂ /MoS ₂ photodetector with other	r PtSe ₂
based reported heterostructures	103



Chapter-1: Introduction

This chapter starts with a brief introduction of the two-dimensional (2D) materials followed by group-10, transitional metal dichalcogenides (TMDCs) with particular focus on PtS₂ and PtSe₂. A detailed discussion on distinct properties of PtX₂ (X=S, Se) and their common synthesis methods are also described in this chapter. With focus on photodetector application of PtX₂ and their heterostructure, the important figure of merits of photodetectors and their working mechanism are also explained one by one. Finally, the chapter concludes with scope and objective of the current doctoral thesis.

1.1 Back ground

From the last few decades nano materials are highlighted for their distinct properties. The high surface-to-volume ratio, tunable electrical, mechanical and optical properties with size make them the first priority for the development of future micro electronics devices [1]. Owing to nano scale size, nano materials can be grown on flexible substrates and can be utilize in flexible electronics. After the fabrication of first two-dimensional (2D) material, graphene, by Geim and Novoselov for which they were awarded with 2010 Nobel Prize. Thereafter, 2D materials are the center of interest in the field of nano materials for their interesting properties. The high mechanical strength, high carrier mobility, high transmittance, and stability make graphene a wonder material [2]. However, owing to absence of band gap, it suffers from high dark current and low on-off ratio. Due to thinner nature, it is also victim of low absorption. Hence, to resolve this problem, many other 2D materials such as transitional metal dichalcogenides (TMDCs), black phosphorus (BP), and hexagonal boron nitride (h-BN) etc. have been synthesized in the laboratory. BP is well recognized for its wide tunable band gap (0.3 eV-1.8 eV), however, it suffers from poor air stability [3]. The h-BN is stable but its high band gap of ~ 6 eV restricts to use to detect the infrared radiation. Moreover, TMDCs are considered the best suitable materials for optoelectronics devices due to their moderate band gap and high ambient stability. In addition, thickness depended tunable band gap, strong light interaction, high absorption coefficient, and no dangling bonds make TMDC on high priority for basic and applied research [4, 5].

1.2 Transitional metal dichalcogenides

Transitional metal dichalcogenides (TMDCs) are unique materials with wide range of interesting properties as mentioned earlier and offer numerous opportunities to develop future

Chapter 1: Introduction

microelectronic and optoelectronic devices. TMDCs have great potential to develop transistors, photodetectors, gas sensors, catalysis, hydrogen evolution reactions, and many more [7-9]. The general nomenclature of TMDCs is MX₂, where M indicates a transitional metal varies from group 4 to 10 and X denotes the chalcogen (S, Se, Te), as exhibited in Figure 1.1 (a). The M and X exhibit a +4 and -2 oxidation state. MoS₂, WS₂, PtS₂, PtSe₂ and ReS₂ etc. are few examples of TMDCs. In Figure 1.1 (a), the highlighted elements mainly form the layered TMDC whereas the partially highlight elements (Co, Rh, Ir and Ni) exhibit layered structure with selective chalcogens. For example, NiTe₂ is a layered compound, while NiS₂ found to exist as an apyrite structure [8]. Each monolayer of layered TMDC consist of three atomic layers with layer of transitional metal (M) sandwich between two chalcogen layers with X-M-X structure. Within each X-M-X layer the M-X atoms are attached by covalent bond and weak van der Waals interaction is present between the interlayer. This weak van der Waals interaction makes these 2D materials easily exfoliate from their bulk 3D counterpart with a simple scotch tape that was also used during the synthesis of graphene [2]. Usually, the thickness of monolayer TMDCs is of the order of 0.6-0.7 nm. The metal coordination of the layered TMDCs can be either octahedral (O_h or D_{3d}) or trigonal prismatic (D_{3h}) as depicted in Figure 1.1 (b, c) [8]. MoS₂, which is a group-6 TMDC, is the most studied material. However, lately group-10 TMDCs such as PtS₂, PtSe₂ and PtTe₂, which bless with captivating properties including high carrier mobility, narrow band gap range and high ambient stability, have emerge a fascinating material [9-12]. Hence, to build broadband photodetector, a device that convert the light signal to electrical signal with high performance in NIR region, Pt-dichalcogenides are considered the best suitable materials. In the present thesis we will predominately focus on PtS₂ and PtSe₂.

$1.3 \text{ PtX}_2 \text{ (X=S, Se)}$

In recent years, group-10 TMDC, especially PtS₂ and PtSe₂ are highlighted for their interesting properties [11, 13]. Unlike MoS₂, the band gap of PtS₂ is highly tunable from 0.25 eV (in bulk) to 1.6 eV (for monolayer) which covers most of the near-infrared region [10]. Similarly, the band gap of PtSe₂ varies from 0 eV (semimetal for bulk) to 1.2 eV (for monolayer) which can go easily upto mid infrared region (MIR) [11]. For example, using mechanical exfoliation (ME) method Yu et al. have fabricated a bilayer PtSe₂ photodetector which can detect upto 10.0 μm wavelength (MIR region) [14]. Thus, narrow band gap of PtX₂ has a high potential to make high performance infrared or broadband photodetectors. Furthermore, a theoretical study by Huang et al. confirmed high carrier mobility of 3942 (4038) cm²V⁻¹s⁻¹ for PtS₂ (PtSe₂) [12].

Chapter 1: Introduction

Experimental study of Zhao et al. have fabricated a few layers $PtSe_2$ FET using ME method and demonstrated its high room temperature carrier mobility (~210 cm²V⁻¹s⁻¹) and high ambient stability (>1 year) [11]. In another work by Wang et al. have shown that few layer PtS_2 based field effect transistor (FET) has a high on-off ratio of 10^6 and room temperature carrier mobility of 62.5 cm²V⁻¹s⁻¹ [15]. Thus, these fundamental studies have corroborated that PtX_2 are promising materials for future optoelectronics devices.

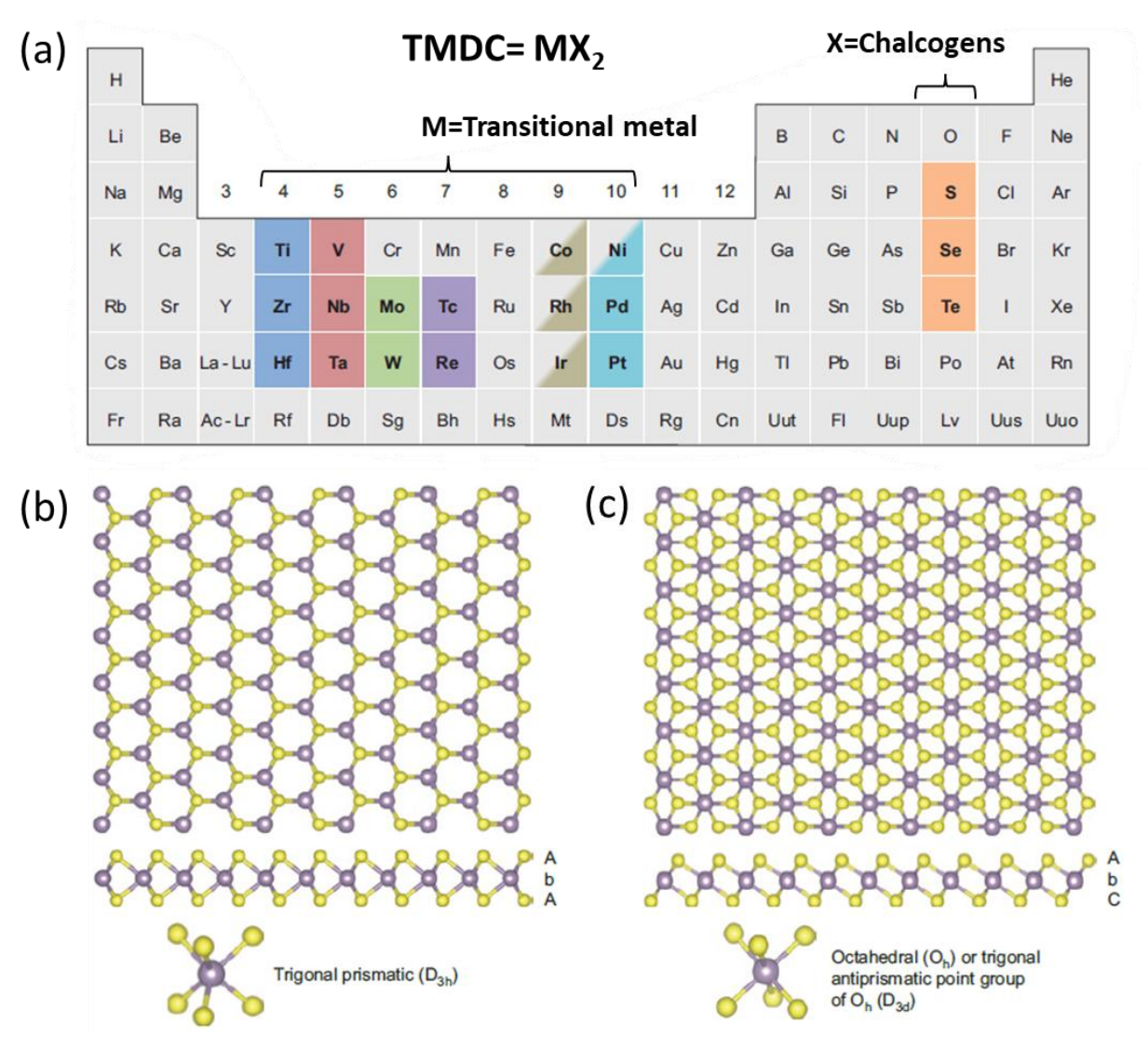


Figure 1.1 (a) Periodic table showing the elements forming the TMDC compounds with transition metals (group 4-10) and chalcogens. The complete highlighted elements mainly form layered TMDC, whereas partially highlighted (Co, Rh, Ir and Ni) exhibits that selected dichalcogenides form layered structure. (b, c) crystal structure view of atoms along top, side of single layer TMDC with trigonal prismatic (b) and (c) octahedral coordination [8].

1.4 Properties of PtX₂ (X=S, Se)

1.4.1 Crystal structure

Single layer TMDC can exist in two coordinate phases, 2H (D_{3h} , trigonal prismatic) or 1T (D_{3d} , octahedral) as depicted in Figure 1.1 (b, c) [8]. Most of the group-6 TMDC possesses 2H phase, however, for the case of group-10 PtX₂, 1T phase is more stable. The reason behind this can be explained on the different number of d-electrons present in the valance shell. Group-10 metals contain rich d electrons and few d-orbitals are involved in coupling, hence they mostly tends to form d^2sp^3 hybridization and thermodynamically favored 1T phase [10]. In 1T phase or octahedral structure, each Pt atom is coordinated with other six X (=S, Se) atoms and each Pt atom layer is sandwiched between two X chalcogens layers as shown in Figure 1.2 (a, b). The crystal structure of PtS₂ belongs to P-3m1 space group with unit parameters, a= b= 0.3537, c=0.5019 nm, $\alpha=\beta=90^{\circ}$, $\gamma=120^{\circ}$. The PtSe₂ crystal related to D_{3d}^3 (P $\bar{3}$ m1) space group and unit cell parameters are a= b= 0.3731, c=0.5072 nm, $\alpha=\beta=90^{\circ}$, $\gamma=120^{\circ}$ [16].

1.4.2 Electronic band structure

The electronic band structure of TMDCs mainly relies on number of d-electrons and coordination environment of the metal atoms [17, 18]. In PtX₂ (X=S, Se), owing to strong interlayer interaction, their band gap is highly tunable with number of layers. Zhao et al. have evaluated the band structure of monolayer PtS₂, as shown in Figure 1.3 (a) with an indirect band gap of 1.8 eV [10]. In the same band diagram nearly two degenerate (difference of 0.1 meV) valence band maximum (VBM) exist between the K- Γ and Γ -M sides and the conduction band minimum (CBM) lies between the Γ and M symmetry points [11]. For bilayer PtS₂, the band gap value reduces to 0.99 eV maintaining indirect nature but position of VBM (CBM) shifted towards the Γ (K) points and finally converse to these points for bulk PtS₂ as depicted in Figure 1.3 (b). The experimentally calculated band gap for different PtS₂ layers is shown in Figure 1.3 (c) with value of 0.25 eV (for bulk) and 1.6 eV (for monolayer). Figure 1.3 (d) exhibits the comparison plot of the band gap calculated by experimentally and theoretically which follows the same trend (decrease with increasing thickness) [10].

The band gap of PtSe₂ decreases with increasing the thickness and beyond few layers it behaves as a semimetal. Zhao et al. have calculated the band structure of PtSe₂ by DFT [11]. Figure 1.4 (a) exhibits an indirect band gap of 1.17 eV for the monolayer PtSe₂ where VBM is located at the Γ point, comprised of Se p_x and p_y orbitals. The position of CBM, contributed by the p states of Se and d states of Pt atoms lies between the Γ and M points [11]. Figure 1.4 (b)

exhibits the band structure of bulk PtSe₂ with VBM value exceeding that of CBM value and semimetal behavior is confirmed. Moreover, when move from monolayer to bulk PtSe₂, semiconductor to semimetal transition occurred, attributed to the strong interlayer interaction between the layers. The band gap calculated for different PtSe₂ thicknesses by Tuac plot is depicted in Figure 1.4 (c), where for monolayer PtSe₂ the value is 1.13 eV and for bulk no band gap is observed [11].

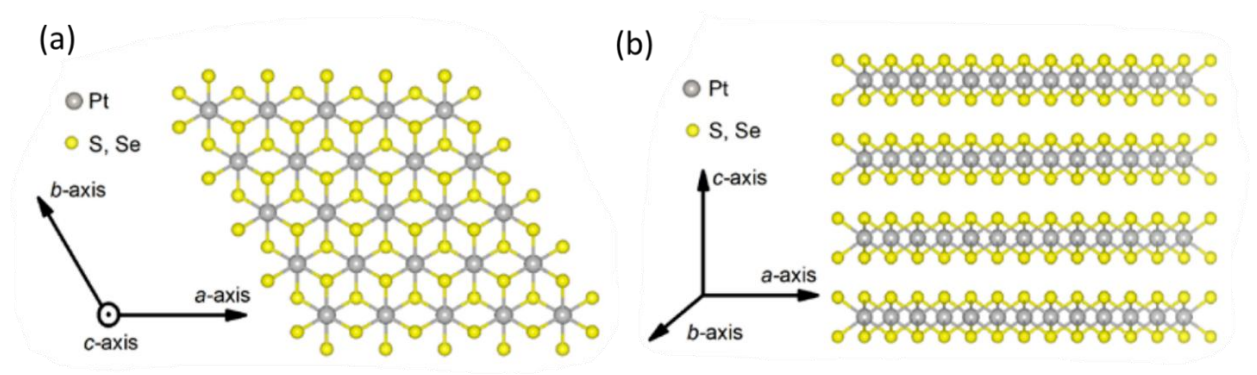


Figure 1.2 Crystal structure of PtS₂ and PtSe₂ with atoms arrangements under different direction views [16].

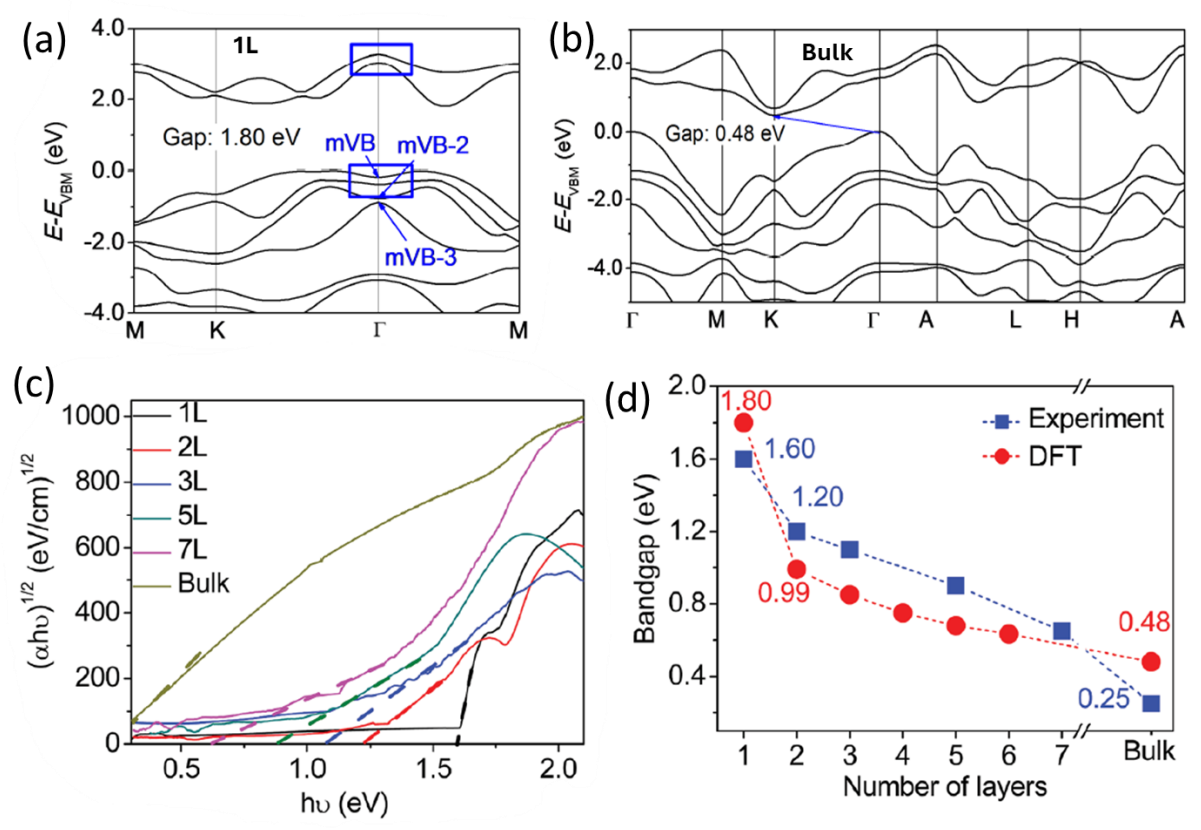


Figure 1.3 Electronic band structure of (a) monolayer (1L) (b) bulk PtS₂ (c) Band gap calculated for different thickness PtS₂ layers by Tuac plot (d) Variation of experimentally and theoretically (DFT) calculated band gap of PtS₂ with thickness [10].

1.4.3 Vibration mode (Raman) of PtX2

Raman spectroscopy is widely employed as a characterization technique in the area of 2D materials. Its non-destructive nature and ease of use make it very popular. It is mainly used to study the lattice vibrations, defects, or strain present within the material. For the case of PtS₂, three prominent vibration modes E_g^1 , A_{1g}^1 and A_{1g}^2 are observed as shown in Figure 1.5 (a), where $E_g^{\ 1}$ is the in-plane vibration mode and later two, $A_{1g}^{\ 1}$ and $A_{1g}^{\ 2}$, are out of plane vibrations modes [10]. With increasing thickness of PtS_2 , the E_g^{-1} mode blue shifted while A_{1g}^{-2} red shifted and almost no change in A_{1g}^{1} mode, as displayed in Figure 1.5 (a). Figure 1.5 (b) exhibits the variation of peak positions of different vibration modes of PtS₂ with number of layers [10]. The Raman spectra of PtSe₂ at different thickness is display in Figure 1.5 (c) with two prominent peaks, Eg and Alg. The former peak Eg corresponding to the in-plane vibration mode and later A_{1g.} peak related to the out of plane vibration mode [19, 20]. Apart from these two peaks another small peak called longitudinal optical (LO) mode, which is the resultant of A_{2u} and E_u infrared active modes, also observed [19]. Figure 1.5 (c) illustrates the thickness depended Raman spectra of PtSe₂ in which the position of E_g mode highly red shifted with increasing thickness while A_{1g} mode a little red shifted upto seven number of layers then largely red shifted for higher PtSe₂ thickness, as also demonstrated in Figure 1.5 (d). The schematic showing the different vibration modes in PtSe₂ is shown in Figure 1.5 (e) [20].

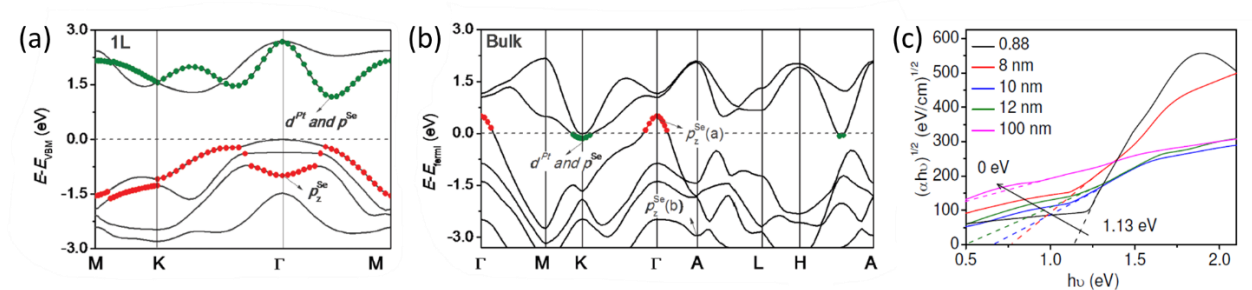


Figure 1.4 Electronic band structure of (a) Monolayer (1L) and (b) bulk PtSe₂ (c) Tuac plot using experimentally band gap calculated for different PtSe₂ thickness [11].

1.5 Synthesis Methods of PtX₂ (X=S, Se)

In this section, we briefly discuss the common synthesis method employed for the growth of PtS₂ and PtSe₂. The synthesis approach plays a critical role in determining the film quality, size, and device performance. Conventionally, thin film can be grown by two approaches, top-down and bottom-up methods [21]. In top-down method, thin films are achieved by breaking down the interlayer interaction of the bulk crystal under the presence of external force. Whereas in bottom-up method, the film is grown by sequentially atoms or molecules deposition.

However, in present section we will discuss only the most common method used for the growth of PtS₂ and PtSe₂.

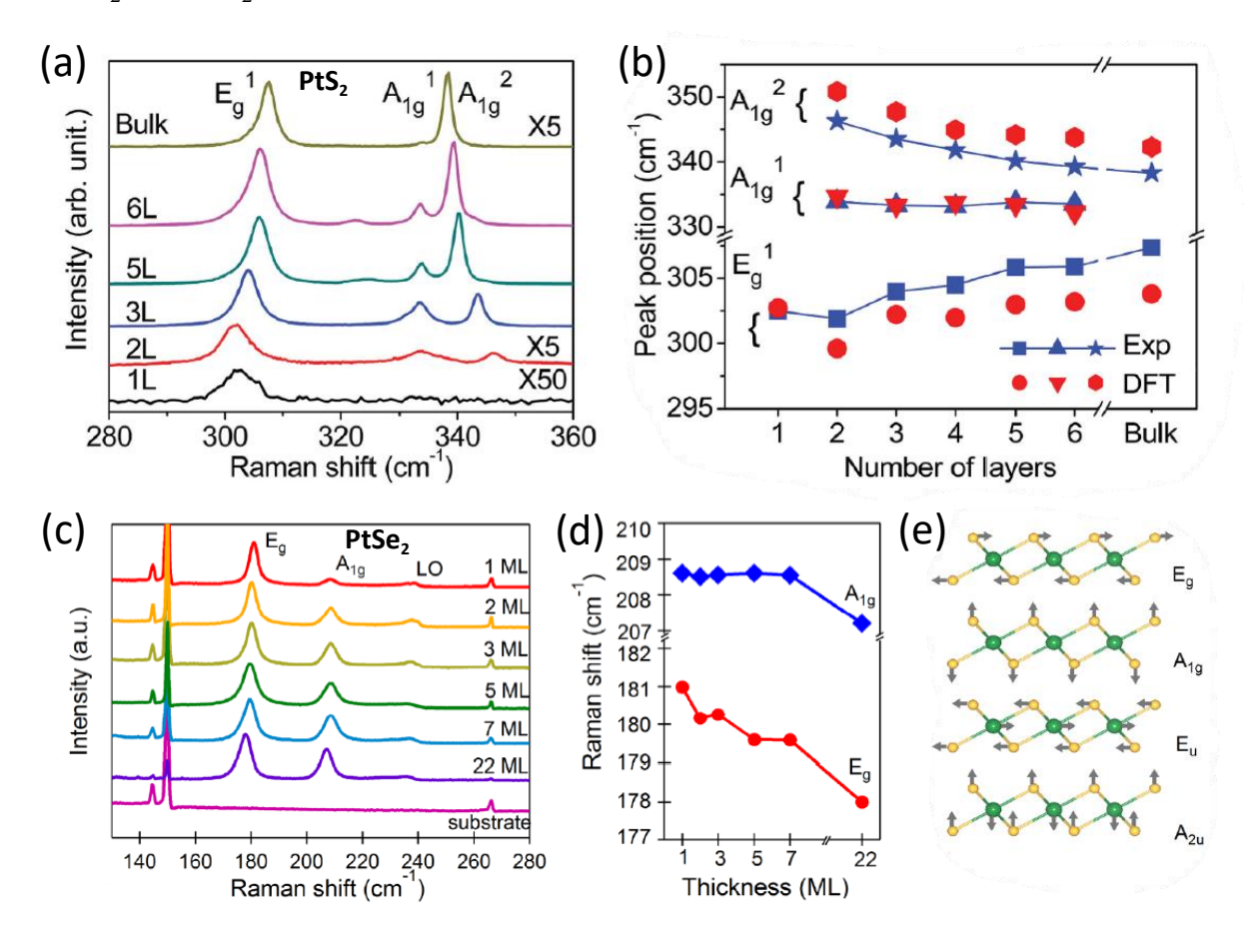


Figure 1.5 (a) Layer depended Raman spectra of PtS_2 under 633 nm laser illumination. (b) Peak position variation of E_g^1 , A_{1g}^1 and A_{1g}^2 vibrational modes with increasing number of layers. (c) Layer depended Raman spectra of $PtSe_2$ (d) Thickness depended peak position variation of A_{1g} and E_g vibration modes of $PtSe_2$ (e) Schematic showing the Raman vibrational mode in $PtSe_2$ [11, 22].

1.5.1 Mechanical Exfoliation

Mechanical exfoliation (ME) is a top-down technique and most commonly utilized method to obtain 2D materials including graphene, h-BN, and TMDC. In this method monolayer to multilayer films can be achieved by peeling off the high-quality bulk crystal using adhesive tape (mostly scotch tape), as shown in Figure 1.6 (a) [22]. The repeated adhesion and splitting of the exfoliated bulk crystal over tape breaks the inter Van der Waals interaction and then transfer on the required substrate. Using same ME method, Zhao et al. have fabricated monolayer to few-layer PtSe₂ and PtS₂ films with high crystalline quality [10, 11]. This method gives high quality of 2D layers with clean surface and crystallinity, and consider the best

method for fundamental research. However, low yield, less thickness control, and non-uniformity are the few limitations of this method.

1.5.2 Chemical vapor deposition

Chemical vapor deposition (CVD) is a well-known bottom-up technique utilized to grow high quality 2D materials with controllable thickness, scalable size, and crystallinity. In CVD, film is deposited by chemical reactions between the precursors occur in the enclosed chamber (tube) under the presence of high temperature. Usually, the precursors are evaporated upto the desired temperature and transport by carrier gas flow and finally film is deposited on the target substrate with a chemical reaction. Some volatile by-products often generate during the chemical reaction are extracted from the tube by the gas flow stream. For the growth of PtSe₂, the common Pt precursors like PtCl₄, PtCl₂, H₂PtCl₆ and Se powder are used, as illustrated in Figure 1.6 (b) [14, 23-25]. Whereas for the growth of PtS₂, owing to limited literature, PtCl₂ and S powder are only used precursors so far [26, 27]. The quality of growth film directly depends upon the growth parameters such as precursors amount (or type), growth temperature, pressure, carrier gas flow rate, substrate position and distance from precursors etc [28]. However, high-temperature need, toxic precursors, uniformity issue on large area are few constraints in CVD process. The reported literature of synthesis of PtS₂ and PtSe₂ by CVD is mentioned in Table 1.1.

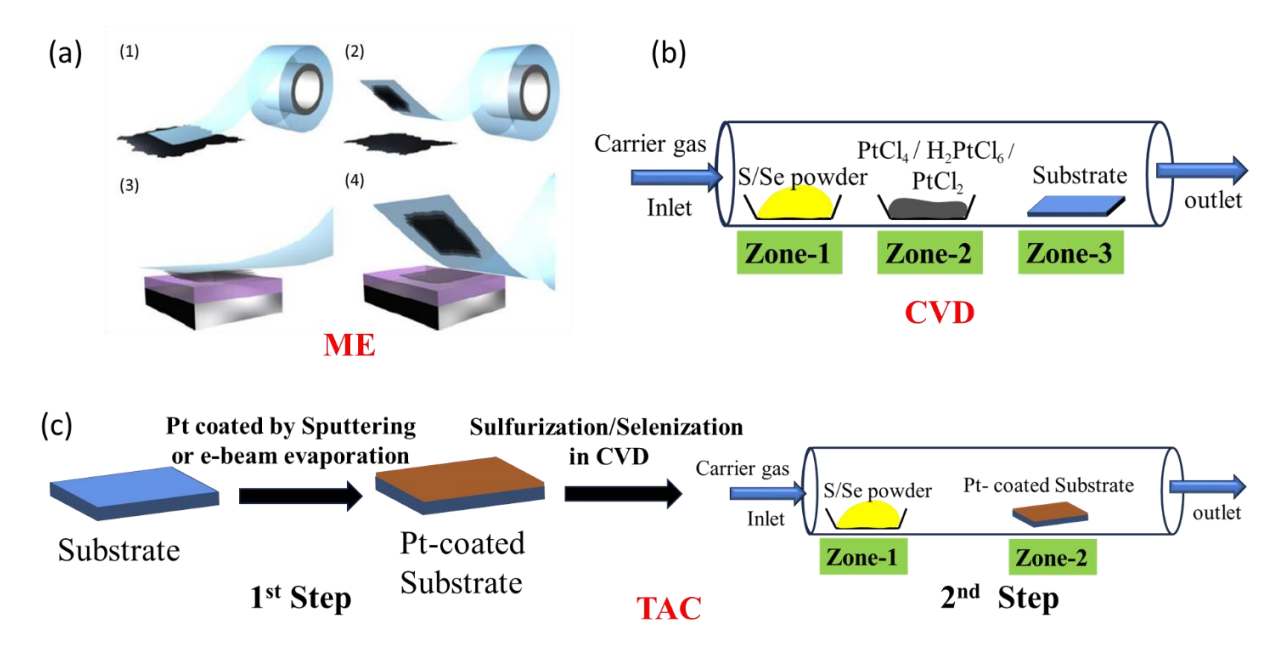


Figure 1.6 Common synthesis methods to grow PtX₂ film (a) Mechanical exfoliation (ME) method (b) Chemical vapor deposition (CVD) method, where Pt and S/Se precursors are used in powder form and also known as one-step CVD (c) Thermally assisted conversion (TAC) method or also known as two-step CVD method [22].

Table 1.1 The Reported literature of PtS₂ and PtSe₂ synthesized by CVD method

Material	Substrate	Precursors	Precurs	or tempe	rature (°C)	Gas flow rate	PtX ₂	Ref.	
			Se or S	Pt Substrate		(sccm)	thickness (nm)		
	Sapphire	H ₂ PtCl ₆ , Se	300	200- 900	900	100 (Ar) +10 (H ₂)	3.5-10	[24]	
	Sapphire	PtCl ₄ , Se	200	300	500	200(Ar) +20 (H ₂)	1.6, 2.8	[29]	
	Au foil	PtCl ₂ , Se	450	800- 850	850	85 (Ar) +15 (H ₂)	0.8, 1.5, 2.2	[30]	
PtSe ₂	SiO ₂ /Si	PtCl ₄ , Se	200	310	500	210 (Ar) +25 (H ₂)	1.85	[31]	
	SiO ₂ /Si	PtCl ₄ , Se	200	310	500	210 (Ar) +25 (H ₂)	2.00	[32]	
	Sapphire	PtCl ₄ , Se	200	400	400	90 (Ar) +10 (H ₂)	2.0-7.8	[33]	
	Sapphire	PtCl ₂ , Se	NA	NA	350-450	60 Ar	2.2	[34]	
PtS ₂	Au foil	PtCl ₂ , S	250	750- 850	NA	80 (Ar) +10 (H ₂)	0.71	[27]	
_	Mica	PtCl ₂ , S	250	650- 750	NA	90 (Ar) +10 (H ₂)	1.36	[26]	

1.5.3 Thermally assisted conversion

For the growth of group-10 TMDC, thermally assisted conversion (TAC) is most popular method [35-39]. It is two-step method where 1st step involves the growth of thin film of transition metal (Pt for present case) using either via sputtering or electron beam evaporation (EBE) process. In the 2nd step, the same Pt coated film is sulfurized (selenization) in the CVD for growth of PtS₂ (PtSe₂), respectively, as exhibited in Figure 1.6 (c). TAC is the best method to grow large area, controllable thickness and high crystallinity quality of 2D materials. The thickness of 2D material can be control by modulating pre metal (Pt) coated film thickness. In 2015, Wang et al. used same approach to grow single crystal monolayer PtSe₂ by selenization of Pt (111) substrate in ultrahigh vaccum [40]. Moreover, they have also shown that monolayer PtSe₂ possesses a semiconductor nature by Angle resolved photoemission spectroscopy measurements (ARPES) [40]. Xu et al. have grown a large area PtS₂ film by using the TAC method with S temperature of 200°C and Pt-coated substrate temperature of 400-500 °C. Usually, during the growth of PtX₂, lower temperature (~500 °C) is needed than MoS₂ (~800 °C), which is beneficial to grow PtS₂ on multiple substrates. Table 1.2 demonstrates the reported literature of PtSe₂ and PtS₂ synthesized by TAC method.

Chapter 1: Introduction

Table 1.2 The reported literature of PtS2 and PtSe2 synthesized by TAC method.

Material	Substrate	Pt deposited	Pt Thickness	Growt	th temperat	PtX ₂	Ref.		
		by	(nm)	Se or Pt- S coated		Gas flow rate (sccm)	thickness (nm)		
	SiO ₂ /Si	Sputtering	1-5	~220	400	150 (Ar/H ₂ =9:1)	6-29 L	[36]	
	SiO ₂ /Si	Sputtering	0.5-5	~220	450	150 (Ar/H ₂ =9:1)	NA	[19]	
	SiO ₂ /Si	Sputtering	0.5, 12	220	420	50 (Ar)	~35	[38]	
	SiO ₂ /Si	Sputtering	NA	220	450	50 (Ar)	~37.2	[37]	
	SiO ₂ /Si	Sputtering	NA	220	450	50 (Ar)	~22	[35]	
PtSe ₂	SiO ₂ /Si	EBE	0.8	220	450	60 (Ar)	~2.7	[41]	
	SiO ₂ /Si	EBE	0.75-10	~200	400	100 (Ar)	4-5 times of Pt	[42]	
	SiO ₂ /Si	EBE	NA	NA	400	NA	NA	[43]	
	Si	EBE	~5	~220	~450	50 (Ar)	13 (or 17L)	[39]	
	SiO ₂ /Si	Sputtering	1	NA	~460	50 (Ar)	~3.2	[44]	
	SiO ₂ /Si	NA	NA	~200	400-500	100 (N ₂ /H ₂ =9:1)	NA	[45]	
PtS ₂	SiO ₂ /Si	Sputtering	0.5-5	NA	500	150 (N ₂ /H ₂ = 9:1)	0.5-20	[46]	
	SiO ₂ /Si	Sputtering	3.4	280	800	10 (Ar)	12.7	[47]	
	SiO ₂ /Si	Sputtering	NA	300	500	75 (1.1% H ₂ +Ar)	5	[48]	

L=number of layers, EBE= electron beam evaporation

1.6 Applications of PtX₂ (X=S, Se)

Both PtS_2 and $PtSe_2$ have shown great potential in various applications including field effect transistors, photodetectors, photocatalysis, hydrogen evolution reactions, gas sensors etc [18, 40]. Since band gap (E_g) of PtS_2 (E_g =0.25-1.6 eV) and $PtSe_2$ (E_g =0-1.6 eV) largely lie in the infrared region, so they are appropriate materials for near-infrared detection. Besides this, high mobility and stability further make them more highlighted to design fast speed future optoelectronic devices. Herein, we focused on the PtX_2 (X=S, Se) and their heterostructure based photodetector applications.

1.7. Photodetectors

Photodetectors are optoelectronic devices which detect the particular region of light signals by converting them into electrical signals. Depending upon the detection region they can be divided into near-infrared (NIR), ultraviolet (UV), and broadband photodetector which directly rely on the band gap of the material. When photodetector is under illumination with photons energy equal to or greater than the band gap of material, electron-hole pairs are generated and get separated by induced built-in potential or external bias and photocurrent is produced. The general schematic of photodetector device is exhibited in Figure 1.7 (a) which consist of active material, electrodes, and external bias. Photodetectors have numerous applications in optical communications, biomedical imaging, remote sensing, defense security, and astronomy [9, 48, 49]. Hence to develop high-performance photodetector is very essential.

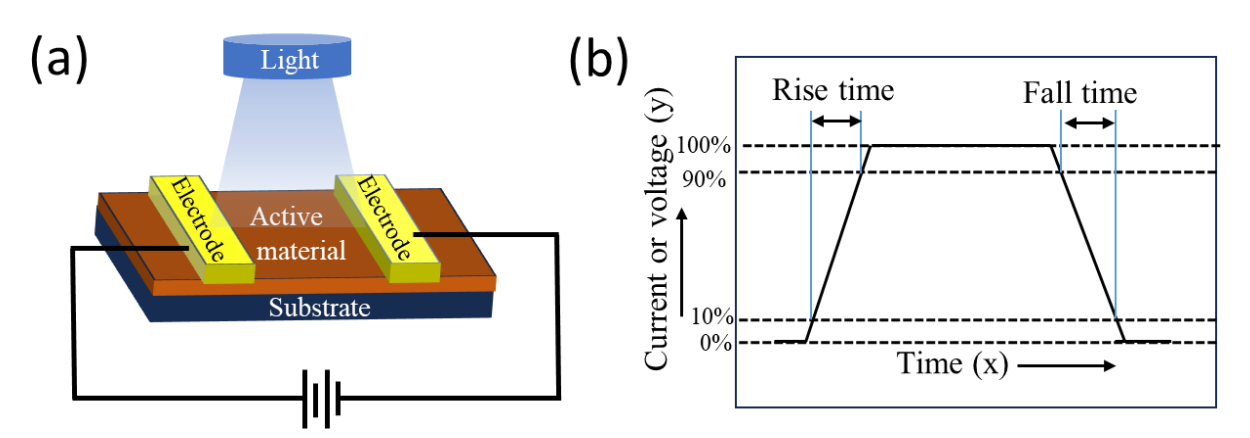


Figure 1.7 (a) Schematic of a Photodetector (b) schematic of a response time with rise and fall time.

1.7.1 Figure of merits of photodetectors

The performance of the photodetector (PD) can be measured from its figures of merit, which also helps to do the comparison with commercial detectors or reported literature. These parameters are briefly discussed below.

Dark Current (I_{dark}): The dark current as name suggests is the current generate in the PD when no light falls on it. Dark current predominately produce due to flow of charge carriers generated under thermal excitation across the band gap or with the assistance of trap states within the band gap [50]. The dark current extensively affects the sensitivity (defined later) and performance of the device. A high dark current can cause overshadow to detect weak signals and lead to low sensitivity.

Responsivity (R): It is the ratio of net photocurrent produced per incident optical power, mathematically it is defined by

$$R = \frac{I_{light} - I_{dark}}{P.A}$$

Where, , I_{dark} is the dark current, I_{light} is the current produce under light. P is the optical power density of the illuminated light and A is the light illuminated effective area. The responsivity depends upon the absorption of the material and incident optical power density.

Specific Detectivity (D*): It signifies how a weak light signal a PD can detect; it is also called sensitivity of the PD. Mathematically it is given by:

$$D^* = \sqrt{\frac{A}{2eI_{dark}}} \times R$$

Where A, e and I_{dark} are the effective area under illumination, charge on the electron and dark current, respectively. R is the responsivity of the PD, as defined above. D* is usually measured in Jones (cm $Hz^{1/2}$ W⁻¹). Other definition of detectivity (D*) when noise is much larger than the dark current is defined by:

$$D^* = \frac{\sqrt{AB}}{NEP}$$

Where A is effective area, B is band width and NEP is the Noise equivalent Power.

Quantum efficiency- The ability of the PD to produce number of electron-hole pairs under light irradiation is called quantum efficiency. The important thing is that not all electron-hole pairs generated initially contribute to the final current because many times recombination of electron-hole pairs can happen and resulting smaller number of carriers reach to the electrodes. Therefore, under illumination, depending on number of electrode-hole pairs initially generated and final reach to the electrode (contribute to the current), quantum efficiency is defined in two forms- External quantum efficiency (EQE) and Internal quantum efficiency (IQE). The IQE is the number of electron-hole pairs generated within the material per incident photons per sec. The EQE is described as the number of electron-hole pairs collected by the electrodes (contribute to the current) per incident photons per sec. Commonly, EQE is preferred over IQE and mathematically given by:

$$EQE = \frac{Rhc}{e\lambda}$$

Chapter 1: Introduction

Here c, e, λ , h and R are the speed of light (in air), electronic charge, wavelength of incident light, Plank's constant and responsivity of the PD, respectively.

Response time-To check the speed of the PD, how fast it works is usually measured from its response time, lower the response time means faster the speed of the PD. Response time is measured in seconds (s). Experimentally, response time is measured in terms of rise and fall time, where rise time is the time taken from 10% to 90 % of the net current value and decay time is the time taken from 90% to 10% of the net current value as illustrated in Figure 1.7 (b).

Photoconductive gain- The ability power of device to generate multiple carriers by a singular photon is study by photoconductive gain. This parameter also helps to explain the reason for getting more than 100% EQE value. It is given by

$$G = \frac{\tau_{life}}{\tau_{tran}}$$

Where τ_{life} and τ_{tran} are carrier life time and transit time respectively, τ_{tran} further depends upon applied bias (V_{bias}), length of the channel (L) and carrier mobility (μ) as below

$$\tau_{tran} = \frac{L^2}{\mu V_{bias}}$$

1.7.2. Working mechanism of a photodetector

The working of the PDs is usually defined as three step process (1) generation of photoinduced carriers under illumination of light (2) transport of photoinduced carriers (3) extraction of charge carriers or production of current at the electrodes. The performance of the PDs depends upon the architecture of the device, absorption coefficient, wavelength (or intensity) of the incident light, electrodes nature, and biasing to the materials. Depending upon these parameters, there may be different mechanisms of current production.

Photo conductive effect (PCE)- In this type of PD the current is generated due to change in the conductivity (or increase in electron-hole pairs concentration) of the material. Device under illumination with photons energy more than band gap of material generates more number of electron-hole pairs as compared to in dark and further this leads to difference in their conductivity. The excess electron-hole pairs are separated by external bias. Under biasing, the net photocurrent (I_p) generates in the device is the difference between current under light (I_{light}) and dark (I_{dark}) i.e I_p = I_{light} - I_{dark} . In photoconductor device, the external bias is needed to

Chapter 1: Introduction

separate the electron-holes pairs and ohmic contact is preferred. Normally large dark current, low detectivity and slow response time are few drawbacks of PCE based PDs.

Photo voltaic effect (PVE)- The problem of high dark current and slow speed in photoconductor devices can be resolved in Photovoltaic detector. Usually, it consists of two different types of doped semiconductors having different polarity to make p-n junction at the interface. Due to the p-n junction formation, a strong built-in electric field generated at the junction, which further helps in separation of light illuminated charge carriers and produced current. Furthermore, the built-in-electric potential induced at the junction, sometime give additional advantage of its self-bias working where no external biasing is required. Also, Schottky barrier photodiodes are sub types of photovoltaic PD, in which Schottky barrier is formed between the metal and semiconductor, and due to this barrier the dark current reduces. PDs following PVE depict non-linear current-voltage (I-V) characteristics.

Photogating effect- It is a special case of Photo conducting effect, in which trap states or defects are used to increase the carrier life time of the charge carriers and hence responsivity of the photodetector can be modulated. Under light illumination, when electron-hole pairs are generated then one type of charge carrier (either hole or electron) traps in these trap states, and opposite charge carrier continues move through the circuit until it recombine with opposite charge carrier or reach to the electrode which leads to an increase in gain and responsivity of the PD. Photogating devices are mostly used where we want to increase the responsivity of the photodetector.

Photothermoelectric effect- In photothermoelectric effect, photovoltage in the semiconductor device is produced due to a local temperature gradient induced by non-uniform heating. Specifically, when the illuminated laser spot area is smaller than the semiconductor channel, then it generates a temperature difference (ΔT) across the two ends of the device channel. This temperature difference then generates a photovoltage via the Seebeck effect which is proportional to the temperature difference.

Photobolometric effect- This effect depends upon the resistivity change of the heat-sensitive material. Under thermal irradiation and external biasing, the resistance of the material either increase or decrease and corresponding the current across the device also change. The main difference between the Photobolometric effect and Photothermoelectric effect is that for Photobolometric effect we always need external bias (similar to photo conductive effect), whereas Photothermoelectric effect can work without bias as well.

1.8 History and current Scenario in the field of PtX₂ based photodetectors (PDs)

The 1st PtS₂ based phototransistor was fabricated by Li et al. group using a mechanical exfoliation method in 2017 [55]. In this work, they compared the performance of PtS₂ FET devices grown on SiO₂/Si and hBN-coated SiO₂/Si substrates. The device made of few layers of PtS₂ grown on h-BN coated SiO₂/Si substrate exhibited a high responsivity of 1560 AW⁻¹ but with a slow response of 0.46 s. In 2018, Yuan et al. fabricated a PtS₂/PtSe₂ photodetector that showed a broad response of 405-2200 nm and fast response of 66 ms /75 ms (rise time/fall time) [41]. Yu et al. fabricated the 1st bilayer PtSe₂ photodetector using mechanical exfoliation, which exhibited a wide response from 632 nm to 10 μm (mid-infrared region), high responsivity of 4.5 AW⁻¹, and rise /fall time of 1.2 ms/1.2 ms [14]. Figure 1.8 (a, b) exhibits the progress in research so far reported in PtS₂ (PtSe₂) and its heterostructure based photodetector performance, which clearly shows the inevitable trade-off between the response time and responsivity. The rectangular shaded region in both the graph of Figure 1.8 (a, b) is the required target performance of these photodetectors to enable them for commercialization and use for future optoelectronic devices.

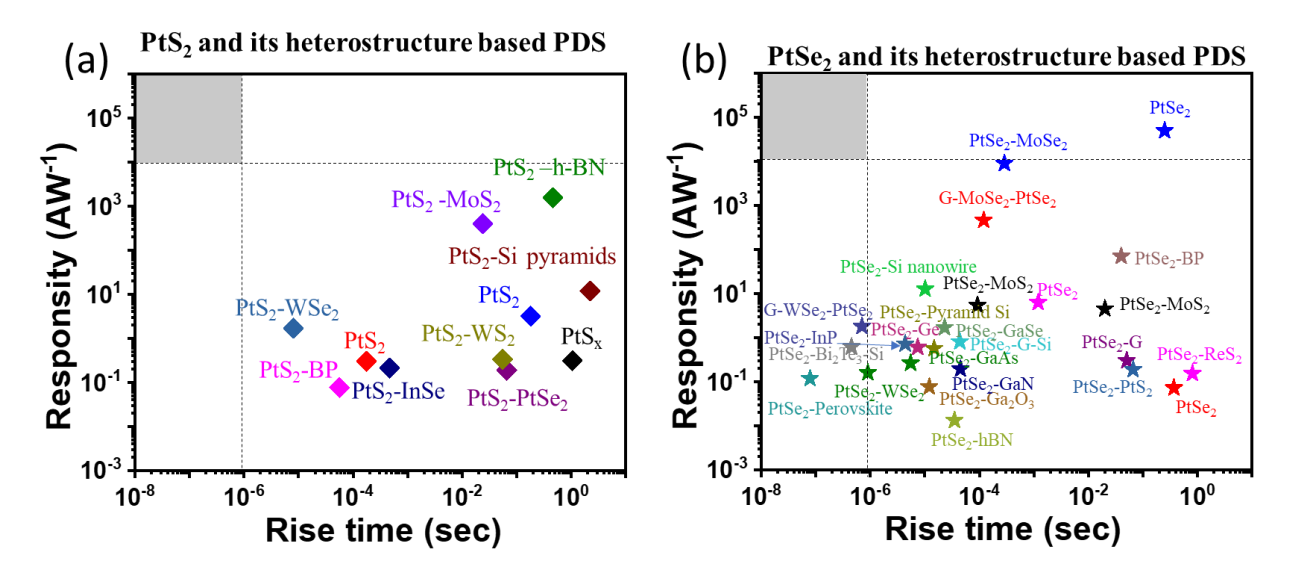


Figure 1.8 Performance comparison in the current scenario in (a) PtS₂ and its heterostructure (b) PtSe₂ and its heterostructure based photodetectors (PDs). The data in Figures has been taken from Ref. [15, 37, 38, 44, 51-70].

1.9 Types of Heterostructure

Although bare TMDCs are considered suitable materials for broadband photodetection, still they endure from limited light absorption, high recombination rate, limited light detection range, and slow response. To compensate this issue, make their heterostructure with

appropriate candidate is best strategy to enhance the overall device performance. Heterostructures are combination of two different semiconductor materials having different band gaps and nature. Heterostructure helps to enhance the overall device performance by modulating their absorption, increase broad detection range, and enhance detection speed. The built-in potential created at the heterojunction assists in rapid charge carrier separation and tune the device properties from their constitute materials. Depending upon the stacking pattern, heterostructure may be lateral or vertical. Furthermore, depending on type of band alignment between the composite materials, heterostructure can be classified as type-I (Straddling gap), Type-II (Staggered gap), and type-III (Broken gap) heterostructures as exhibited in Figure 1.9

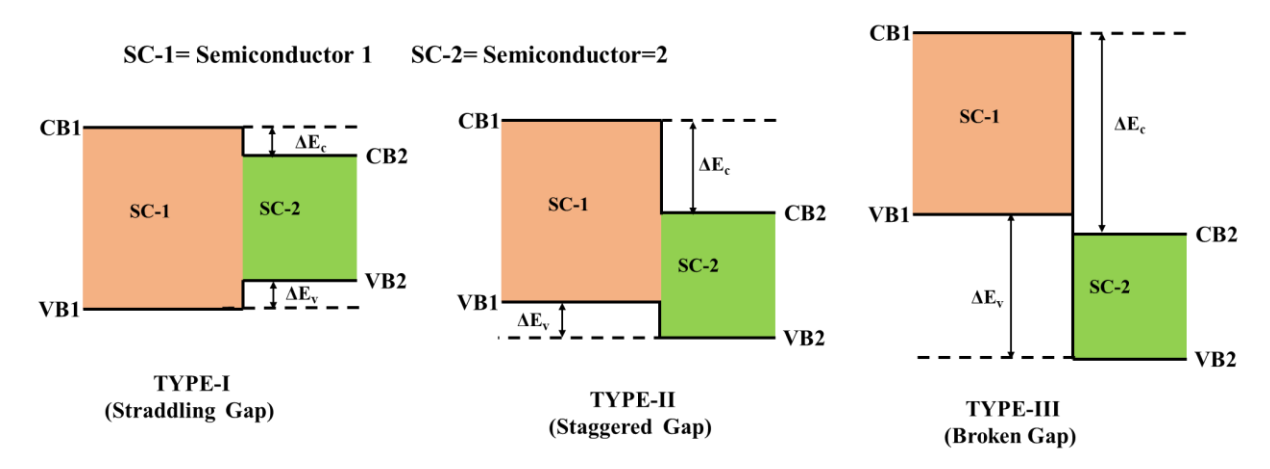


Figure 1.9 Different type of heterostructures based on their band alignment.

1.10 Challenges and Motivations

The main challenge during the growth of PtS₂ by thermally assistant conversion (TAC) is the formation of intermediate phase PtS which is easily formed due to its more stability than PtS₂ [45, 46]. Therefore, it is very difficult to precisely control the growth of PtS₂. Moreover, scalable growth of PtS₂ on multiple substrates with a single approach was also not explored. To mitigate these problems, understanding of growth parameters like pre Pt-coated thickness, sulfur amount (during sulfurization), and carrier gas flow rate in CVD can play an imperative role to control the growth of PtS₂. Optimizing these parameters and understanding of growth mechanism can assist to optimized the growth of PtS and PtS₂.

During the fabrication of photodetector, it becomes very essential to build device with high responsivity, broad detection and fast speed. However, in a single TMDC material it is very rare to find all these things simultaneously. For example, group-6 TMDC, especially MoS₂ has a band gap of 1.2-1.8 eV, which mostly lies in the visible region and also exhibits maximum response in this range. In addition, moderate mobility, finite absorption, and lack of strong

Chapter 1: Introduction

built-in potential make its overall device performance inferior. Similarly, in the case of Ga₂O₃ which has a band gap of 4.5-4.9 eV and best known for ultraviolet (UV) detection, but has a trivial response in visible and NIR regions. In such cases, building their heterostructure with a potential material, such as PtS₂, governed with a narrow band gap range (0.25-1.6 eV) and high mobility is the best approach. Heterostructure can modulate the device performance by generating built-in potential, increasing absorption, and fast carrier separation.

Group-10 TMDC, PtSe₂ became the first choice for fabricating infrared photodetectors attributed to its narrow band gap (0-1.2 eV), high carrier mobility, and ambient stability. Despite this, PtSe₂ exhibits a high dark current and substandard on-off ratio ascribed to its narrow or semimetal nature. Again, the best remedy to reduce dark current and enhance the device's performance is to build a heterostructure. Heterostructure can create a barrier height at the heterojunction which limits the flow of the charge carrier under dark and helps to reduce the dark current. Moreover, strong built-in potential generated at the heterojunction further supports in fast carrier separation and increase the speed of the device.

1.11 Objectives of the present thesis work

- 1. Controlled and large-area growth of PtS₂ on various substrates and its photodetector studies.
- 2. Fabrication of large area PtS₂ heterostructure (PtS₂/MoS₂, PtS_{2-x}/Ga₂O₃) based broadband photodetector.
- 3. In-depth interface study of PtS₂ heterostructure, PtS₂/MoS₂, PtS_{2-x}/Ga₂O₃ and their band alignment.
- 4. Increase the performance of bare PtSe₂ photodetector by making its heterostructure to reduce dark current and achieve ultra-fast response time.

1.12 Outline of the thesis

The thesis is organized into following six chapters to accomplish predefined objectives.

Chapter 1: Introduction

This chapter explains brief introduction about the TMDCs with especially focus on PtS₂, PtSe₂ and their properties. Moreover, a detailed discussion of their synthesis methods (ME, CVD and TAC) is also described. With focus on photodetector application, their working mechanism and

Chapter 1: Introduction

important figures of merits are also explained in detail. Finally, chapter concludes with motivations and objective of the present thesis.

Chapter 2: Fabrication and characterization techniques

This chapter discusses the working mechanism of various synthesis methods and characterization used in the present thesis work. Moreover, it also summarizes the photodetector device testing equipment used during the work.

Chapter 3. Large area and controlled growth of PtS2 on various substrates

This chapter includes the systematic study of the effect of growth parameters (sulfur amount, Pt thickness, and carrier gas flow) employed in the thermally assisted conversion method to achieve the large area growth of PtS₂ on various substrates. Next, this chapter also includes the detail growth mechanism to understand the growth of PtS₂ and its photodetector performance on various substrates.

Chapter 4. Large area 2D PtS₂ heterostructures for broadband photodetection

In this chapter, large-area PtS₂ heterostructures, including PtS₂/MoS₂ and PtS_{2-x}/Ga₂O₃ heterostructure fabrication and their broadband photodetector study are discussed. Furthermore, a detailed interface study of the heterojunction with their band alignment study and carrier transport mechanism is highlighted.

Chapter 5. 2D PtSe₂ heterostructure for photodetector study

This chapter summarizes the importance of PtSe₂/MoS₂ heterostructure to enhance the overall device performance compared to bare PtSe₂. A detailed carrier transport mechanism and ultrafast response of PtSe₂/MoS₂ is also explained.

Chapter 6. Summary and scope for future studies

This chapter summarizes the entire thesis work and presents future directions for the further development of TMDC growth and devices.

References

- 1. Baig, N., I. Kammakakam, and W. Falath, *Nanomaterials: a review of synthesis methods, properties, recent progress, and challenges.* Materials Advances, 2021. **2**(6): p. 1821-1871.
- 2. Novoselov, K.S., et al., *Electric Field Effect in Atomically Thin Carbon Films*. Science, 2004. **306**(5696): p. 666-669.
- 3. Wood, J.D., et al., Effective Passivation of Exfoliated Black Phosphorus Transistors against Ambient Degradation. Nano Letters, 2014. **14**(12): p. 6964-6970.
- 4. Ganatra, R. and Q. Zhang, Few-Layer MoS2: A Promising Layered Semiconductor. ACS Nano, 2014. **8**(5): p. 4074-4099.
- 5. Long, M., et al., *Progress, Challenges, and Opportunities for 2D Material Based Photodetectors*. Advanced Functional Materials, 2019. **29**(19): p. 1803807.
- 6. Jariwala, D., et al., Emerging Device Applications for Semiconducting Two-Dimensional Transition Metal Dichalcogenides. ACS Nano, 2014. **8**(2): p. 1102-1120.
- 7. Tedstone, A.A., D.J. Lewis, and P. O'Brien, Synthesis, Properties, and Applications of Transition Metal-Doped Layered Transition Metal Dichalcogenides. Chemistry of Materials, 2016. **28**(7): p. 1965-1974.
- 8. Chhowalla, M., et al., *The chemistry of two-dimensional layered transition metal dichalcogenide nanosheets.* 2013. **5**(4): p. 263-275.
- 9. Bassi, G., et al., Controlled and tunable growth of ambient stable 2D PtS2 thin film and its high-performance broadband photodetectors. Journal of Alloys and Compounds, 2023. 955: p. 170233.
- 10. Zhao, Y., et al., Extraordinarily Strong Interlayer Interaction in 2D Layered PtS2. Advanced Materials, 2016. **28**(12): p. 2399-2407.
- 11. Zhao, Y., et al., *High-Electron-Mobility and Air-Stable 2D Layered PtSe2 FETs*. Advanced Materials, 2017. **29**(5): p. 1604230.
- 12. Huang, Z., W. Zhang, and W. Zhang, Computational Search for Two-Dimensional MX2 Semiconductors with Possible High Electron Mobility at Room Temperature. Materials, 2016. **9**(9).
- 13. Zhang, W., et al., Two-dimensional semiconductors with possible high room temperature mobility. Nano Research, 2014. 7(12): p. 1731-1737.
- 14. Yu, X., et al., *Atomically thin noble metal dichalcogenide: a broadband mid-infrared semiconductor.* Nature Communications, 2018. **9**(1): p. 1545.
- 15. Wang, Z., et al., A Noble Metal Dichalcogenide for High-Performance Field-Effect Transistors and Broadband Photodetectors. Advanced Functional Materials, 2020. **30**(5): p. 1907945.
- 16. Ermolaev, G.A., et al. *Broadband Optical Properties of Atomically Thin PtS2 and PtSe2*. Nanomaterials, 2021. **11**, DOI: 10.3390/nano11123269.
- 17. Gong, Y., et al., *Two-Dimensional Platinum Diselenide: Synthesis, Emerging Applications, and Future Challenges.* Nano-Micro Letters, 2020. **12**(1): p. 174.
- 18. Pi, L., et al., *Recent Progress on 2D Noble-Transition-Metal Dichalcogenides*. Advanced Functional Materials, 2019. **29**(51): p. 1904932.
- 19. O'Brien, M., et al., Raman characterization of platinum diselenide thin films. 2D Materials, 2016. **3**(2): p. 021004.
- 20. Yan, M., et al., *High quality atomically thin PtSe2 films grown by molecular beam epitaxy.* 2D Materials, 2017. **4**(4): p. 045015.
- 21. Dong, R. and I. Kuljanishvili, *Review Article: Progress in fabrication of transition metal dichalcogenides heterostructure systems.* Journal of Vacuum Science & Technology B, 2017. **35**(3): p. 030803.

- 22. Hu, Z., Z.-B. Liu, and J.-G. Tian, *Stacking of Exfoliated Two-Dimensional Materials: A Review.* Chinese Journal of Chemistry, 2020. **38**(9): p. 981-995.
- 23. Gulo, D.P., et al., *Temperature-dependent optical and vibrational properties of PtSe2 thin films*. Scientific Reports, 2020. **10**(1): p. 19003.
- 24. Wang, Z., et al., Facile Synthesis of Single Crystal PtSe2 Nanosheets for Nanoscale Electronics. Advanced Materials, 2016. **28**(46): p. 10224-10229.
- 25. Zhang, H., et al., *PtSe2 Field-Effect Phototransistor with Positive and Negative Photoconductivity.* ACS Applied Electronic Materials, 2022. **4**(11): p. 5177-5183.
- 26. Zhao, Y.-Q., et al., Chemical vapor deposition of uniform bilayer PtS2 flakes for electrocatalytic hydrogen evolution. Physical Chemistry Chemical Physics, 2023. **25**(16): p. 11311-11315.
- 27. Jiang, S., et al., *Nonlinear electronic and ultrafast optical signatures in chemical vapor-deposited ultrathin PtS2 ribbons*. Nano Research, 2022. **15**(5): p. 4366-4373.
- 28. Cai, Z., et al., Chemical Vapor Deposition Growth and Applications of Two-Dimensional Materials and Their Heterostructures. Chemical Reviews, 2018. **118**(13): p. 6091-6133.
- 29. Xu, H., et al., Controlled Doping of Wafer-Scale PtSe2 Films for Device Application. Advanced Functional Materials, 2019. **29**(4): p. 1805614.
- 30. Shi, J., et al., Chemical Vapor Deposition Grown Large-Scale Atomically Thin Platinum Diselenide with Semimetal—Semiconductor Transition. ACS Nano, 2019. **13**(7): p. 8442-8451.
- Wang, W., et al., *Investigation of the band alignment at MoS2/PtSe2 heterojunctions*. Applied Physics Letters, 2019. **114**(20): p. 201601.
- 32. Li, K., et al., *Lattice vibration properties of MoS2/PtSe2 heterostructures*. Journal of Alloys and Compounds, 2020. **820**: p. 153192.
- 33. Xie, J., et al., Optical properties of chemical vapor deposition-grown PtSe2 characterized by spectroscopic ellipsometry. 2D Materials, 2019. **6**(3): p. 035011.
- 34. Chung, C.-C., et al., Atomic-Layer Controlled Interfacial Band Engineering at Two-Dimensional Layered PtSe2/Si Heterojunctions for Efficient Photoelectrochemical Hydrogen Production. ACS Nano, 2021. **15**(3): p. 4627-4635.
- Wu, E., et al., In Situ Fabrication of 2D WS2/Si Type-II Heterojunction for Self-Powered Broadband Photodetector with Response up to Mid-Infrared. ACS Photonics, 2019. **6**(2): p. 565-572.
- 36. Yim, C., et al., *Wide Spectral Photoresponse of Layered Platinum Diselenide-Based Photodiodes.* Nano Letters, 2018. **18**(3): p. 1794-1800.
- 37. Zeng, L., et al., *Ultrafast and sensitive photodetector based on a PtSe2/silicon nanowire array heterojunction with a multiband spectral response from 200 to 1550 nm.* NPG Asia Materials, 2018. **10**(4): p. 352-362.
- 38. Zeng, L.-H., et al., Fast, Self-Driven, Air-Stable, and Broadband Photodetector Based on Vertically Aligned PtSe2/GaAs Heterojunction. Advanced Functional Materials, 2018. **28**(16): p. 1705970.
- 39. Zhou, K., et al., *Broadband photodetector based on 2D layered PtSe2 / silicon heterojunction at room-temperature*. Physica E: Low-dimensional Systems and Nanostructures, 2020. **123**: p. 114147.
- 40. Wang, Y., et al., Monolayer PtSe2, a New Semiconducting Transition-Metal-Dichalcogenide, Epitaxially Grown by Direct Selenization of Pt. Nano Letters, 2015. **15**(6): p. 4013-4018.

- 41. Yuan, J., et al., Wafer-Scale Fabrication of Two-Dimensional PtS2/PtSe2 Heterojunctions for Efficient and Broad band Photodetection. ACS Applied Materials & Interfaces, 2018. 10(47): p. 40614-40622.
- 42. Han, S.S., et al., *Horizontal-to-Vertical Transition of 2D Layer Orientation in Low-Temperature Chemical Vapor Deposition-Grown PtSe2 and Its Influences on Electrical Properties and Device Applications*. ACS Applied Materials & Interfaces, 2019. **11**(14): p. 13598-13607.
- 43. Shawkat, M.S., et al., Two-Dimensional/Three-Dimensional Schottky Junction Photovoltaic Devices Realized by the Direct CVD Growth of vdW 2D PtSe2 Layers on Silicon. ACS Applied Materials & Interfaces, 2019. 11(30): p. 27251-27258.
- 44. Wu, D., et al., *Highly sensitive solar-blind deep ultraviolet photodetector based on graphene/PtSe2/β-Ga2O3 2D/3D Schottky junction with ultrafast speed.* Nano Research, 2021. **14**(6): p. 1973-1979.
- 45. Xu, H., et al., *Strategy for Fabricating Wafer-Scale Platinum Disulfide*. ACS Applied Materials & Interfaces, 2019. **11**(8): p. 8202-8209.
- 46. Cullen, C.P., et al., *Synthesis and characterisation of thin-film platinum disulfide and platinum sulfide*. Nanoscale, 2021. **13**(15): p. 7403-7411.
- 47. Zhao, D., et al., Synthesis of large-scale few-layer PtS2 films by chemical vapor deposition. AIP Advances, 2019. **9**(2): p. 025225.
- 48. Bassi, G., R. Wadhwa, and M. Kumar, *Broadband and High-Performance Photodetector Fabricated Using Large Area and Transfer-Free 2D–2D PtS2/MoS2 Heterostructure*. Advanced Optical Materials, 2024. **12**(7): p. 2301899.
- 49. Bassi, G., et al., 2D–3D heterostructure of PtS2-x/Ga2O3 and their band alignment studies for high performance and broadband photodetector. Nanotechnology, 2024. **35**(32): p. 325706.
- 50. Zhang, X., et al., Dark Current Mechanisms and Suppression Strategies for Infrared Photodetectors Based on Two-Dimensional Materials. Laser & Photonics Reviews, 2024. **18**(5): p. 2300936.
- 51. Aftab, S., et al., Platinum Disulfide (PtS2) and Silicon Pyramids: Efficient 2D/3D Heterojunction Tunneling and Breakdown Diodes. ACS Applied Electronic Materials, 2022. 4(3): p. 917-924.
- 52. Gui, T., et al., *In-situ fabrication of PtSe2/MoS2 van der Waals heterojunction for self-powered and broadband photodetector.* Materials & Design, 2024. **238**: p. 112722.
- 53. Kim, H.-S., et al., Broadband and ultrafast photodetector based on PtSe2 synthesized on hBN using molecular beam epitaxy. Applied Surface Science, 2023. 638: p. 158103.
- 54. Li, H. and Z. Yang *Highly Responsive and Self-Powered Photodetector Based on PtSe2/MoS2 Heterostructure*. Molecules, 2024. **29**, DOI: 10.3390/molecules29112553.
- 55. Li, L., et al., Few-Layered PtS2 Phototransistor on h-BN with High Gain. Advanced Functional Materials, 2017. **27**(27): p. 1701011.
- 56. Li, X., et al., Mixed-Dimensional PtSe2/Bi2Te3/Pyramid Si Heterojunction with a Light-Trapping Structure for Highly Sensitive Ultrabroadband Photodetection. ACS Photonics, 2024. 11(5): p. 2070-2076.
- 57. Long, M., et al., Scalable fabrication of long-wave infrared PtSe2-G heterostructure array photodetectors. Applied Physics Letters, 2020. 117(23): p. 231104.
- 58. Ma, M., et al., Multilayered PtSe2/pyramid-Si heterostructure array with light confinement effect for high-performance photodetection, image sensing and light trajectory tracking applications. Journal of Materials Chemistry C, 2021. 9(8): p. 2823-2832.

- 59. Song, Y., et al., *High-Performance Photodetector Based on the ReSe2/PtSe2 van der Waals Heterojunction*. ACS Applied Electronic Materials, 2023. **5**(5): p. 2748-2757.
- 60. Wang, J., et al., *PtSe2/InP Mixed-Dimensional Schottky Junction for High-Performance Self-Powered Near-Infrared Photodetection*. Advanced Optical Materials, 2024. **12**(29): p. 2401035.
- Wang, L., et al., *A high-performance near-infrared light photovoltaic detector based on a multilayered PtSe2/Ge heterojunction.* Journal of Materials Chemistry C, 2019. **7**(17): p. 5019-5027.
- 62. Wang, S., et al., Unipolar Barrier Photodetectors Based on Van Der Waals Heterostructure with Ultra-High Light On/Off Ratio and Fast Speed. Advanced Science, 2025. n/a(n/a): p. 2413844.
- 63. Wang, X., et al., A Self-Powered Photodetector Based on Graphene Enhanced WSe2/PtSe2 Heterodiode with Fast Speed and Broadband Response. Advanced Optical Materials, 2024. **12**(18): p. 2400052.
- 64. Wang, Z., et al., *Type-I Heterostructure Based on WS2/PtS2 for High-Performance Photodetectors*. ACS Applied Materials & Interfaces, 2022. **14**(33): p. 37926-37936.
- 65. Xu, Z., et al., Self-Powered Broadband UV-NIR Photodetectors Based on InSe/PtS2 Van der Waals Heterostructure. Advanced Optical Materials, 2024. **12**(30): p. 2401379.
- 66. Zhang, H., et al., *Type-I PtS2/MoS2 van der Waals heterojunctions with tunable photovoltaic effects and high photosensitivity.* Nanoscale, 2022. **14**(43): p. 16130-16138.
- 67. Zhang, K., et al., *Polarization-sensitive infrared photodetectors based on van der Waals heterojunction with the unilateral depletion region*. Journal of Physics D: Applied Physics, 2022. **55**(49): p. 495106.
- 68. Zhang, Z.-X., et al., *Ultrafast, Self-Driven, and Air-Stable Photodetectors Based on Multilayer PtSe2/Perovskite Heterojunctions*. The Journal of Physical Chemistry Letters, 2018. **9**(6): p. 1185-1194.
- 69. Zhuo, R., et al., *In-situ fabrication of PtSe2/GaN heterojunction for self-powered deep ultraviolet photodetector with ultrahigh current on/off ratio and detectivity.* Nano Research, 2019. **12**(1): p. 183-189.
- 70. Che, M., et al., *High-Efficiency Self-Powered Broadband Photodetector Based on PtSe2/MoSe2 Heterojunction*. ACS Photonics, 2024. **11**(4): p. 1693-1702.

Chapter 2: Fabrication and characterization techniques

This chapter briefly reviews the fabrication and characterization techniques employed to deposit PtX₂ (X=S, Se) and MoS₂ thin films. In the present thesis work, radio frequency (RF) magnetron sputtering and thermally assisted conversion (TAC) were used to synthesize the MoS₂ and PtX₂ films, respectively. The various characterization tools are performed to characterize the grown films. The optical properties are examined by Raman, Photoluminescence (PL), and UV-vis-NIR spectroscopy. The morphology and structural properties are studied by X-ray diffraction (XRD), Field emission Scanning electron microscope (FE-SEM), Transmission electron microscopy (TEM) and atomic force microscopy (AFM). The chemical composition is determined by X-ray photoelectron microscopy (XPS). Finally, the photodetector device fabrication and its performance measurements are discussed.

2.1 Deposition techniques

2.1.1 Magnetron sputtering

Sputtering is a physical vapor deposition (PVD) technique in which thin film is deposited by sputter (or ejection) of target material's atoms through energetic ion bombardment. It is a widely used method to deposit various types of materials in a scalable manner. Figure 2.1 (a) shows the schematic illustrating the sputtering system. A high-purity target is used as a cathode, and the sample stage as an anode. Prior to deposition, a high vacuum is created inside the growth chamber, which helps to remove unwanted impurities and increase the mean free path for the sputter atoms. For the deposition of thin film, external power is supplied to the target material which ionizes the argon gas atoms (supplied during deposition) to form Ar⁺ ions, which bombard with target material and eject the target atoms and form plasma (combination of electrons, Ar atoms, Ar ions, sputtered atoms etc). Moreover, magnets behind the target further assist in intensifying and confining the plasma near the target and increase the sputtering rate [1, 2]. Therefore, it is called magnetron sputtering. Depending upon the external power supply, sputtering can be categorized as radio frequency (RF) sputtering and direct current (DC) sputtering. In the present thesis work, RF magnetron sputtering (make - EXCEL INSTRUMENTS, India) was used for the Pt and MoS₂ deposition at the standard RF frequency of 13.56 MHz. Figure 2.1(b) exhibits the image of equipment used for sputtering in our lab with features of vacuum system generation (rotary for rough vacuum and turbo molecular pump

for high vacuum), Alicat mass flow controller (for Ar gas flow rate), and vacuum gauges (Pirani for low vacuum and penning for high vacuum).

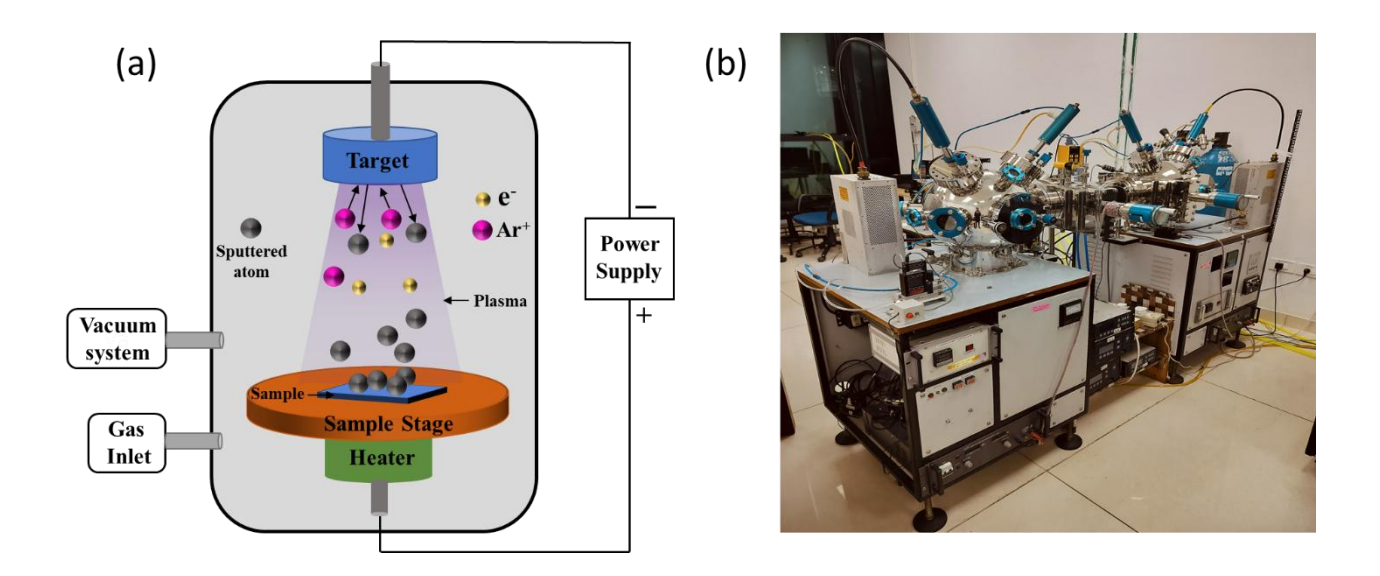


Figure 2.1 (a) Schematic illustrating the Sputtering system (b) Sputtering system employed in our lab to deposit platinum (Pt) and MoS₂ thin film.

2.1.2 Chemical Vapor Deposition

Chemical vapor deposition (CVD) is a widely utilized method for fabricating 2D materials and thin films. A chemical reaction occurs between the loaded precursors in the presence of high temperature. The various growth parameters in CVD, such as precursors amount, , temperature, pressure, gas flow rate and substrate distance from precursors, help to control the growth of high-quality films [3]. There are different types of CVD, including atmospheric pressure CVD (APCVD), metal-organic CVD (MOCVD), low-pressure CVD (LPCVD), and plasma-enhanced CVD (PECVD). The fundamental steps which are common in all types of CVD is illustrated in Figure 2.2 (a). The precursors after converting in gasses phases are transported towards the substrate surface by a carrier gas. A chemical reaction occurs between the precursors in the vapor phase or on the surface of the substrate and a solid film deposited on the substrate. The gas flow stream removes the undesirable volatile by-products produced during the chemical reaction through the tube. For example, MoS₂ can be synthesized from MoO₃ and S precursors, and SO₂ is produced as a by-product. In a CVD method, different heating zones are used to evaporate the precursor materials, and the substrate is placed in one of the heating zones.

In the present thesis work, we utilized APCVD, which operates at normal atmospheric pressure. The APCVD system is equipped with three separate heating zones with a maximum heating capacity of 1100 °C and is controlled by a PID controller. The CVD tube of length 140 cm and inner diameter 50 cm were used during the deposition. The photo of CVD (made by Ants Innovations Pvt. Ltd, India) used for the sulfurization/selenization of Pt film is shown in Figure 2.2 (b).

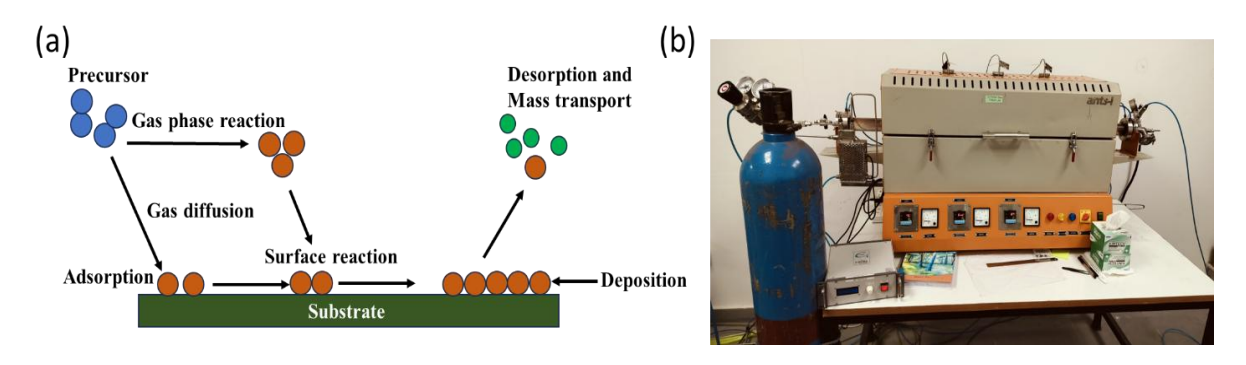


Figure 2.2. (a) Schematic illustrating the common elementary steps occurring in the CVD process (b) CVD equipment used for the growth of PtX_2 (X=S, Se).

2.1.3 Thermally assisted conversion

Thermally assisted conversion (TAC) is a two-step process in which pre-coated Pt film is sulfurized (selenization) in the CVD for the growth of PtS₂ (PtSe₂), respectively. TAC is the best method to grow scalable area uniform 2D material film where its thickness can be controlled by pre-coated Pt thickness. In the present thesis work, PtS₂ and PtSe₂ were synthesized using the TAC method. The sputtering system used for Pt deposition is shown in Figure 2.1 (b). The Pt-coated substrate was placed in one zone of the CVD with a temperature of around 500 °C and sulfur (selenium) power was loaded in the zirconia boat and placed in another zone with a temperature of 300 °C (250 °C), respectively. Here, we employed a tube-in-tube arrangement where Pt-coated substrate and S(Se) powder were placed in a small quartz tube (both sides open) with a separation of 14 cm and then loaded in a bigger CVD quartz tube, as shown in Figure 2.3 schematic. The tube-in-tube arrangement helps to confine the chalcogens (S, Se) vapors within the tube and increase the reaction rate. Moreover, both sides open quartz tube helps to maintain the uniform gas flow within the tube. Figure 2.3 displays the schematic of the TAC method used to grow PtX₂ (X=S, Se). Figure 2.2 (b) exhibits the CVD system used for sulfurization (selenization) of the Pt film.

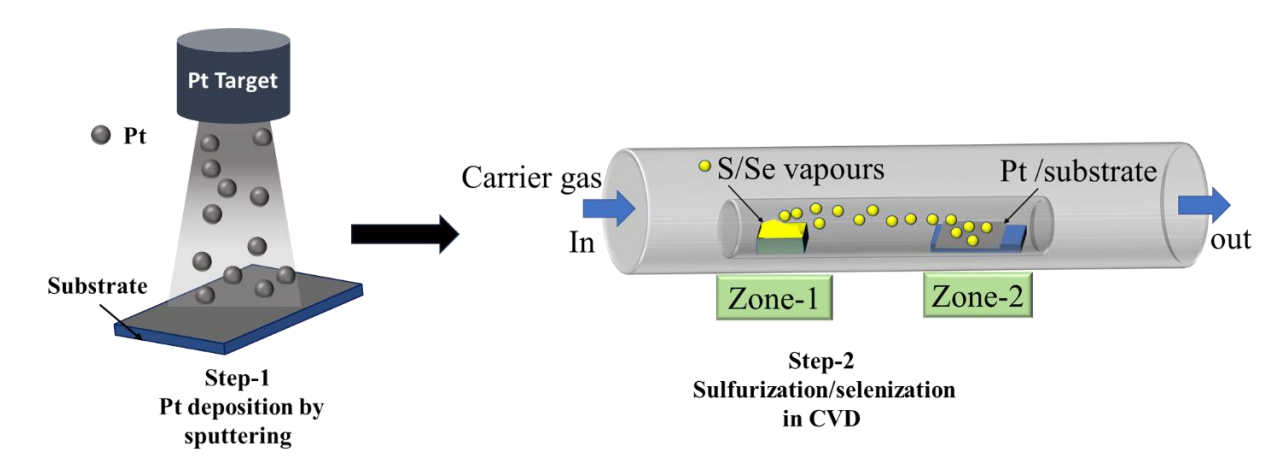


Figure 2.3 The schematic exhibiting the steps used for the growth of PtX₂ (X=S, Se) by TAC method.

2.2 Characterization techniques

During the thesis work, various characterization techniques were performed to characterize the grown film as discussed below:

2.2.1 Optical characterizations

The optical characterization was performed with Raman spectroscopy, Ultraviolent-Visible (UV-Vis) spectroscopy and photoluminescence (PL) spectroscopy. The Raman and PL spectroscopy was performed with a LabRAM Horiba scientific model with a 50× objective lens and 532 nm laser illumination source at room temperature. The non-destructive nature of Raman spectroscopy makes it a widely used technique for studying the lattice vibrations of a material. When incident light interacts with the material, it can scatter the light either with the same or a different wavelength. The scattering in which the wavelength of the scattered photons remains same as of the incident photons is known as Rayleigh (elastic) scattering. Meanwhile, scattering, in which the wavelength (or energy) of scattered photons changes from incident photons, is called the Raman scattering [4]. The energy (or wavelength) separation of scattered and incident photons is referred as Raman shift. Figure 2.4 (a) illustrates the interaction of an incident photon with a molecule leads to Rayleigh and Raman scattering. The different possible vibration modes for PtX₂ film are already discussed in section 1.4.3 of Chapter 1.

Photoluminescence spectroscopy is also widely used characterization technique to study the optical properties of materials. A monochromator laser source excites the electrons from the ground state (in valence band) to a higher energy state (in conduction band). The excited electrons come back to the ground state as a combination of non-radiative transition (phonons)

and radiative transitions (photons), as illustrated in Figure 2.4 (b). Moreover, Figure 2.4 (b) shows that for PL analysis of the material, the energy of the illuminated source should be more than the band gap of the material. Using PL spectroscopy, we can determine the material's band gap, defects, and recombination mechanism within the material [4].

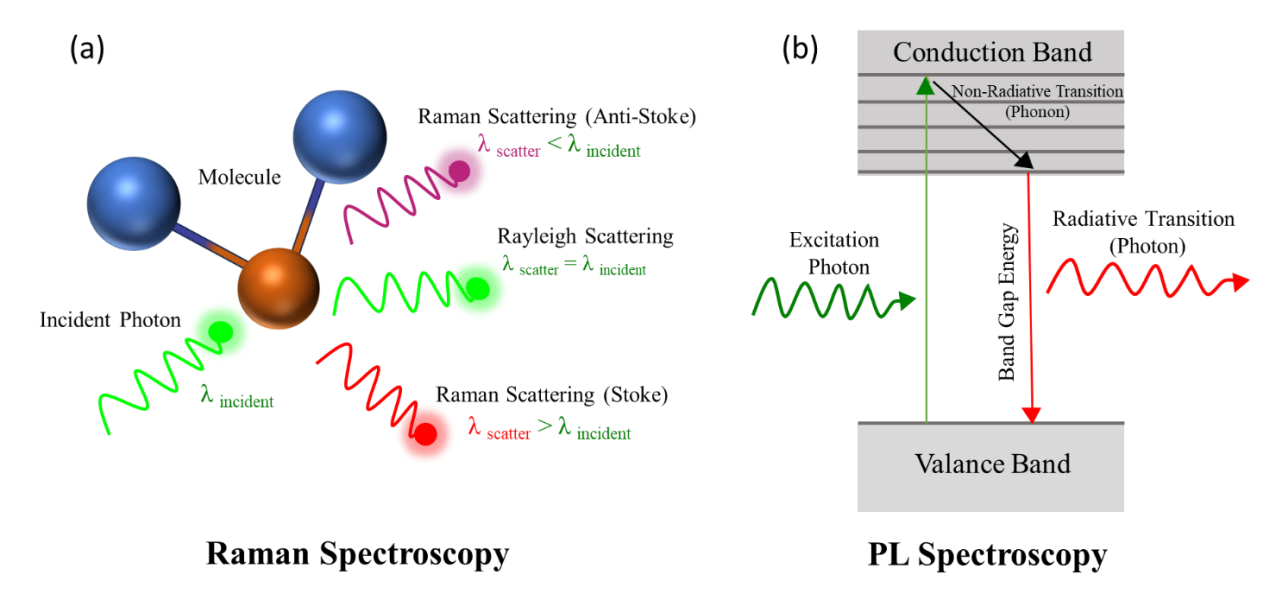


Figure 2.4 (a) Schematic demonstrating the light interacted with molecule leads to Raman and Rayleigh scattering (b) Schematic shows the band diagram of a material under electron excitation and de-excitation in PL spectroscopy.

The absorption measurement of all samples was done using UV-Vis spectroscopy with a Perkin Elmer Lambda 950 UV-Vis-NIR spectrometer instrument. The band gap (E_g) of a material is calculated using Tuac Plot, which is a graph between (ahv) $^{1/m}$ (along y-axis) vs. hv (x-axis) and uses the following equation [5]

$$(ahv)^{\frac{1}{m}} = C(hv - E_g)$$
 (2.1)

which a is the absorption coefficient, h is the plank constant, hv is the incident photon energy, C is a proportionality constant, m is the Tauc exponent and its value is m=2 for indirect band material and m=1/2 for direct band material. The band gap of the materials is calculated by taking linear extrapolation of the $(ahv)^{1/m}$ vs. hv curve on the energy (hv) axis.

2.2.2 Morphological characterizations

FE-SEM and AFM were performed to characterize the morphology of the films. FE-SEM is an extensively used tool for analyzing the morphology of the material and imaging its microstructures [6]. The FE-SEM was carried out with JEOL-JSM-7610F model and AFM was

Chapter 2: Fabrication and characterization techniques

recorded with Bruker Multimode 8 Scanning Probe Microscope in tapping mode. Moreover, AFM is also used to calculate the root mean square (RMS) roughness, line profile, and surface topography of the thin films [7, 8].

2.2.3 Crystal Structure Characterization

Transmission Electron Microscopy (TEM) and X-ray diffraction (XRD) are used to determine the crystallinity quality of the films. XRD provides important information on lattice parameters of crystalline solids and thin films. The stress/strain, phase, and crystallite size of the materials can also be determined using XRD technique [9]. In Chapter 4 the Grazing incidence XRD (GIXRD) was performed with PANalytical X'pert Pro MPD model with Cu K α (λ = 0.1504 nm) as a radiation source and in Chapter 5 XRD was performed with Rigaku MiniFlex instrument. In Chapter 5, the TEM and High-resolution TEM (HR-TEM) were performed with Model Themis 300 KV, which is equipped with an energy-dispersive X-ray (EDS) facility.

2.2.4 Chemical composition analysis and band alignment studies

X-ray photoelectron spectroscopy (XPS) is a surface-sensitive technique (~10 nm) used to study the chemical composition of the material. In Chapter 3, the XPS measurements were performed with Thermo Fisher Thermofisher scientific: Nexsa base instrument, while in Chapters 4 and 5, it was carried out with Thermo Fisher Scientific ESCALAB Xi+ model instrument. In XPS measurements, sample is kept in an ultra-high vacuum chamber and irradiated with an X-rays source (usually Al K_{α} , $h\nu$ = 1486.86 eV). The ejected electrons from the core levels of the material, including their kinetic energy and intensity, are measured using an electron energy analyzer. The XPS technique gives the best estimation of stoichiometry and ionic states of the elements present in the material [10]. Moreover, the band alignment between two semiconductors can be calculated using Kraut's rule and XPS data analysis [11].

2.3 Device fabrication and characterization

2.3.1 Device fabrication

The gold metal contacts were deposited on the grown film by a thermal evaporation method using stainless-steel shadow masks (interdigitated or strip geometry), as shown in Figure 2.5 (a). Figure 2.5 (b) is the thermal evaporated system used to evaporate the metal. Thermal evaporation is a PVD system where a high vacuum of the order of 10^{-6} - 10^{-7} hPa is created inside the chamber to remove unnecessary impurities and increase the mean free path. The metal

pallets loaded in a boat are evaporated by passing a high current through the boat, which forms the metal vapors and then deposited on the required film-grown sample.

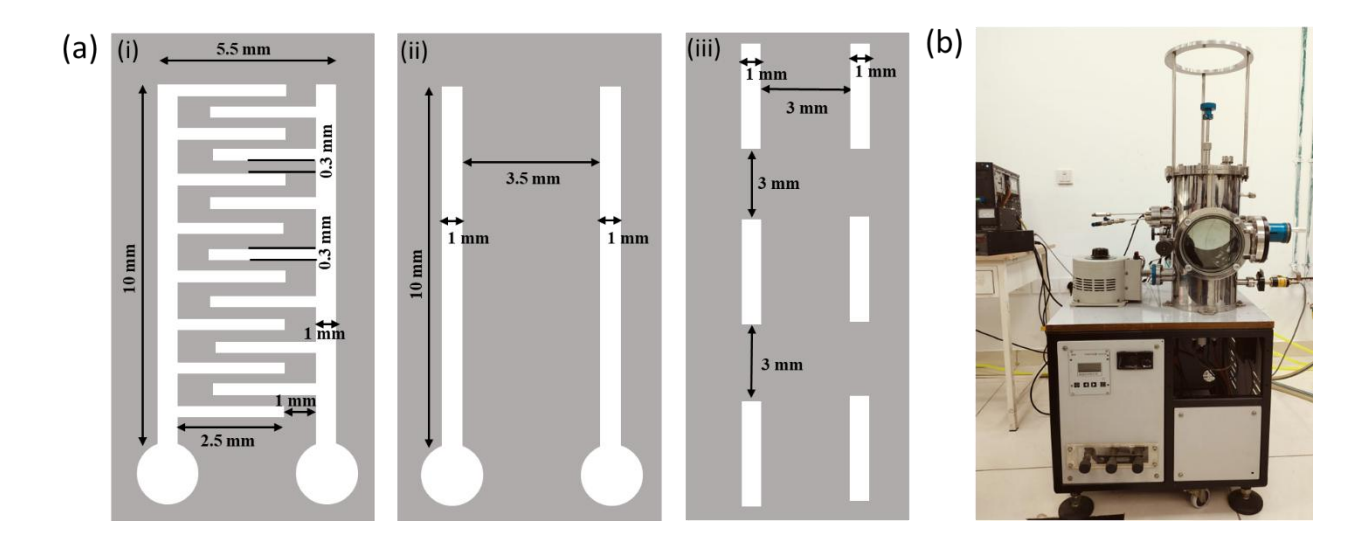


Figure 2.5 (a) Physical shadow mask used for electrode deposition with different geometry shapes of (i) interdigitated (ii) strips (iii) lines strips (b) Thermal evaporator system employed for metal electrode deposition.

2.3.2 Photodetector device measurements

The PtX₂ (X=S, Se) and its heterostructure photodetectors device measurements were carried out by a home-built photodetector set-up, as exhibited in Figure 2.6. It consists of a Bentham (PVE 300) model equipped with a monochromator (TMC 300), 100 W quartz halogen and 75 W xenon lamps, a lock-in amplifier, and a chopper that was connected to a sub-femtoamp sensitive Keithley-6430 SMU. In the present thesis work, light illumination sources of 250-1200 nm wavelength are produced by a monochromator with power density of each wavelength is shown in Table 2.1. The other sources 650 nm and 532 nm lasers (HOLMARC, 5 mW Power), and 254 nm UV lamp (Cole Parmer, 4.4 mW cm⁻² intensity) were used. The sample testing was done in an enclosed chamber box to avoid the outside ambient light interface, as displayed in Figure 2.6. The sample stage with two probes is also shown in top right image of Figure 2.6, where testing sample was placed. The current-voltage (I-V) and current-time (I-T) measurements of the sample were recorded using 6430 SMU Keithley instrument, controlled by software installed in the computer, which also save the final recorded data.

 Table 2.1 Incident beam Power density of each wavelength.

Wavelength (nm)	250	400	500	600	700	800	900	1000	1100	1200
Optical power	0.05	0.233	0.580	0.582	0.245	0.200	0.190	0.203	0.159	0.845
density of incident										
radiation ($\mu W/$										
<i>cm</i> ²)										

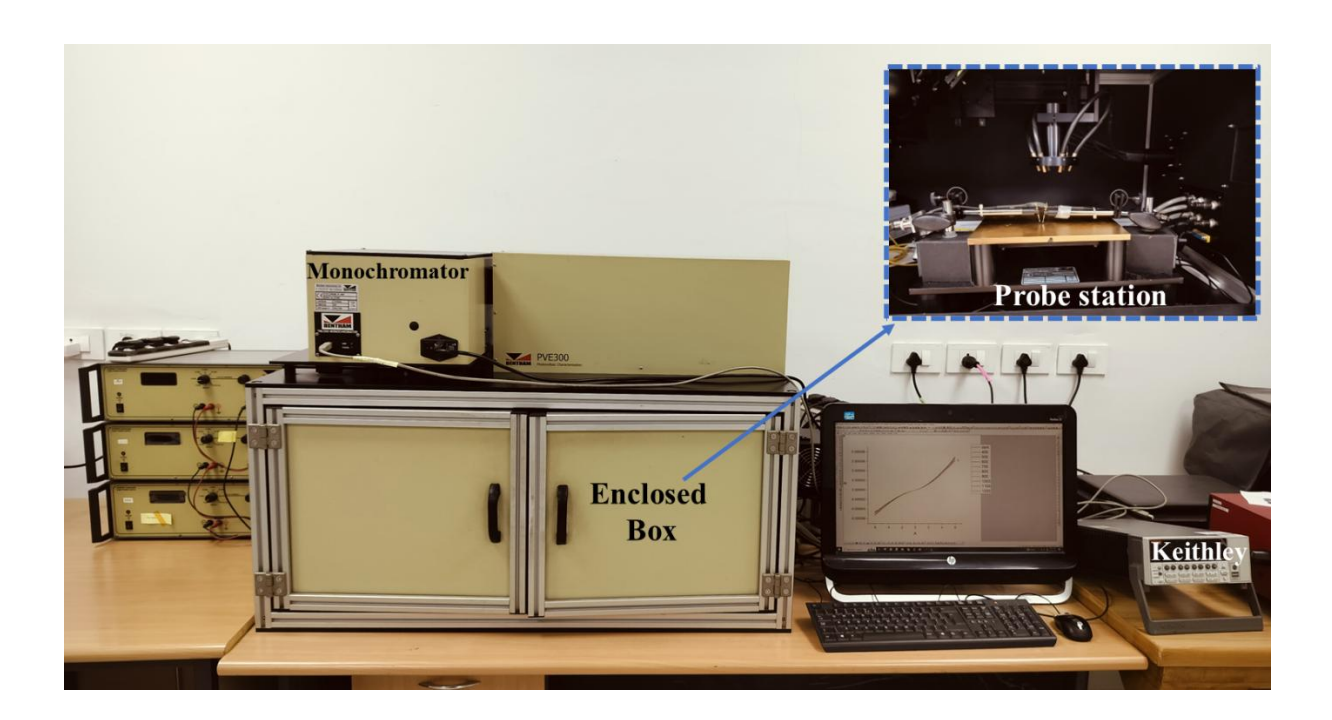


Figure 2.6 Testing equipment used for photodetector device measurements which consist of light source, monochromator, probe station, 6430 SMU Keithley and computer.

Chapter 2: Fabrication and characterization techniques

References

- 1. Mattox, D.M., Handbook of Physical Vapor Deposition (PVD) Processing. 2010: Elsevier.
- 2. Ohring, M., *The Materials Science of Thin Films*. 2002: Elsevier.
- 3. Cai, Z., et al., Chemical Vapor Deposition Growth and Applications of Two-Dimensional Materials and Their Heterostructures. Chemical Reviews, 2018. 118(13): p. 6091-6133.
- 4. PERKOWITZ, S., Optical Characterization of Semiconductors. 1993: Elsevier.
- 5. Makuła, P., M. Pacia, and W. Macyk, *How To Correctly Determine the Band Gap Energy of Modified Semiconductor Photocatalysts Based on UV–Vis Spectra*. The Journal of Physical Chemistry Letters, 2018. **9**(23): p. 6814-6817.
- 6. Gerhard Dehm, J.M.H., Josef Zweck, *In-situ Electron Microscopy: Applications in Physics, Chemistry and Materials Science*. 2012: John Wiley & Sons.
- 7. Khan, M.K., Q.Y. Wang, and M.E. Fitzpatrick, *1 Atomic force microscopy (AFM) for materials characterization*, in *Materials Characterization Using Nondestructive Evaluation (NDE) Methods*, G. Hübschen, et al., Editors. 2016, Woodhead Publishing. p. 1-16.
- 8. Alsteens, D., et al., *Atomic force microscopy-based characterization and design of biointerfaces*. Nature Reviews Materials, 2017. **2**(5): p. 17008.
- 9. Stock, B.D.C.a.S.R., *Elements of X-Ray Diffraction*. Third ed. 2014: Pearson Education Limited.
- 10. Stevie, F.A. and C.L. Donley, *Introduction to x-ray photoelectron spectroscopy*. Journal of Vacuum Science & Technology A, 2020. **38**(6): p. 063204.
- 11. Kraut, E.A., et al., Precise Determination of the Valence-Band Edge in X-Ray Photoemission Spectra: Application to Measurement of Semiconductor Interface Potentials. Physical Review Letters, 1980. 44(24): p. 1620-162

Chapter 3: Large area and controlled growth of PtS₂ on various substrates

In this chapter, a detailed discussion on the large area growth of PtS₂ thin film on various substrates by thermally assisted conversion (TAC) method is discussed. The large area-controlled growth of PtS₂ film is achieved by varying the growth parameters such as Pt film thickness, sulfur (S) amount, and gas flow rate. Moreover, a detailed PtS₂ growth mechanism under these parameters is also discussed. The Raman and X-ray photoelectron spectroscopy (XPS) characterization were carried out on different PtS₂ samples to show the transition from PtS to PtS₂. The growth of PtS₂ film on various substrates including SiO₂/Si, Si, Sapphire and flexible mica is achieved. Finally, photodetector performance of PtS₂ on different substrates is discussed.

3.1 Requirement of large area and controlled growth of PtS2 film

Predominately, PtS₂ thin films are synthesized by mechanical exfoliation (ME) method [1-4], which produces high-quality flakes. However, in the ME method, flakes are randomly distributed on the substrate, leading to non-uniformity and small size. Thus, this method is not suitable for large-scale device applications. To overcome the limitation of the ME, thermally assisted conversion (TAC) is employed which can grow large area PtS₂ thin films with controlled thickness (usually by controlling initial Pt thickness) [5-7]. During the synthesis of PtS₂, an intermediate-phase, Platinum sulfide (PtS), can easily form due to its higher stability, thus making the growth of PtS₂ really challenging. PtS is a non-layered material with a tetragonal structure [6]. Although, few reports have been published on the PtS₂ synthesis by the TAC method, [5-7] still, the controllable and large-area growth of PtS₂ with proper growth mechanism is missing. Additionally, as per our knowledge a universal method that can be used to grow PtS₂ on different substrates with a high-performance photodetector device based on the TAC method is still lacking.

3.2 Experimental section

3.2.1 Synthesis of PtS₂

PtS₂ thin film was synthesized by the TAC method, which involves the sulfurization of precoated Pt thin film on different substrates. Before deposition, the substrates were cleaned sequentially by ultrasonication with soap solution (composed of water, surfactants and EDTA Na4 (ethylenediaminetetraacetic acid tetrasodium salt)), deionized water, acetone, and

propanol for 30 minutes each and dried with a nitrogen jet. First, Pt thin film was deposited on the substrate by RF magnetron sputtering using a pure (99.99 %) 1-inch target at room temperature with a power of 30 W and deposition pressure of 3.8 mTorr, as shown in Figure 3.1 (a). In the 2nd step, the same Pt-coated substrate (mounted on a zirconia plate) and sulfur powder (99.98%, Sigma-Aldrich) (taken in a small zirconia boat) were loaded inside a small quartz tube having both ends open with a separation of 14 cm. This small quartz tube was placed in a bigger quartz tube equipped with 3 zone furnace, as shown in Figure 3.1 (b). The length and inner diameter of the bigger quartz tube were 140 cm and 5 cm, respectively. Before sulfurization, the furnace was purged with Ar gas at 300 sccm flow rate for 20 minutes to create an inert environment inside the tube. The sulfur powder was first heated up to a temperature of 120-200 °C to create a sulfur rich ambient inside the tube and then zone-2 with Pt-coated substrate was heated. The peak temperature for S powder and Pt-coated substrate was set at 300 °C and 500 °C for 1 hour under the presence of carrier gas (mixture of 1.1% H₂ balance Ar gas) in atmospheric pressure CVD (APCVD), as shown in Figure 3.1 (c). After 1 hour of deposition, the furnace was cooled down naturally to room temperature in the presence of the gas flow. Here, the tube-in-tube arrangement is used as it confines the sulfur vapours inside the tube and increases the rate of sulfurization.

3.2.2 Characterizations of PtS₂

Raman measurements were performed using a LabRAM HR 800-HORIBA spectrometer at room temperature with a 532 nm laser. The Atomic force microscope (AFM) measurements were performed by Bruker (Multimode 8) Scanning Probe Microscope in the tapping mode. Nikon ECLIPSE LV100ND was used for optical images. The XPS measurements were done with Thermofisher scientific model: Nexsa base instrument.

3.2.3 Photodetector fabrication and measurements

For device fabrication, an interdigitated gold (Au) electrode was patterned on a PtS₂ film with a thickness of ~150 nm through a thermal evaporation method using a physical shadow mask. The photodetector measurements of the fabricated device were performed with a Bentham PVE 300 system, consisting of a TMc monochromator with 75 W Xenon, and 100 W quartz halogen lamps and connected to sub-femtoamp 6430 Keithley SMU. The incident optical power density of the monochromator light (400-1100 nm) was measured using standard Silicon (Si) detector. The active area (A) of the device was 0.125 cm²

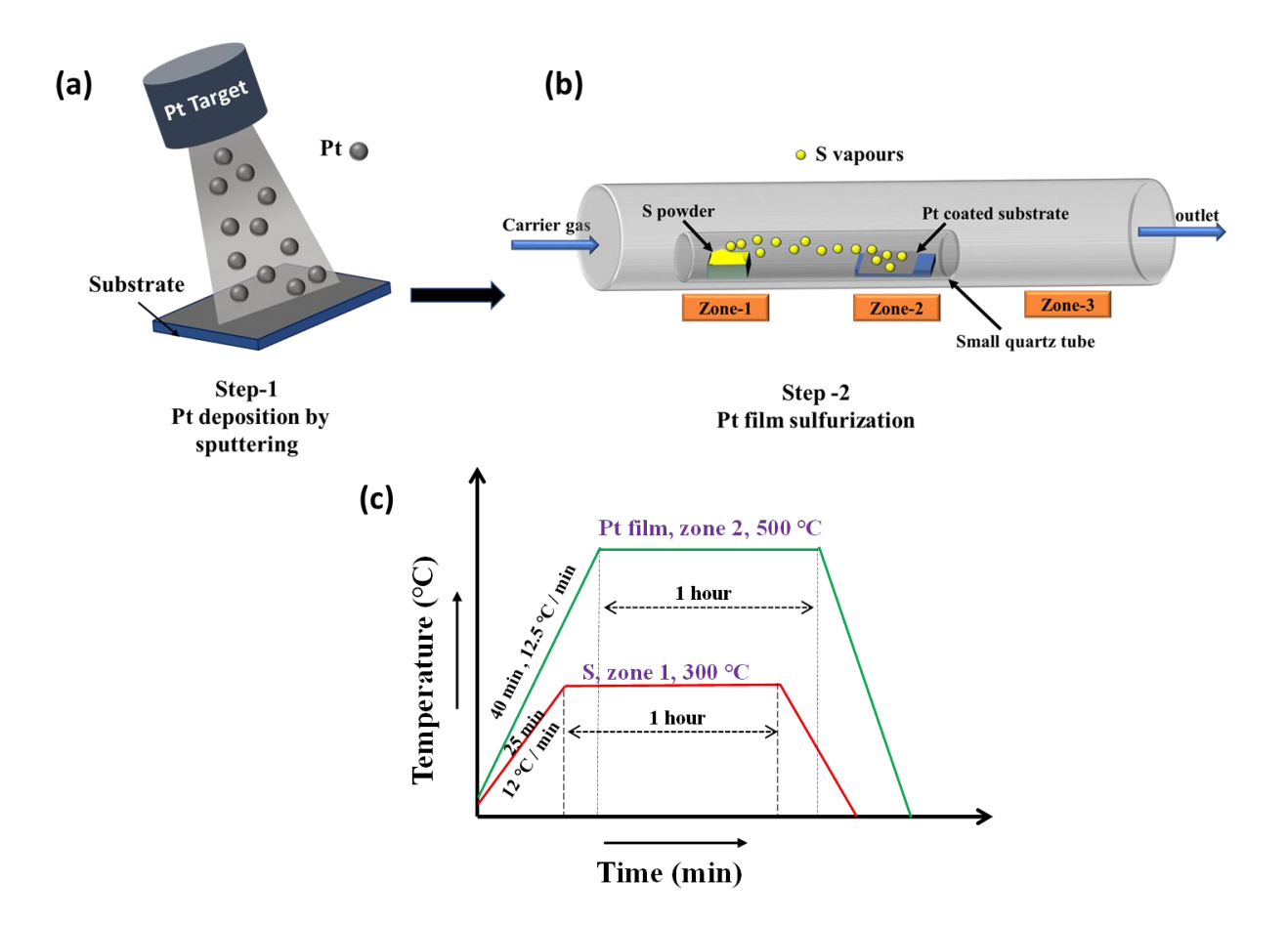


Figure 3.1 (a) 1st step of Pt coated on substrate by magnetron sputtering, and (b) 2nd step of sulfurization of Pt coated substrate in a tube-in-tube APCVD (c) Temperature profile of Sulfur (S) and Pt coated substrate in APCVD.

3.3 Results and Discussion

The impact of different growth parameters such as sulfur amount, Pt thickness, and gas flow rate are studied one-by-one by keeping other parameters constant.

3.3.1 Effect of Sulfur amount

For the synthesis of PtS_2 , sulfur (S) amount plays a critical role. A deficiency of sulfur supply can lead to the formation of undesired PtS phase. Therefore, an optimal amount of S is always required for PtS_2 formation. Impact of the sulfur amount was studied with 0.4 g, 0.8 g, 1.2 g and 1.6 g by keeping other parameters constant such as gas flow (150 sccm), Pt thickness (2.4 nm), and distance (d) between Pt coated substrate and S powder at 14 cm. Figure 3.2 (a) shows the Raman Spectra of PtS_x (x=1, 2) at different S amounts. At a lower sulfur amount of 0.4 g, only one Raman peak at ~331.7 cm⁻¹ (B_{1g}) is obtained, corresponding to PtS [8] implying that at low sulfur amount, PtS is formed. Further, when the sulfur amount was increased to 0.8 g,

three Raman peaks appeared at 301.6 cm⁻¹, 331.7 cm⁻¹, and 343.5 cm⁻¹ corresponding to E_g^1 , A_{1g}^1 , and A_{1g}^2 , respectively, of PtS₂[5]. Here, E_g^1 is the in-plane vibration mode, and A_{1g}^1 and A_{1g}^2 are the out-of-plane vibration modes in PtS₂. At 1.2 g of S, again, three prominent peaks at 300.1 cm⁻¹ (E_g^1), 331.5 cm⁻¹ (A_{1g}^1), and 341.4 cm⁻¹ (A_{1g}^2) are observed with increased intensity of A_{1g}^2 peak than A_{1g}^1 as compared to PtS₂ grown at 0.8 g sulfur, signifying the excellent quality of PtS₂ formation. Further increasing of S amount to 1.6 g leads to no significant changes in Raman spectra (see Figure 3.2 (a)), implying a saturation reached in the growth of PtS₂ after a certain amount of S. Consequently, 1.2 g of sulphur is taken as the optimal amount for PtS₂ growth for further studies. Thus, the aforementioned results demonstrate that with an increasing of S amount, there is more probability of formation of PtS₂ than PtS.

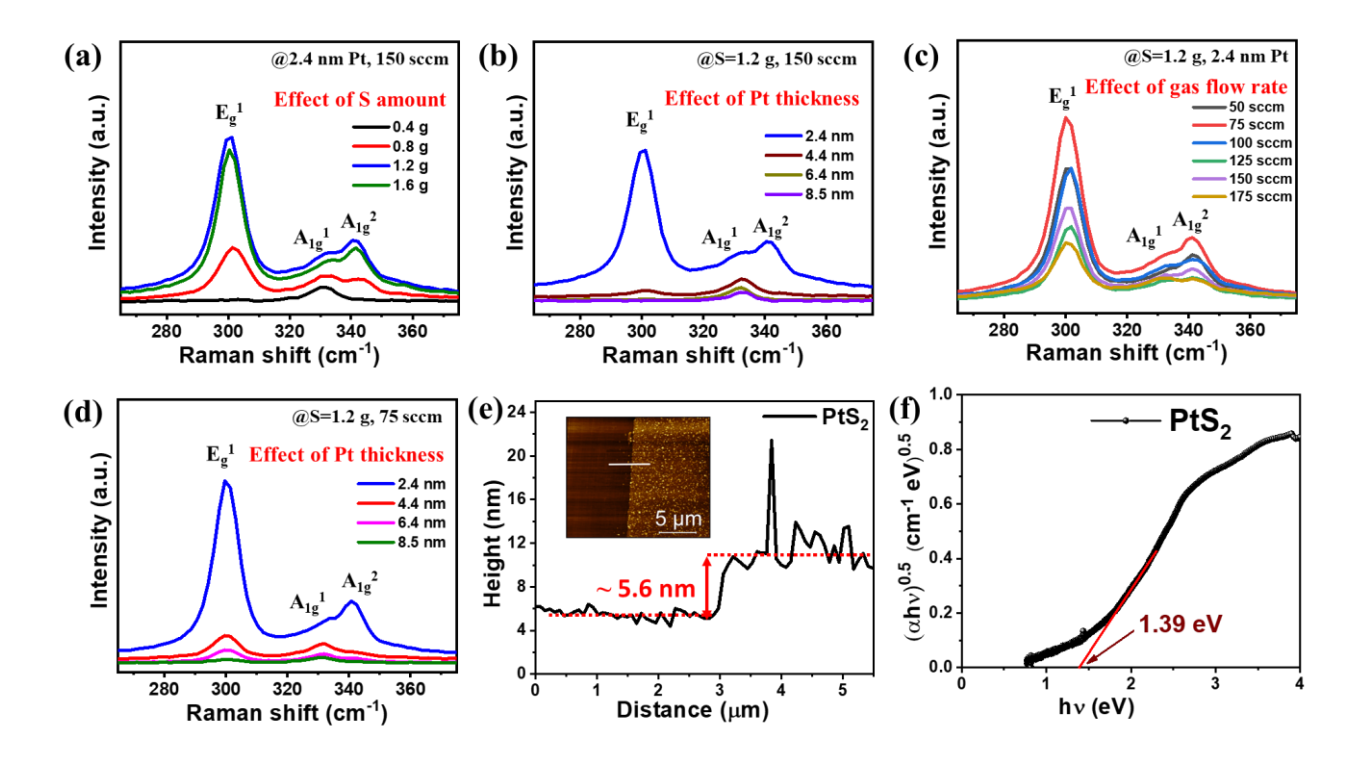


Figure 3.2 (a) Raman spectra of PtS_x (x=1, 2) thin films synthesized at different sulfur amount 0.4 g, 0.8 g, 1.2 g, and 1.6 g (b) Raman spectra of PtS_x films obtained after sulfurizing different Pt thickness (c) Raman spectra of PtS_2 films prepared at different gas flow rate in APCVD (d) Raman spectra of PtS_2 synthesized from different Pt thickness at 75 sccm carrier gas flow rate. (e) Thickness of PtS_2 film calculated by AFM grown by TAC method with 2.4 nm Pt, 1.2 g sulfur, and 75 sccm gas flow rate growth parameters (f) band gap value of best grown PtS_2 thin film calculated by Tauc plot.

3.3.2 Effect of Pt thickness

As PtS₂ thin films were grown by sulfurization of pre-deposited Pt film. Therefore, PtS₂ thickness primarily depends on initial Pt thickness. To investigate the influence of Pt thickness on PtS₂ growth, four different Pt thicknesses, ~2.4 nm, ~4.4 nm, ~6.4 nm, and ~8.5 nm were used. Figure 3.2 (b) represents the Raman spectra of PtS_x (x=1, 2) obtained after sulfurizing different Pt thicknesses at S amount of 1.2 g. Initially, sulfurization of 2.4 nm Pt film gives three Raman peaks observed at 300.1 cm⁻¹ (Eg¹), 331.5 cm⁻¹ (A_{1g}¹), and 341.4 cm⁻¹ (A_{1g}²), which correspond to PtS₂ [5]. Furthermore, for 4.4 nm Pt thickness, only two peaks are seen at 301.3 cm⁻¹ (Eg¹) and 332.7 cm⁻¹ (A_{1g}¹), which again corroborates the growth of PtS₂. However, here the peak intensity of A_{1g}¹ is more than Eg¹, representing the growth of mixed phase of PtS₂ and PtS in the sample. For higher Pt thickness samples such as 6.4 nm and 8.5 nm, only one peak at ~332.5 cm⁻¹ appears correlating the growth of PtS [8]. Therefore, these results manifest that with increasing Pt thickness, there are more chances of PtS formation than PtS₂.

3.3.3 Effect of gas flow rate

A mixture of 1.1% H₂ balance Ar was used as a carrier gas throughout this study. Figure 3.2 (c) represents the Raman spectra of PtS₂ obtained from sulfurizing of 2.4 nm Pt at different carrier gas flow rates (50-175 sccm) in APCVD. For each gas flow rate, we get three characteristic peaks of Raman at $\sim 301 \text{ cm}^{-1} (E_g^{-1})$, $\sim 332 \text{ cm}^{-1} (A_{1g}^{-1})$, and $\sim 341 \text{ cm}^{-1} (A_{1g}^{-2})$ (with minor shifting in their positions) corresponding to the PtS₂. However, for sulfurizing higher Pt thickness (more than 2.4 nm), the gas flow shows distinct behaviour. Figure 3.2 (b) and Figure 3.2 (d) represent the Raman spectra of $PtS_x(x=1, 2)$ after sulfurizing different Pt thicknesses at 150 sccm and 75 sccm gas flow rates, respectively. At 75 sccm gas flow, we get one common E_g¹ (~300.7 cm⁻¹) peak for all the Pt thicknesses (Figure 3.2(d)), which shows that predominately PtS₂ formed [5]. However, for 150 sccm gas flow with increasing Pt thickness, the $E_g^{\ 1}$ peak disappears (Figure 3.2 (b)), which signifies that PtS formed at higher Pt thicknesses. Moreover, at 75 sccm gas flow, we get sharp peaks $(E_g{}^1,\,A_{1g}{}^1,\,$ and $A_{1g}{}^2)$ among all the gas flows, as shown in Figure 3.2 (c). This study suggests that 75 secm is the optimal gas flow rate for PtS2 synthesis in our work, even for higher Pt thicknesses. The thickness of best PtS₂ film grown with 2.4 nm Pt, 1.2 g sulfur, and 75 sccm gas flow rate is determined by AFM and found a value of ~5.6 nm, as shown in Figure 3.2 (e). Moreover, Figure 3.2 (f) exhibits that a band gap of 1.39 eV (calculated by Tauc plot) is obtained for the same PtS₂ sample.

3.3.4 XPS data analysis

To understand the impact of growth parameters in more detail and support our Raman results, XPS measurement were performed on three samples grown at different conditions, as demonstrated in Figure 3.3. The carbon peak of 284.8 eV is used as an energy calibration to eliminate the effect of charging on the surface. Figure 3.3 (a) and 3.3 (d) show the core level spectra of Pt 4f and S 2p respectively, grown at 0.4 g sulfur amount and 150 sccm gas flow rate. Figure 3.3 (a) exhibits two pairs of doublet peaks and one small peak obtained in Pt 4f core level spectra. The two prominent peaks at 72.35 eV and 75.70 eV correspond to the Pt $4f_{7/2}$ and Pt $4f_{5/2}$ core levels region of PtS which depicts that predominantly PtS is formed at the low sulfur amount [9]. In addition, another pair of doublet gives two peaks at 73.9 eV and 77.3 eV respective to Pt $4f_{7/2}$ and Pt $4f_{5/2}$ of PtS₂ [6, 10]. A small peak at 71.1 eV shows the Pt $4f_{7/2}$ core level of the elemental Pt [11], which further conveys that Pt thin film is not completely sulfurized at the low sulfur amount. As shown in Figure 3.3 (d), the S 2p core level spectra of the 0.4 g sample exhibit three peaks. The prominent two peaks at 162.78 eV and 163.98 eV are ascribed to the S 2p_{3/2} and S 2p_{1/2} state of the PtS, and one small peak at 161.70 eV represents the polysulfide formation [9, 12]. The calculated stoichiometric of Pt/S is 1:0.987 also shows that Pt thin film is not completely sulfurized at low sulfur amount.

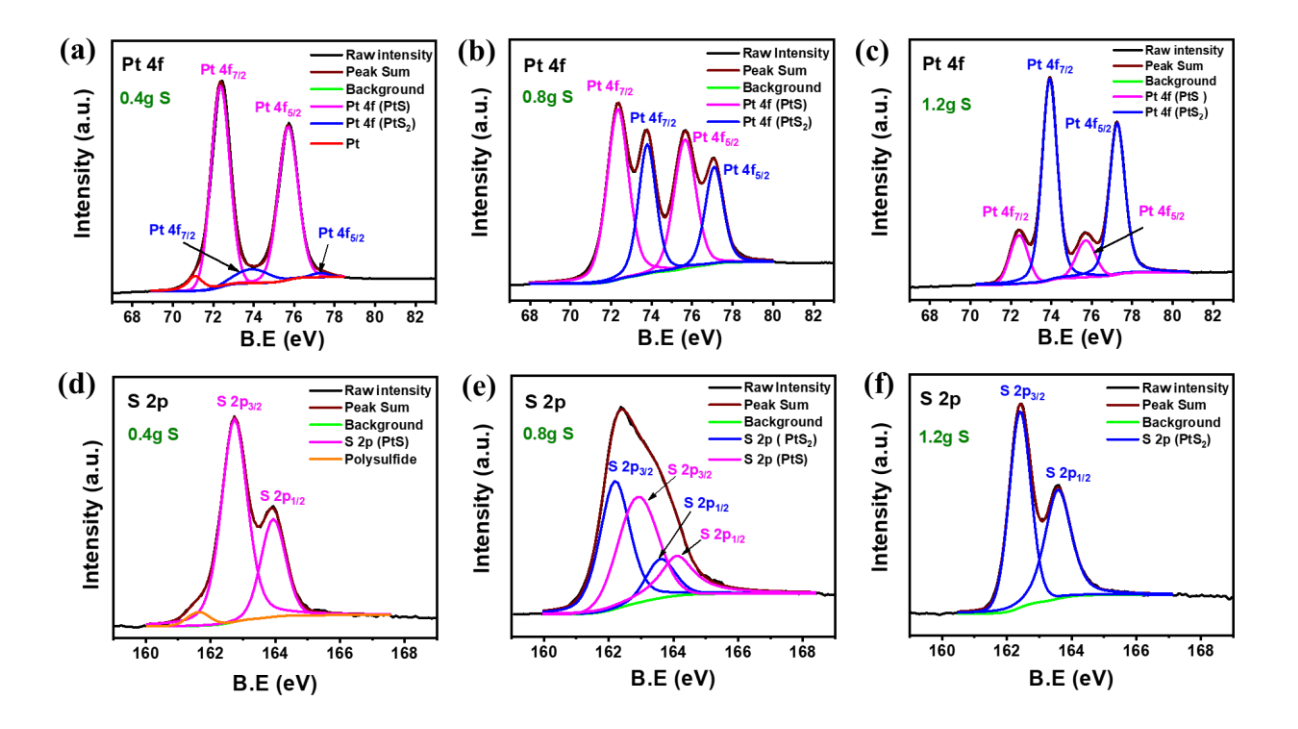


Figure 3.3 XPS spectra of Pt 4f and S 2p core level regions of the PtS_x grown on SiO_2/Si substrate at different growth conditions of (a, d) 0.4 g sulfur and 150 sccm gas flow rate, (b, e) 0.8 g sulfur and 75 sccm gas flow rate and (c, f) 1.2 g sulfur and 75 sccm gas flow rate.

The XPS spectra of thin film grown at 0.8 g sulfur and 75 sccm gas flow with Pt 4f and S 2p core levels are shown in Figure 3.3 (b) and 3.3 (e), respectively. Double pairs of peaks are obtained in Pt 4f is shown in Figure 3.3 (b). With the addition of two peaks at 72.33 eV and 75.65 eV corresponding to Pt $4f_{7/2}$ and Pt $4f_{5/2}$ core levels spectra of PtS, the other two peaks at 73.81 and 77.13 eV relating to Pt $4f_{7/2}$, and Pt $4f_{5/2}$ core levels of PtS₂ are obtained [6, 9, 10]. Figure 3.3 (e) depicts the S 2p core level spectra of the same sample in which four peaks are observed. Two peaks at 162.28 eV and 163.55 eV correspond to the S 2p_{3/2} and S 2p_{1/2} state of the PtS₂, and other peaks at 162.9 eV and 164.1 eV relative to S 2p_{3/2} and S 2p_{1/2} state of the PtS. Here both Pt 4f (Figure 3.3 (b)) and S 2p (Figure 3.3 (e)) spectra signify that PtS and PtS₂ mixed phase is formed as the area of both doublet peaks are comparative. In addition, the calculated stoichiometric ratio of Pt/S is 1:1.637, which is more than for PtS and less than for PtS₂ also shows that a mixed state is formed. Moreover, no elemental peak of Pt metal is obtained implying that at higher sulfur amounts, Pt thin film is more sulfurized as compared to the lower sulfur amount corroborating our Raman results. For the last sample grown at 1.2 g sulfur and 75 sccm gas flow rate, the corresponding Pt 4f and S 2p XPS spectra are shown in Figure 3.3 (c) and 3.3 (f), respectively. In Pt 4f (Figure 3.3 (c)), two leading peaks at 73.92 eV and 77.25 eV represent the Pt $4f_{7/2}$ and Pt $4f_{5/2}$ core levels of PtS₂ and two minor peaks at 72.33 eV and 75.65 eV corresponding to PtS [9, 10]. Furthermore, in S 2p spectra (Figure 3.3 (f)), only two peaks at a position of 162.41 eV and 163.58 eV relative to the S 2p_{3/2} and S 2p_{1/2} state of the PtS₂ are obtained. The value of the stoichiometric ratio of Pt/S is 1:1.820, which is much closer to the ideal PtS₂. Therefore, these XPS results reveal that control growth of PtS to PtS₂ can be obtained by carefully controlling growth parameters.

3.4 PtS₂ grown on different substrates

Further, we have used our optimized growth condition (1.2 g sulfur, 2.4 nm Pt thickness, and 75 sccm gas flow) to deposit PtS₂ on different substrates such as SiO₂/Si, sapphire, p-type Si, and flexible substrate mica. Figure 3.4 (a) shows the Raman spectra of PtS₂ synthesized on these substrates. PtS₂ film deposited on each substrate displays two prominent Raman peaks, E_g^1 and A_{1g}^2 . For the PtS₂ thin film synthesized on the Si substrate, two Raman peaks, E_g^1 and A_{1g}^2 , at 303.3 cm⁻¹ and 345.0 cm⁻¹ respectively, was achieved. Three characteristic Raman peaks are demonstrated by PtS₂ film grown on the sapphire substrate at 302.6 cm⁻¹ (E_g^1), 334.4 cm⁻¹ (A_{1g}^1), and 343.7 cm⁻¹ (A_{1g}^2), is shown in Figure 3.4 (a).

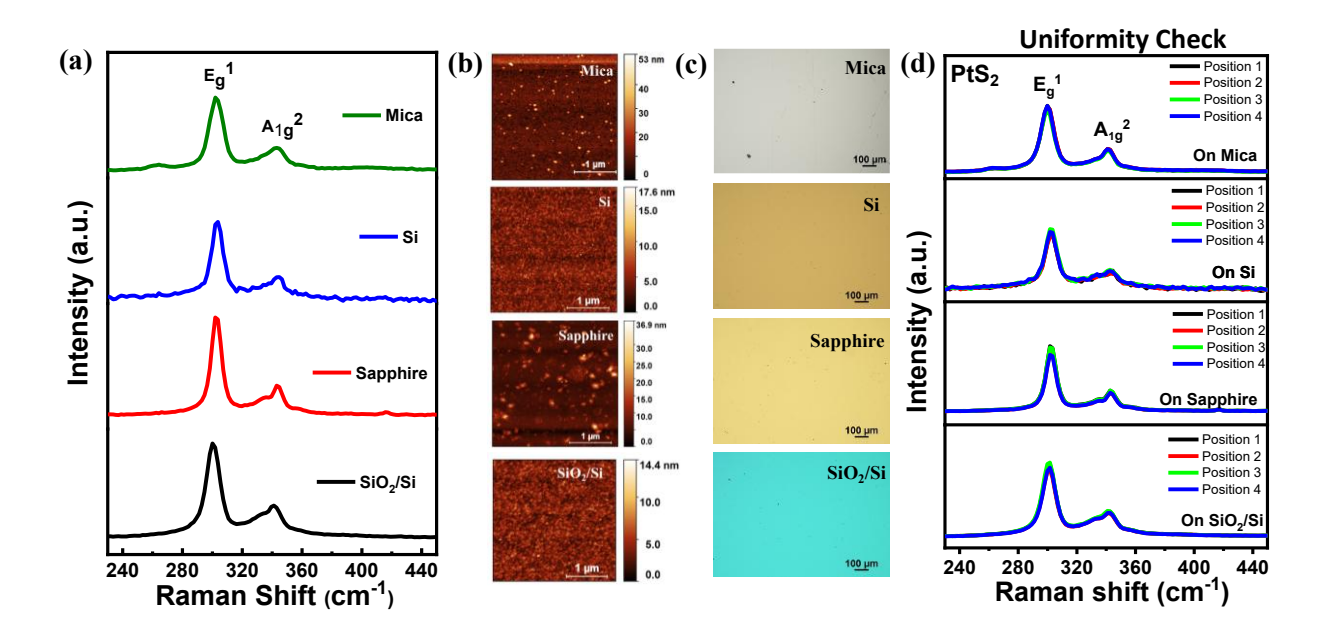


Figure 3.4 (a) Raman spectra of PtS₂ film synthesized on different substrates (mica, Si, Sapphire, and SiO₂/Si) (b) AFM surface topography images of PtS₂ film grown on these substrates with a scale bar of 1 μ m and scan area of 3 μ m×3 μ m (c) Optical images of the same PtS₂ film synthesized on mica, Si, Sapphire, and SiO₂/Si with scale bar 100 μ m. (d) Uniformity of PtS₂ on different substrates (mica, Si, Sapphire, SiO₂/Si) is confirmed by performing the Raman on different positions (near the edges of the samples) of size 1×1 cm² area.

Moreover, PtS₂ film on SiO₂/Si substrate also shows three characteristics Raman peaks at 300.4 cm⁻¹ (Eg¹), 334.0 cm⁻¹ (A_{1g}¹), and 341.31 cm⁻¹ (A_{1g}²). For the mica substrate, two prominent peaks at 302.54 cm⁻¹ and 343.02 cm⁻¹ correspond to Eg¹ and A_{1g}² of PtS₂ are observed. It can be seen from Figure 3.4 (a) that the Eg¹ peak of PtS₂ grown on Sapphire and Si substrate is blue-shifted as compared to PtS₂ grown on SiO₂/Si. This Raman shift may be due to the substrate's distinct properties (lattice constant, crystallinity, transparency, conductivity) and interaction of substrate with the deposited PtS₂ film [13-15]. Moreover, the impurities and defects at the interface (between the substrate and film) changes with the substrate's nature which might be another reason for the Raman shift [13-15]. Further, AFM measurements were performed on PtS₂ films grown on these various substrates to see the surface topography and calculate their root mean square (RMS) roughness. Figure 3.4 (b) displays the topography image of PtS₂ film on mica, Si, sapphire, and SiO₂/Si substrates with RMS values of 4.16 nm, 1.43 nm, 2.76 nm, and 1.34 nm, respectively. A low RMS value of PtS₂ thin film on SiO₂/Si substrate is obtained compared to other substrates. The optical images

of PtS₂ on different substrates are shown in Figure 3.4 (c), clearly showing a high uniformity of film and colour contrast change with varying substrates. In addition, the uniformity of PtS₂ on these substrates (mica, Si, Sapphire and SiO₂/Si) is confirmed by Raman spectroscopy. Figure 3.4 (d) demonstrates the Raman spectra taken over the different positions over the substrates and corroborates the highly uniformity of the PtS₂ film grown on these substrates

3.5 Proposed growth Mechanism of PtS₂

In the CVD growth process, various parameters play a crucial role in controlling the morphology, domain size, and number of layers in nanomaterial synthesis. These parameters include the amount of precursors, carrier gas flow rate, temperature, pressure, substrate, and precursor positions [16, 17]. In addition to these parameters, theoretical calculations of energies, such as formation energy, deformation energy, and surface energy along different miller indices planes, can help to explain the experimental results [18, 19]. However, predicting the formation of either PtS or PtS₂ is quite challenging as the literature still presents conflicting values for formation energy. Previous reports suggest that the expected formation energy for PtS₂ and PtS lies in the range of -0.685 to -0.382 eV/atom and -0.659 to -0.431 eV/atom, respectively [20-22]. Such inconsistencies have resulted in contradictory results about the relative stability of both semiconductors. Therefore, to have actual control over the growth of PtS₂, understanding its growth mechanism is crucial. The growth of PtS₂ is assumed to be a two-step reaction in which the first S atoms react with Pt to form PtS (because of its stability) followed by the 2nd step where PtS reacts with more S atoms to finally form PtS₂ (shown by reaction (3.1) and (3.2)). We used a tube-in-tube arrangement to make 2nd step more feasible with the addition of a sulfur-rich environment. This tube-in-tube arrangement helps to confine more sulfur vapours inside the smaller tube, forcing more sulfur atoms to react with Pt film and increase the sulfurization rate [5, 23, 24]. Moreover, the nature of gas flow (turbulent or laminar) inside the CVD tube can also impact the sulfurization rate. In turbulent flow, molecules randomly move in all directions, contrary to laminar, where S vapours move in a particular direction [25-27]. Hence, an optimized gas flow should be required to control largearea growth of PtS₂. The detailed growth mechanism of the PtS and PtS₂ under different growth parameters is shown in Figure 3.5. In addition, the uniformity of PtS₂ on these substrates (mica, Si, Sapphire and SiO₂/Si) is confirmed by Raman spectroscopy. Figure 3.4 (d) demonstrates the Raman spectra taken over the different positions over the substrates and corroborates the highly uniformity of the PtS₂ film grown on these substrates.

The proposed growth mechanism can be explained in five steps, (1) transport of S vapours from the sulfur source towards the Pt surface (by carrier gas), (2) diffusion of S atoms towards the Pt-coated substrate, (3) Adsorption of S vapours on the Pt surface, (4) Chemical reaction between S vapours and Pt thin film (sulfurization) (5) Desorption of the S vapours. PtS and PtS₂ can be synthesized depending on the growth conditions. A typical step in all the growth conditions is shown in Figure 3.5 (a), where sulfur vapours are transported from the sulfur source onto the Pt-coated substrate by carrier gas, then the diffusion and adsorption of these vapours start on the Pt-coated substrate.

Figure 3.5 (b) to 3.5 (d) represent the effect of S amount on the growth of PtS and PtS₂. Initially, sulfur atoms (yellow colour) start adsorbing on the Pt surface and take part in a chemical reaction with Pt atoms (grey colour). When the sulfur amount is lower, less S vapour reacts with Pt atoms and form PtS, as shown in Figure 3.5 (b). In a sulfur-rich environment, at higher S amount, the ambient creates a massive number of S atoms that further sulfurize most of the PtS molecules into PtS₂ and, simultaneously, some unreacted S atoms go out as a by-product (step 5). Finally, when complete sulfurization occurs, the PtS₂ thin film is grown on the substrate, as shown in Figure 3.5 (c). The Raman spectra demonstrating a comparison of the PtS_x (x=1, 2) grown at 0.4 g and 1.2 g S amount, is shown in Figure 3.5 (d).

Figure 3.5 (e) to 3.5 (g) represents the effect of Pt thickness on the growth of PtS and PtS₂ (at fixed 150 sccm gas flow and 1.2 g S amount). At higher Pt thickness (>4.4 nm), sulfur atoms mainly react with the upper surface of the Pt layer and less diffusion occurs inside the depth of Pt film due to Pt nobility nature, top surface Pt atoms prevent the sulfurization of deep Pt atoms as shown in Figure 3.5 (e). Thereby, less sulfurization of Pt film occurs at higher Pt thickness, and the feasibility of PtS formation increases. In the case of lower Pt thickness (2.4 nm), S atoms diffuse almost entirely inside the Pt film (because of less Pt thickness), leading to complete adsorption (step 3) and more sulfurization (step 4) as exhibited in Figure 3.5 (f). Hence, there is more probability of PtS₂ formation at lower Pt thickness. Figure 3.5 (g) illustrates the Raman spectra of PtS₂ (sulfurization of 2.4 nm Pt) and PtS (sulfurization of 8.5 nm Pt), which further confirmed the critical role of Pt thickness on the growth process of Pt chalcogenide films.

The effect of gas flow on the growth of PtS and PtS₂ is illustrated in Figure 3.5 (h) to 3.5 (j). The PtS₂ synthesis even for higher Pt thickness at low gas flow (75 sccm), can be explained based on gas transport theory. The Reynolds number (R_e) helps to understand the type of gas flow through a tube. Numerically, it is defined as $R_e = \frac{\rho v M}{\eta}$, where ρ , v, and η are the gas's

Chapter 3: Large area and controlled growth of PtS₂ on various substrates

density, velocity, and viscosity, respectively, and M is the diameter of the pipe [25]. Since, here, except gas flow, all other parameters are constant, Reynolds number depends solely on the velocity of gas flow. With increasing gas flow velocity, the gas flow nature probably changes from laminar to turbulent flow. This turbulence flow makes gas flow to move in a random direction, as shown in Figure 3.5 (h), leading to less sulfur vapour transport on the substrate (step 1 of mechanism) hence the less sulfurization (step 4 of mechanism), which further leads to the formation of PtS, especially at a large thickness of the Pt. Conversely, at lower gas flow (75 sccm), the flow is laminar and in a particular direction, so it transports more sulfur vapours on the substrate and hence more sulfurization occurs, as shown in Figure 3.5 (i). Therefore, PtS₂ synthesis dominates at low gas flow rate. The comparison of sulfurization of Pt (6.4 nm) at 75 sccm and 150 sccm gas flow is shown in Figure 3.5 (j). In addition, it has been reported that decreasing the gas flow rate can reduce the nucleation rate or help in the formation of large single crystal size with few grain boundaries [17, 27, 28], which can also be another reason for the growth of PtS₂ for higher Pt thickness at lower gas flow rate.

$$Pt + S \rightarrow PtS \dots (3.1)$$

$$PtS + S \rightarrow PtS_2 \dots (3.2)$$

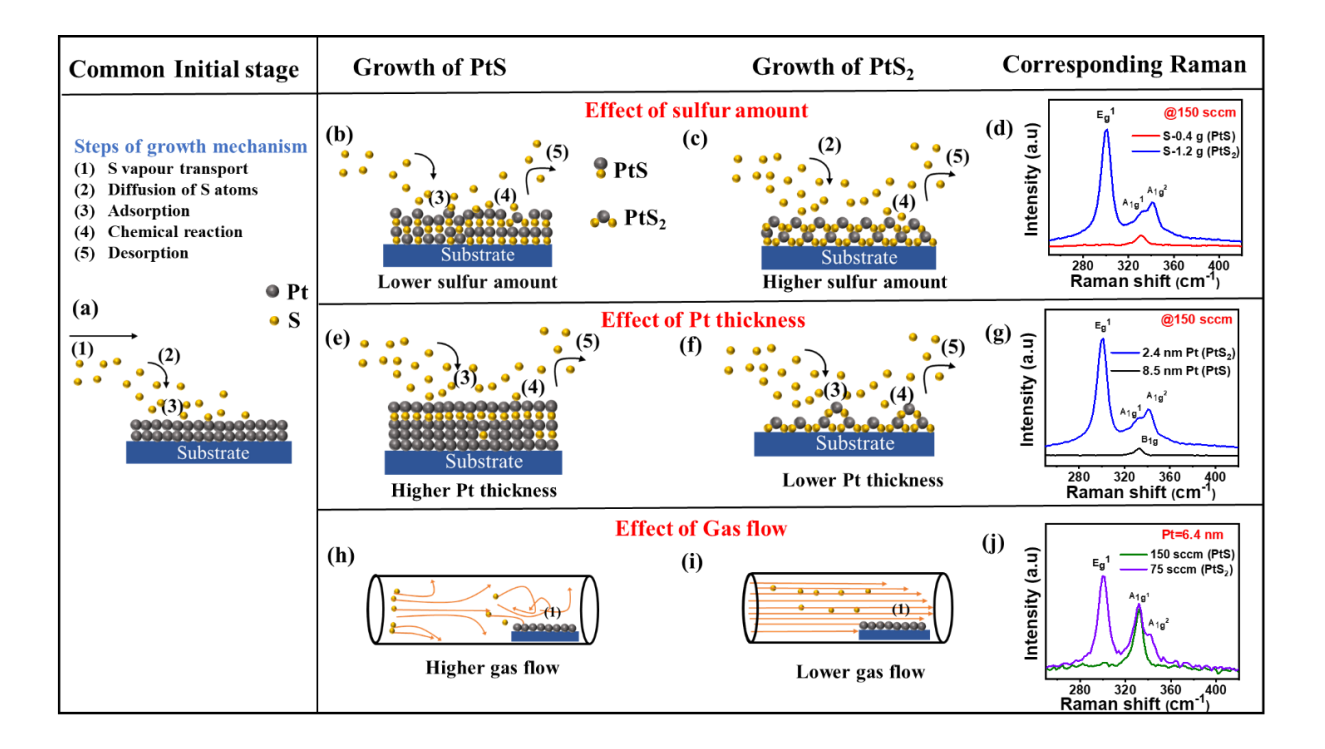


Figure 3.5 Growth mechanism of PtS and PtS₂ at different growth conditions (b)-(d) Effect of sulfur amount, (e)-(g) Effect of Pt thickness, (h)-(j) Effect of gas flow.

3.6 PtS₂ photodetector device performance

Finally, the optoelectronic properties of PtS₂ film were investigated by fabricating its photodetector. Figure 3.6 (a) displays the schematic of the fabricated PtS₂ device on SiO₂/Si substrate. The I-V characteristics of the device in the dark and under illumination of different wavelengths varying from 400-1100 nm is demonstrated in Figure 3.6 (b). The non-linear nature of the I-V curve shows that a Schottky contact is formed between the PtS₂ and Au electrodes. Moreover, it can be seen from the I-V graph that the device gives a good response under 400-1100 nm wavelength illumination. The device performance was evaluated by calculating its figure of merits including responsivity (R), detectivity (D*), external quantum efficiency (EQE), noise equivalent power (NEP), and response time (rise and fall time). The responsivity (R) of photodetector is defined as the ratio of the net photocurrent generated to the incident optical power. Numerically, it is given by equation (3.3)

$$R = \frac{I_{light} - I_{dark}}{P. A} \quad (3.3)$$

Where I_{light}, I_{dark}, P, and A represents the current under illumination, dark current (absence of light), incident optical power density, and active area of the device, respectively. Figure 3.6 (c) depicts the variation of responsivity of the device under visible-NIR (400-1100 nm) illumination at a low bias of 1V. The maximum responsivity of 31.38 AW⁻¹ is obtained at 900 nm illumination with 1V biasing, which shows that our device responds well in the NIR region. The reason for the decrease in responsivity values at the 500 nm and 600 nm wavelengths can be attributed to the responsivity formula, which states that responsivity is inversely proportional to the optical power density (P). During our experiment, we used a monochromator that provided different power densities for different wavelengths. This behaviour is similar to the emission of light by a blackbody radiation source, which emits light of different wavelengths with varying intensities [29, 30]. Hence, in spite of the high photocurrent observed in the 500-600 nm range, the overall P value dominates over the photocurrent value, resulting in a decrease in the responsivity value at these wavelengths.

The detectivity (D*), which is another important figure of merit of the photodetector, specified how weak signal a photodetector can detect is also calculated using a mathematical equation given as (3.4)

$$D^* = \sqrt{\frac{A}{2eI_{dark}}} \times R \quad ... \quad (3.4)$$

where e is the electronic charge and R is the responsivity of the device as defined previously The detectivity calculated for different wavelengths (400-1100 nm) at 1 V is shown in Figure 3.6 (d). Similar to the responsivity, the maximum detectivity of 3.92×10^{13} Jones is obtained under 900 nm wavelength at 1 V bias. This high value of responsivity and detectivity illustrates the superior device performance.

Another parameter, external quantum efficiency (EQE), defines the number of charge carriers (electron-hole pair) collected per unit incident photon. Mathematically it is evaluated by using equation (3.5)

$$EQE = \frac{Rhc}{e\lambda} \quad \quad (3.5)$$

where h, c, e, λ , and R are the Plank's constant, speed of light, electronic charge, wavelength of the incident light, and responsivity of the photodetector, respectively.

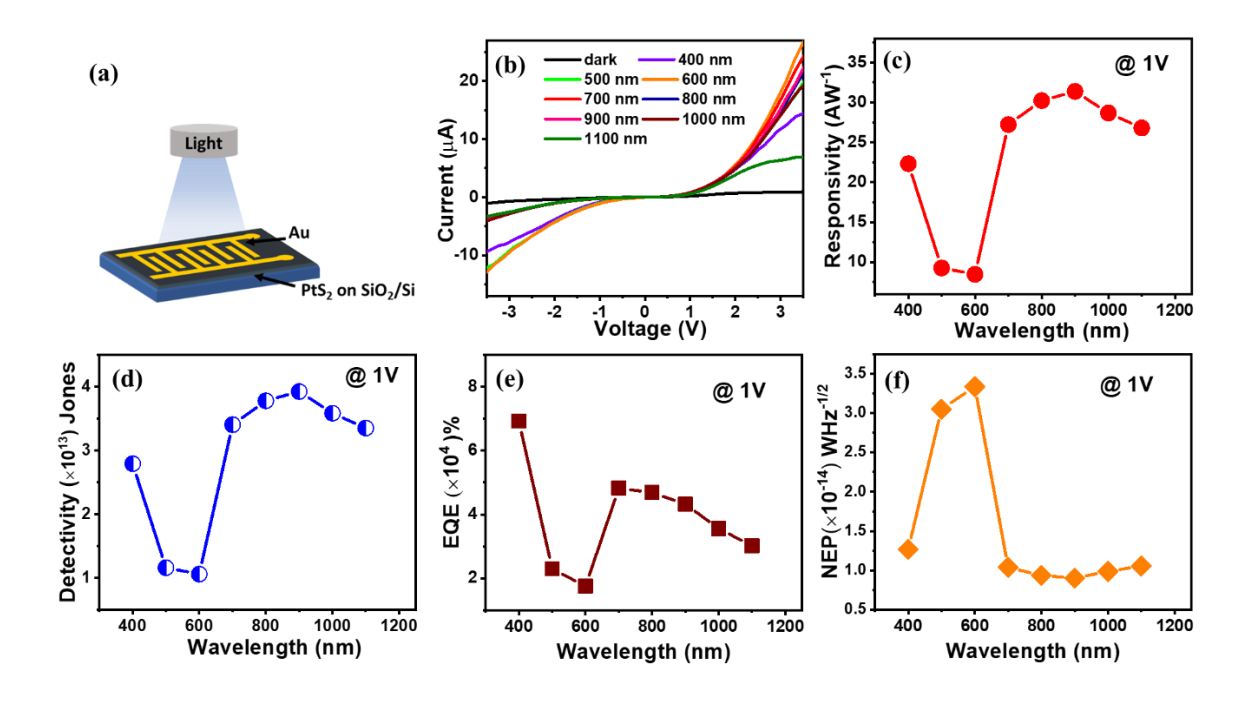


Figure 3.6 (a) Schematic of PtS₂ photodetector device (b) I-V characteristics of PtS₂ device under dark and illumination of different wavelengths (c), (d), (e) and (f) represents the variation of Responsivity, Detectivity, EQE, and NEP, respectively as a function of wavelength at low voltage (1V) biasing.

Our device also exhibited high EQE at low 1 V biasing. Figure 3.6 (e) shows the variation of EQE with wavelength (400-1100) at 1 V. EQE exceeds 100% for all wavelengths because of high photoconductive gain in the TMDC photodetectors [2, 31, 32]. In addition, we calculated

noise equivalent power (NEP), which is the minimum power required to get the signal-to-noise ratio of unity at unit bandwidth (B=1 Hz). Numerically, it is given by

$$NEP = \frac{\sqrt{A \times B}}{D}$$
(3.6)

NEP is inversely proportional to the detectivity, thus least value of NEP is obtained at the highest value of detectivity. Figure 3.6 (f) demonstrates the variation of NEP with different wavelengths (400-1100 nm). Its lowest value of 9.01×10⁻¹⁵ WHz^{-1/2} is obtained for 900 nm wavelength. At last, we also evaluated the time response of the device. Usually, response time is measured in terms of rise time (t_r) (time taken to reach from 10% to 90% of maximum current under illumination) and fall time (t_f) (time taken to come down from 90% to 10% of maximum current under illumination off). The device responds well to the visible-NIR (400-1100 nm) region, as shown in Figure 3.7 (a). For our device, at 500 nm illumination (and 1 V biasing), the rise and fall time was 231 ms and 158 ms, respectively, as represented in Figure 3.7 (b). The high rise or fall time of device can be understood from the defects or trap states present in the device. In PtS₂ the defects or trap states could be generated during growth or due to the sulfur vacancies [2, 15, 16]. These trap states promote high photo-gain and thus, enhance the responsivity of the device (as in our case we also observed high responsivity of 31.38 AW-1 at low 1 V) and slow down the speed of the device. Same phenomenon has also been reported in other 2D material where high responsivity is obtained with a trade-off of slow speed [33-36]. Additionally, higher value of external quantum efficiency (EQE) at 1 V obtained in this device can be directly understood from photo-gain which further helps to understand the trap state present inside the material [32, 37-39]. The photo-gain is given by:

$$G = \frac{\tau}{\tau_t} = \frac{\tau \mu V}{L^2} \dots (3.7)$$

where τ and τ_t are the photo generated carrier lifetime and carrier transit time respectively, μ is the carrier mobility, V is applied bias voltage and L is the channel length. As from above mathematical relation it can be seen that photo gain is directly proportional to the photo generated carrier lifetime (τ). The high photo gain is owing to the long carrier lifetime of carrier in trap state of the material. In other words, when light is incident on the device, it generates photo-excited electron-hole pairs and one charge carrier trapped in these trap states, and other types of carriers keep moving through the device until it reaches to the electrode or recombines with the opposite charge carrier. This increases the carrier lifetime of photo-generated charge carriers and obtain high photo gain in the fabricated device which also convey that trap states

present in the device could be the main reason of slow speed of the device. The comparison of our PtS₂ photodetector device with other reported TMDC based photodetector devices is shown in Table 3.1.

For practical application of the device especially in 2D material, high stability of device in ambient condition is an important concern. Here, the stability of PtS_2 photodetector device is confirmed by Raman spectroscopy and its responsivity measurements after six months. The Raman spectra of PtS_2 synthesised at optimized condition (2.4 nm Pt, 1.2g sulfur, and 75 sccm gas flow rate) in fresh condition (called pristine sample) and after six months is shown in Figure 3.7 (c) confirmed that PtS_2 is highly stable as no significant change in peak (E_g^{-1} , A_{1g}^{-1} and A_{1g}^{-2}) positions is observed. Moreover, trivial change in responsivity value at 1V of the same device after six months is shown in Figure 3.7 (d) also justify that device is highly stable in ambient conditions.

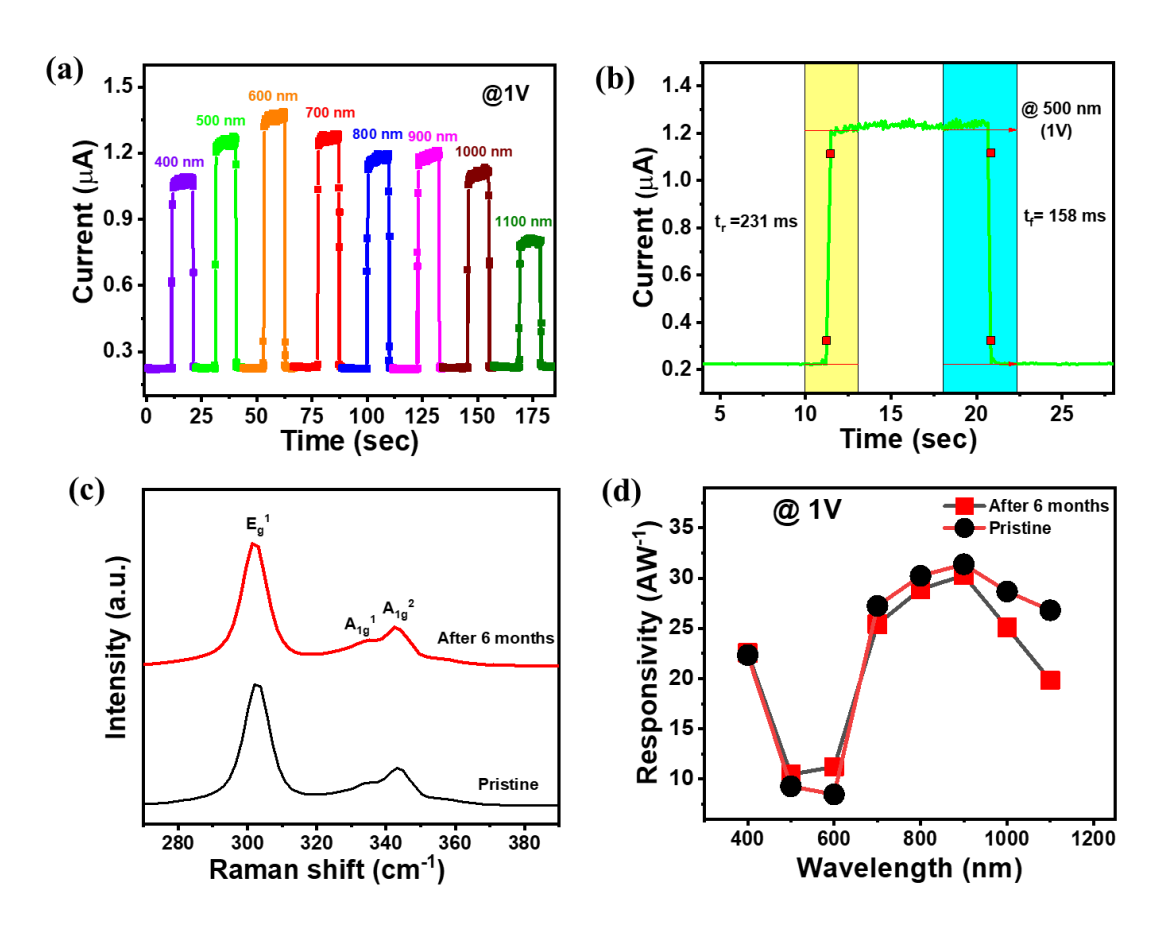


Figure 3.7 (a) Time dependent photoresponse of the fabricated PtS₂ device under broad visible-NIR range (400-1100 nm) at 1V bias (b) Calculated response time (rise and fall time) of PtS₂ photodetector at 500 nm (1V bias). (c, d) Raman spectra and responsivity of pristine PtS₂ and after 6 months kept in ambient conditions device.

Chapter 3: Large area and controlled growth of PtS₂ on various substrates

Along with this, we also study the temporal photoresponse of the PtS₂ photodetector devices fabricated on SiO₂/Si, sapphire, and mica substrate under incident radiation of 532 nm laser (5 mW) at 3V bias. Figure 3.8 shows the I-T characteristics of PtS₂ film grown on SiO₂/Si, sapphire, and flexible mica substrate. It can be seen from Figures 3.8 (a)-(c) that PtS₂ grown on these substrates gives a satisfactory response to a 532 nm laser. In addition, we also evaluated the response time (rise and fall time) on these substrates, as shown in Figures 3.8 (d)-(f). The lowest rise/ fall time of 138 ms/163 ms is obtained on the PtS₂ device synthesized on SiO₂/Si substrate. The PtS₂ device fabricated on sapphire and mica substrates exhibits a rise /fall time of 310 ms/664 ms and 484 ms/986 ms, respectively. These results further confirmed that PtS₂ is a potential material for broadband photodetector application.

Table 3.1 Comparison of our fabricated PtS₂ photodetector performance with other reported literature based on TMDCs photodetector.

Active material for Device	Substrate	Responsivity (AW-1)	Detectivity (Jones)	Response time (sec)	Growth optimized for different substrates	Ref.
PtS ₂	SiO ₂ /Si	-	-	4.6	-	[5]
PtS ₂ /PtS ₂	SiO ₂ /Si	0.188	-	0.066/0.075	-	[7]
PtS_x	SiO ₂ /Si	0.24	6.62×10 ⁹	0.308	sapphire	[15]
PtS_2	SiO ₂ /Si	3.20	1.24×10 ⁷	0.18/0.2	-	[40]
WS_2	SiO ₂ /Si	0.70	2.7×10 ⁹	4.1/4.4	-	[41]
MoS ₂ - MoSe ₂	SiO ₂ /Si	1.3	2.6×10 ¹¹	-	-	[42]
WSe_2	SiO ₂ /Si	7.55	3×10 ¹²	0.33×10 ⁻³ / 0.55×10 ⁻³	-	[43]
PtS ₂	SiO ₂ /Si	31.38	3.92×10 ¹³	0.23/0.15	Si, SiO ₂ /Si, Sapphire, mica	This work

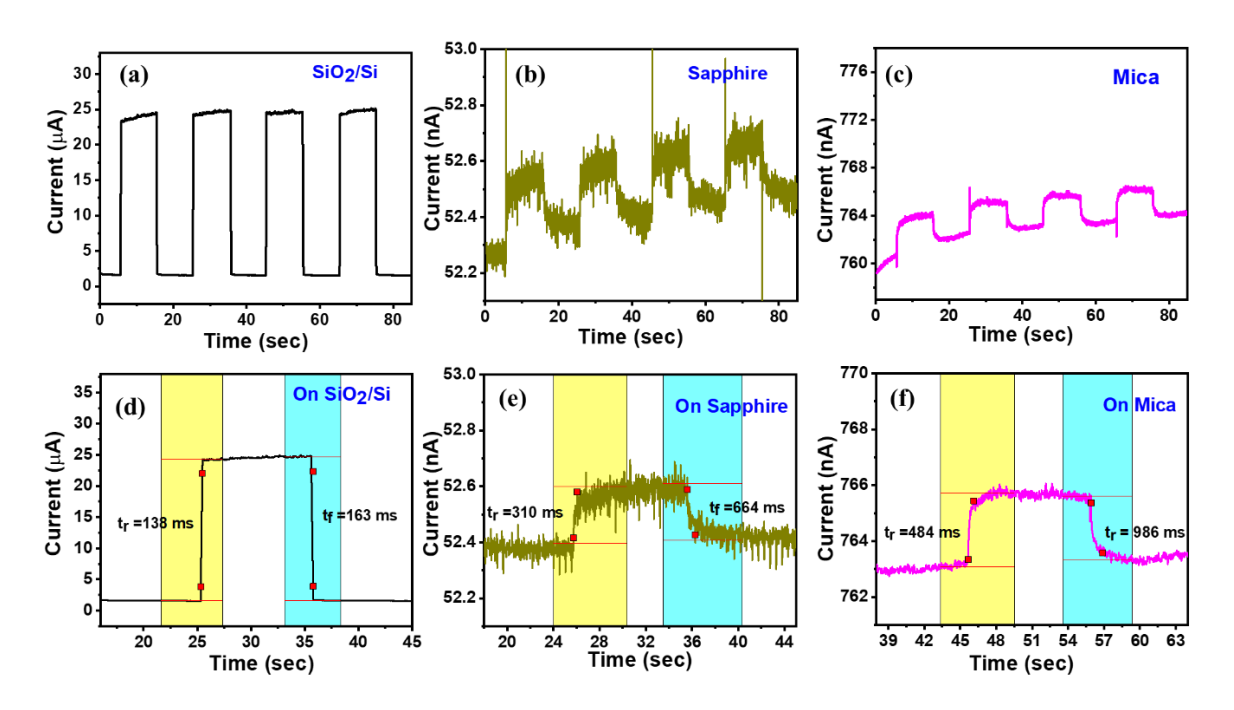


Figure 3.8 I-T characteristics of PtS₂ photodetector grown on different substrates (a) Si/SiO₂ substrate (b) Sapphire (c) Mica, under illumination of 532 nm at 3V. (d)-(f) Response time of the fabricated photodetector on Si/SiO₂, Sapphire and mica, respectively.

3.7 Conclusion

In conclusion, we have synthesized a large area PtS₂ thin film by sulfurization of Pt thin film in APCVD with a tube-in-tube arrangement. The growth of PtS₂ is highly reproducible, further confirmed by its growth on different substrates such as SiO₂/Si, sapphire, Si, and mica. Our study suggests that growth parameters such as sulfur amount, Pt thickness, and gas flow rate are crucial in controlling the growth of PtS₂ and PtS. Raman spectroscopy and XPS results confirmed that there is more probability to form PtS₂ at low Pt thickness, higher sulfur amount, and optimized gas flow (75 sccm). Moreover, a high-performance PtS₂ photodetector is fabricated on SiO₂/Si substrate with high responsivity and detectivity of 31.38 AW⁻¹ and 3.92×10¹³ Jones, respectively, at a low biasing of 1V. The device also shows a broadband detection ranging from visible to NIR (400-1100 nm). Moreover, photoresponse is measured for PtS₂ synthesized on SiO₂/Si, sapphire, and mica substrates under visible (532 nm) incident radiation. This work offers a facile approach to synthesize large-area 2D noble metal dichalcogenides for next-generation optoelectronic applications.

References

- 1. Zhao, Y., et al., Extraordinarily Strong Interlayer Interaction in 2D Layered PtS2. Advanced Materials, 2016. **28**(12): p. 2399-2407.
- 2. Li, L., et al., Few-Layered PtS2 Phototransistor on h-BN with High Gain. Advanced Functional Materials, 2017. **27**(27): p. 1701011.
- 3. Pi, L., et al., *Temperature dependence of Raman responses of few-layer PtS*<*sub*>*2*<*/sub*>. Nanotechnology, 2018. **29**(50): p. 505709.
- 4. Wang, Z., et al., A Noble Metal Dichalcogenide for High-Performance Field-Effect Transistors and Broadband Photodetectors. Advanced Functional Materials, 2020. **30**(5): p. 1907945.
- 5. Xu, H., et al., *Strategy for Fabricating Wafer-Scale Platinum Disulfide*. ACS Applied Materials & Interfaces, 2019. **11**(8): p. 8202-8209.
- 6. Cullen, C.P., et al., Synthesis and characterisation of thin-film platinum disulfide and platinum sulfide. Nanoscale, 2021. **13**(15): p. 7403-7411.
- 7. Yuan, J., et al., Wafer-Scale Fabrication of Two-Dimensional PtS2/PtSe2 Heterojunctions for Efficient and Broad band Photodetection. ACS Applied Materials & Interfaces, 2018. 10(47): p. 40614-40622.
- 8. Huang, J., et al., Surface-State Assisted Carrier Recombination and Optical Nonlinearities in Bulk to 2D Nonlayered PtS. ACS Nano, 2019. **13**(11): p. 13390-13402.
- 9. Dembowski, J., L. Marosi, and M. Essig, *Platinum Sulfide by XPS*. Surface Science Spectra, 1993. **2**(2): p. 104-108.
- 10. Dembowski, J., L. Marosi, and M. Essig, *Platinum Disulfide by XPS*. Surface Science Spectra, 1993. **2**(2): p. 133-137.
- 11. Matin, M.A., et al., Rational syntheses of core-shell Fe@(PtRu) nanoparticle electrocatalysts for the methanol oxidation reaction with complete suppression of Copoisoning and highly enhanced activity. Journal of Materials Chemistry A, 2015. **3**(33): p. 17154-17164.
- 12. Fantauzzi, M., et al., *Exploiting XPS for the identification of sulfides and polysulfides*. RSC Advances, 2015. **5**(93): p. 75953-75963.
- 13. Liu, J. and J. Zhang, Nanointerface Chemistry: Lattice-Mismatch-Directed Synthesis and Application of Hybrid Nanocrystals. Chemical Reviews, 2020. **120**(4): p. 2123-2170.
- 14. Yin, H., et al., Substrate effects on the CVD growth of MoS2 and WS2. Journal of Materials Science, 2020. **55**(3): p. 990-996.
- 15. Wang, Y., et al., Large area uniform PtSx synthesis on sapphire substrate for performance improved photodetectors. Applied Materials Today, 2021. 25: p. 101176.
- 16. Cai, Z., et al., Chemical Vapor Deposition Growth and Applications of Two-Dimensional Materials and Their Heterostructures. Chemical Reviews, 2018. 118(13): p. 6091-6133.
- 17. Qin, B., et al., Substrates in the Synthesis of Two-Dimensional Materials via Chemical Vapor Deposition. Chemistry of Materials, 2020. **32**(24): p. 10321-10347.
- 18. Peng, M., et al., *Blackbody-sensitive room-temperature infrared photodetectors based on low-dimensional tellurium grown by chemical vapor deposition*. Science Advances. 7(16): p. eabf7358.
- 19. Ma, L.-J. and H. Shen, *Activating PtSe2 monolayer for hydrogen evolution reaction by defect engineering and Pd doping*. Applied Surface Science, 2021. **545**: p. 149013.

- 20. Bannister, F.A., *Determination of minerals in platinum concentrates from the Transvaal by X-ray methods*. Mineralogical magazine and journal of the Mineralogical Society, 1932. **23**(138): p. 188-206.
- 21. Karzhavin, V.K., Sulfides, selenides, and tellurides of platinum and palladium: Estimation of thermodynamic properties. Geochemistry International, 2007. **45**(9): p. 931-937.
- Wang, A., et al., *A framework for quantifying uncertainty in DFT energy corrections*. Scientific Reports, 2021. **11**(1): p. 15496.
- 23. Agrawal, A.V., et al., Controlled Growth of MoS2 Flakes from in-Plane to Edge-Enriched 3D Network and Their Surface-Energy Studies. ACS Applied Nano Materials, 2018. 1(5): p. 2356-2367.
- 24. Cullen, C.P., et al., Synthesis and characterisation of thin-film platinum disulfide and platinum sulfide. 2021. **13**(15): p. 7403-7411.
- 25. Ohring, M., Materials science of thin films: depositon & structure. 2001: Elsevier.
- 26. Du, H., W. Zhang, and Y. Li, Effects of growth parameters on the yield and morphology of Si3N4 microcoils prepared by chemical vapor deposition. Materials Research Bulletin, 2014. **50**: p. 57-62.
- 27. Eres, G., et al., Cooperative Island Growth of Large-Area Single-Crystal Graphene on Copper Using Chemical Vapor Deposition. ACS Nano, 2014. **8**(6): p. 5657-5669.
- 28. Li, X., et al., *Graphene Films with Large Domain Size by a Two-Step Chemical Vapor Deposition Process.* Nano Letters, 2010. **10**(11): p. 4328-4334.
- 29. Bullock, J., et al., *Polarization-resolved black phosphorus/molybdenum disulfide midwave infrared photodiodes with high detectivity at room temperature*. Nature Photonics, 2018. **12**(10): p. 601-607.
- 30. Chen, Y., et al., *Unipolar barrier photodetectors based on van der Waals heterostructures*. Nature Electronics, 2021. **4**(5): p. 357-363.
- 31. Agrawal, A.V. and M. Kumar, *Enhance near infrared performance of n-type vertically aligned MoS*<*sub*>*2*</*sub*> *flakes photodetector with active p-type CZTS electrodes.* Materials Research Express, 2019. **6**(11): p. 115011.
- 32. Wadhwa, R., et al., *Investigation of charge transport and band alignment of MoS2-ReS2 heterointerface for high performance and self-driven broadband photodetection*. Applied Surface Science, 2021. **569**: p. 150949.
- 33. Lopez-Sanchez, O., et al., *Ultrasensitive photodetectors based on monolayer MoS2*. Nature Nanotechnology, 2013. **8**(7): p. 497-501.
- 34. Kufer, D. and G. Konstantatos, *Highly Sensitive, Encapsulated MoS2 Photodetector with Gate Controllable Gain and Speed.* Nano Letters, 2015. **15**(11): p. 7307-7313.
- 35. Fang, H. and W. Hu, *Photogating in Low Dimensional Photodetectors*. Advanced Science, 2017. **4**(12): p. 1700323.
- 36. Zhang, W., et al., *High-Gain Phototransistors Based on a CVD MoS2 Monolayer*. Advanced Materials, 2013. **25**(25): p. 3456-3461.
- 37. Arora, K., et al., Ultrahigh Performance of Self-Powered β-Ga2O3 Thin Film Solar-Blind Photodetector Grown on Cost-Effective Si Substrate Using High-Temperature Seed Layer. ACS Photonics, 2018. **5**(6): p. 2391-2401.
- 38. Zeiske, S., et al., Sensitivity of Sub-Bandgap External Quantum Efficiency Measurements of Solar Cells under Electrical and Light Bias. ACS Photonics, 2020. 7(1): p. 256-264.
- 39. Kaur, D., et al., *Phase dependent radiation hardness and performance analysis of amorphous and polycrystalline Ga2O3 solar-blind photodetector against swift heavy ion irradiation.* Journal of Applied Physics, 2020. **128**(6): p. 065902.

Chapter 3: Large area and controlled growth of PtS2 on various substrates

- 40. Zhang, Y., et al. Fabrication of Large-Area Short-Wave Infrared Array Photodetectors under High Operating Temperature by High Quality PtS2 Continuous Films. Electronics, 2022. 11, DOI: 10.3390/electronics11060838.
- 41. Yao, J.D., et al., Stable, highly-responsive and broadband photodetection based on large-area multilayered WS2 films grown by pulsed-laser deposition. Nanoscale, 2015. 7(36): p. 14974-14981.
- 42. Chen, X., et al., *In-Plane Mosaic Potential Growth of Large-Area 2D Layered Semiconductors MoS2–MoSe2 Lateral Heterostructures and Photodetector Application*. ACS Applied Materials & Interfaces, 2017. **9**(2): p. 1684-1691.
- 43. Zhou, C., et al., Self-driven WSe2 photodetectors enabled with asymmetrical van der Waals contact interfaces. npj 2D Materials and Applications, 2020. 4(1): p

Chapter 4: Large area 2D PtS₂ heterostructures for broadband photodetection

This chapter discussed the large area PtS₂ heterostructures fabrication and their broadband photodetector applications. By utilizing the properties of heterostructure to enhance the overall device performance, this chapter mainly focuses on the large area PtS₂/MoS₂ (2D-2D) and PtS_{2-x}/Ga₂O₃ (2D-3D) heterostructure fabrication and their broadband (Vis-NIR/UV-NIR) photodetector performance. In PtS₂/MoS₂ heterostructure fabrication, the PtS₂ film was directly grown on the MoS₂ film by TAC method, and it shows broad response from 400-1200 nm (Vis-NIR) wavelength. Whereas in PtS_{2-x}/Ga₂O₃ heterostructure work, the PtS₂ film was wet transferred over the Ga₂O₃ film and exhibits wide response covering UV-C to NIR (250-1100 nm) region. Using photoelectron spectroscopy (XPS and UPS), a detailed interface investigation of the heterojunction (PtS₂/MoS₂ and PtS_{2-x}/Ga₂O₃) with their band alignment study and carrier transport mechanisms are also explored.

4.1 Requirement of highly sensitive, fast and broadband photodetectors

The widespread applications of broadband photodetectors across various fields, including optical communications, environmental monitoring, defence security, and medical imaging, [1, 2] have led to a pressing need to develop high-performance broadband photodetectors with high responsivity, detectivity, and fast response speed. However, in pristine semiconductor materials (MoS₂ and Ga₂O₃ for present case) limited light detection owing to their band gap constraint is the major problem. For example, MoS₂ is a semiconductor material with a band gap range of 1.2-1.8 eV, depending upon its thickness value, and mostly lies in the visible region and show very weak response in NIR range. Similarly, Ga₂O₃ is a wide band gap (4.5-4.9 eV) semiconductor material and show its best response in ultraviolet (UV)-C region. Therefore, to tackle this problem, making their heterostructure with appropriate material (PtS₂) with a narrow band gap (0.25-1.6 eV) and high mobility is an effective approach to enhance the response towards NIR region and make broadband photodetector.

4.2 PtS₂/MoS₂ heterostructure

Molybdenum disulfide (MoS₂), a member of the group-6 TMDC family, stands out as one of the most extensively studied material due to its unique properties, including layer-dependent optical band gap ranging from 1.2 eV to 1.8 eV, strong light-matter interaction, and moderate carrier mobility [3, 4]. It has been reported that MoS₂ exhibits a wide range of applications, including photodetectors, transistors, catalysis, gas sensors, and many others [5, 6]. However,

in bare MoS₂, the limited light absorption and high recombination of photo-generated carriers constrain to achieve the desired photodetector device performance in the infrared region. To overcome this problem, stacking MoS₂ with suitable 2D material such as PtS₂ with narrow band gap and high mobility creating van der Waals heterostructures with no dangling bonds and lattice mismatch is a novel approach to enhance device performance [7-9]. Heterostructures not only improve optical absorption but also promote strong interlayer coupling at the junction, leading to increased carrier generation and enhance detection range [4, 10]. Additionally, heterostructures offer greater modulation of their electrical and optical properties by selecting suitable synthesis approach and type of alignment [8, 9, 11, 12]. In present work, we discussed the fabrication of large area PtS₂/MoS₂ heterostructure and its broadband photodetector performance.

4.2.1 Experiment section

Synthesis of PtS₂: The PtS₂ thin film were synthesized by TAC method as illustrated in Figure 4.1 (a). First, the Pt thin film is coated by RF magnetron sputtering method at optimized parameters and then sulfurized it in CVD using sulfur powder (1.2 g) for 1 hour interval in the present of carrier gas (1.1% H₂ balance Ar mixture) with a flow rate of 75 sccm.

Synthesis of MoS2: MoS2 thin films were grown on SiO2/Si substrates by RF magnetron sputtering with high purity (99.99 %, Kurt J. Lesker) MoS2 target. To create an optimal environment for deposition, the chamber was evacuated to a high vacuum of approximately 2×10^{-6} Torr. Subsequently, the MoS2 thin film was deposited at room temperature for 10 minutes, employing a power of 25 W, Ar gas flow rate of 20 sccm, and a deposition pressure of 3.8 mTorr. Then, same deposited MoS2 samples were annealed in a quartz tube furnace at 700 °C for 2 hours in the presence of 5% H₂S and 95% Ar with a flow of 20 sccm and allowed to cool the furnace naturally.

Synthesis of PtS₂/**MoS**₂ **device**: Figure 4.1 (b) depicts the complete synthesis procedure employed for PtS₂/MoS₂ heterostructure device. The PtS₂ thin film was grown onto MoS₂ sample by the thermally assisted Conversion (TAC) method. To achieve this, we first deposited a thin Pt film on the partially covered MoS₂ sample (Figure 4.1 (b)) via RF magnetron sputtering at room temperature using a high-purity Pt target (99.99%) at a power of 30 W for 30 sec. Subsequently, this Pt-coated MoS₂ sample (Pt/MoS₂/SiO₂/Si) underwent sulfurization in a chemical vapour deposition (CVD) in the presence of sulfur powder (1.2 g) for 1 hour with a tube-in-tube arrangement and gas flow rate of 75 sccm (1.1% H₂ balance Ar) as were

optimized in the previous chapter for the growth of PtS₂ [13]. The temperature was set to 500 °C and 300 °C for Pt coated on MoS₂ (Pt/MoS₂/SiO₂/Si) sample and sulfur powder, respectively. After the completion of deposition, the system was left to cool down naturally. Finally, gold (Au) strips electrodes with a thickness of ~150 nm and 3.5 mm separation were deposited by thermal evaporation technique utilizing a physical shadow mask. The Au electrodes were positioned with one gold strip on the PtS₂ film and the other on the MoS₂ film, as shown in Figure 4.1 (b). The sample image of PtS₂/MoS₂ heterostructure showing its large area growth is display in Figure 4.1 (b) (above final device schematic).

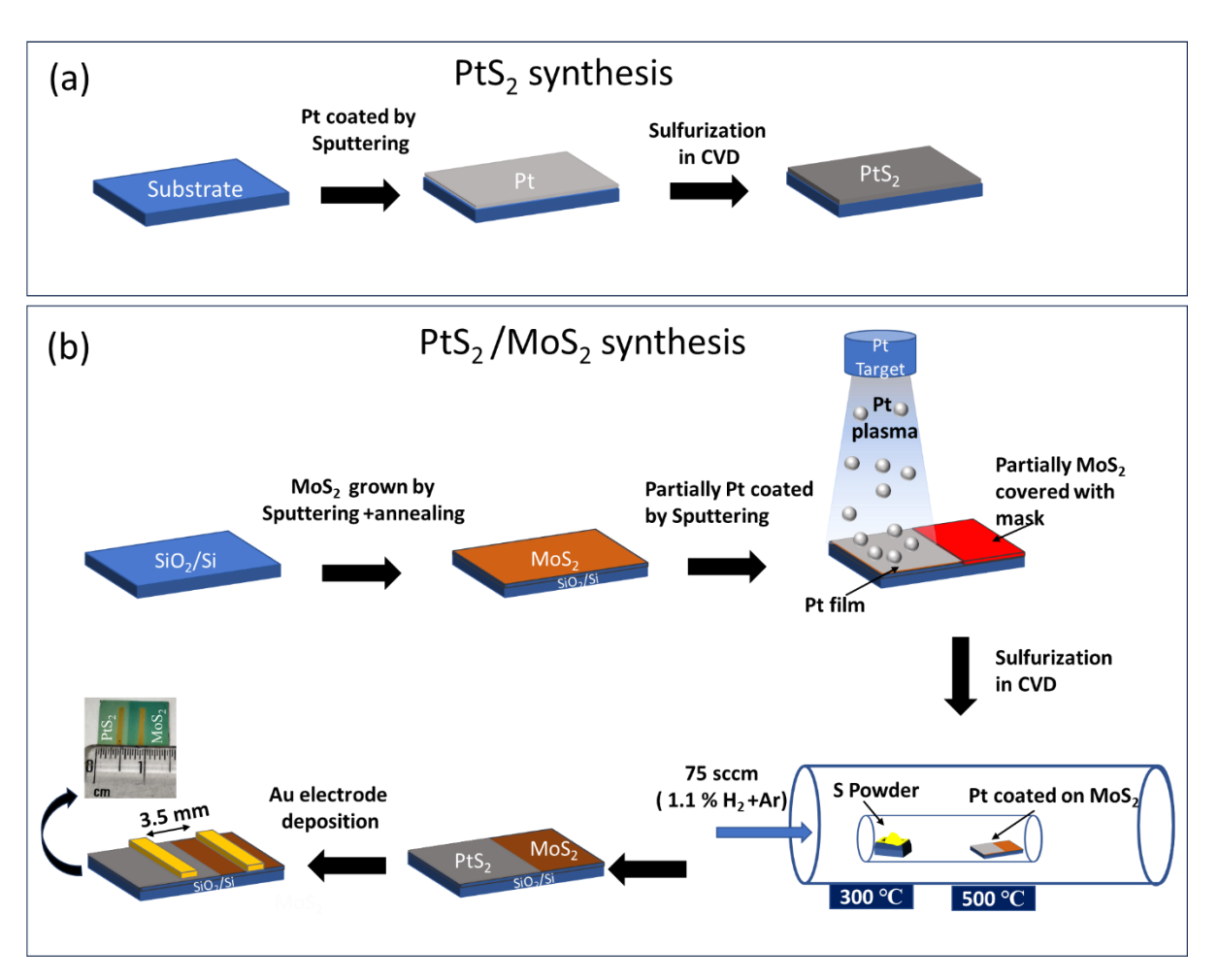


Figure 4.1 (a) Schematic of the PtS₂ thin film synthesis by TAC method (b) Schematics of PtS₂/MoS₂ heterostructure device fabrication by multiple steps.

Characterizations used and device measurement: Raman and PL measurements of the samples were carried out with 532 nm laser illumination at room temperature (RT) using HORIBA LabRAM HR 800 instrument. The thickness of the samples was evaluated by atomic force microscope (AFM) in tapping mode using Bruker (Multimode 8) Scanning Probe

Microscope model. The absorption spectra of the samples synthesized on quartz substrates was carried out with a Perkin Elmer Lambda 950 instrument. Thermofisher Scientific ESCALAB Xi⁺ model instrument was utilized for the XPS measurements with Al Kα as X-ray source. The morphology of the heterostructure is revealed by JEOL-JSM-7610F model. The photodetector studies of the devices from 400-1200 nm were done using a Bentham PVE TMc 300 monochromator and Keithley 6430 SMU. The temporal response of the devices under 532 nm and 650 nm were recorded using HOLMARC lasers with an optical chopper and Keithley 4200A-SCS

4.2.2 Results and discussion

Figure 4.2 (a) shows the Raman spectra of bare PtS₂, MoS₂, and PtS₂/MoS₂ heterostructure grown on SiO2/Si substrate. The Raman spectra of bare MoS2 exhibits two distinct characteristics peaks E_{2g}¹ and A_{1g} located at positions of 381.4 cm⁻¹ and 406.3 cm⁻¹, respectively. These peaks align well with the previously reported study of MoS₂, providing strong evidence of successful growth of MoS₂ [1, 6]. The peak at 381.4 cm⁻¹ (E_{2g}¹) corresponds to the in-plane vibration modes of the S and Mo atoms in the opposite direction. Whereas peak at position of 406.3 cm⁻¹ (A_{1g}) represents the out-of-plane vibration modes of S atoms with Mo atom at the stationary position. The difference between these two peak positions of 24.9 cm⁻¹ confirms the growth of a few layers of MoS₂. Similarly, for bare PtS₂, two prominent peaks at $301.2~\text{cm}^\text{-1}$ and $341.8~\text{cm}^\text{-1}$ corresponding to $E_g{}^1$ and $A_{1g}{}^2$ vibration modes and confirm the growth of PtS_2 [13]. Here, $E_g^{\ 1}$ and $A_{1g}^{\ 2}$ peaks signifies the in-plane and out-of-plane Raman vibration mode respectively. Moreover, PtS₂/MoS₂ heterostructure (Figure 4.2 (a)) displays four prominent peaks at positions of 301.3 cm⁻¹ (E_g^{-1}), 342.1 cm⁻¹ (A_{1g}^{-2}), 381.3 cm⁻¹ (E_{2g}^{-1}), and 406.3 cm^{-1} (A_{1g}), demonstrating the co-existence of both PtS₂ and MoS₂ in the heterostructure. The peak at 520.0 cm⁻¹ is consistently present in all spectra, representing the Si peak of the SiO_2/Si substrate. A slight blue shift of 0.1 eV in E_g^{-1} and 0.3 eV in A_{1g}^{-2} peak positions is observed in the PtS₂/MoS₂ heterostructure compared to bare PtS₂. This shift in peaks could be attributed to stress or strain produced in the film or charge carrier transfer at the interface [4, 14, 15]. Additionally, stretching-induced in-plane lattice and compression of interlayer array arising from strong interlayer interaction near the junction could contributed to the observed Raman shift [16]. However, no significant shifting of peak positions for E2g1 and A1g is observed in the heterostructure compared to bare MoS2, suggesting that after PtS2 grown over MoS₂, no stress or strain is induced in the MoS₂ film.

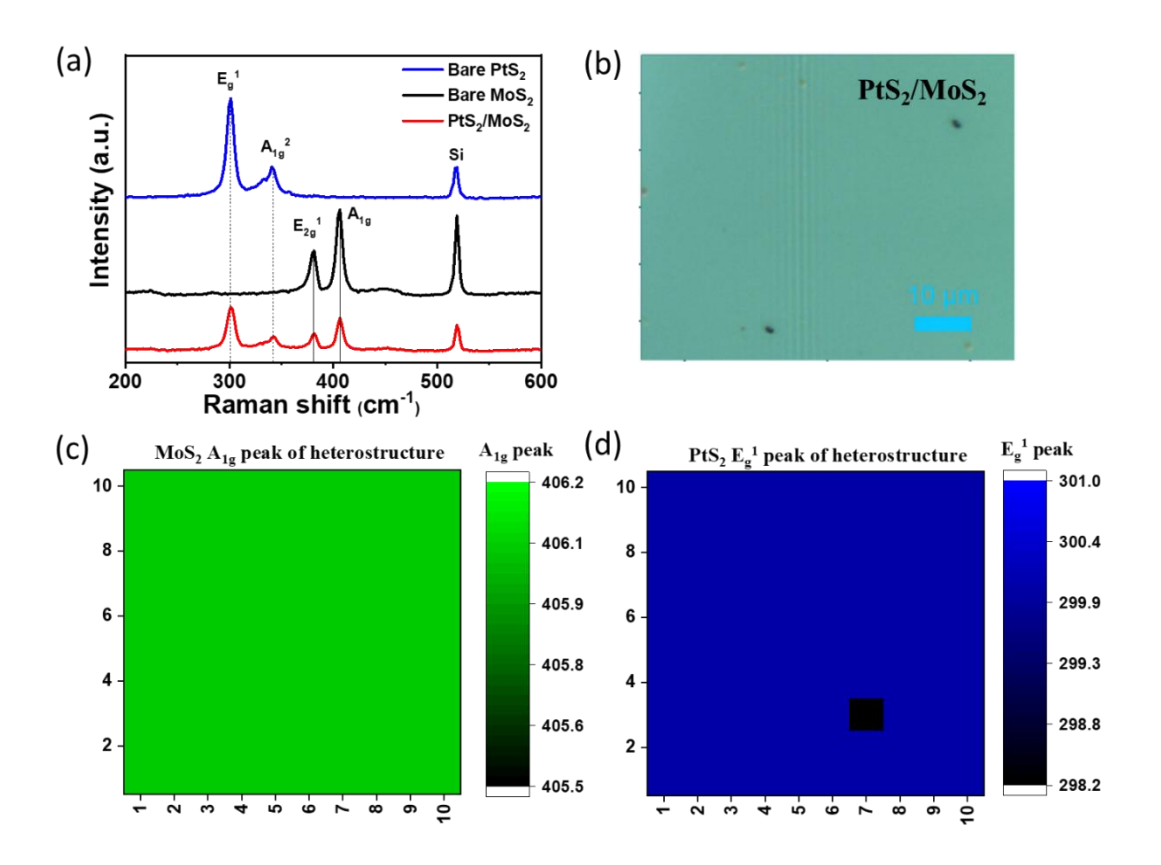


Figure 4.2 (a) Raman spectra of bare PtS_2 , MoS_2 and PtS_2/MoS_2 (b) Optical image of PtS_2/MoS_2 heterostructure with a scale bar of 10 μ m where Raman mapping was performed (c) A_{1g} peak Raman mapping of MoS_2 in heterostructure (d) E_g^1 peak Raman mapping of PtS_2 in heterostructure.

Further to reveal the uniformity of the PtS_2/MoS_2 heterostructure device, Raman mapping was performed on a 40 μ m × 40 μ m area of heterostructure as shown in the optical image (Figure 4.2 (b)) with a 532 nm excitation laser at room temperature on 100 points (10×10) with a step interval of 4 μ m. The Raman mapping was performed on dominant peaks such as A_{1g} (for MoS_2) and E_g^{-1} (for PtS_2) of the heterostructure as shown in Figure 4.2 (c) and 4.2 (d), respectively which clearly demonstrate high uniformity of the heterostructure. The AFM measurements were carried out on individual samples to determine their thickness. The estimated thickness of MoS_2 and PtS_2 was around 9.5 nm and 5 nm, respectively as shown in Figure 4.3 (a, b). Furthermore, to investigate the optical properties of the heterostructure, photoluminescence (PL) was performed on MoS_2 and PtS_2/MoS_2 sides of the heterostructure sample, as illustrated in Figure 4.4 (a). For better clarity of peaks, their PL spectra is deconvoluted into two main peaks (A and B) by Gaussian fitting. On the MoS_2 side, two prominent peaks (Figure 4.4 (a)) are observed approximately at 1.83 eV and 1.97 eV, corresponding to A and B excitons, respectively. These two peaks arise due to the splitting in

the valence band at the K point of the Brillouin zone, resulting from interlayer interactions and spin-orbit coupling [17, 18]. Sequentially, PL spectra obtained from the PtS₂/MoS₂ side show a quenching effect with decrease in B peak intensity peak from 57 a.u. to 36 a.u. (display by downward arrow in Figure 4.4 (a)) compared to PL of MoS₂ signifies the strong interlayer coupling and charge transfer between the constitutes material (PtS₂ and MoS₂) [1].

Figure 4.4 (b) depicts the comparison plot of the absorption of bare MoS₂, PtS₂, and PtS₂/MoS₂ heterostructure, all grown on quartz substrates within the wavelength range of 400-1200 nm. For bare PtS₂, a broad absorption peak (Figure 4.4 (b)) is observed in the 400-800 nm wavelength range, followed by a decrease in absorption beyond 800 nm. The absorption spectrum of bare MoS₂ film (Figure 4.4 (b)) displays two prominent peaks, A and B, corresponding to the valence band splitting at the K point owing to spin-orbit coupling and an additional broad peak C arises by excitons related to van Hove singularity [19]. In contrast, the absorption spectrum of PtS₂/MoS₂ (Figure 4.4 (b)) shows increased absorption compared to its individual constituent materials. This enhancement can be attributed to the synergistic effect, where both MoS₂ and PtS₂ contribute collectively to absorption due to strong interlayer interaction and increased thickness in the heterostructure. Furthermore, Figures 4.4 (c) and 4.4 (d) exhibit the band gap evaluated for bare MoS₂ and bare PtS₂, respectively, using the Tauc plot method. The calculated band gap is approximately 1.7 eV for bare MoS₂ (Figure 4.4 (c)) and 1.3 eV for PtS₂ (Figure 4.4 (d)). These band gap values will be used in the subsequent band alignment study.

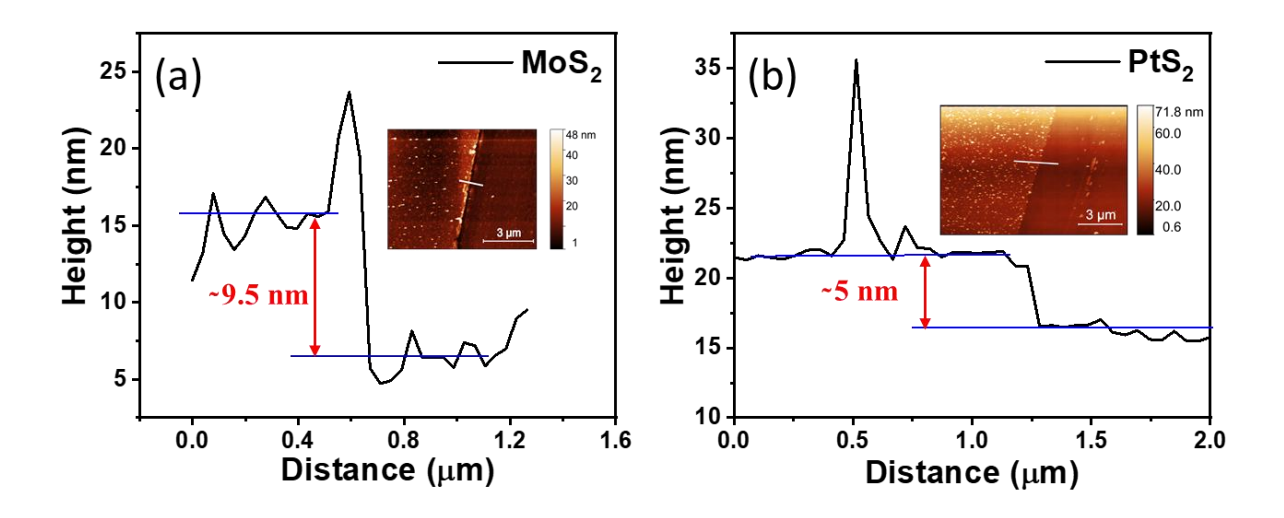


Figure 4.3. (a) Thickness of MoS₂ and (b) thickness of PtS₂ estimated from AFM with inset showing their actual step.

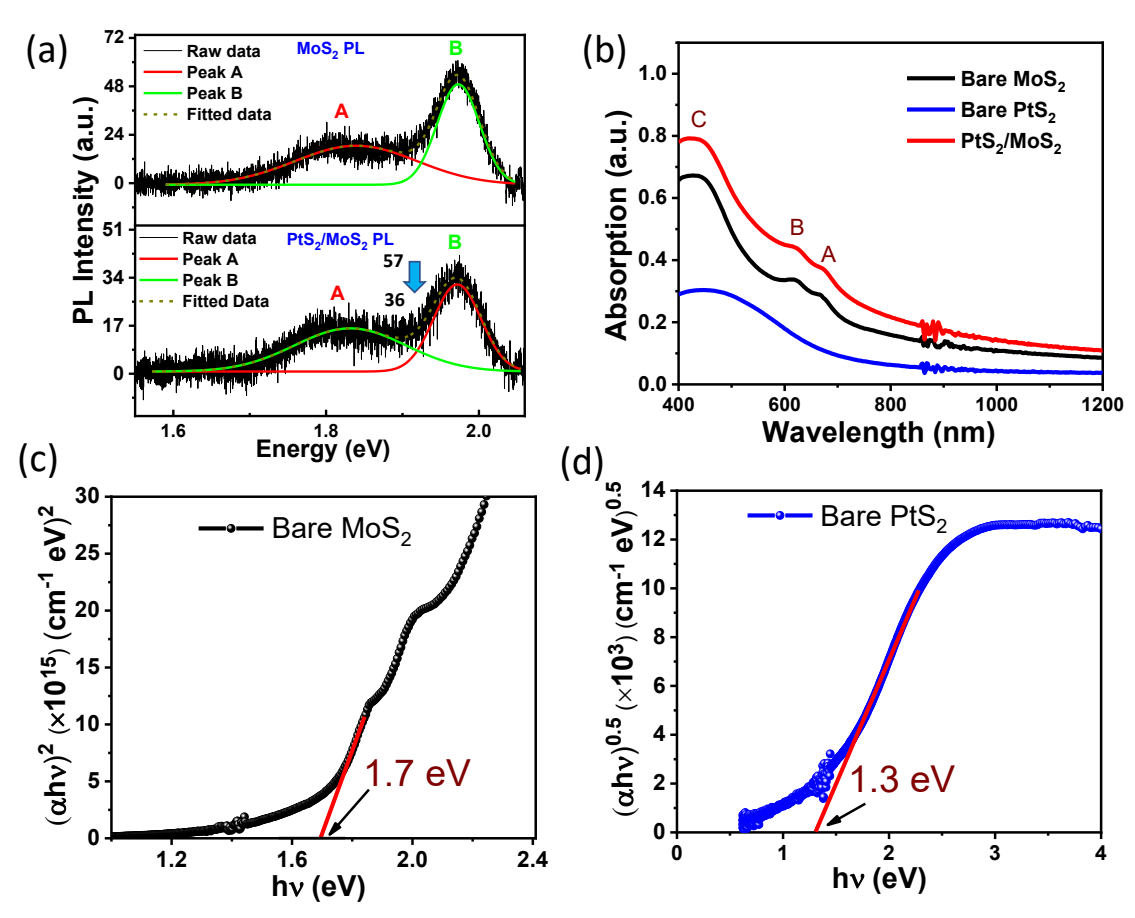


Figure 4.4 (a) Photoluminescence (PL) spectra of bare MoS₂ and PtS₂/MoS₂ (b) Comparison plot of absorption spectra of bare PtS₂, MoS₂, and PtS₂/MoS₂ film grown on quartz substrates. Band gap calculated of (c) bare MoS₂ and (d) bare PtS₂ using Tauc plot.

4.2.2.1 Band alignment study

XPS is a highly surface-sensitive technique, making it a valuable tool for investigating the local environment of the material, band alignment, and charge transfer (CT) mechanism [1, 20, 21]. As the performance of heterostructure devices critically depends on the nature of their interfaces, a comprehensive understanding of band alignment and interface properties is essential [22, 23]. To explore the interface between PtS₂ and MoS₂ in this study, we conducted XPS measurements on bare MoS₂, PtS₂, and PtS₂/MoS₂ samples. To mitigate charging effects and facilitate binding energy calculations, we referenced the adventitious carbon peak at 284.8 eV. Figure 4.5 (a) depicts the Mo 3d core level binding energy spectra and valence band spectra of bare MoS₂. The Mo 3d core levels split into Mo 3d_{5/2} and Mo 3d_{3/2} peaks at positions of 229.4 eV and 232.6 eV, respectively, owing to spin-orbit coupling. This splitting, consistent with the Mo⁺⁴ state, confirms the presence MoS₂ [21]. Additionally, a small peak at 226.7 eV related to S 2s core level is observed alongside these peaks. The value of VBM of bare MoS₂

is evaluated by extrapolating the leading edge of the valence band spectra (Figure 4.5 (a)), has a value of 1.03 eV, relative to the fermi level position.

The relative energy separation of Mo $3d_{5/2}$ core level from VBM is determined to be 228.37 eV, as shown in Figure 4.5 (a). Figure 4.5 (b) displays the combined valence band spectra and Pt 4f core level spectra of bare PtS₂. Two leading peaks at 74.1 eV (Pt $4f_{7/2}$) and 77.4 eV (Pt $4f_{5/2}$) represent the S-Pt-S bond with Pt⁺⁴ oxidation state, supporting the growth of PtS₂. The other two smaller peaks with positions of 72.6 eV (Pt $4f_{7/2}$) and 75.9 eV (Pt $4f_{5/2}$) are ascribed to Pt⁺² (PtS) phase, which is generally present during the PtS₂ synthesis due to its more stability as reported in literature [13, 24, 25]. Since the Raman spectra (Figure 4.2 (a)) shows two prominent peaks (Eg¹ and A_{1g}²) correspond to PtS₂ and XPS spectra (Figure 4.5 (b)) confirm the dominant PtS₂ phase, we consider PtS₂ as the main constituent phase for further study. Figure 4.5 (b) manifest the calculated VBM (1.00 eV) for PtS₂ and its separation (73.1 eV) from the Pt $4f_{7/2}$ core level.

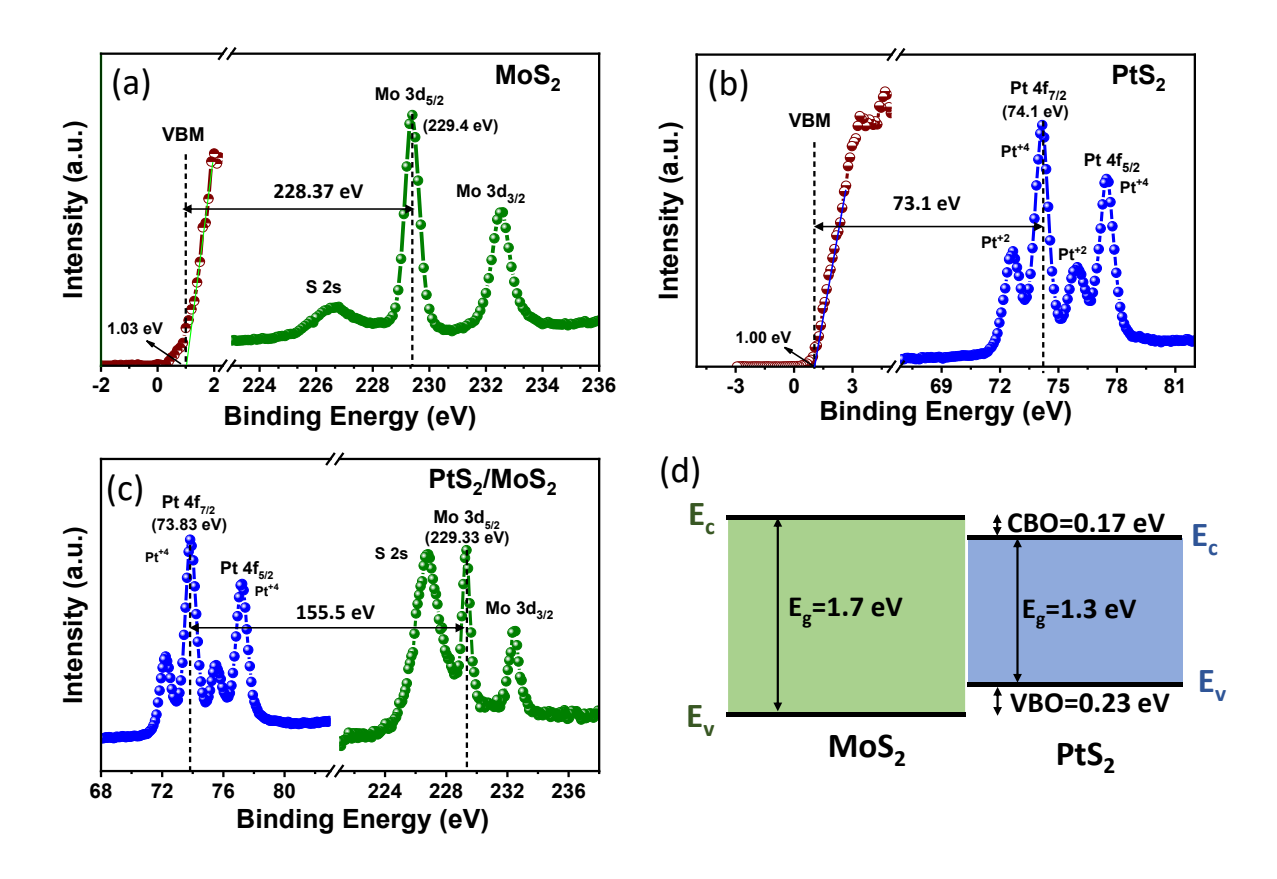


Figure 4.5 (a) Valence band spectra and Mo core level binding energy spectra of bare MoS₂ (b) Pt 4f core level binding energy spectra and valence band spectra of PtS₂ (c) Core level spectra of Pt 4f and Mo 3d of the PtS₂/MoS₂ heterostructure (d) Band alignment (Type-I) between PtS₂ and MoS₂.

Next, Figure 4.5 (c) shows the Pt 4f and Mo 3d core level spectra of the PtS₂/MoS₂ heterostructure. The prominent Pt 4f peaks Pt 4f_{7/2} (73.83 eV) and Pt 4f_{5/2} (77.23 eV) again corroborate the Pt⁺⁴ oxidation state of the PtS₂ film, with two minor peaks attributed to the presence of a small PtS phase, as explained earlier. Additionally, three peaks at 229.33 eV (Mo 3d_{5/2}), 232.53 eV (Mo 3d_{3/2}), and 226.83 eV (S 2s) confirm the presence of MoS₂ in the heterostructure. The reduced intensity of Mo 3d peaks in the heterostructure, compared to bare MoS₂, is attributed to the coverage of PtS₂ (~5 nm thickness) over the MoS₂, which reduces the contribution of the MoS₂ film. The estimated binding energy difference between the Pt 4f_{7/2} and Mo 3d_{5/2} core levels of the heterostructure is around 155.5 eV.

The Valence band offset (VBO) between PtS₂ and MoS₂ is calculated using Kraut's rule [49] using equation (4.1)

$$VBO = (E_{Pt\,4f_{7/2}}^{PtS_2/MoS_2} - E_{Mo\,3d_{5/2}}^{PtS_2/MoS_2}) - (E_{Pt\,4f_{7/2}}^{PtS_2} - E_{VBM}^{PtS_2}) + (E_{Mo\,3d_{5/2}}^{MoS_2} - E_{VBM}^{MoS_2}) - \cdots - (4.1)$$

Where $E_{Pt\ 4f_{7/2}}^{PtS_2/MoS_2}$ and $E_{Mo\ 3d_{5/2}}^{PtS_2/MoS_2}$ terms represent the core level binding energy (B.E) of Pt $4f_{7/2}$ and Mo $3d_{5/2}$, respectively of the heterostructure and $E_{Pt\ 4f_{7/2}}^{PtS_2}$, $E_{Mo\ 3d_{5/2}}^{MoS_2}$ denotes the core level B.E of bare PtS₂ and MoS₂, respectively. $E_{VBM}^{PtS_2}$ and $E_{VBM}^{MoS_2}$ denotes the VBM of PtS₂ and MoS₂, respectively. The calculated VBO value for PtS₂/MoS₂ interface was -0.23 \pm 0.1 eV, indicating that the position of the valence band (VB) of MoS₂ is situated below the VB of PtS₂.

The conduction band offset (CBO) between MoS_2 and PtS_2 is evaluated by using the VBO value and band gap of PtS_2 ($E_g^{PtS_2}$) and MoS_2 ($E_g^{MoS_2}$) with the following mathematical expression (equation (4.2))

CBO =
$$E_g^{MoS_2} - E_g^{PtS_2} + VBO.....(4.2)$$

The band gap of 1.7 eV for MoS₂ and 1.3 eV for PtS₂ was evaluated using Tauc's plots method, as displayed in Figure 4.4 (c, d). Consequently, a CBO of 0.17 ± 0.1 eV is obtained at PtS₂/MoS₂ interface. Integrating the CBO and VBO results, a type-I band alignment (Figure 4.5 (d)) was found between the MoS₂ and PtS₂. Additionally, from VBM and band gap values of MoS₂ and PtS₂ it confirmed that both MoS₂ and PtS₂ exhibit n-type nature due to their fermi level is closer to respective conductive band.

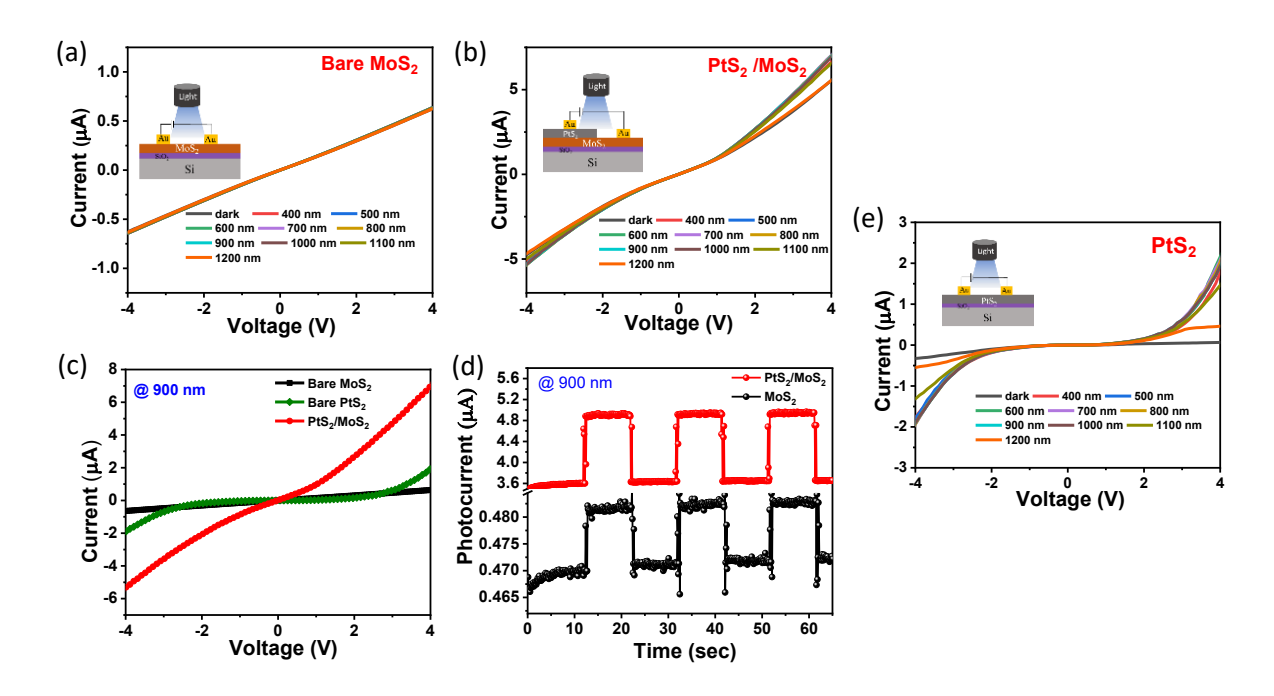


Figure 4.6 Current-voltage (I-V) characteristics of (a) bare MoS₂ (b) PtS₂/MoS₂ device with inset shows their respective device structure (c) Comparison plot of photocurrent of bare MoS₂ and PtS₂/MoS₂ device under 900 nm illumination light (d) Comparison temporal response of PtS₂/MoS₂ and MoS₂ device under 900 nm (3V) illumination (e) I-V characteristics of PtS₂ under 400-1200 nm light illumination with inset displaying its device structure.

4.2.2.2 Photodetector device performance

The photodetector device performance of bare MoS₂, bare PtS₂ and PtS₂/MoS₂ heterostructure fabricated on SiO₂/Si substrate is demonstrated in Figure 4.6 (a), 4.6 (e) and 4.6 (b), respectively. In all devices, gold strips electrode with a separation of 3.5 mm is employed for the photodetector study. Figure 4.6 (a) represents the I-V characteristics of a bare MoS₂ device under dark and 400-1200 nm light illumination with an inset displaying the cross-section device structure. The linear I-V characteristics (Figure 4.6 (a)) indicate an ohmic behavior between the MoS₂ and metal electrode. Figure 4.6 (a) clearly evident that bare MoS₂ device exhibits no significant photocurrent enhancement under different light illuminations (400-1200 nm) compared to its dark current, indicating poor device performance. This might be attributed to the fast recombination rate of photo-generated carriers and the absence of a built-in electric field. In contrast, Figure 4.6 (b) demonstrates that the PtS₂/MoS₂ device exhibits improved performance compared to its bare MoS₂ counterpart, in terms of more increase in the current value. The I-V characteristics of PtS₂/MoS₂ (Figure 4.6 (b)) represents a characteristic in between ohmic and Schottky or refer to it as a near-ohmic contact for clarity. Additionally, the

non-rectification behavior of the heterostructure can be explained based on its band alignment. Since, the rectifier behavior of the heterostructure device depends upon the conduction band and valence band offset of the stacking materials and Schottky barrier at their interface [27-29]. The carrier transport in PtS₂/MoS₂ heterostructure is dominated by electrons owing to ntype character of both MoS₂ and PtS₂. A crucial factor contributing to the non-rectifying behavior is the relatively small difference of 0.06 eV between the valence band offset (0.23 eV) and conduction band offset (0.17 eV) within the heterostructure. This small difference effectively results in a nearly equal Schottky barrier height for electron transport under both negative and positive bias conditions, as shown in the Figure 4.7 (c) and 4.7 (d), respectively. This alignment is the primary reason for the observed non-rectifying behavior in the heterostructure device. The inset of Figure 4.6 (b) represents the cross-section schematic of the PtS₂/MoS₂ device. The enhanced photocurrent in PtS₂/MoS₂ device is attributed to strong interlayer interaction and transfer of charge carrier between the PtS₂ and MoS₂ heterojunction. This observation aligns with the PL quenching (Figure 4.4 (a)) and increased net absorption (Figure 4.4 (b)) in the heterostructure, supporting the idea of improved device performance. Here reduce recombination rate, improved net absorption, and a strong built-in electric field near the junction could be the main factors contributing to the enhanced device performance [1, 21].

Figure 4.6 (c) presents a comparison of the photocurrent under 900 nm irradiation for bare MoS_2 , PtS_2 and PtS_2/MoS_2 devices, revealing that the heterostructure (PtS_2/MoS_2) significantly increases the device's photocurrent. Additionally, Figure 4.6 (d) displays the temporal response of both the bare MoS_2 and PtS_2/MoS_2 devices under 900 nm illumination (3V bias). The results show a negligible increase in photocurrent from 0.468 μA to 0.482 μA for the bare MoS_2 device, indicating poor performance. In contrast, the PtS_2/MoS_2 device exhibits a substantial increment in photocurrent from 3.6 μA to 5 μA , highlighting its enhanced performance under the same illumination condition (900 nm).

Considering the XPS and VBS results, we propose a charge carrier transport mechanism for the PtS₂/MoS₂ heterojunction under light illumination (400-1200 nm) to gain insights into the photodetector working. Figure 4.7 illustrates the band alignment between PtS₂ and MoS₂ before and after contact under different biasing conditions (V=0, V<0, V>0) with respect to PtS₂. Figure 4.7 (a) presents the band structure of MoS₂ and PtS₂ before contact, displaying their band gap (E_g), conduction band (E_c), valence band (E_v), core levels (CL), and Fermi levels (E_f) with different colour representation. Utilizing previously reported work function values for

MoS₂ (4.99 eV) and PtS₂ (5.09 eV) [28], we observe that the Fermi level of MoS₂ is higher than PtS₂. When PtS₂ and MoS₂ come into contact, electrons will transfer from MoS₂ to PtS₂, achieving an equilibrium condition (Fermi level alignment) and causing band bending near the junction (Figure 4.7 (b)). The migration of electrons from MoS₂ to PtS₂ generates an electron depletion region on the MoS₂ side and an accumulation region on the PtS₂ side, creating a space charge region within the interface and establishing a built-in-electric potential.

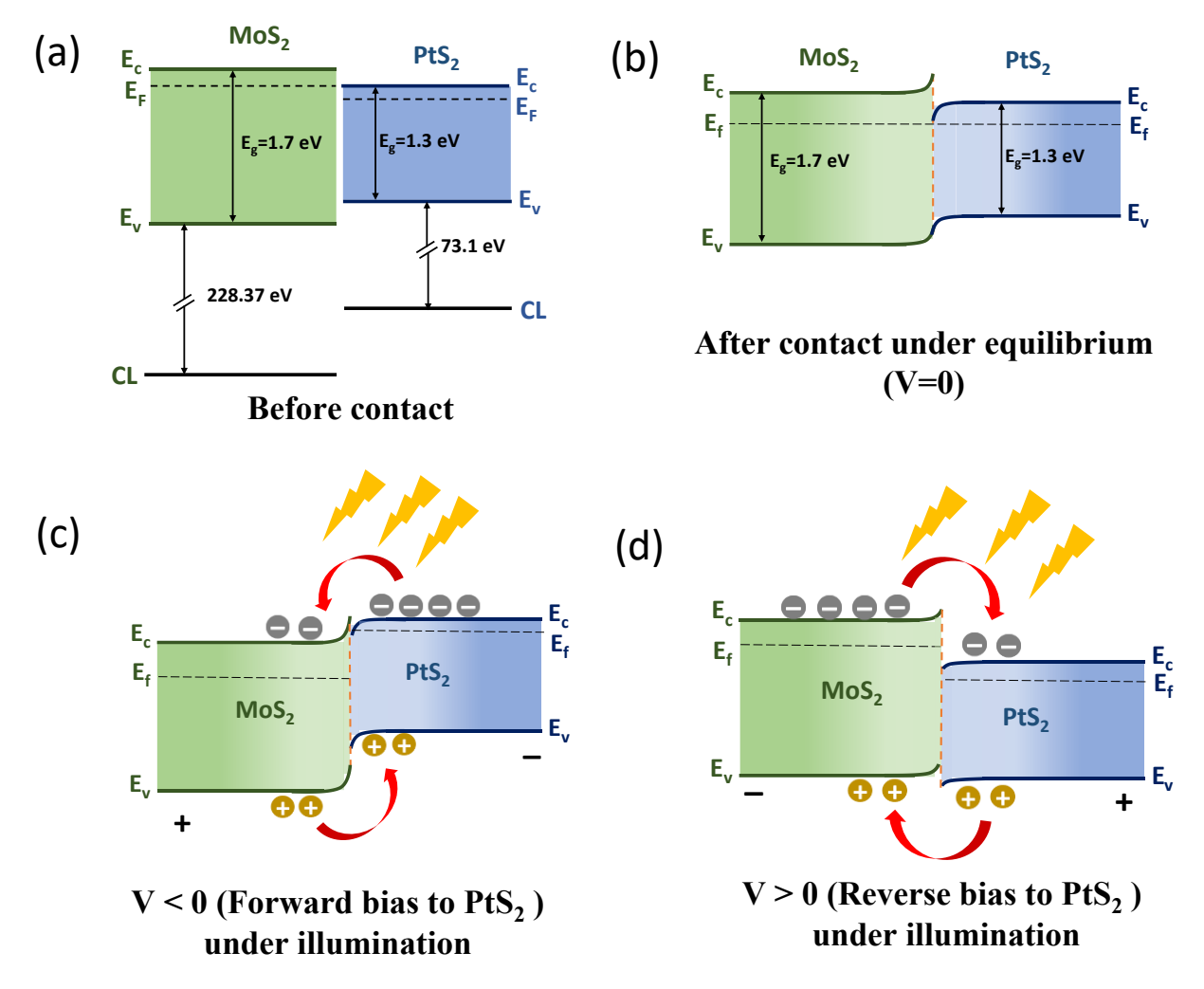


Figure 4.7 (a) Energy band diagram of PtS₂ and MoS₂ before contact (b) Energy band gap diagram of PtS₂/MoS₂ heterojunction after contact under equilibrium (V=0). Energy band gap diagram of PtS₂/MoS₂ heterojunction under illumination (c) V<0 (forward bias with respect to PtS₂) (d) V>0 (reverse bias with respect to PtS₂)

Under V<0 biasing on the PtS₂ side (or forward biasing with respect to n-type PtS₂), Figure 4.7 (c) illustrates that the fermi-level of PtS₂ shift upward, the barrier height at the interface reduces, and changing the band alignment from type-I to type-II. The small VBO value (0.17)

eV) makes this possible to shifting band alignment. Owing to n-type behavior of both MoS₂ and PtS₂ under light illumination (with V<0 condition) majority of the current will be flow due to electrons and they will move from PtS₂ to MoS₂ and minority carrier holes will migrate from MoS₂ to PtS₂. Furthermore, from Figure 4.7 (c) it clearly seen there is very low Schottky barrier height for the electron to move from PtS₂ to MoS₂ and they can cross more easily at higher under external bias and under illumination showing nearly ohmic character at higher external bias (Figure 4.6 (b)).

In contrast, applying V>0 bias to the PtS₂ side (or reverse biasing to n-type PtS₂) become forward bias for MoS₂ (due to n-type of MoS₂) shift the PtS₂ fermi level downward (Figure 4.7 (d)), and MoS₂ fermi level upwards resulting transform the band alignment from type-I (Figure 4.7 (b)) to type-II (Figure 4.7 (d)). This shifting is again possible due to the small CBO value (0.23 eV) compared to external biasing. In such cases, majority electrons will migrate from MoS₂ to PtS₂, and minority holes from PtS₂ to MoS₂ under illumination. Since again here the Schottky barrier height for electrons is nearly same as it was under V<0, therefore it again shows a nearly ohmic character (Figure 4.6 (b)) in reverse bias and this is the reason that PtS₂/MoS₂ not exhibits any rectifier behavior. Similar shifting of band alignment from type-I to type-II (or type-III to type-II) under different biasing conditions has been reported earlier [1, 29, 30]. The type-II band alignment (under bias) observed for PtS₂/MoS₂ heterostructure further helps to enhance the device performance under the influence of built-in electric field and strong interlayer coupling. Moreover, type-II band alignment further assist in fast photo carrier separation and enhance the speed of the photodetector.

Further, for more comparison of PtS₂/MoS₂ photodetector device with bare MoS₂ their figures of merits including responsivity (R), detectivity (D*), external quantum efficiency (EQE), and response time (rise time and fall time) is calculated. Responsivity of a photodetector expresses the net photocurrent produce per unit incident light power. Mathematically, it is given by equation (4.3)

$$R = \frac{I_{light} - I_{dark}}{P. A} \dots (4.3)$$

Where I_{light} , I_{dark} and P denotes the photocurrent (generated under light), dark current, and incident light power density, respectively. A is an effective area of the device, which was 0.175 cm² for both MoS₂ and PtS₂/MoS₂ (heterostructure) devices.

Figure 4.8 (a) demonstrates the responsivity comparison of bare MoS₂ (left axis, black line) and PtS₂/MoS₂ heterostructure (right axis, red line) under different light illuminations (400-1200 nm) at 3V bias. The maximum responsivity of 0.31 AW⁻¹ and 30.2 AW⁻¹ are obtained for bare MoS₂ and PtS₂/MoS₂, respectively, at 900 nm illumination. A 97-fold increase in the responsivity of the heterostructure compared to bare MoS₂ confirms the high performance of the heterostructure, especially in the NIR region. The rise in responsivity is attributed to the increased current value in heterostructure, as also observed in Figure 4.6 (b), where both MoS₂ and PtS₂ contribute to the generation of electron-hole pair with increased absorption. The nonlinear trend of responsivity for both MoS₂ and PtS₂ with different wavelengths is mainly ascribed to two factor one is different absorption of light (Figure 4.4 (b)) which generates different photocurrent for different wavelengths, and another is different power density of illumination light as given in Table 2.1. The combined influence of these two factors leads to a non-linear trend of responsivity with varying wavelengths.

Specific detectivity (D*), another parameter that indicates the ability of the photodetector to detect weak signals, was evaluated by using equation (4.4) [31].

$$D^* = \sqrt{\frac{A}{2eI_{dark} + \frac{4k_BT}{R_S}}} \times R.....(4.4)$$

Where A is effective area, R is responsivity, I_{dark} is dark current, k_B is the Boltzmann constant, T is the temperature of the device (T=300 K) and R_s is the resistance of the device, e is electronic charge.

Here we include shot noise ($S_s = \sqrt{2eI_{dark}}$) and thermal noise ($S_{tn} = \sqrt{\frac{4k_BT}{R_s}}$) (ignoring 1/f noise) for detectivity calculation. For bare MoS₂ and PtS₂/MoS₂ value of R_s is around 6 M Ω and 0.8 M Ω , respectively. The reason of include thermal noise in the present work was to see whether it affect the detectivity value or not and we found that it has negligible effect (0.9 % change) in detectivity value. Therefore, in other work we calculated the detectivity without including thermal noise.

The comparison plot of detectivity of bare MoS₂ and PtS₂/MoS₂ under 400-1200 nm light irradiation is displayed in Figure 4.8 (b). Throughout the 400-1200 nm wavelength range, the detectivity of PtS₂/MoS₂ is higher than that of bare MoS₂. A maximum detectivity of 1.12×10¹³ Jones for PtS₂/MoS₂ and 3.4×10¹¹ Jones for MoS₂ at 900 nm wavelength and 3V bias further confirms the enhancement of PtS₂/MoS₂ device performance compared to bare MoS₂. In addition, a higher value of detectivity of heterostructure (~33 times more) than bare MoS₂ indicates that it has more ability to detect weak signals.

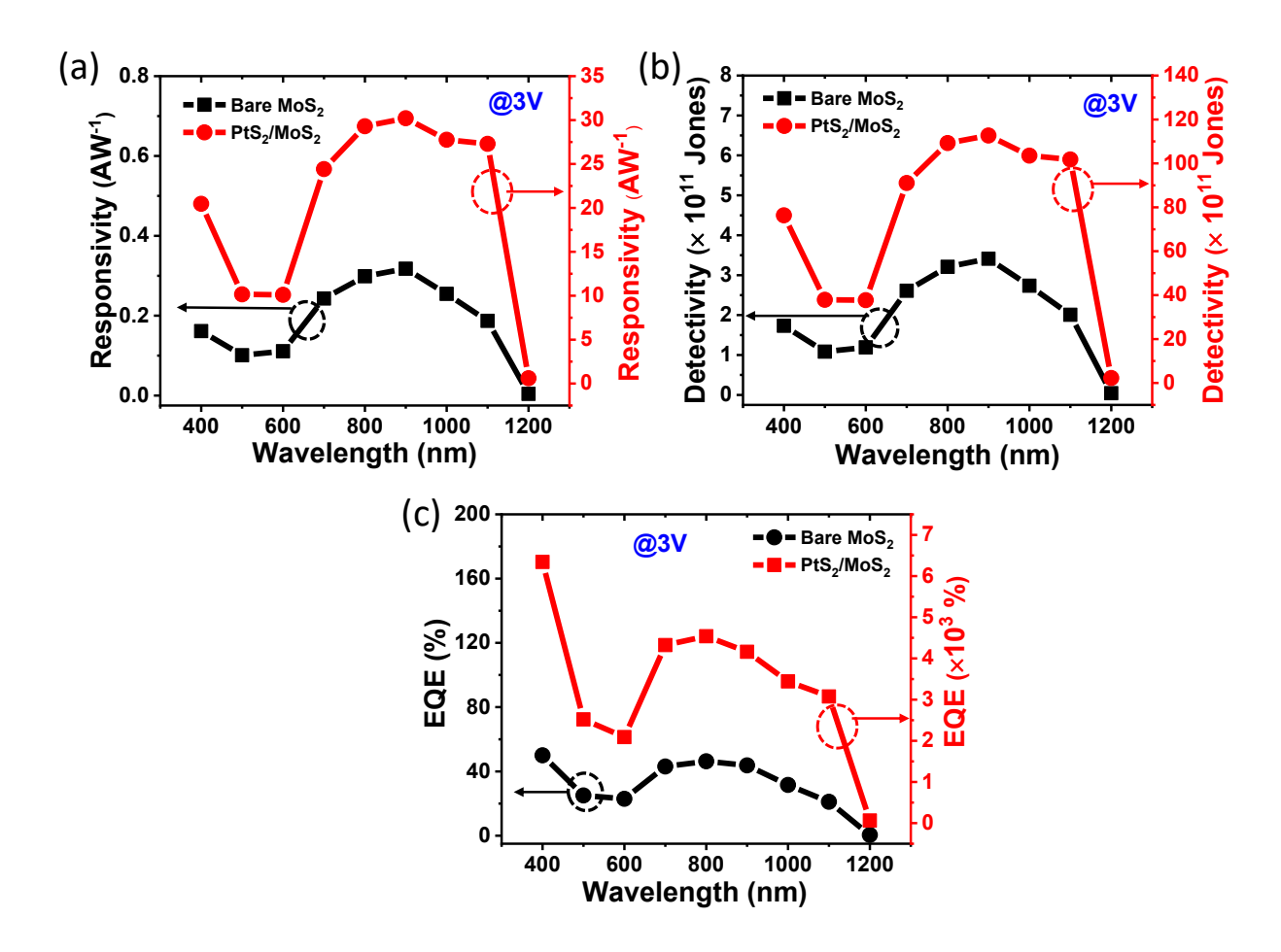


Figure 4.8 Comparison of (a) Responsivity, (b) Detectivity, and (c) EQE of PtS₂/MoS₂ photodetector with bare MoS₂ device at 3V bias with variation with wavelength of 400-1200 nm.

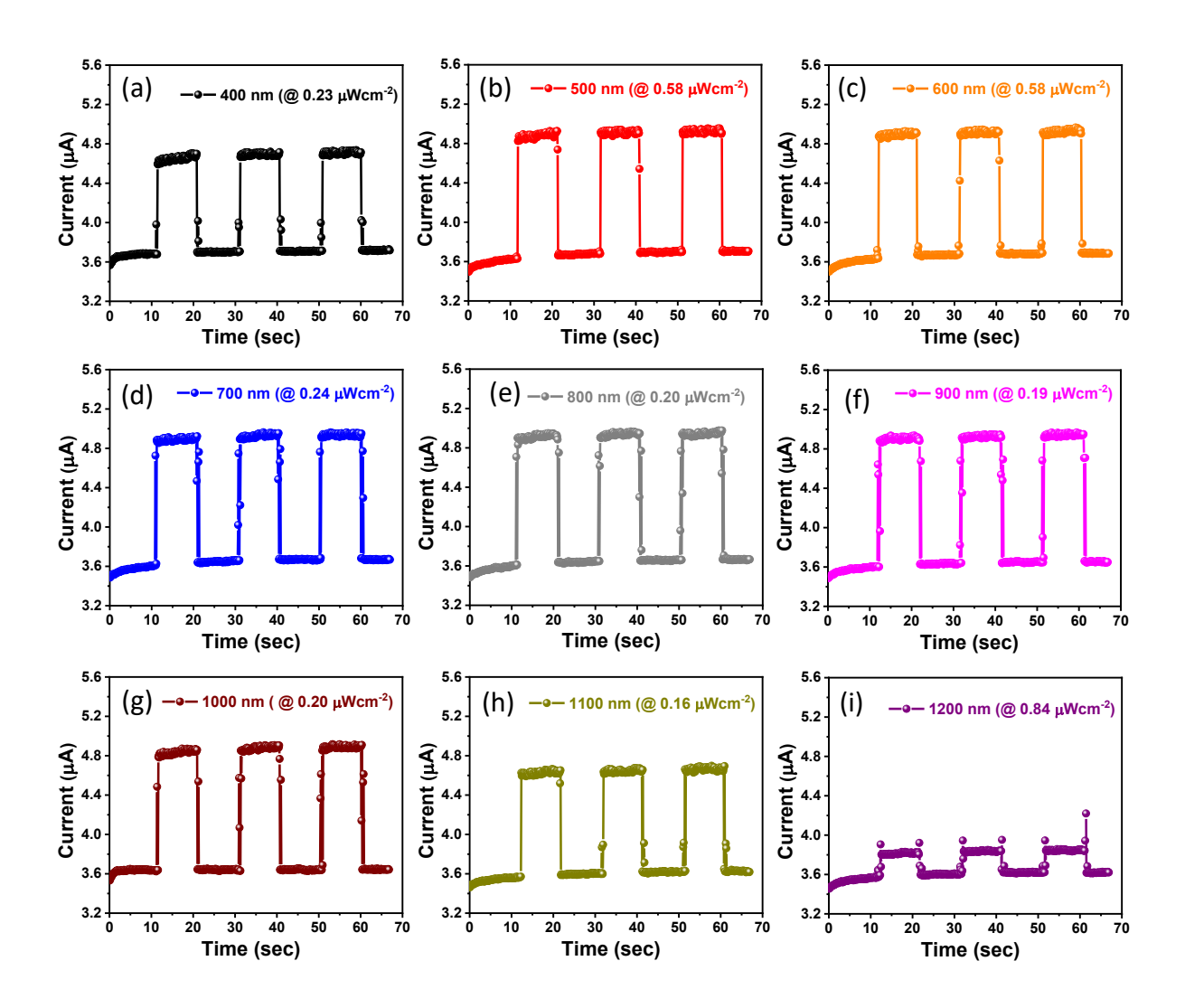


Figure 4.9 (a-i) Temporal response of PtS₂/MoS₂ photodetector device under 400 nm-1200 nm light illumination at 3V bias.

External quantum efficiency (EQE) is another important parameter that indicates how many electron-hole pairs contribute to the final photocurrent per unit incident photons. Mathematically, it is given by the relation of equation (4.5)

$$EQE = \frac{hcR}{e\lambda}....(4.5)$$

Where e, h, and c are the electronic charge, Plank's constant, and speed of light, respectively. and λ represents the wavelength of light illuminated on the device, and R is responsivity of the photodetector (defined earlier)

The comparison study of EQE for bare MoS₂ and PtS₂/MoS₂ devices is presented in Figure 4.8 (c), providing further support for the enhanced performance of the PtS₂/MoS₂ device compared to the bare MoS₂ device. For instance, at a wavelength of 900 nm, the EQE values are 43.76%

and 4161.8% for bare MoS₂ and PtS₂/MoS₂, respectively are obtained. The EQE of the heterostructure is more than 100% and 95 times higher than that of bare MoS₂, indicating a higher number of electron-hole pairs contributing to the final photocurrent, as also verified by the increase in photocurrent value for the heterostructure (Figure 4.6 (c)). An EQE value of more than 100% in the heterostructure is attributed to the enhanced photoconductive gain in the 2D material photodetectors [1, 13].

To further confirm the broadband detection capability of the PtS₂/MoS₂ device, its temporal response (I-T characteristics) is measured under 400-1200 nm light illumination. Figure 4.9 (ai) represents the temporal response of the PtS₂/MoS₂ device under 400-1200 nm light irradiation at 3V bias, with measurements taken at intervals of 100 nm. During this measurement, the light is periodically turned on and off with a gap of 10 seconds to record the temporal response. The PtS₂/MoS₂ device demonstrates a satisfactory response, covering a wide range from the visible to NIR (400-1200 nm) region, as displayed in Figure 4.9. These results demonstrate the superior performance and broad spectral detection capability of the PtS₂/MoS₂ heterostructure, making it a promising candidate for photodetector applications across various wavelengths. The device response upto to 1200 nm can be explained based on the strong interlayer coupling that occurred between the MoS₂ and PtS₂. As previously there are many reports on heterostructure published which confirmed that owing to strong interlayer coupling in type-II band alignment heterostructures extend their detection limit than their stack materials [32-34]. The strong interlayer coupling between PtS₂ and MoS₂ is confirmed by PL spectra (Figure 4.4 (a)) in which PL intensity of heterojunction (PtS₂/MoS₂) decreased (PL quenching) as compared to MoS₂. Furthermore, this interlayer coupling boost electrons to transfer from the valence band of one material to the conduction band of another material under an external incentive source and requires less energy to excite electrons than their individual band gap excitation and enhances the detection range (towards the infrared region, 1200 nm) [32-34].

The speed of a photodetector is crucial for fast detection and modern optoelectronic applications. Typically, it is measured in terms of its response time, which includes the rise time (time taken to reach from 10% to 90% of the total current generated under light-on conditions) and fall time (time taken to reach from 90% to 10% of the total current generated under light-off conditions).

To assess the response time of the PtS₂/MoS₂ device at different wavelengths, including 532 nm, 650 nm, 900 nm, and 1100 nm, we conducted measurements. Figure 4.10 (a, b) displays the I-T characteristics of the heterostructure device under 532 nm and 650 nm lasers, each having a power of 5 mW. These measurements were performed with the help of an optical chopper moving at a frequency of 5 Hz. The calculated rise/fall time for the 532 nm (650 nm) laser is found to be 16/8 ms (11/10 ms), respectively at 2V indicates the fast speed of the PtS₂/MoS₂ device. Furthermore, we compared the performance of our fabricated PtS₂/MoS₂ photodetector device with other reported MoS₂ van der Waals heterostructure devices, as summarized in Table 4.1.

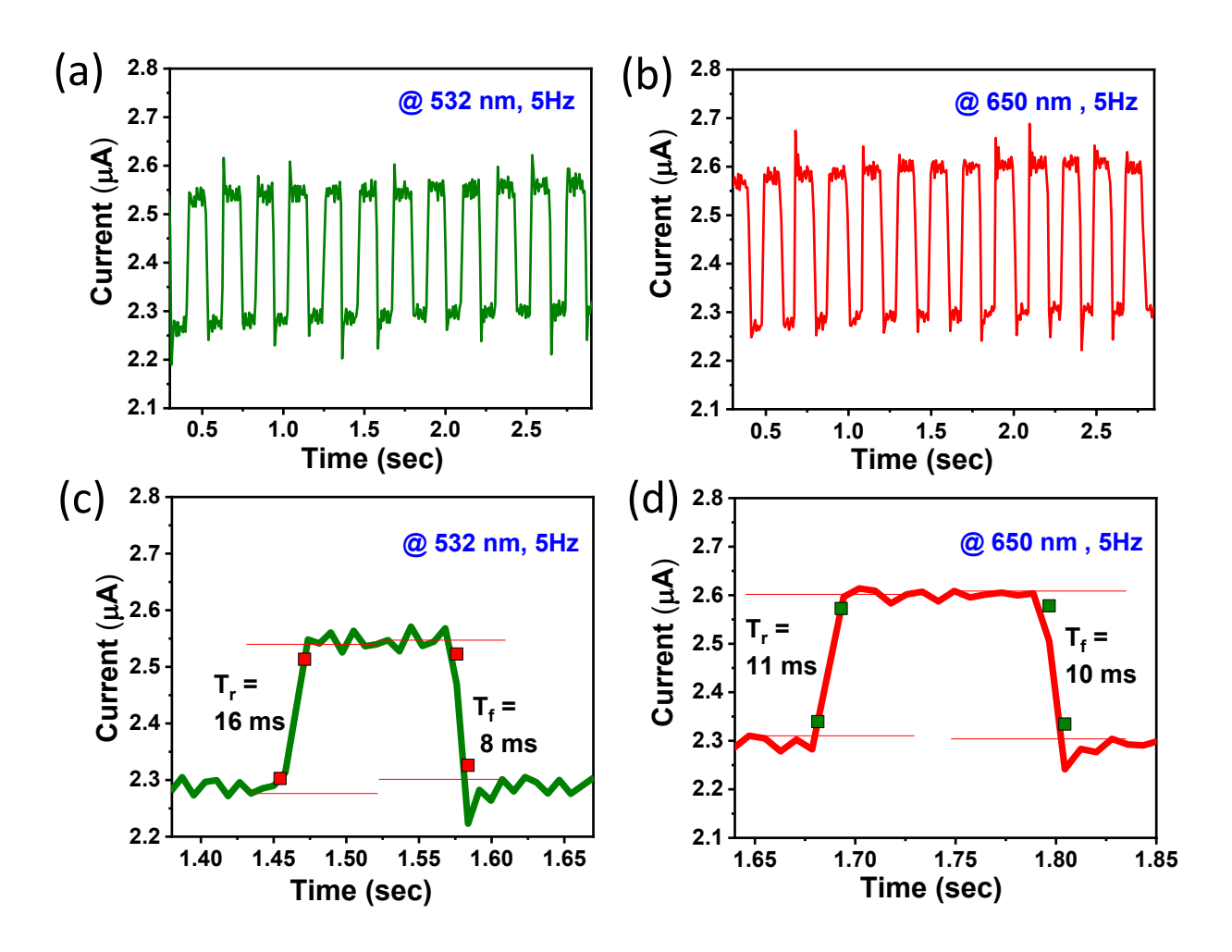


Figure 4.10 Temporal response of PtS₂/MoS₂ device under the illumination of (a) 532 nm laser (5 mW) (b) 650 nm laser (5 mW) at 2V bias and 5Hz frequency (c), (d) represent the rise and fall time under 532 nm and 650 nm laser illumination, respectively, at 2V bias by considering their one respective cycle.

Table 4.1 Comparison of PtS₂/MoS₂ photodetector device performance with reported MoS₂ based heterostructures.

Device material	Detection	Responsivity	Detectivity	Response	Ref
	range	$[AW^{-1}]$	[Jones]	time [ms]	
PtS ₂ / MoS ₂	405-685 nm	403 @ 685 nm	1.07×10 ¹¹	24/21	[28]
$MoS_2/MoSe_2/Au$	300-900 nm	2.54 @ 505 nm		10470/15160	[35]
NP					
$MoTe_2/MoS_2$	470-800 nm	0.322 @ 470 nm		25	[36]
MoS ₂ /NiTe ₂	405 nm	0.392 @ 405 nm	1.2×10^9	5.6/18.4	[37]
$PdSe_{2}/MoS_{2}$	532 nm	600 @ 532 nm	10^{11}	100/37	[38]
MoS_2/WS_2	400-1100	2.15 @ 560 nm	2.05×10^{11}	50	[39]
	nm				
MoS ₂ /Graphene	400-1000	0.835 @ 540 nm		20/30	[40]
	nm				
PtS_2/MoS_2	400-1200	30.2 @ 900 nm	1.12×10^{13}	11/10	Present
	nm				work

4.2.3 Conclusion

The large area PtS₂/MoS₂ heterostructure was fabricated by growing PtS₂ film on the MoS₂ sample by the thermally assisted (TAC) method. Furthermore, XPS measurements provided crucial insights into the band alignment study between MoS₂ and PtS₂, revealing a type-I band alignment between the two materials. Interestingly, the heterostructure's performance was significantly enhanced under external biasing due to the conversion of band alignment from type-I to type-II, which is generally favourable for efficient carrier separation. The increased absorption and PL quenching in heterostructure further suggest the strong interlayer coupling and improved absorption. The PtS₂/MoS₂ photodetector demonstrated a broadband detection range from 400-1200 nm (visible to NIR). Compared to bare MoS₂, the PtS₂/MoS₂ photodetector performance was enhanced by a 97-fold increase in responsivity and ~33 times in detectivity under 900 nm light illumination at 3V bias. The heterostructure device shows maximum responsivity (R) and detectivity (D*) of 30.2 AW⁻¹ and 1.12×10¹³ Jones, upon 900 nm irradiation at 3V bias, with a fast response speed of 11 ms/10 ms. This work introduces a novel approach to designing large-area, high-performance van der Waals heterostructures, opening up exciting possibilities for next-generation optoelectronics device applications.

4.3 PtS_{2-x}/Ga₂O₃ heterostructure

Gallium oxide (Ga₂O₃) is well recognized for deep ultraviolet (UV-C) photodetectors owing to its ultra-wide band gap (4.5 to 4.9 eV), high thermal stability, and indirect band gap nature [41-43]. However, its detection is limited within the UV-C range owing to ultra-wide band gap nature. Hence, to enhance its detection range especially from UV-C to near infrared (NIR) region and cover broad spectrum, its heterostructure with narrow band gap material such as PtS₂ is a suitable approach. Moreover, heterostructure with Ga₂O₃ sensing in UV and PtS₂ broad response in visible and IR range can broaden the spectrum from UV to NIR and to build broadband photodetector. To the best of our knowledge, no study of PtS₂-Ga₂O₃ heterostructure has been reported so far, which motivates us to explore PtS_{2-x}/Ga₂O₃ heterostructure. In this work, we fabricated a 2D-3D PtS_{2-x}/Ga₂O₃ heterostructure based broadband photodetector with detection from UV-C to NIR region

4.3.1 Experiment section

Synthesis of PtS_{2-x} (0<x<1): The PtS_{2-x} thin film was synthesized by the thermally assisted conversion (TAC) method, which is a sulfurization of pre-Pt coated film on SiO₂/Si substrate, as shown in Figure 4.11 (a). In short, a thin film of Pt was first coated on a SiO₂/Si substrate by radio frequency (RF) magnetron sputtering using a pure 99.99 % Pt target for 30 seconds at a power of 30 W and 20 sccm Ar flow rate. After that, the same Pt film-coated sample was sulfurized in chemical vapor deposition (CVD) in the presence of sulfur powder with a 75 sccm (1.1 % H₂ balance Ar mixture) gas flow rate. A temperature of 300 °C for zone 1 (S powder placed) and 500 °C for zone 2 (Pt coated on SiO₂/Si sample) was used during the deposition for 1 hour and after the system left to cool down naturally. In this work, we used PtS_{2-x} nomenclature instead of PtS₂ because the contribution of PtS phase is present in it (due to its more stability) and it is high in PtS_{2-x}/Ga₂O₃ heterostructure (confirmed from XPS data, Figure 4.13 (a)) which was not the case as in previous PtS₂/MoS₂ work.

Synthesis of β-Ga₂O₃ and Device Fabrication: The polycrystalline film of Ga₂O₃ was grown on p-Si (100) substrate by RF magnetron sputtering using a pure 99.99 % Ga₂O₃ target, as shown in Figure 4.11 (b). In brief, a seed layer of Ga₂O₃ (~15 nm) was grown at 700 °C with post-annealing of 30 minutes. A thin film of ~300 nm was then deposited over this seed layer at 650 °C and at a power of 100 W for 90 minutes in an Ar ambient with 3% O₂. After that, a large PtS_{2-x} film (grown on SiO₂/Si) was transferred over Ga₂O₃ film by PMMA-assisted wet transfer method for making a heterostructure device. Figure 4.11 (c) shows the final schematic of the heterostructure, and Figure 4.11 (d) exhibits the actual PtS_{2-x}/Ga₂O₃ heterostructure

sample formed and confirmed its large area growth. Finally, using a physical shadow mask gold electrode of thickness ~150 nm with 3 mm spacing was deposited on the heterostructure sample by thermal evaporation technique. The photodetector measurements were done with Bentham PVE system containing TMc monochromator (250-1100 nm light source), 254 nm pen-ray UV Cole Parmer lamp, and Keithley 6430 SMU.

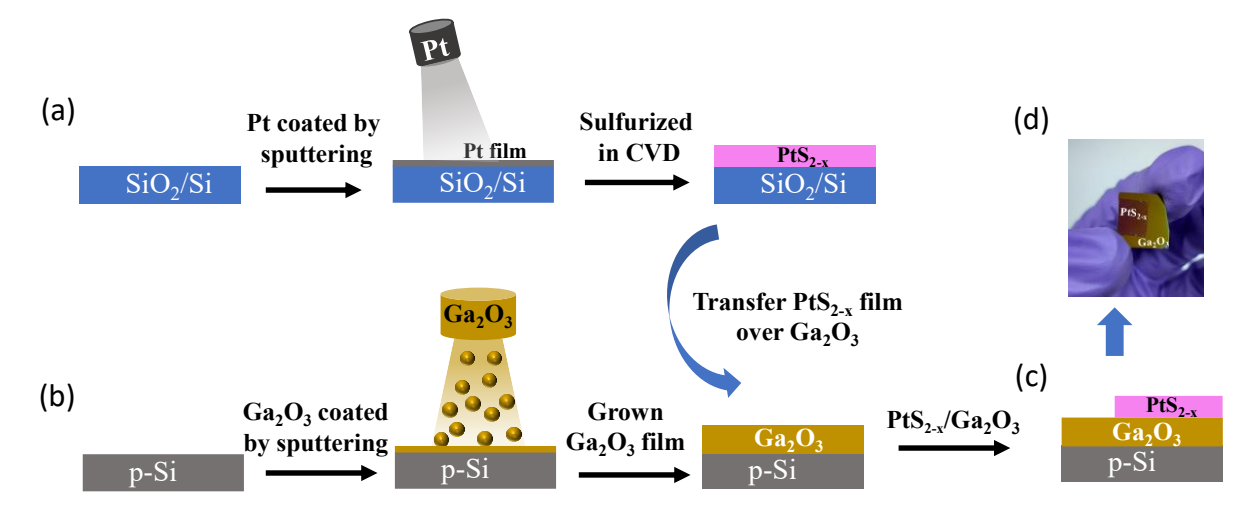


Figure 4.11 (a) Fabrication steps of PtS_{2-x} thin film by TAC method (b) synthesis of Ga₂O₃ film by sputtering (c) PtS_{2-x}/Ga₂O₃ heterostructure schematic (d) PtS_{2-x}/Ga₂O₃ heterostructure image.

4.3.2 Results and discussion

The schematic of the PtS_{2-x}/Ga_2O_3 heterostructure is shown in Figure 4.12 (a) in which PtS_{2-x} film was transferred over the Ga_2O_3 film (grown on p-Si), as explained earlier in the experiment section. Figure 4.12 (b) represents the Raman spectra of PtS_{2-x} and PtS_{2-x}/Ga_2O_3 heterostructure. In PtS_{2-x} , three prominent peaks at positions of 301.3 cm⁻¹ (E_g^{-1}), 333.5 cm⁻¹ (A_{1g}^{-1}), and 342.4 cm⁻¹ (A_{1g}^{-2}) are observed, which represent the formation of PtS_{2-x} [13, 44, 45]. Here, E_g^{-1} denotes the in-plane vibration mode, and the other two modes, A_{1g}^{-1} and A_{1g}^{-2} , indicate the out-of-plane vibration modes. Similarly, in PtS_{2-x}/Ga_2O_3 heterostructure, three Raman peaks with a minor reduction in the intensity are observed, as shown in Figure 4.12 (a). A small (0.9 cm⁻¹) red shift in the E_g^{-1} peak position of heterostructure with respect to PtS_{2-x} denotes the stress or strain induced at the interface [46]. However, no significant shifting of other peak positions A_{1g}^{-1} and A_{1g}^{-2} are observed. The thickness of the PtS_{2-x} film transferred on SiO_2/Si was evaluated by AFM. Figure 4.12 (c) illustrates that the thickness of PtS_{2-x} film is around 7 nm, close to what was reported in our previous work [46]. The crystalline quality of the Ga_2O_3 film was determined by performing GIXRD on Ga_2O_3 thin film grown on a Si substrate, as

depicted in Figure 4.12 (d). It shows 2θ peaks at 30.1° , 44.39° , 54.64° , and 64.03° which corresponds to (400), (-601), (203) and (-204) planes of the polycrystalline β -Ga₂O₃ phase (JCPDS-041-1103, 180) and assured the growth of polycrystalline β -Ga₂O₃ film.

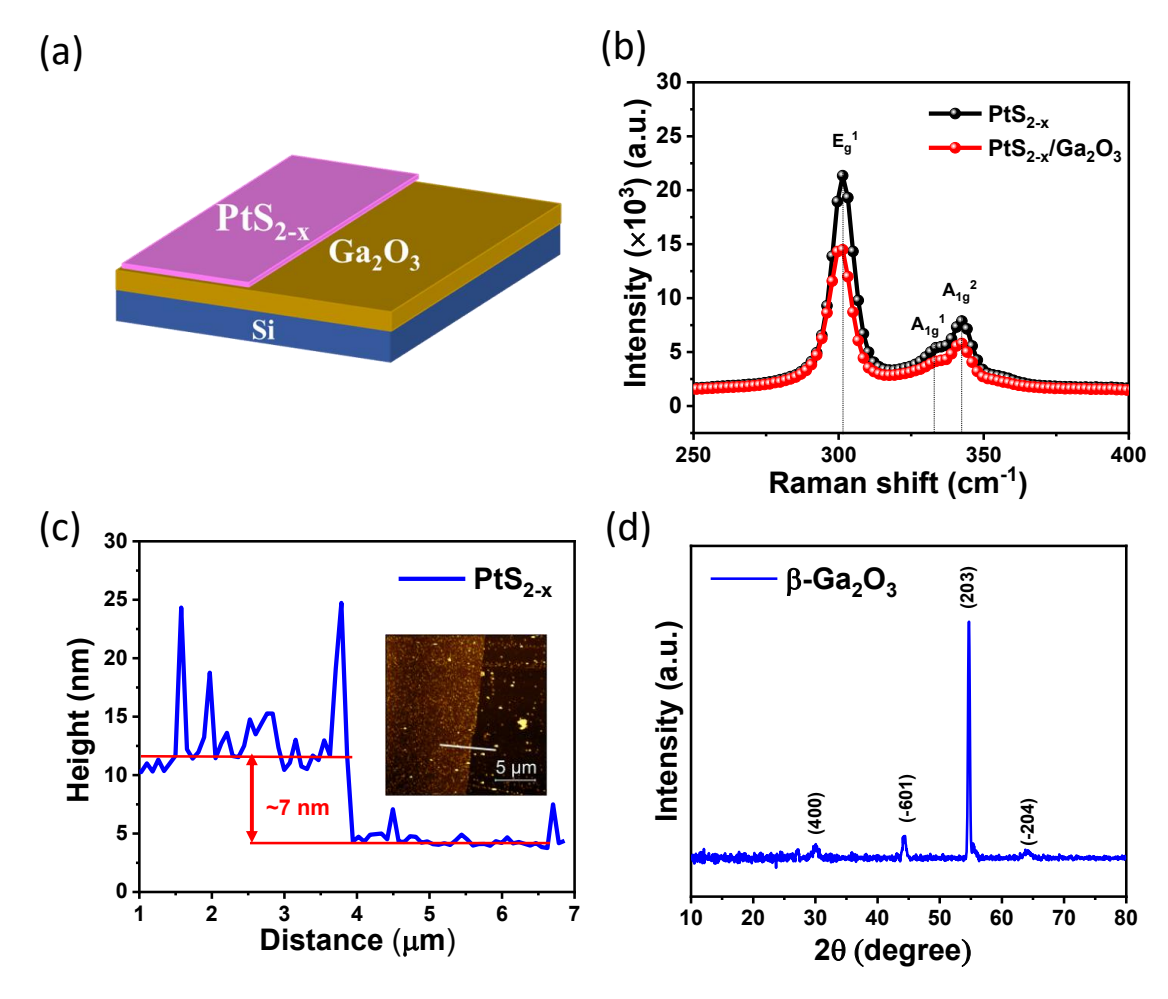


Figure 4.12 (a) Schematics of PtS_{2-x}/Ga_2O_3 heterostructure (b) Raman spectra of PtS_{2-x} and PtS_{2-x}/Ga_2O_3 thin films performed with 532 nm laser (c) Thickness of PtS_{2-x} thin film transferred on SiO_2/Si substrate measured by AFM (d) GIXRD of Ga_2O_3 grown on Si substrate.

4.3.2.1 Band alignment study

In heterostructure devices, the band alignment of the stack materials plays a crucial role in determining device performance [22, 23]. Therefore, it becomes essential to uncover the hidden concept at the interface. Recently, XPS has been well recognized for its surface-sensitive nature and diverse applications in different fields to explore band alignment of the heterostructures [1, 20, 46]. In addition, it also helps to investigate the carrier transport (CT) mechanism, valence band offset, conduction band offset, and many more [1, 46]. In this work, XPS was carried out on bare PtS_{2-x}, Ga₂O₃, and PtS_{2-x}/Ga₂O₃ heterostructure samples to determine the band alignment between PtS_{2-x} and Ga₂O₃. The carbon peak position of 284.8 eV is employed

as a reference peak for calibrating other elements' peaks. The valence band maximum (VBM) of bare PtS_{2-x} and Ga₂O₃ was estimated by linear fitting of the edge line of the valence band spectra. Usually, the heterostructure's valence band offset (VBO) is evaluated by considering the core level binding energy of the parent materials, heterostructure, and their VBM values. Later, the conduction band offset (CBO) is calculated by combining the VBO and band gap values of the stack materials. In this direction, we have taken Pt $4f_{7/2}$ and Ga 3d as core-level energies for further calculations. Figure 4.13 (a) represents the Pt 4f core level binding energy spectra of PtS_{2-x} and PtS_{2-x}/Ga₂O₃ heterostructure. In bare PtS_{2-x}, two major peaks at 73.8 eV (Pt $4f_{7/2}$) and 77.1 eV (Pt $4f_{5/2}$) are related to Pt⁺⁴ oxidation state of PtS₂ and two minor peaks with peak positions at 72.3 eV (Pt $4f_{7/2}$) and 75.6 eV (Pt $4f_{5/2}$) corresponds to the Pt⁺² oxidation state of PtS [25, 46]. The reason for coming PtS peaks along PtS₂ peaks is ascribed to its more stability than PtS₂ as reported earlier [25, 46, 47]. Therefore, we used PtS_{2-x} nomenclature instead of PtS₂ owing to the presence of PtS phase in it. The Pt 4f core level spectra (Figure 4.13 (a)) of PtS_{2-x}/Ga₂O₃ heterostructure also exhibited four peaks with one pair of peaks at 73.0 eV and 76.35 eV corresponding to the Pt⁺⁴ (PtS₂) phase and other two at 71.45 eV and 74.75 eV related to the Pt⁺² (PtS) phase. The intensity of Pt⁺⁴ peaks decreases in PtS_{2-x}/Ga₂O₃ heterostructure as compared to in bare PtS_{2-x} film and could be due to the partially conversion of PtS₂ to PtS phase during heating or chemical etching used in the transferring of PtS_{2-x} film over Ga₂O₃ [24].

The core level XPS spectra of Ga 3d of bare Ga₂O₃ and PtS_{2-x}/Ga₂O₃ samples are shown in Figure 4.13 (b). In bare Ga₂O₃, two Ga 3d deconvoluted peaks at locations of 19.29 eV and 20.28 eV respective to Ga⁺ (oxygen deficiency or sub stoichiometric state) and Ga³⁺ (Ga₂O₃ stochiometric) are received and match well with the literature [1, 48]. In PtS_{2-x}/Ga₂O₃, the Ga⁺ and Ga³⁺ peaks at 19.15 eV and 20.35 eV, respectively, are obtained. In addition to these peaks, a small peak centered around 23.5 eV related to O 2s is observed in both bare Ga₂O₃ and PtS_{2-x}/Ga₂O₃ films. A shifting of peak position in Pt 4f and Ga 3d core levels of the heterostructure are observed compared with their respective bare materials, for example, 0.8 eV red shift in Pt 4f_{7/2} of Pt⁺⁴ and 0.07 eV blue shift in Ga³⁺ of PtS_{2-x}/Ga₂O₃ signify the strong interlayer coupling at the interface. The VBM value of 0.85 eV for PtS_{2-x} and 3.23 eV for Ga₂O₃ are obtained as shown in Figure 4.13 (c), which was calculated from the leading edge of the valence band spectra, as mentioned earlier.

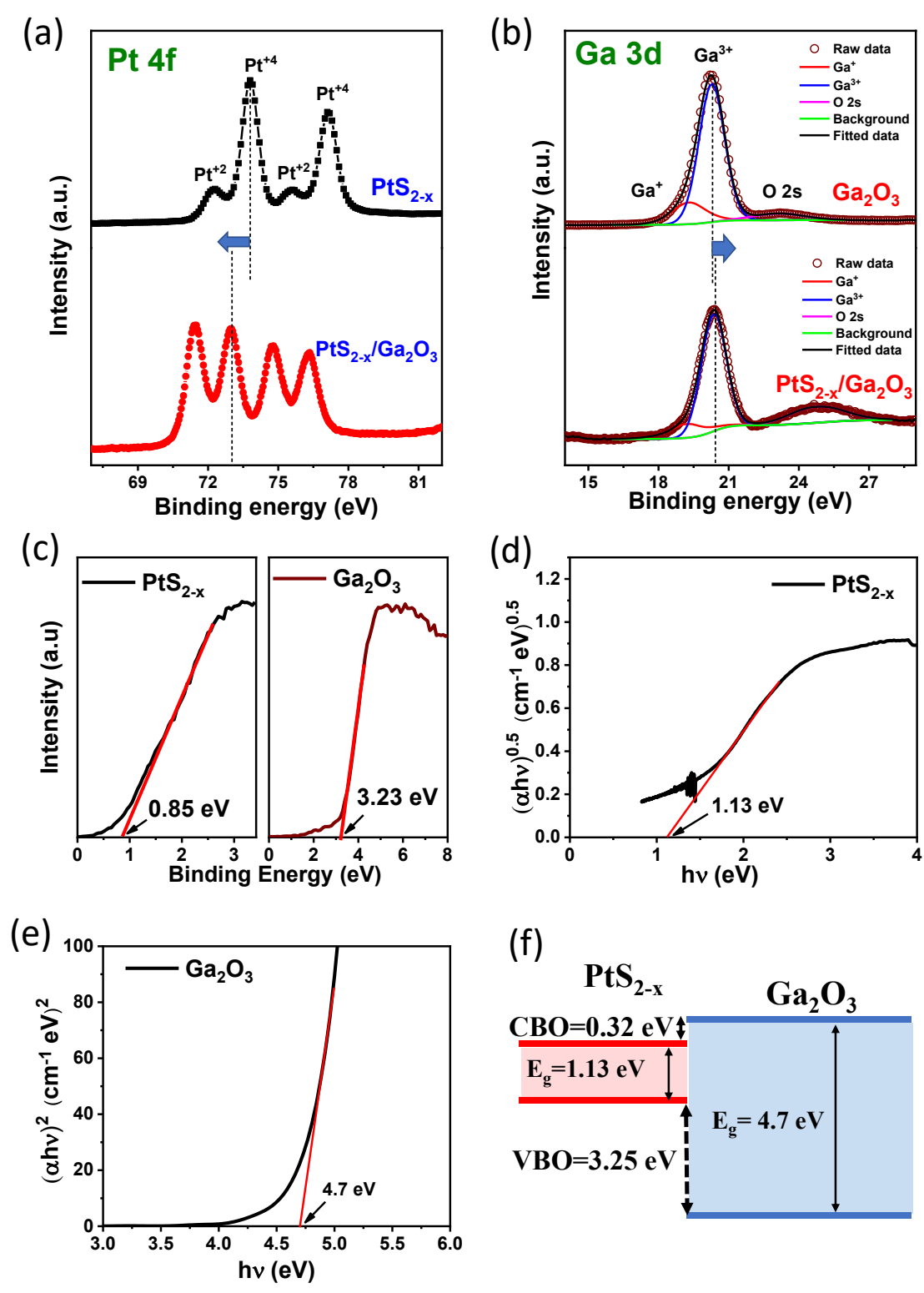


Figure 4.13 (a) XPS Pt 4f core level spectra of bare PtS_{2-x} and PtS_{2-x}/Ga₂O₃ heterostructure (b) XPS Ga 3d core level spectra of bare PtS_{2-x} and PtS_{2-x}/Ga₂O₃ heterostructure (c) Valence band maximum (VBM) of bare PtS_{2-x} and bare Ga₂O₃. The band gap of (d) PtS_{2-x} and (e) Ga₂O₃ calculated using Tauc's plot method. (f) Type-I band alignment between the PtS_{2-x} and Ga₂O₃.

The VBO between the PtS_{2-x} and Ga₂O₃ is estimated using the Kraut's rule [49] with the following equation

$$VBO = (E_{Pt\ 4f_{7/2}}^{PtS_{2-x}} - E_{VBM}^{PtS_{2-x}}) - (E_{Ga\ 3d}^{Ga_2O_3} - E_{VBM}^{Ga_2O_3}) + (E_{Ga\ 3d}^{PtS_{2-x}/Ga_2O_3} - E_{Pt\ 4f_{7/2}}^{PtS_{2-x}/Ga_2O_3}) - \cdots (4.6)$$

Where $(E_{Ga\ 3d}^{PtS_{2-x}/Ga_2O_3} - E_{Pt\ 4f_{7/2}}^{PtS_{2-x}/Ga_2O_3})$ term represents the binding energies separation of Ga 3d and Pt $4f_{7/2}$ core levels of the heterojunction. Similarly, $(E_{Pt\ 4f_{7/2}}^{PtS_{2-x}} - E_{VBM}^{PtS_{2-x}})$ and $(E_{Ga\ 3d}^{Ga_2O_3} - E_{VBM}^{Ga_2O_3})$ terms exhibit the binding energy difference of Pt $4f_{7/2}$ and Ga 3d core levels from their VBM positions. The obtained VBO was 3.25 ± 0.1 eV.

The CBO was calculated from VBO and band gap values with the following equation.

$$CBO = E_g^{Ga_2O_3} - E_g^{PtS_{2-x}} - VBO.....(4.7)$$

The band gap of PtS_{2-x} 1.13 eV ($E_g^{PtS_2-x}$) and Ga_2O_3 4.7 eV ($E_g^{Ga_2O_3}$) was determined from Tauc's plot method, as shown in Figures 4.13 (d) and 4.13 (e), respectively. Consequently, the CBO of 0.32 eV \pm 0.1 eV value is obtained, and a type-I band alignment is confirmed between the PtS_{2-x} and Ga_2O_3 , as shown in Figure 4.13 (f). Moreover, VBM values (which are measured with respect to the fermi level) of both PtS_{2-x} and Ga_2O_3 are closer to their conduction band. Hence, here an n-n-type heterostructure is formed.

4.3.2.2 Photodetector study

In addition to the band alignment study discussed above, the PtS_{2-x}/Ga₂O₃ photodetector and its depth study have also been carried out in this work. Figure 4.14 (a) displays the schematic of the PtS_{2-x}/Ga₂O₃ device with external biasing (V) given to the device. Figure 4.14 (b) exhibits the current-voltage (I-V) characteristics of the PtS_{2-x}/Ga₂O₃ device under dark and 250-1100 nm light illumination with non-linear (rectifier) nature with more current generated in positive bias than negative bias. For comparison perspective and to show PtS_{2-x}/Ga₂O₃ broadband detection, the current-time (I-T) response of bare Ga₂O₃ and PtS_{2-x}/Ga₂O₃ devices under 254 nm and 1100 nm light illumination are shown in Figure 4.14 (c) and 4.14 (d), respectively which confirmed that PtS_{2-x}/Ga₂O₃ device response well in NIR (1100 nm) and UV-C (254 nm) whereas Ga₂O₃ restrict to only UV-C region. This is attributed to the PtS_{2-x} film covered over the Ga₂O₃ film and its low band gap of 1.13 eV which lies in the NIR (1100 nm) range that absorbs this wavelength and enhance the detection range.

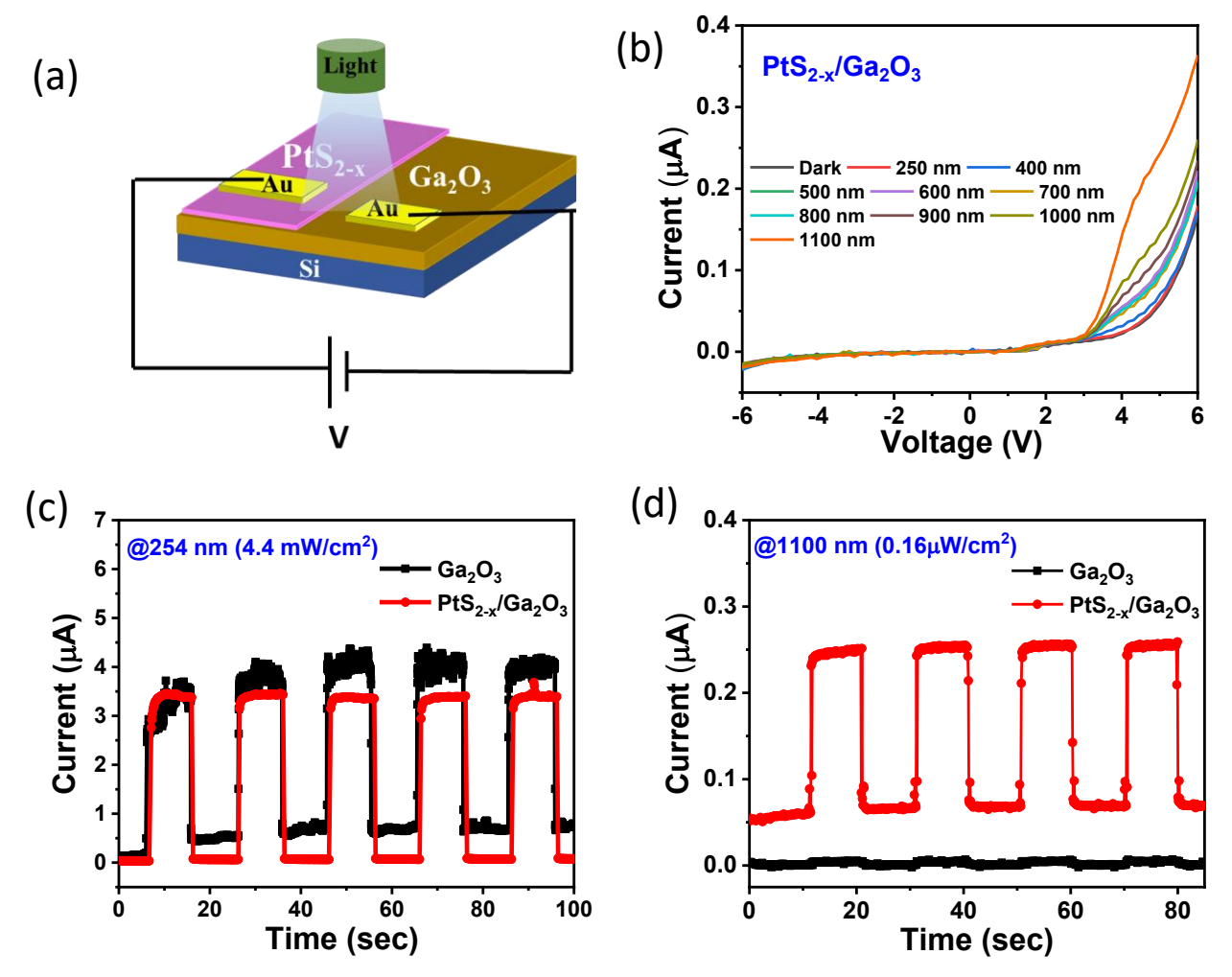


Figure 4.14 (a) Schematic of the PtS_{2-x}/Ga_2O_3 device with external biasing V (b) Current-Voltage (I-V) characteristics of PtS_{2-x}/Ga_2O_3 device under dark and 250-1100 nm wavelength illumination. I-T comparison of bare Ga_2O_3 and PtS_{2-x}/Ga_2O_3 under (c) 254 nm illumination at 4V (d) 1100 nm illumination at 5V.

Next, different photodetector parameters, such as responsivity (R), specific detectivity (D*), and external quantum efficiency (EQE), were evaluated for the PtS_{2-x}/Ga₂O₃ photodetector device. Responsivity is the ratio of net photocurrent generated per incident optical power. Mathematically, it is given by

$$R = \frac{I_{light} - I_{dark}}{P. A} \quad \dots (4.8)$$

Where I_{light} , I_{dark} , P, and A are the photocurrent, dark current, incident light power density, and effective area (3 mm²), respectively.

The calculated responsivity of PtS_{2-x}/Ga₂O₃ as a function of wavelength range from 250-1100 nm at 5V bias is shown in Figure 4.15 (a). A higher responsivity of PtS_{2-x}/Ga₂O₃ towards visible

and NIR region is observed than UV region. Similar behavior has also been observed in MoS₂-ZnS and MoS₂-Ga₂O₃ heterostructures [1, 50]. Moreover, another factor of non-linear responsivity is the different power density of the individual illuminated light source (250-1100 nm) used as given in Table 2.1. A high responsivity value of 38.7 AW⁻¹ for 1100 nm and 2.6 AW⁻¹ for 250 nm wavelengths were obtained for the PtS_{2-x}/Ga₂O₃ device, corroborating that it responds well from UV-C to NIR region and exhibits broadband detection. The built-in potential, strong interlayer coupling, and increased absorption are a few factors that promote the current generation and high responsivity in the heterostructure devices [9, 46, 51].

The specific detectivity (D*), another essential parameter, gives information about the photodetector's sensitivity and quantifies the photodetector's capability to detect weak signals was calculated using the following formula.

$$D^* = \sqrt{\frac{A}{2eI_{dark}}} \times R \dots (4.9)$$

Where e is the electronic charge, R is the responsivity, and other parameters are defined earlier. The variation of detectivity (D*) of PtS_{2-x}/Ga_2O_3 device within wavelength range 250-1100 nm at 5V is exhibited in Figure 4.15 (b) with a maximum value of 4.8×10^{13} Jones for 1100 nm (NIR) illumination and 3.2×10^{12} Jones for 250 nm (UV-C) illumination. Again, the high detectivity value confirmed the heterostructure's high-performance broadband photodetector.

The EQE of the heterostructure device was evaluated using the following formula

EQE =
$$\frac{hcR}{e\lambda}$$
 (4.10)

Where h is plank constant, c is the speed of light in air, λ is an incident light wavelength, and other parameters are defined earlier.

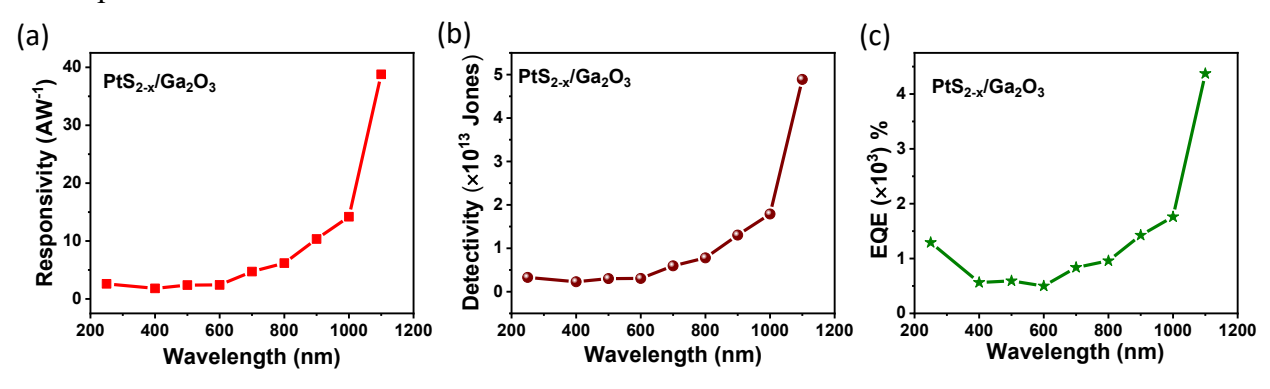


Figure 4.15 (a) Variation of (a) Responsivity (b) Detectivity (c) External quantum efficiency (EQE) of PtS_{2-x}/Ga₂O₃ device with wavelength range 250-1100 nm at 5V bias.

Table 4.2. Comparison of PtS_{2-x}/Ga₂O₃ device with other Ga₂O₃ heterostructure based reported photodetector in literature.

Device	Detection	Responsivity	Detectivity	Ref.	
	range	(AW^{-1})	(Jones)		
MoS ₂ /β-Ga ₂ O ₃	215-400 nm	0.002 @ 245	1.21×10^{11}	[52]	
		nm, 0V			
MoS_2/α - Ga_2O_3	254-365 nm	33.9 @ 254 nm,		[48]	
		10V			
MoS_2/β - Ga_2O_3	200-700 nm	0.0072@260	2.4×10^{11}	[53]	
		nm, -10V			
Graphene/PtSe ₂ /	245 nm	0.076 @ 245	1.93×10^{13}	[54]	
β -Ga ₂ O ₃		nm, 0V			
Graphene/β-	254 nm	12.8 @ 254 nm,	10^{13}	[55]	
Ga_2O_3		-6V			
$PtS_{2-x}/\beta\text{-}Ga_2O_3$	250-1100 nm	38.7 @1100 nm,	4.8×10^{13}	Present work	
		5V			

Figure 4.15 (c) represents the plot of EQE calculated for a wavelength range of 250-1100 nm. High EQE with more than 100% value in PtS_{2-x}/Ga₂O₃ device is obtained due to high photoconductive gain and responsivity of the photodetector [1, 13]. In order to show the broad detection range of the PtS_{2-x}/Ga₂O₃, the I-T measurements were performed using 400-1100 nm monochromator light and 254 nm UV-C lamp source. Figure 4.16 (a) exhibits the comparison I-T plot of the PtS_{2-x}/Ga₂O₃ device under 400-1100 nm wavelength light illumination in which maximum current is produced under 1100 nm wavelength, which corresponds to the band gap of PtS_{2-x} (1.13 eV). On combining both Figures 4.14 (c) and 4.16 (a), we can say that PtS₂₋ _x/Ga₂O₃ responds well from UV-C (254 nm) to NIR region (1100 nm) and confirms the broad detection. The response time of the photodetector, which determines its speed, was evaluated from its rise and fall time. Under 1100 nm illumination, a fast response with a rise time of 90 ms and a fall time of 87 ms is obtained for the PtS_{2-x}/Ga₂O₃ device, as illustrated in Figure 4.16 (b). The comparison plot of our fabricated device with the reported literature is shown in Table 4.2. The stability of the PtS_{2-x}/Ga₂O₃ photodetector was also checked after 5 months under broad range of illumination (254 nm-1100 nm), as shown in Figure 4.17. It clearly shows that except for little change in I-T for 254 nm wavelength, the device has consistent performance and is highly stable.

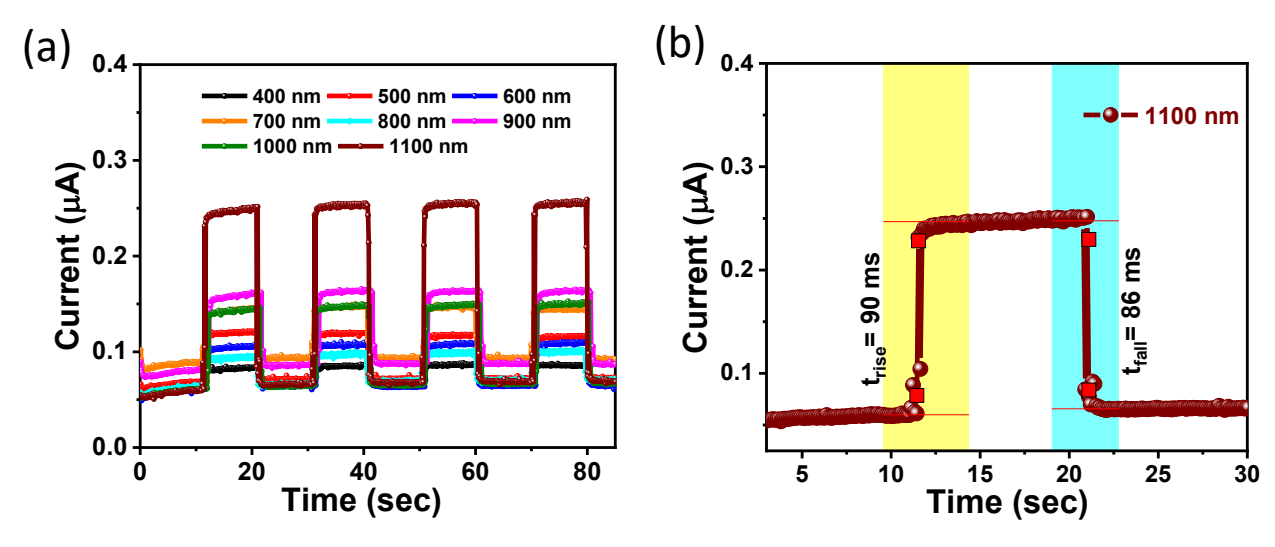


Figure 4.16 (a) Photoresponse of PtS_{2-x}/Ga₂O₃ device under 400-1100 nm wavelength range at 5V bias (b) response time (rise or fall time) of PtS_{2-x}/Ga₂O₃ under 1100 nm irradiation at 5V.

We have also performed power depended current measurements for a PtS_{2-x}/Ga₂O₃ heterostructure device under broad illumination (254-1100 nm). Figure 4.18 shows the log (current) vs log (power density) plot with fitted data using equation, $I_{net}=BP^{\alpha}$, where I_{net} is the net photocurrent, B is the proportionality constant, P is power density, and α is the power exponent that indicates the defect states between the conduction band edge and fermi level [53]. In our case, α varies from 0.24 to 0.81 for different wavelengths, as shown in Figure 4.18. The variation of α value from 1 depicts the presence of defect/trap states within the material. The greater deviation of α value from 1 indicates that more defect states present and support the photogating effect [56]. Moreover, these trap/defect states may trap the photogenerated charge carrier and thus affect the recombination rate and the overall device performance. Furthermore, in-depth study of defects the transient response of heterostructure device under 600 nm light illumination is shown in Figure 4.19 and fitted with $I = I_0 + Ae^{-t/\tau_1} + Be^{-t/\tau_2}$ equation, where A and B are constants, I_0 is steady state current, t is the time, and τ_1 and τ_2 are the time relaxation constants. The τ_{r1} (τ_{r2}) and τ_{d1} (τ_{d2}) depict the fast (slow) components of the rise and fall time, respectively. The slow component illustrates the trap or defect present within the material. For 600 nm light illumination, the $\tau_{r1}(\tau_{r2})$ and $\tau_{d1}(\tau_{d2})$ values of 0.08 s (2.4 s) and 0.03 s (0.23 s) were obtained, as shown in Figure 4.19. Here, slow rise (2.04 s) may be attributed to the presence of structural defect and vacancies (e.g., gallium, oxygen, sulfur) at the surface or interface which lead to the trap of charge carriers and slow the response.

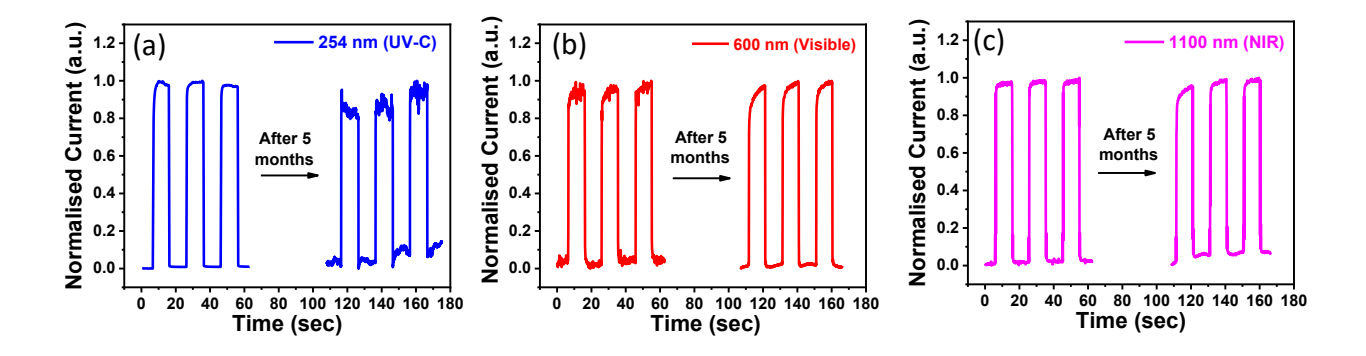


Figure 4.17 I-T measurement showing the stability of the PtS_{2-x}/Ga₂O₃ device after 5 months under illumination of (a) 254 nm at 4V (b) 600 nm at 5V (c) 1100 nm at 5V covering broad UV-C to near infrared (NIR) region.

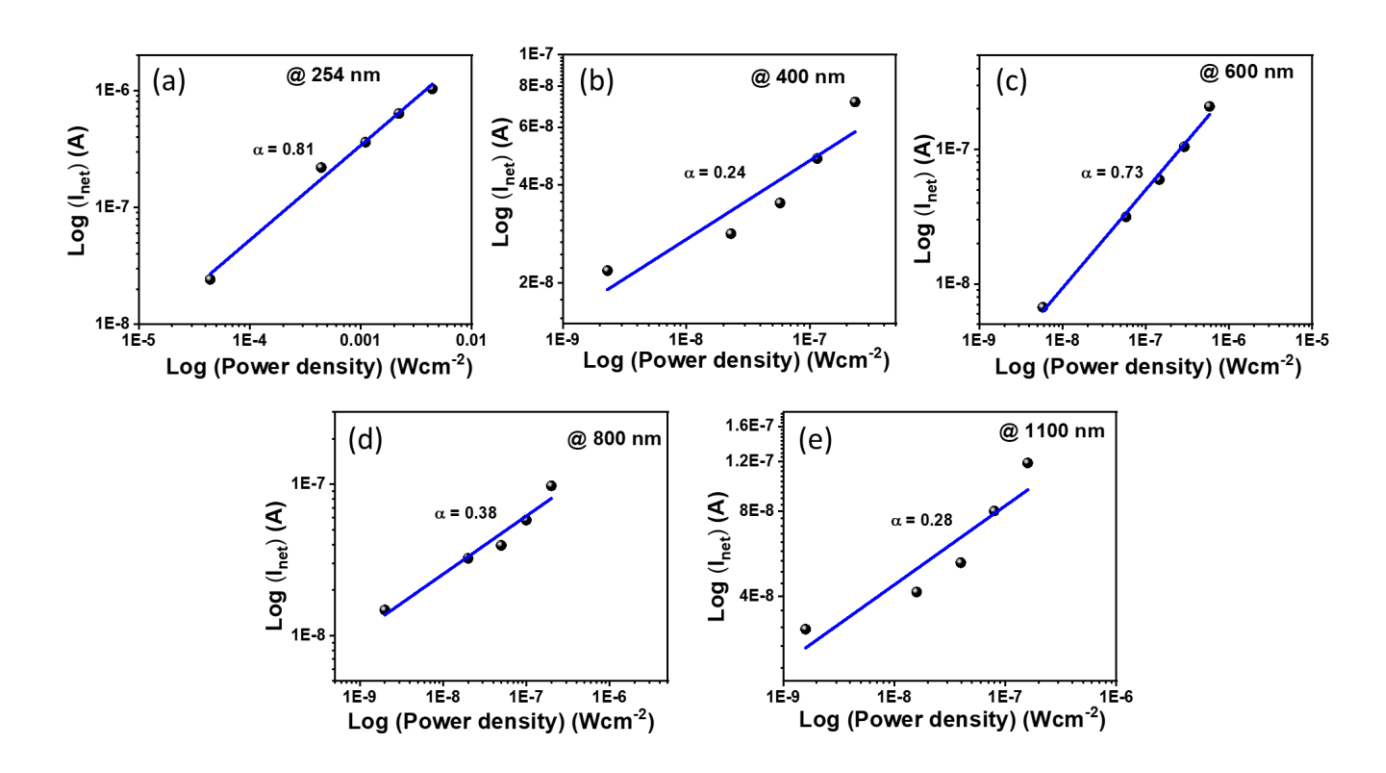


Figure 4.18 Logarithmic plot of photocurrent vs power density at 5V under the illumination of (a) 254 nm (b) 400 nm (c) 600 nm (d) 800 nm (e) 1100 nm

Finally, the charge transport mechanism at the PtS_{2-x}/Ga₂O₃ interface was proposed based on their band alignment study. Since here, n-n heterostructure is formed hence, the majority of the

current will flow due to the electrons. The computed work function of 4.44 eV for Ga_2O_3 and 5.05 eV for PtS_{2-x} from ultraviolet spectroscopy (UPS) (Figure 4.20) implying that Ga_2O_3 fermi level is at a higher position than PtS_{2-x} fermi level. Hence, when PtS_{2-x} and Ga_2O_3 contact each other, electrons will diffuse from Ga_2O_3 to the PtS_{2-x} side to attain the equilibrium condition and form a depletion region (shaded region) on Ga_2O_3 and an accumulation region on the PtS_{2-x} side, which generates a built-in potential within the interface as shown in Figure 4.21 (a).

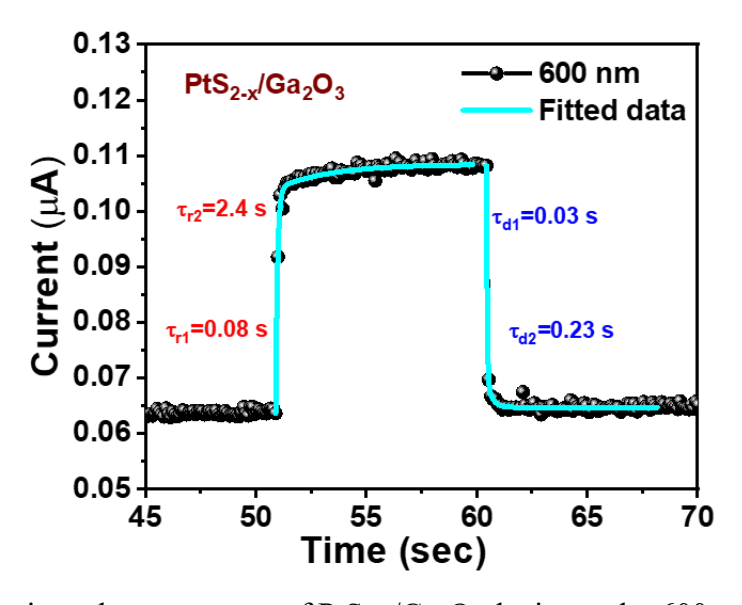


Figure 4.19 Transient photo response of PtS_{2-x}/Ga₂O₃ device under 600 nm wavelength

Under forward biasing (V) to Ga₂O₃ (negative terminal of the voltage connected to n-type Ga₂O₃) and with increasing its value the fermi level of Ga₂O₃ moves upward and decreases the barrier height for the electrons (Figure 4.21 (b)) leads to more dark current is produced in the forward bias (Figure 4.14 (b)). As mentioned earlier, here, both materials are n-type. Therefore, the majority of current will be dominated by electrons. At low forward biasing and under illumination, there is also a possibility that photogenerated holes can move from the valence band of the Ga₂O₃ to the valence band of PtS_{2-x} and lead to recombination and decrease the current value (as also confirmed from Figure 4.14 (b) that upto 3V less current is produced). However, at higher positive biasing especially greater than threshold voltage (V_T) around 3V here (Figure 4.14 (b)) given to the PtS_{2-x}, impedes the path of these photogenerated holes towards PtS_{2-x} by increasing the barrier height for holes. This reduces the recombination rate and supports the fast increase in electron separation or current, which dominates here. Moreover, additional external electric field and built-in electric field further give the additional hand to enhance the current value and thus overall, more current is observed in forward bias.

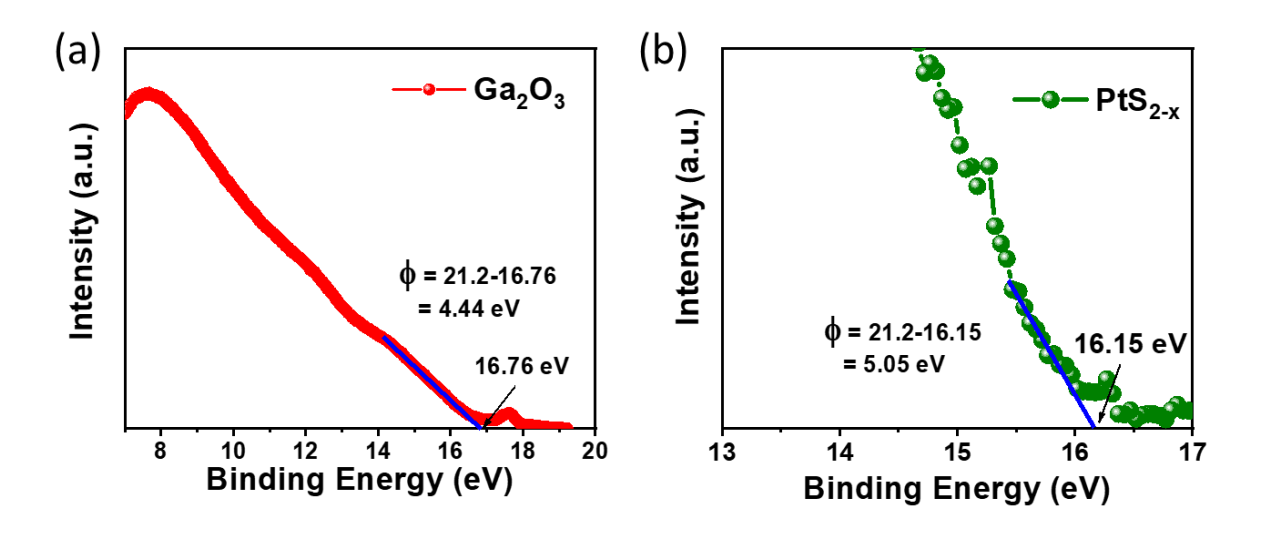


Figure 4.20 Work function calculated for (a) Ga₂O₃ (b) PtS_{2-x} from Ultraviolet photoelectron spectroscopy (UPS) spectroscopy

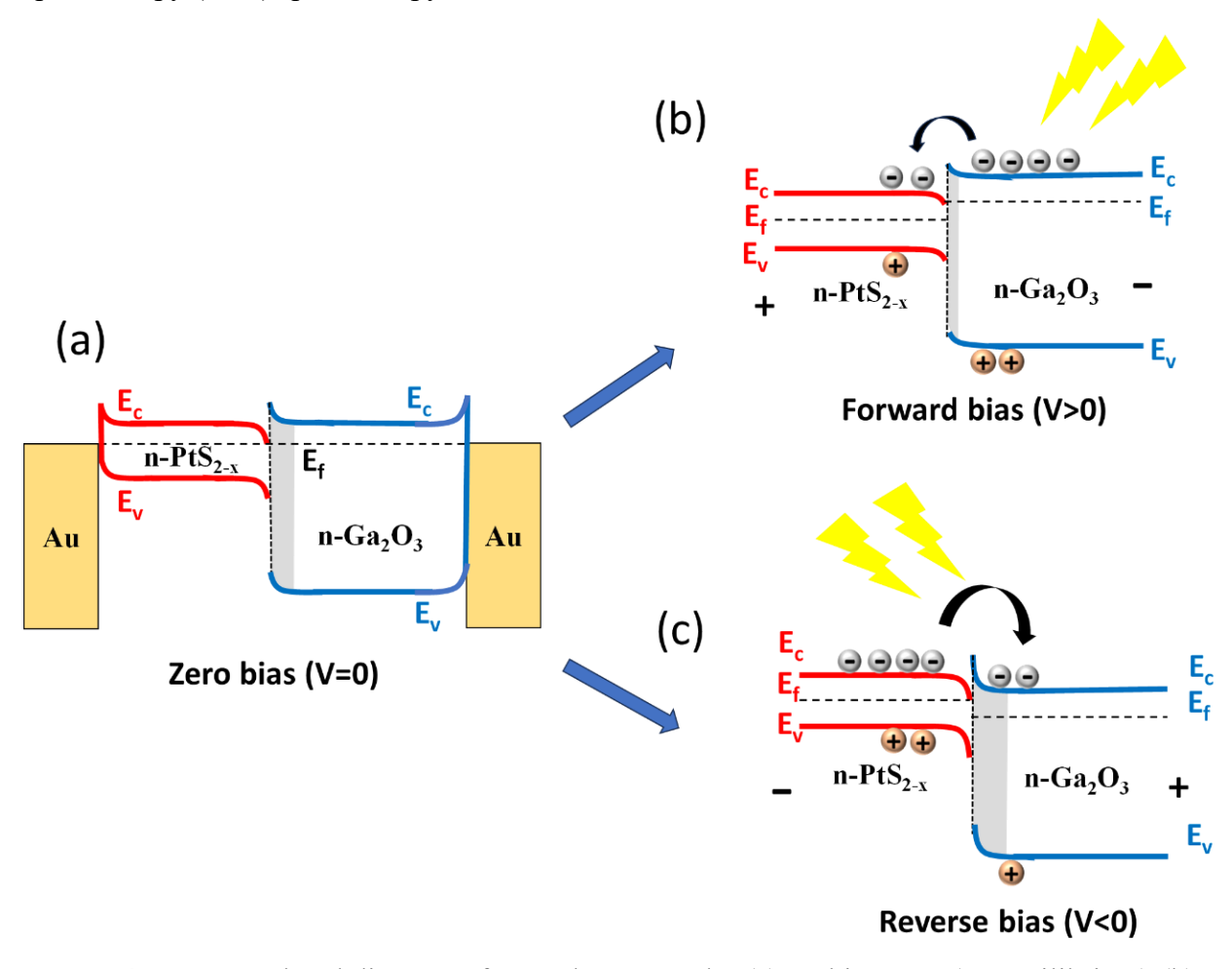


Figure 4.21 Energy band diagram of PtS_{2-x}/Ga_2O_3 under (a) no bias V=0 (or equilibrium) (b) Forward bias (V>0) with respect to Ga_2O_3 . (c) Reverse bias (V<0) with respect to Ga_2O_3 .

Chapter 4: Large area 2D PtS₂ heterostructures for broadband photodetection

In the case of reverse bias to Ga₂O₃, its fermi level moves downward compared to PtS_{2-x} fermi level and increases the barrier height for electrons to move from PtS_{2-x} to Ga₂O₃ side as shown in Figure 4.21 (c) which hinder the flow of electrons. Under light illumination and reverse bias this barrier height hinders the separation of photogenerated electrons and increase the recombination rate. Therefore, less current is observed in reversed bias as compared to the forward bias.

4.3.3 Conclusion

In summary, a large area of PtS_{2-x}/Ga₂O₃ heterostructure was fabricated using the PMMA-assisted wet transfer method by transferring PtS_{2-x} film over Ga₂O₃ grown film. A detailed interface study between the PtS_{2-x} and Ga₂O₃ film was carried out using X-ray photoelectron spectroscopy and revealed a type-I band alignment with a valence band offset (VBO) of 3.25 eV and a conduction band offset (CBO) of 0.32 eV. Furthermore, a high-performance broadband photodetector was fabricated based on PtS_{2-x}/Ga₂O₃, which covers a broad range from UV-C to NIR regions. The maximum responsivity of 38.7 AW⁻¹ and detectivity of 4.8×10¹³ Jones at 5V bias for PtS_{2-x}/Ga₂O₃ device is obtained under 1100 nm illumination, further showing the photodetector's high performance. Moreover, a fast response of milli second order in the NIR region corroborated the fast speed of the device. Finally, a carrier transport mechanism was illustrated based on their band alignment study. This work opens a new path to fabricating large-area, high-performance 2D-3D heterostructures for future optoelectronics devices

References

- 1. Wadhwa, R., et al., Fast response and high-performance UV-C to NIR broadband photodetector based on MoS2/a-Ga2O3 heterostructures and impact of band-alignment and charge carrier dynamics. Applied Surface Science, 2023. 632: p. 157597.
- 2. Xie, C., et al., High-performance broadband heterojunction photodetectors based on multilayered PtSe2 directly grown on a Si substrate. Nanoscale, 2018. 10(32): p. 15285-15293.
- 3. Wadhwa, R., A.V. Agrawal, and M. Kumar, A strategic review of recent progress, prospects and challenges of MoS2-based photodetectors. Journal of Physics D: Applied Physics, 2022. 55(6): p. 063002.
- 4. Wadhwa, R., et al., Investigation of charge transport and band alignment of MoS2-ReS2 heterointerface for high performance and self-driven broadband photodetection. Applied Surface Science, 2021. 569: p. 150949.
- 5. Ganatra, R. and Q. Zhang, Few-Layer MoS2: A Promising Layered Semiconductor. ACS Nano, 2014. 8(5): p. 4074-4099.
- 6. Venkata Subbaiah, Y.P., K.J. Saji, and A. Tiwari, Atomically Thin MoS2: A Versatile Nongraphene 2D Material. Advanced Functional Materials, 2016. 26(13): p. 2046-2069.
- 7. Frisenda, R., et al., Atomically thin p—n junctions based on two-dimensional materials. Chemical Society Reviews, 2018. 47(9): p. 3339-3358.
- 8. Cai, Z., et al., Chemical Vapor Deposition Growth and Applications of Two-Dimensional Materials and Their Heterostructures. Chemical Reviews, 2018. 118(13): p. 6091-6133.
- 9. Pham, P.V., et al., 2D Heterostructures for Ubiquitous Electronics and Optoelectronics: Principles, Opportunities, and Challenges. Chemical Reviews, 2022. 122(6): p. 6514-6613
- 10. Xu, L., et al., Two-Dimensional MoS2-Graphene-Based Multilayer van der Waals Heterostructures: Enhanced Charge Transfer and Optical Absorption, and Electric-Field Tunable Dirac Point and Band Gap. Chemistry of Materials, 2017. 29(13): p. 5504-5512.
- 11. Hu, Z., et al., Interfacial charge and energy transfer in van der Waals heterojunctions. InfoMat, 2022. 4(3): p. e12290.
- 12. Cai, W., et al., Strain-Modulated Photoelectric Responses from a Flexible α-In2Se3/3R MoS2 Heterojunction. Nano-Micro Letters, 2021. 13(1): p. 74.
- 13. Bassi, G., et al., Controlled and tunable growth of ambient stable 2D PtS2 thin film and its high-performance broadband photodetectors. Journal of Alloys and Compounds, 2023. 955: p. 170233.
- 14. Chakraborty, B., et al., Symmetry-dependent phonon renormalization in monolayer MoS\${}_{2}\$ transistor. Physical Review B, 2012. 85(16): p. 161403.
- 15. Mitra, S., et al., Tailoring phonon modes of few-layered MoS2 by in-plane electric field. npj 2D Materials and Applications, 2020. 4(1): p. 6.
- 16. Zhao, Y., et al., Extraordinarily Strong Interlayer Interaction in 2D Layered PtS2. Advanced Materials, 2016. 28(12): p. 2399-2407.
- 17. Splendiani, A., et al., Emerging Photoluminescence in Monolayer MoS2. Nano Letters, 2010. 10(4): p. 1271-1275.
- 18. Mak, K.F., et al., Atomically Thin \$\\mathrm{MoS}}_{2}\$: A New Direct-Gap Semiconductor. Physical Review Letters, 2010. 105(13): p. 136805.
- 19. Klots, A.R., et al., Probing excitonic states in suspended two-dimensional semiconductors by photocurrent spectroscopy. Scientific Reports, 2014. 4(1): p. 6608.

- 20. Wang, W., et al., Investigation of the band alignment at MoS2/PtSe2 heterojunctions. Applied Physics Letters, 2019. 114(20): p. 201601.
- 21. Agrawal, A.V., K. Kaur, and M. Kumar, Interfacial study of vertically aligned n-type MoS2 flakes heterojunction with p-type Cu-Zn-Sn-S for self-powered, fast and high performance broadband photodetector. Applied Surface Science, 2020. 514: p. 145901.
- 22. Liao, W., et al., Interface engineering of two-dimensional transition metal dichalcogenides towards next-generation electronic devices: recent advances and challenges. Nanoscale Horizons, 2020. 5(5): p. 787-807.
- 23. Chen, Y., et al., Tuning Electronic Structure of Single Layer MoS2 through Defect and Interface Engineering. ACS Nano, 2018. 12(3): p. 2569-2579.
- 24. Xu, H., et al., Strategy for Fabricating Wafer-Scale Platinum Disulfide. ACS Applied Materials & Interfaces, 2019. 11(8): p. 8202-8209.
- 25. Cullen, C.P., et al., Synthesis and characterisation of thin-film platinum disulfide and platinum sulfide. Nanoscale, 2021. 13(15): p. 7403-7411.
- 26. Moriya, R., et al., Large current modulation in exfoliated-graphene/MoS2/metal vertical heterostructures. Applied Physics Letters, 2014. 105(8): p. 083119.
- 27. Huang, M., et al., Multifunctional high-performance van der Waals heterostructures. Nature Nanotechnology, 2017. 12(12): p. 1148-1154.
- 28. Zhang, H., et al., Type-I PtS2/MoS2 van der Waals heterojunctions with tunable photovoltaic effects and high photosensitivity. Nanoscale, 2022. 14(43): p. 16130-16138.
- 29. Ghosh, S., et al., Polarity-Tunable Photocurrent through Band Alignment Engineering in a High-Speed WSe2/SnSe2 Diode with Large Negative Responsivity. ACS Nano, 2022. 16(3): p. 4578-4587.
- 30. Sun, X., et al., Recent Advances in Two-Dimensional Heterostructures: From Band Alignment Engineering to Advanced Optoelectronic Applications. Advanced Electronic Materials, 2021. 7(7): p. 2001174.
- 31. Yang, Y., et al., High-responsivity PtSe2 photodetector enhanced by photogating effect. Applied Physics Letters, 2021. 118(1): p. 013103.
- 32. Wang, G., et al., Interlayer Coupling Induced Infrared Response in WS2/MoS2 Heterostructures Enhanced by Surface Plasmon Resonance. Advanced Functional Materials, 2018. 28(22): p. 1800339.
- 33. Zhang, K., et al., Interlayer Transition and Infrared Photodetection in Atomically Thin Type-II MoTe2/MoS2 van der Waals Heterostructures. ACS Nano, 2016. 10(3): p. 3852-3858.
- 34. Yu, Y., et al., Equally Efficient Interlayer Exciton Relaxation and Improved Absorption in Epitaxial and Nonepitaxial MoS2/WS2 Heterostructures. Nano Letters, 2015. 15(1): p. 486-491.
- 35. Mathew, S., et al., Band alignment and charge transport study of Au nanoparticles decorated over MoS2/MoSe2 hybrid heterostructure for plasmon enhanced photodetection. Materials Science in Semiconductor Processing, 2023. 156: p. 107302.
- 36. Pezeshki, A., et al., Electric and Photovoltaic Behavior of a Few-Layer α-MoTe2/MoS2 Dichalcogenide Heterojunction. Advanced Materials, 2016. 28(16): p. 3216-3222.
- 37. Zhai, X., et al., Enhanced Optoelectronic Performance of CVD-Grown Metal–Semiconductor NiTe2/MoS2 Heterostructures. ACS Applied Materials & Interfaces, 2020. 12(21): p. 24093-24101.
- 38. Wang, H., et al., Junction Field-Effect Transistors Based on PdSe2/MoS2 Heterostructures for Photodetectors Showing High Responsivity and Detectivity. Advanced Functional Materials, 2021. 31(49): p. 2106105.

- 39. Bose, S., et al., One-pot liquid-phase synthesis of MoS2-WS2 van der waals heterostructures for broadband photodetection. Nanotechnology, 2023. 34(12): p. 125704.
- 40. Liu, Q., et al., Printable Transfer-Free and Wafer-Size MoS2/Graphene van der Waals Heterostructures for High-Performance Photodetection. ACS Applied Materials & Interfaces, 2017. 9(14): p. 12728-12733.
- 41. Kaur, D. and M. Kumar, A Strategic Review on Gallium Oxide Based Deep-Ultraviolet Photodetectors: Recent Progress and Future Prospects. Advanced Optical Materials, 2021. 9(9): p. 2002160.
- 42. Qin, Y., et al., Review of deep ultraviolet photodetector based on gallium oxide*. Chinese Physics B, 2019. 28(1): p. 018501.
- 43. Kaur, D., et al., Surface nanopatterning of amorphous gallium oxide thin film for enhanced solar-blind photodetection. Nanotechnology, 2022. 33(37): p. 375302.
- 44. Kaur, D., et al., Strain effects on the optoelectronic performance of ultra-wide band gap polycrystalline β-Ga2O3 thin film grown on differently-oriented Silicon substrates for solar blind photodetector. Applied Surface Science, 2023. 616: p. 156446.
- 45. Pi, L., et al., Temperature dependence of Raman responses of few-layer PtS2. Nanotechnology, 2018. 29(50): p. 505709.
- 46. Bassi, G., R. Wadhwa, and M. Kumar, Broadband and High-Performance Photodetector Fabricated Using Large Area and Transfer-Free 2D–2D PtS2/MoS2 Heterostructure. Advanced Optical Materials, 2023. n/a(n/a): p. 2301899.
- 47. Zhussupbekov, K., et al., Electronic and structural characterisation of polycrystalline platinum disulfide thin films. RSC Advances, 2020. 10(69): p. 42001-42007.
- 48. Yang, Y., et al., Low Deposition Temperature Amorphous ALD-Ga2O3 Thin Films and Decoration with MoS2 Multilayers toward Flexible Solar-Blind Photodetectors. ACS Applied Materials & Interfaces, 2021. 13(35): p. 41802-41809.
- 49. Kraut, E.A., et al., Precise Determination of the Valence-Band Edge in X-Ray Photoemission Spectra: Application to Measurement of Semiconductor Interface Potentials. Physical Review Letters, 1980. 44(24): p. 1620-1623.
- 50. Gomathi, P.T., P. Sahatiya, and S. Badhulika, Large-Area, Flexible Broadband Photodetector Based on ZnS–MoS2 Hybrid on Paper Substrate. Advanced Functional Materials, 2017. 27(31): p. 1701611.
- 51. Wang, H., et al., Van der Waals Integration Based on Two-Dimensional Materials for High-Performance Infrared Photodetectors. Advanced Functional Materials, 2021. 31(30): p. 2103106.
- 52. Zhuo, R., et al., A self-powered solar-blind photodetector based on a MoS2/β-Ga2O3 heterojunction. Journal of Materials Chemistry C, 2018. 6(41): p. 10982-10986.
- 53. Sharma, M., et al., Ultraflexible and Transparent MoS2/β-Ga2O3 Heterojunction-Based Photodiode with Enhanced Photoresponse by Piezo-Phototronic Effect. ACS Applied Electronic Materials, 2023. 5(4): p. 2296-2308.
- 54. Wu, D., et al., Highly sensitive solar-blind deep ultraviolet photodetector based on graphene/PtSe2/β-Ga2O3 2D/3D Schottky junction with ultrafast speed. Nano Research, 2021. 14(6): p. 1973-1979.
- 55. Lin, R., et al., High-Performance Graphene/β-Ga2O3 Heterojunction Deep-Ultraviolet Photodetector with Hot-Electron Excited Carrier Multiplication. ACS Applied Materials & Interfaces, 2018. 10(26): p. 22419-22426.
- 56. Li, L., et al., Few-Layered PtS2 Phototransistor on h-BN with High Gain. Advanced Functional Materials, 2017. 27(27): p. 1701011.

Chapter 5: 2D PtSe₂ heterostructure for photodetector study

In this chapter, we discussed the $PtSe_2/MoS_2$ heterostructure fabrication and its broadband photodetector study. The $PtSe_2/MoS_2$ heterostructure was fabricated by wet transfer of $PtSe_2$ film over MoS_2 coated substrate. The heterostructure device shows broadband response from 400-1200 nm, covering visible to NIR region with maximum responsivity of 17.9 AW⁻¹ in NIR (900 nm) region which is much better than the reported literature. Moreover, heterostructure device exhibits $\sim 10^3$ order of reduction in dark current as compared to bare $PtSe_2$ with improved in detectivity value and ultrafast response with rise/fall time of 103 μ s /117 μ s. Finally, to understanding the working of $PtSe_2/MoS_2$ photodetector, a detailed interface carrier transport mechanism is also explained.

5.1 Requirement of PtSe₂/MoS₂ heterostructure

PtSe₂, group-10 TMDC get enormous recognition owing to its captivating properties such as narrow band gap range (0-1.2 eV), high carrier mobility (>1000 cm²V⁻¹s⁻¹), and high ambient stability [1-4]. However, in bare PtSe₂ devices high dark current, low on-off ratio, and weak sensitivity diminish to build a high-performance broadband photodetector [5]. In photodetection, the dark current plays a crucial role. High dark current critically limits the specific detectivity of the device and conceals the weak light signals to detect [6]. To overcome this bottleneck, fabricating its van der Waals heterostructure is the best strategy to suppress the dark current and increase the overall device performance [6, 7]. Moreover, heterostructure offers strong built-in potential, fast carrier separation, increased absorption, and enhanced detection range over bare semiconductor devices [7-10]. Since no dangling bonds are present in the 2D materials so van der Waals heterostructure can be synthesize without any concerns of lattice mismatch. The most studied group-6 TMDC is MoS₂ which has a band gap of 1.2-1.8 eV, high absorption coefficient, moderate mobility and high-stability [11-13]. Therefore, it considers as a potential candidate to fabricate the heterostructure with PtSe2 to design highperformance broadband photodetector. Recently few studies on PtSe₂/MoS₂ heterostructure based photodetector have been reported [14-16]. However, these heterostructures are synthesized either by mechanical exfoliation (ME) method or a combination of thermally assisted conversation and ME (TAC+ ME) method which results small area of heterostructure devices. For practical application and scalable production, the large area growth of PtSe₂/MoS₂ heterostructure is highly demanding which is missing in these reports. In addition, considering the importance of NIR region there is still need to fabricate a photodetector that shows high

responsivity and specific detectivity in the NIR region. Furthermore, the carrier transport mechanism at PtSe₂/MoS₂ heterointerface to suppress dark current and achieve ultra-fast speed is also less explored.

5.2 Experimental section

5.2.1 Growth of PtSe₂ film

PtSe₂ thin films were grown by thermally assisted conversion (TAC) method where selenization of pre-sputtered Pt film was carried out in a chemical vapor deposition (CVD) system. In detail, first Pt film was coated on SiO₂/Si using radio frequency (RF) magnetron sputtering at room temperature with high-purity (99.99%) 1-inch Pt target. The film was deposited for 1 minute at a power of 30 W and deposition pressure of 3.8×10⁻³ torr. The other parameters such as base pressure of ~1×10⁻⁶ torr and 20 sccm Ar flow rate was used during the deposition. Sequentially, the Pt-coated substrate and selenium powder (in the boat) were loaded in a small quartz tube (both sides opened) with a separation of 14 cm. Next, this whole arrangement was loaded in the main tube of the CVD with a temperature profile of 250 °C for Se powder and 500 °C for Pt-coated SiO₂/Si substrate. A gas flow rate of 75 sccm of 1.1% H₂ balance Ar mixture was used as a carrier gas throughout the deposition. After 1 hour of deposition, the system was left to cool down naturally before samples were taken out.

5.2.2. Fabrication of MoS₂ film and PtSe₂/MoS₂ heterostructure device

MoS₂ thin film was grown on SiO₂/Si substrate using RF magnetron sputtering with 99.99% purity MoS₂ target at optimized parameters [17]. MoS₂ film was sputter at a temperature of 400 °C for 6 minutes at a power of 50W, 1×10⁻² Torr deposition pressure, and 20 sccm Ar gas environment. This sample is nomenclature as MoS₂/SiO₂/Si for future use. For PtSe₂/MoS₂ heterostructure fabrication, PtSe₂ film was transferred on the MoS₂ using a polymethyl methacrylate (PMMA) assisted wet transfer method. The PtSe₂ (grown on SiO₂/Si) thin film is coated with PMMA solution, followed by immersing it in 1M NaOH solution at a temperature of 90 °C to separate it from the underlying SiO₂/Si substrate. After this, peeled PMMA/PtSe₂ film was soaked multiple times in deionized water to remove unwanted residues. Sequentially, this film is slowly transferred onto MoS₂/SiO₂/Si substrate and dries on a hot plate for some time. The final PMMA is removed by dipping the sample into acetone and propanol to get the desired PtSe₂/MoS₂ heterostructure. The gold electrode of thickness around 150 nm is deposited on the heterostructure sample using a thermal evaporated method and physical

shadow mask. For a better understanding of heterostructure fabrication, a schematic including multiple steps are displayed in Figure 5.1.

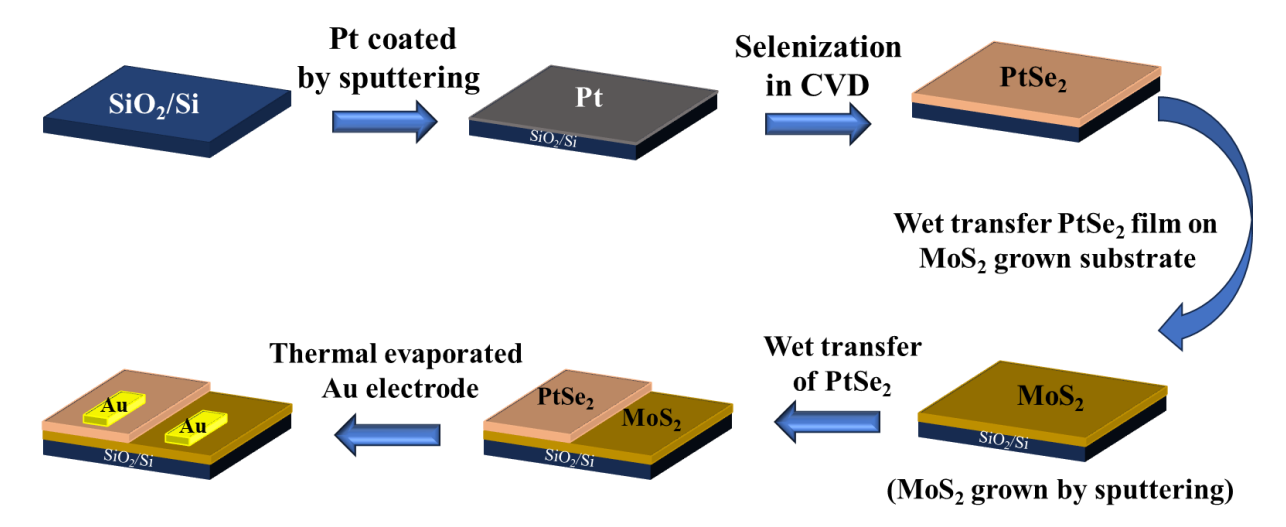


Figure 5.1 Schematic showing the multiple steps used for the fabrication of PtSe₂/MoS₂ heterostructure device.

5.2.3. Device measurement and characterization

The optoelectronic measurements of the samples were carried out with Keithley 6430 SMU, Bentham PVE 300 set up including TMc 300 monochromator light source (400-1200 nm). The transmission electron microscope (TEM) and high-resolution transmission electron microscope (HRTEM) measurements were performed with Model Themis 300 KV. The Raman spectroscopy was performed at room temperature using 532 nm laser irradiation with the HORIBA LabRAM HR Evolution spectrometer in the backscattering configuration. The X-ray photoelectron spectroscopy (XPS) and Ultraviolet photoelectron spectroscopy (UPS) were performed with Thermo Fisher Scientific ESCALAB Xi+ using Al K $_{\alpha}$ as an X-ray source. Atomic force microscopy (AFM) determined the thickness of the samples with the multimode-8 (Bruker) model in tapping mode. The Optical and field emission scanning electron microscope (FESEM) were performed with Nikon ECLIPSE LV100ND and JEOL-JSM-7610F, respectively instruments. The Perkin Elmer Lambda 950 instrument was used for absorption measurements. Rigaku MiniFlex was employed for X-ray diffraction (XRD) measurements.

5.3 Results and discussion

For the testimony of growth of PtSe₂ and MoS₂ film various characterizations were performed. First, XPS was performed on PtSe₂ and MoS₂ films grown on SiO₂/Si substrate as illustrated in Figure 5.2. The peak position of 284.8 eV was employed as a reference to make a carbon

correction in the XPS peaks for other elements. Figure 5.2 (a) and (b) demonstrate the Pt 4f and Se 3d core level XPS spectra. In Pt 4f spectra, two prominent peaks at 73.7 eV (4f_{7/2}) and 77.1 eV (4f_{5/2}), respectively are obtained, whereas in Se 3d spectra two peaks at 55.1 eV and 55.9 eV corresponding to Se 3d_{5/2} and Se 3d_{3/2}, respectively are observed. These XPS peaks match well with the reported XPS spectra of PtSe₂ hence confirmed the growth of PtSe₂ [18]. The thickness of PtSe₂ was measured using AFM and found to be around 10.6 nm using thickness profile, as shown in Figure 5.2 (c), with its AFM image shown in the inset. Further, Figures 5.2 (d) and 5.2 (e) represent the core level XPS spectra of Mo 3d and S 2p, respectively. After deconvoluting Mo 3d spectra, it exhibits two major peaks at 229.4 eV and 232.6 eV related to core levels of Mo 3d_{5/2} and Mo 3d_{3/2} and is consistent with the Mo⁺⁴ oxidation state of MoS₂ [9]. In addition, one minor peak of S 2s at 226.5 eV was also observed in the same spectra. No Pt-O and Mo-O related peak is observed in both PtSe₂ and MoS₂ core levels spectra, which signifies the high quality of PtSe₂ and MoS₂ films grown. Figure 5.2 (f) manifests the AFM line profile of MoS₂ film grown on SiO₂/Si substrate with a thickness of around 42 nm with the inset of AFM image.

For more insight into the crystallinity and atomic structure of PtSe₂, TEM and HRTEM were performed on PtSe2 film by transferring it on copper grid using PMMA assisted wet transfer method. Figures 5.3 (a) and 5.3 (b) depict the TEM and HRTEM image of the PtSe₂ with multiple grains present and thus confirm the polycrystalline nature of PtSe2. The inset of Figure 5.3 (b) shows the interplanar spacing of 0.20 nm which corresponds to (102) plane of PtSe₂. Figure 5.3 (c) exhibits the selected area electron diffraction (SAED) pattern rings and moving from inside to outside ascribed to (100), (102), (111), and (103) planes of the PtSe₂ and again corroborate the polycrystalline nature of the PtSe₂. The energy dispersive spectroscopy (EDS) spectra of PtSe₂ films were also probed during TEM measurement as depicted in Figure 5.3 (d) and verified the presence of both Pt and Se elements related to the PtSe₂. The signature of Cu is coming due to supporting Cu grid. Moreover, PtSe₂ crystallinity was also examined by Xray diffraction (XRD) as shown in Figure 5.4 (a), where distinct peaks related to (001), (101), and (003) planes are obtained which corresponds to the polycrystalline nature of PtSe₂ film (JCPDS-00-018-0970). The thickness of ~10 nm PtSe₂ film transferred over MoS₂ coated substrate is estimated as displayed in Figure 5.4 (b) is highly consistent with thickness measured directly on SiO₂/Si grown substrate (~10.6 nm, Figure 5.2 (b)).

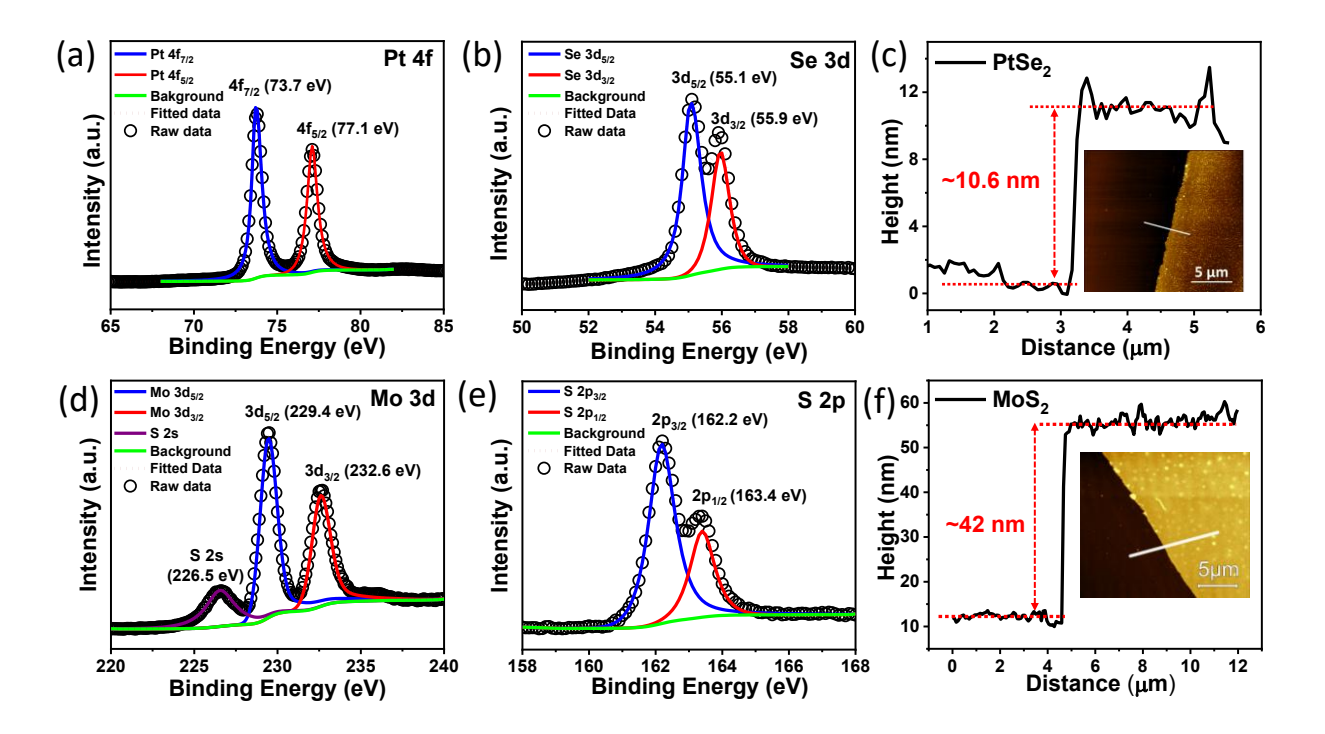


Figure 5.2 (a, b) Pt 4f and Se 3d core level XPS spectra of PtSe₂ (c) Thickness of PtSe₂ calculated by AFM and inset displaying its AFM image with step mark (d, e) XPS spectra of Mo 3d and S 2p core levels of MoS₂ (f) Thickness of MoS₂ estimated by AFM with inset shows the AFM image of step.

Figure 5.5 (a) depicts the schematics of PtSe₂/MoS₂ heterostructure formed on SiO₂/Si substrate with PtSe₂ partially covered onto the MoS₂ film. Figure 5.5 (b) shows the optical image of PtSe₂/MoS₂ heterostructure with a large area, high uniformity, and fine junction at the interface. The morphology of the sample is further examined by field emission scanning electron microscope (FESEM) exhibited in Figure 5.5 (c), which also supports high uniformity and fine junction at the interface. The Raman spectra of MoS₂, PtSe₂, and PtSe₂/MoS₂ heterojunction film grown on SiO₂/Si substrate are shown in Figure 5.5 (d). In Raman spectra of MoS₂, two prominent peaks with positions at ~377.8 cm⁻¹ and ~411.4 cm⁻¹ corresponding to E_{2g} and A_{1g} vibration modes validate the growth of MoS₂ [17]. Here, E_{2g} denotes the inplane vibration mode, and A_{1g} signifies the out-of-plane vibration mode of MoS₂. In PtSe₂, two major Raman peaks (Figure 5.5 (d)) at 176.0 cm⁻¹ (E_g) and 205 cm⁻¹ (A_{1g}) are observed, where Eg and Alg represent the in-plane and out-of-plane vibration modes of Se atoms [19, 20]. In addition to these peaks, one minor peak at ~232.2 cm⁻¹, called longitudinal optical (LO) mode was observed, which usually originates from the coupling between A_{2u} and E_u infrared active modes, where out-of-plane Pt atoms and in-plane Se atoms motions contribute to it [20]. In PtSe₂/MoS₂ heterostructure (Figure 5.5 (d)), various distinct Raman peaks at 377.2 cm⁻¹ (E_{2g})

and $410.1~\text{cm}^{-1}$ (A_{1g}) concerned with MoS₂ and $175.8~\text{cm}^{-1}$ (E_g), $204.8~\text{cm}^{-1}$ (A_{1g}) and $232.0~\text{cm}^{-1}$ (LO) peaks associated with PtSe₂ are obtained and corroborate the PtSe₂/MoS₂ heterostructure. Comparison to bare MoS₂, a red shift of $0.6~\text{cm}^{-1}$ in E_{2g} and $1.3~\text{cm}^{-1}$ in A_{1g} peaks is observed in PtSe₂/MoS₂ heterostructure. A similar trend for PtSe₂ peaks is also noticed where the peaks are red-shifted by $0.2~\text{cm}^{-1}$ in heterostructure. This shift might be attributed to the stress or strain induced between the films after (or during) the transfer of PtSe₂ film over MoS₂ [8, 9, 21, 22].

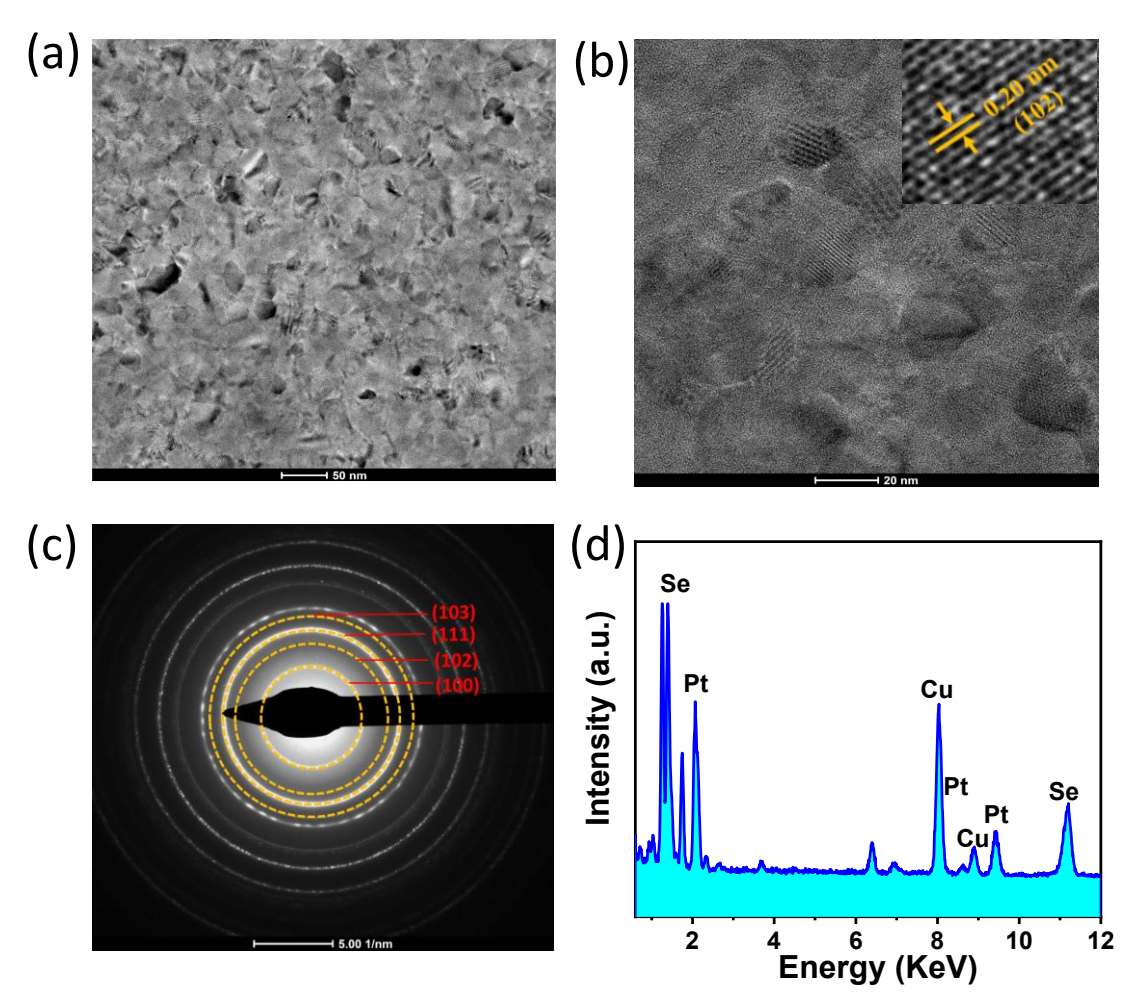


Figure 5.3 (a) TEM image of PtSe₂ showing different grains and polycrystalline nature (b) HRTEM image of PtSe₂ with different grains while the inset shows the interplanar spacing of the selected planes (c) SAED pattern of PtSe₂ film again shows the polycrystalline nature (d) EDS spectra confirmed the growth of PtSe₂ with different elements present in it.

Finally, the performance of photodetector devices made using bare PtSe₂ and PtSe₂/MoS₂ heterojunction have been carried out in detail. Both PtSe₂ and PtSe₂/MoS₂ photodetector were fabricated on SiO₂/Si substrate with gold strip electrode having separation of 3 mm. The current-voltage (I-V) characteristic of PtSe₂ and PtSe₂/MoS₂ devices were performed under dark and broad 400-1200 nm light illumination, and demonstrated in Figures 5.6 (a) and 5.6

(b), respectively. The inset of Figure 5.6 (a, b) displays the schematic of the photodetector device. Figure 5.6 (a) shows the I-V characteristic of bare PtSe₂ with an ohmic nature for both dark and under broad 400-1200 nm light illumination. Moreover, in PtSe₂ device a high dark current is observed which could be due to its narrow band gap (or semimetal) nature. This high value of dark current and inferior on-off ratio cause PtSe₂ to have poor photodetector performance. Figure 5.6 (b) exhibits an I-V plot of the PtSe₂/MoS₂ device under dark and 400-1200 nm light irradiation. In contrast to bare PtSe₂, PtSe₂/MoS₂ device shows non-linear I-V behavior with more net photocurrent (light current-dark current) generation in reverse bias than forward bias. Here, the non-linear I-V character of PtSe₂/MoS₂ device could be attributed to the built-in potential generated at the heterojunction. In photodetectors study, low dark current plays an imperative role in detecting weak signals and determining their specific detectivity. Also, a lower dark current is preferred to enhance the sensitivity of the photodetector.

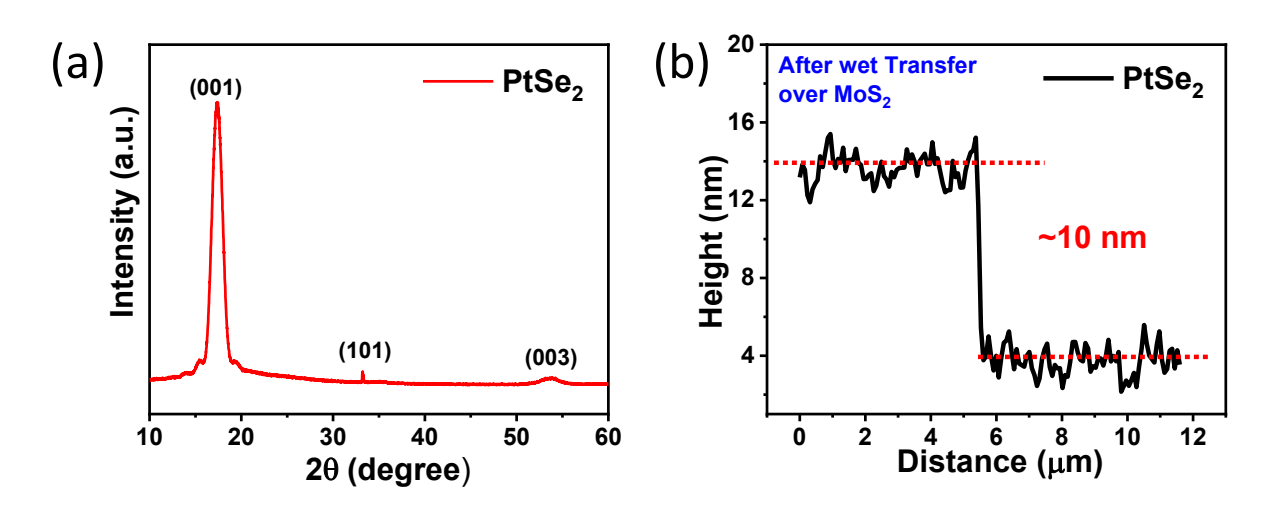


Figure 5.4 (a) X-ray diffraction (XRD) spectra of PtSe₂ film grown on SiO₂/Si substrate (b) AFM thickness of PtSe₂ film transferred over MoS₂ with inset its AFM image.

In our case, after fabricating PtSe₂/MoS₂ heterostructure, ~10³ orders reduction in dark current is observed with respect to bare PtSe₂, as illustrated in Figure 5.6 (c). This could be due to built-in-potential or barrier generated at the interface, which assists in suppressing the value of dark current [6]. The comparative specific detectivity plot of PtSe₂ and PtSe₂/MoS₂ exhibited in Figure 5.6 (d) further supports the fact that lower dark current increases the detectivity of PtSe₂/MoS₂ than PtSe₂. Further, the temporal response (current-time plot) of the PtSe₂ and PtSe₂/MoS₂ device were checked under 400 nm illumination, as shown in Figure 5.6 (e), and found that PtSe₂ shows persistent photoconductivity effect, where its current value consistently increases with time which may be ascribed to defect or traps states present in the PtSe₂ film.

At the same time PtSe₂/MoS₂ device shows a highly stable I-T response under 400 nm irradiation (see Figure 5.6 (e)) which could be attributed to the strong built-in potential generated at the PtSe₂/MoS₂ heterointerface, as described earlier in PtSe₂ heterostructures [18, 23-25]. This facilitates fast separation of charge carriers at the heterojunction. Compared to bare PtSe₂, PtSe₂/MoS₂ device showed reduce dark current, fast microsecond response, and increased on-off ratio which also support the fact of strong built-in potential generated at the heterointerface. In addition, lesser interface defects between the PtSe₂/MoS₂ junction than PtSe₂-SiO₂ junction could be another reason for stable I-T response [26]. To confirm the stability of the PtSe₂/MoS₂ device, the I-T response is further checked under 600 nm illumination (Figure 5.6 (f)) for multiple cycles, where it again maintains the same nature. The I-V and I-T measurements discussed above certified that the performance of PtSe₂/MoS₂ device is far better than bare PtSe₂.

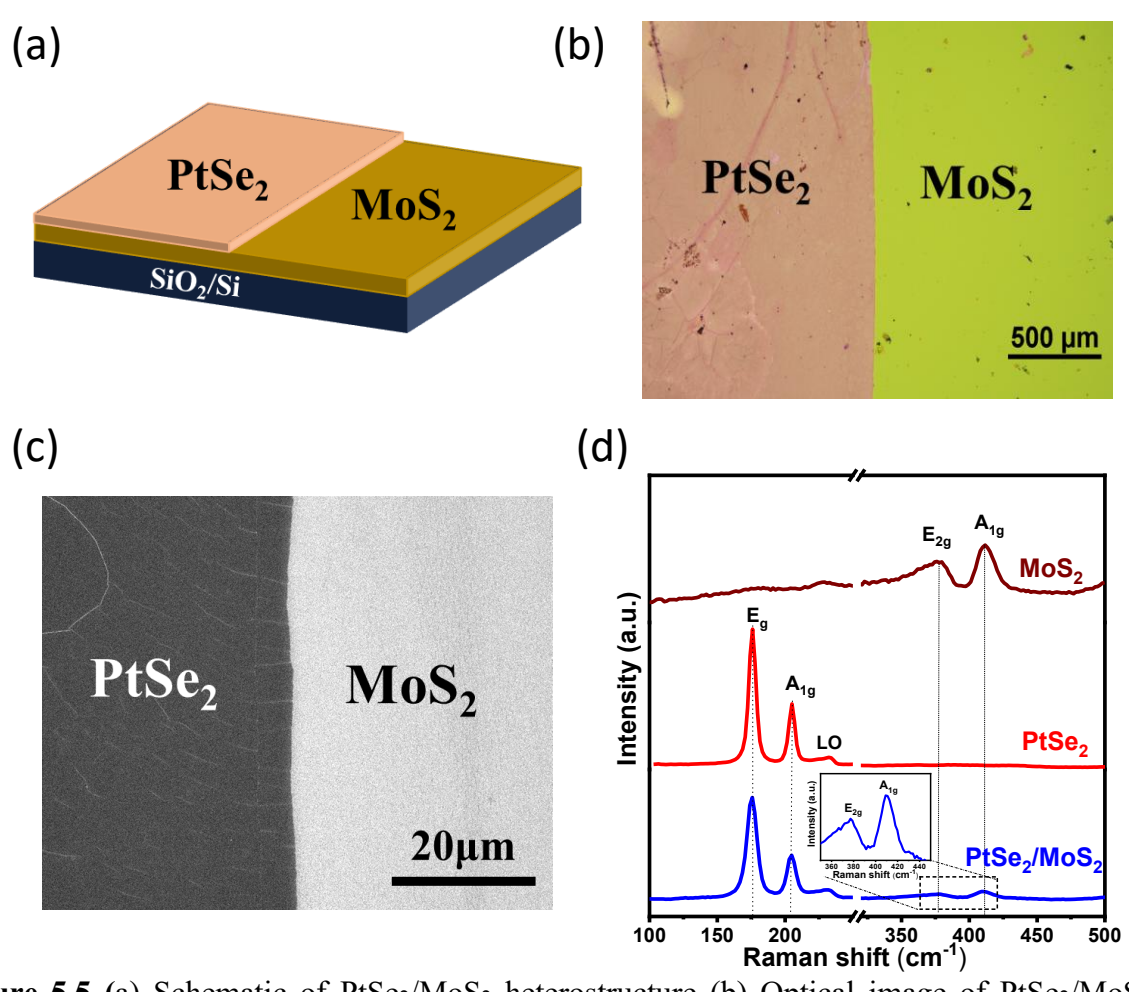


Figure 5.5 (a) Schematic of PtSe₂/MoS₂ heterostructure (b) Optical image of PtSe₂/MoS₂ exhibiting its large area growth and high uniformity (c) FESEM image of PtSe₂/MoS₂ heterostructure (d) Raman spectra of MoS₂, PtSe₂ and PtSe₂/MoS₂ film grown on SiO₂/Si substrates.

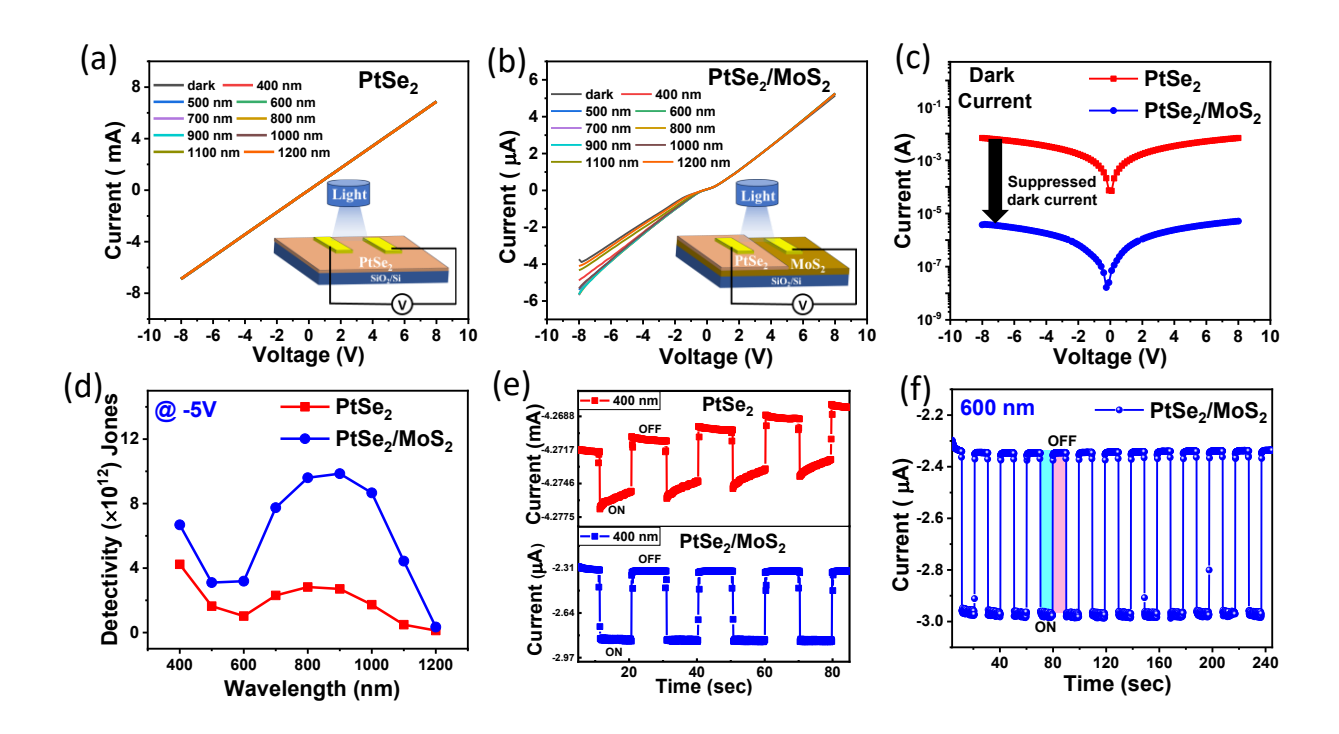


Figure 5.6. I-V characteristics of (a) bare $PtSe_2$ (b) $PtSe_2/MoS_2$ heterostructure under dark and 400-1200 nm light illumination with inset Figure exhibit their device schematic (c) Dark current comparison of $PtSe_2$ and $PtSe_2/MoS_2$ device with a $\sim 10^3$ order ratio difference (d) Detectivity comparison of $PtSe_2$ and $PtSe_2/MoS_2$ device under light illumination of 400-1200 nm at bias of -5V (e) Comparative current-time (I-T) response of $PtSe_2$ and $PtSe_2/MoS_2$ devices under 400 nm irradiation where $PtSe_2/MoS_2$ demonstrate much more stability than $PtSe_2$ (f) multiple I-T cycles show high stability of the $PtSe_2/MoS_2$ device measured under 600 nm light and at -5V bias.

The other critical parameters like responsivity, specific detectivity, and external quantum efficiency (EQE) are also calculated for PtSe₂/MoS₂ heterostructure device. Responsivity (R) is the net photocurrent generated per unit incident power and mathematically it is expressed as:

$$R = \frac{I_{photo} - I_{dark}}{P. A} \dots (5.1)$$

Where I_{photo} , I_{dark} and P are the photocurrent, dark current and incident optical power density, respectively. A is the effective area (0.23 cm²) of device under light illumination.

The specific detectivity (D*), which is a crucial parameter to determine the sensitivity of photodetector to detect weak signals is estimated using the following relation:

$$D^* = \sqrt{\frac{A}{2eI_{dark}}} \times R \dots (5.2)$$

Where e is the electronic charge and R is the responsivity of the photodetector defined earlier. Figure 5.7 (a) demonstrates the calculated responsivity and specific detectivity for the PtSe₂/MoS₂ device for broad 400-1200 nm of illumination at moderate bias of -5V. A maximum responsivity of 17.9 AW⁻¹ and specific detectivity of 9.8×10¹² Jones is obtained for 900 nm (NIR) wavelength, which exhibits that PtSe₂/MoS₂ device responds well in NIR region. Moreover, a high value of responsivity and detectivity (Figure 5.7 (a)) of PtSe₂/MoS₂ photodetector device throughout the 400-1200 nm wavelength range corroborates its high performance. Here, the non-linear behavior of responsivity and detectivity with wavelength is due to the different power densities of 400-1200 nm light from the monochromator as exhibited in Table 2.1.

The external quantum efficiency (EQE) of PtSe₂/MoS₂ device for 400-1200 nm wavelength range is also calculated and is shown in Figure 5.7 (b). The EQE of the device is computed using the following formula

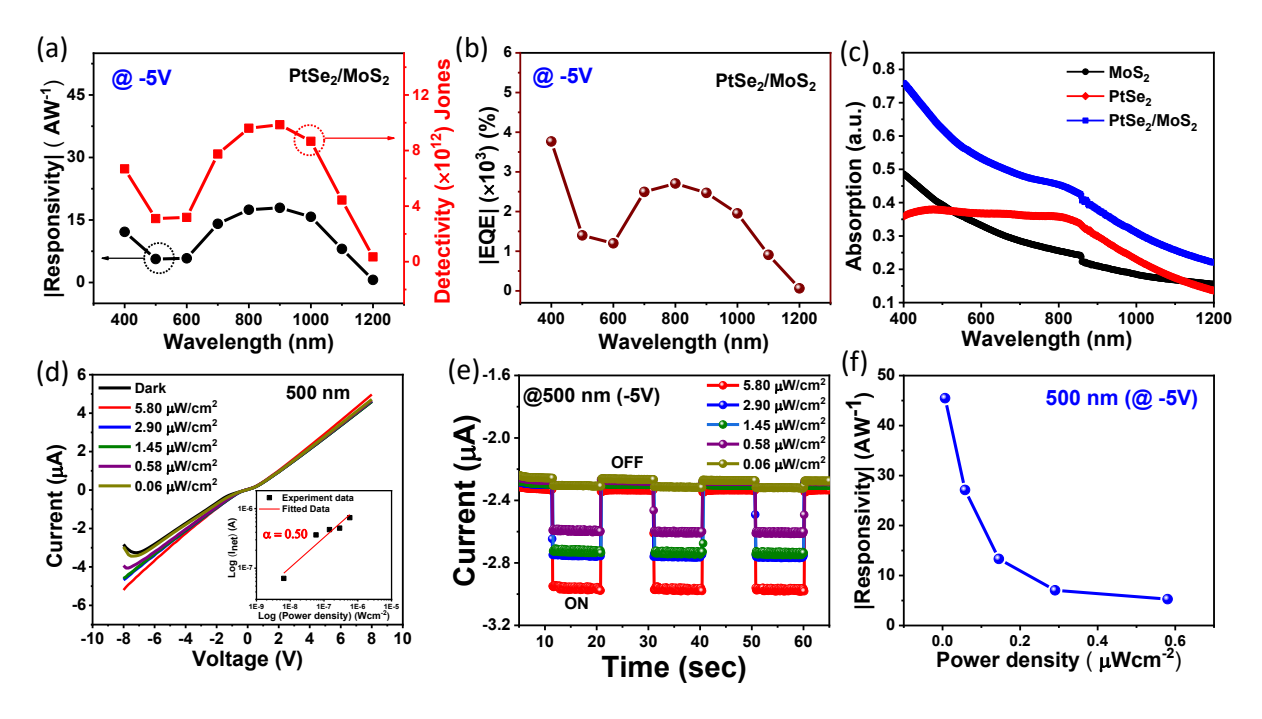


Figure 5.7 Calculated (a) Responsivity, Detectivity, and (b) External quantum efficiency of PtSe₂/MoS₂ device under wide 400-1200 nm wavelength range with -5V biasing. (c) Absorption spectra of PtSe₂, MoS₂ and PtSe₂/MoS₂ films grown on quartz substrate (d) I-V plot of PtSe₂/MoS₂ device under dark and power density of 500 nm light with inset shows the power depended current linear fit graph (e) I-T response of PtSe₂/MoS₂ device under different power density of 500 nm illumination (f) Responsivity variation of PtSe₂/MoS₂ device with different power density of 500 nm light irradiation.

$$EQE = \frac{hcR}{e\lambda} \dots (5.3)$$

Where h, c, and λ are the plank constant, speed of light, and illuminated wavelength, respectively, and other parameters are defined earlier.

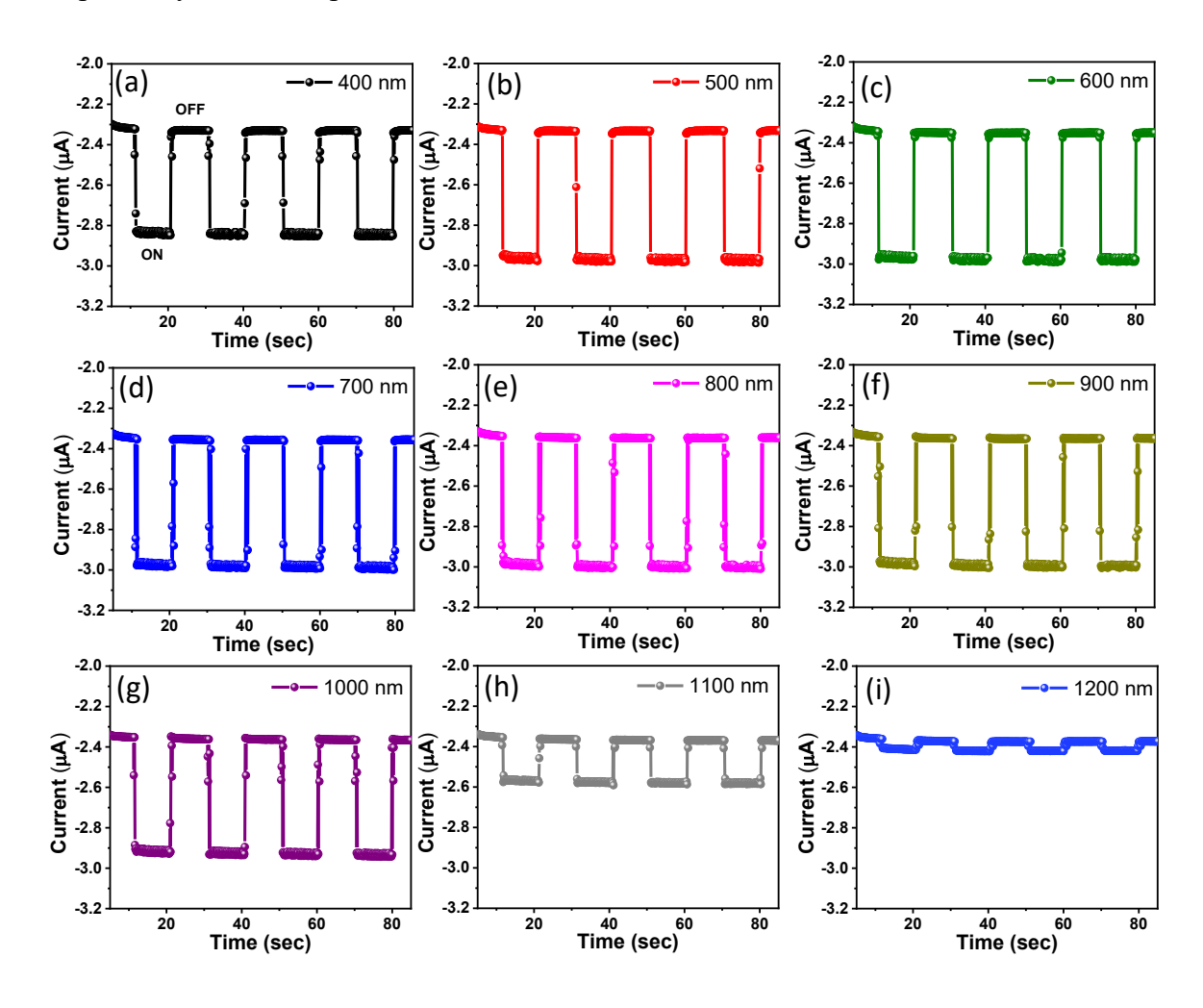


Figure 5.8 (a-i) Time-dependent photo response of PtSe₂/MoS₂ device under broad 400-1200 nm wavelength range at -5V bias.

Interestingly, the PtSe₂/MoS₂ device shows an EQE value of more than 100% for all wavelength range (400-1200 nm) which indicates multiple charge carriers are extracted per unit incident photon and primarily responsible for high responsivity (17.9 AW⁻¹) in the PtSe₂/MoS₂ device. Usually, this high EQE is attributed to the high photoconductive gain owing to the traps either in active layers or at the interface of the heterojunction device [27-29]. Under 900 nm illumination, PtSe₂/MoS₂ displays an EQE of 2.4×10³ % which again supports its high performance. The comparative absorption spectra of PtSe₂, MoS₂, and PtSe₂/MoS₂ films grown on quartz substrates are shown in Figure 5.7 (c), where PtSe₂ shows

maximum absorption within the 400-900 nm wavelength range followed by decrease in the value with increasing wavelength (upto 1200 nm). Compared with bare MoS₂ and PtSe₂, PtSe₂/MoS₂ heterostructure displays excellent broad absorption ability (Figure 5.7 (c)) in entire visible to NIR region and further assists in making it high-performance broadband photodetector.

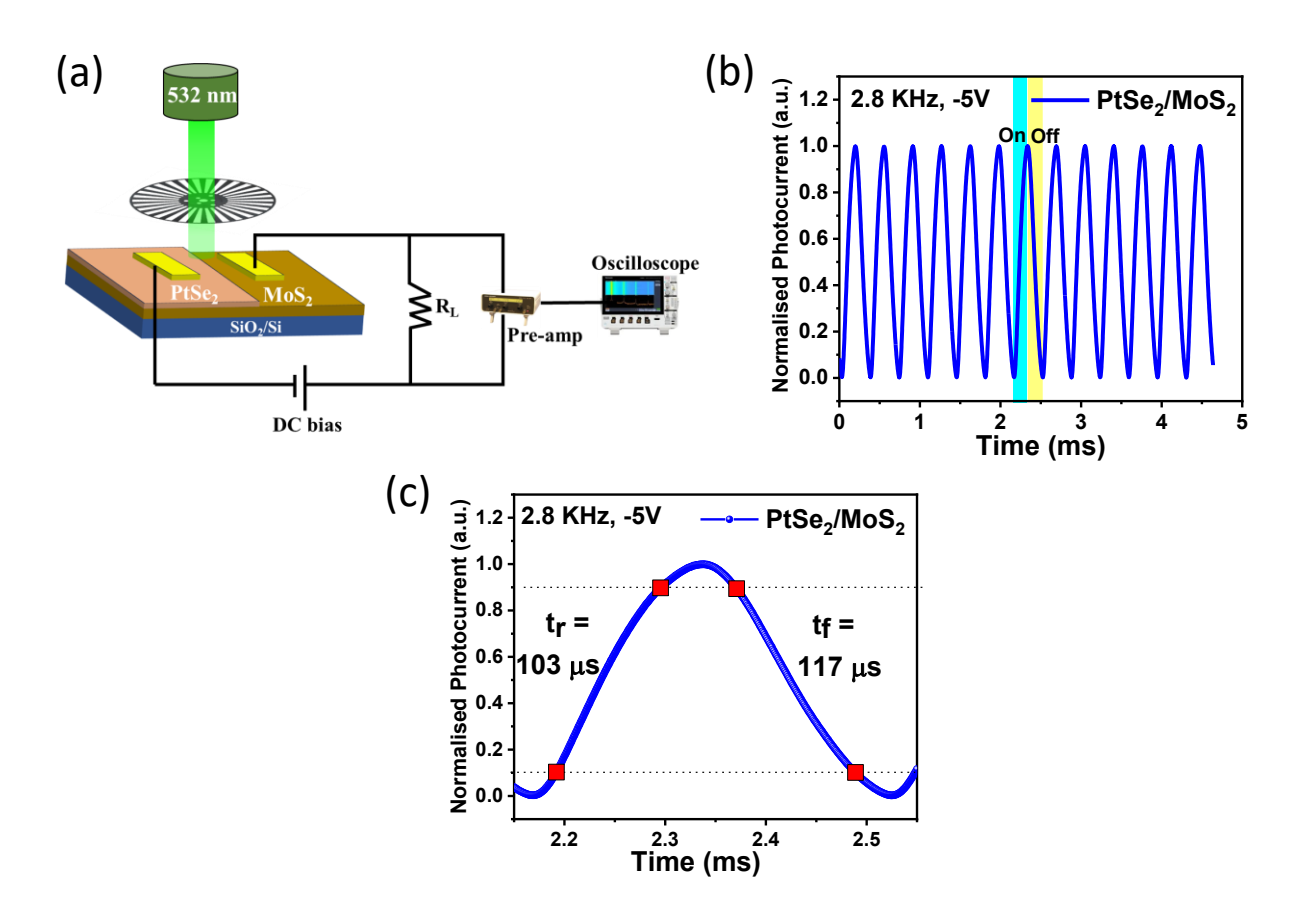


Figure 5.9. (a) Schematic of the experiment set-up utilized to detect fast speed (μs) testing of the PtSe₂/MoS₂ device (b) Temporal response of PtSe₂/MoS₂ device under 532 nm light illumination at -5V with a chopping frequency of 2.8 KHz. (c) An enlarged single cycle shows a rise and fall time of PtSe₂/MoS₂ device under 532 nm illumination and 2.8 KHz chopping frequency.

To reveal more about defects within the $PtSe_2/MoS_2$ heterointerface, power-dependent current measurements were performed under 500 nm illumination. Figure 5.7 (d) exhibits the I-V characteristics of $PtSe_2/MoS_2$ device under dark and at different power densities (0.06-5.80 μWcm^{-2}) of 500 nm light which reveals that with increasing the power density current also increases except near -8V, where the photocurrent decreases for low power density. This may

be due to the negative bias-induced p-type nature in MoS₂ which hindered the transport of the carriers and increased the recombination of the charge carriers and net photocurrent decreases [30, 31]. The inset of Figure 5.7 (d) displays the power-dependent current linear fit plot. This graph was fitted with I_{net}=BP^{\alpha} equation, where I_{net} is the net photocurrent generated in the device, P is power density, B is a proportionality constant and α is power exponent. Often, α value deviates from 1 indicates the defect states present between the conduction band and Fermi level [8]. In our case for PtSe₂/MoS₂ device, 0.5 value of α is obtained, (see inset of Figure 5.7 (d)) which implies that high defect/trap states are present within the material and/or at the interface. Figure 5.7 (e) shows the I-T response of PtSe₂/MoS₂ device under different power densities of 500 nm illumination at a moderate bias of -5V where current is increased with increasing power. The estimated responsivity of the PtSe₂/MoS₂ device at various power densities of 500 nm (-5V) irradiation is depicted in Figure 5.7 (f). The reduction of responsivity with increasing power density could be attributed to the higher recombination rate due to defect or trap states present at the constitute materials and/or at the interface [14, 32, 33]. In PtSe₂, the common defects/trap states could be owing to the Pt or Se vacancy and their antisites (Pt antisites and/or Se antisites) [34, 35]. In MoS₂ the defects/trap states might be possible due to Mo and/or S vacancy [36].

To reinforce the broadband detection performance of the PtSe₂/MoS₂ device, time-dependent (I-T) measurements were performed under different 400-1200 nm illumination, as depicted in Figure 5.8. The I-T measurements were conducted using Bentham monochromator light (400-1200 nm) by manually on-off the light with a cycle of 10 s as shown in Figure 5.8 (a-i). The results show the stable and well-defined I-T response and further confirm that PtSe₂/MoS₂ device response broadband (400-1200 nm) covering from visible to NIR region. The speed of the photodetector plays a pivotal role in fast detection and commercial applications, especially in optical communication and imaging.

The speed of a photodetector is measured from its response time i.e. rise (t_r) or fall (t_f) time. Rise time (fall time) is the time taken by the photodetector to arrive 10% to 90% (90% to 10%) of the total current value when the illumination is on (off), respectively. Figure 5.9 (a) illustrates the schematics of the set-up used for the fast I-T testing of the PtSe₂/MoS₂ device under 532 nm (power 5 mW) illumination. An optical chopper is employed to achieve fast switching of the light and resultant photocurrent is measured using an oscilloscope to determine the response time. Figure 5.9 (b) is the temporal response of the PtSe₂/MoS₂ device under 532 nm

illumination at a chopping frequency of 2.8 KHz. The rise and fall time were calculated by considering the one periodic cycle as shown in Figure 5.9 (c), where PtSe₂/MoS₂ shows an ultra-fast response with a rise time of 103 µs and a fall time of 117 µs. The photodetector shows a fast response and the improved performance is limited due to the testing equipment used. The comparison of performance of fabricated PtSe₂/MoS₂ photodetector device with the other PtSe₂-based reported heterostructure is demonstrated in Table 5.1 and shows that PtSe₂/MoS₂ heterostructure fabricated in this work has much higher responsivity and detectivity in the NIR region (900 nm) compared to other reported PtSe₂ based heterostructures.

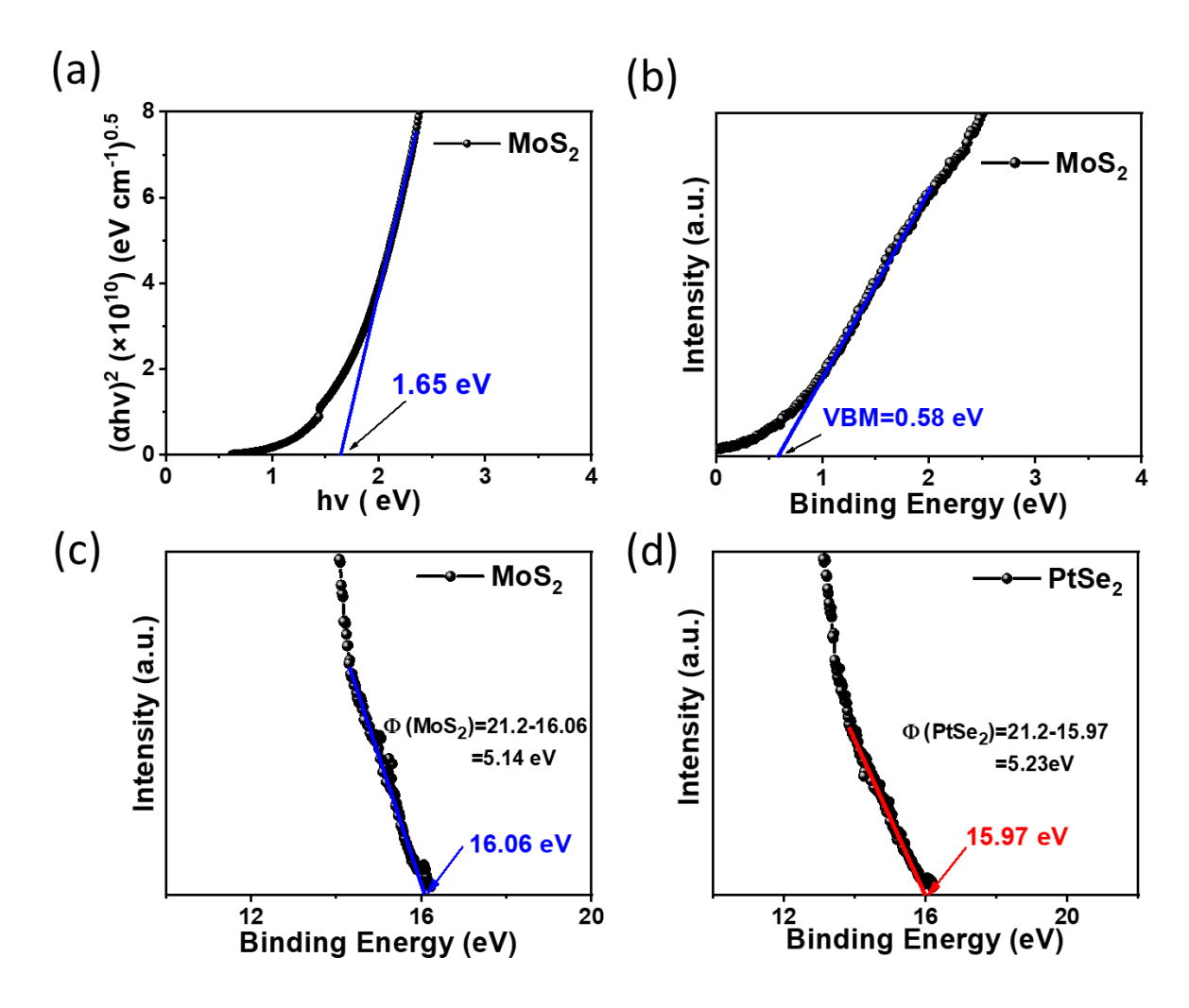


Figure 5.10 (a) Band gap of MoS₂ evaluated by Tauc plot (b) Valence band maxima (VBM) of MoS₂ calculated from ultraviolet photoelectron spectroscopy (UPS) measurements. Work function of (c) MoS₂ and (d) PtSe₂ calculated from UPS measurements.

Chapter 5: 2D PtSe₂ heterostructures for photodetector study

Table 5.1. Performance Comparison of fabricated PtSe₂/MoS₂ photodetector with other PtSe₂ based reported heterostructures

Material	Responsivity [AW-1]	Specific Detectivity [Jones]	EQE [in %]	Large Area growth	Response Time [μs]	Ref.
PtSe ₂ /MoS ₂	5.42 @ 520 nm	2.52×10 ¹⁰	1700	No	92/112	[14]
Graphene- WSe ₂ /PtSe ₂	0.16 @ 405 nm	_	49.3	No	0.9/1.5	[5]
$PtSe_{2}/MoS_{2}$	4.52 @ 405 nm	9.24×10 ¹¹	1880	No	20000/25800	[15]
PtSe ₂ /PtS ₂	0.188 @ 532 nm	_	7.1	Yes	66000/75000	[37]
PtSe ₂ /GaAs	0.262 @ 808 nm	2.25×10^{12}	_	Yes	5.5/6.5	[38]
Graphene/ PtSe ₂ /β-Ga ₂ O ₃	0.076 @ 245 nm	1.93×10 ¹³	_	Yes	12/212	[18]
PtSe ₂ /CdTe	0.506 @ 780 nm	4.2×10 ¹¹	_	Yes	8.1/43.6	[24]
PtSe ₂ /Ge	0.766 @ 1550 nm	1.1×10 ¹¹	61.3	Yes	54.9/56.6	[33]
PtSe ₂ /pyramid Si	0.567 @ 810 nm	1.26×10 ¹³	87	Yes	14.7/17.5	[39]
PtSe ₂ /Planner Si	0.520 @ 808 nm	3.26×10 ¹³	80	_	55.3/170.5	[40]
PtSe ₂ /h BN	0.037 @ 980 nm	_	~10	Yes	17.5/23.5	[26]
PtSe ₂ /GaSe	1.78 @ 520 nm	3.51×10 ¹²	405.8	No	23/20	[41]
PtSe ₂ /Ge	0.602 @ 1550 nm	6.31×10 ¹¹	48.2	Yes	7.4/16.7	[25]
PtSe ₂ /ReS ₂	0.153 @ 635 nm	7.72×10 ¹¹	30	No	811000/72000 0	[42]
PtSe ₂ /Si	0.0178 @ 1550 nm	2.38×10 ⁹	_	_	6/9	[43]
PtSe ₂ /MoS ₂	17.9 @ 900 nm	9.8×10 ¹²	2400	Yes	103/117	This Work

To understand the working mechanism of PtSe₂/MoS₂ photodetector, the band gap (from Tauc plot), work function, and valence band maxima (VBM) from ultraviolet photoelectron spectroscopy (UPS) measurements were calculated. Figure 5.10 (a) exhibits that a band gap of

1.65 eV is obtained for MoS_2 (from Tauc plot). The VBM of 0.58 eV showing p-type nature of MoS_2 (Figure 5.10 (b)). The work function of MoS_2 , ϕ (MoS_2) =5.14 eV and work function of $PtSe_2$, ϕ ($PtSe_2$) =5.23 eV was calculated from its UPS spectra as shown in Figures 5.10 (c) and (d). Here, multilayer $PtSe_2$ (10.6 nm) is considered as semimetal in nature. Using these values, the $PtSe_2/MoS_2$ energy band diagram is proposed as shown in Figure 5.11. Since the work function of $PtSe_2$ (5.23 eV) is slightly higher than that of MoS_2 work function (5.14 eV). So, it implies that the Fermi level of MoS_2 is slightly at higher position than the $PtSe_2$ Fermi level. Therefore, when heterojunction is formed, the electrons move from MoS_2 to $PtSe_2$ side and holes in opposite direction to attain the equilibrium condition (Figure 5.11 (a)) and a built-in electric field is generated at the interface.

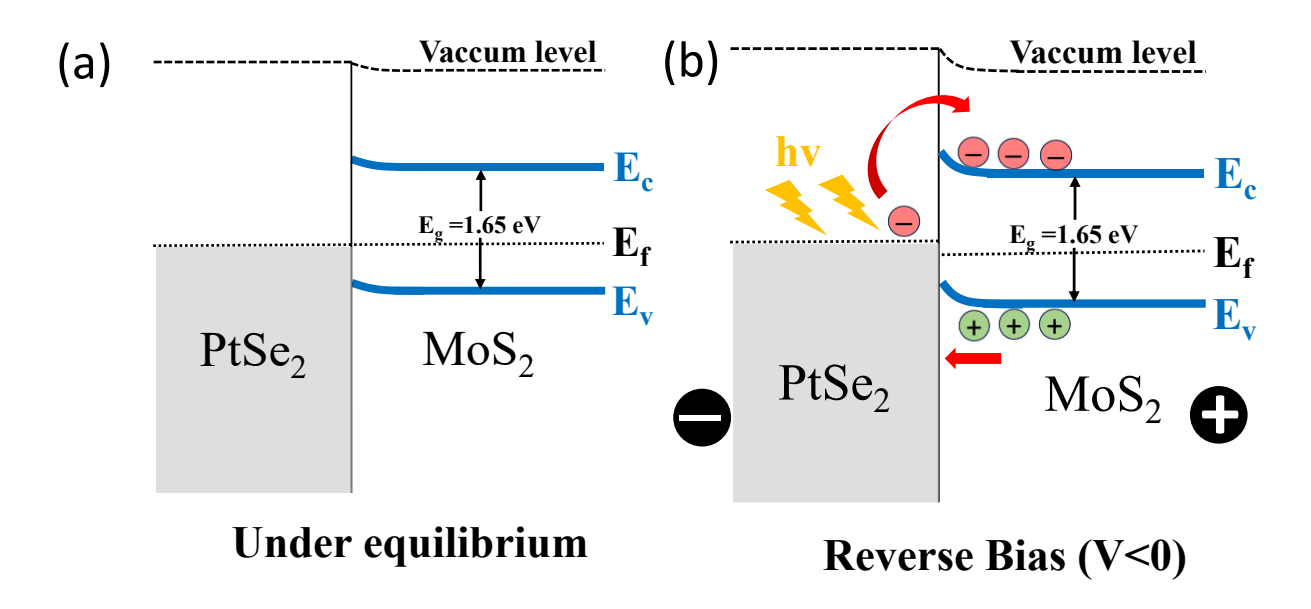


Figure 5.11 Energy band diagram between PtSe₂ and MoS₂ under (a) equilibrium condition and (b) under reverse bias.

Moreover, these electrons motion induced a small upward band bending on the MoS₂ side as shown in Figure 5.11 (a) which may be responsible for Schottky to nearly ohmic I-V behaviour under dark condition. When heterojunction is under illumination at a reverse bias (Figure 5.11 (b)) then photo-generated electrons move from PtSe₂ to MoS₂ side by crossing the barrier and holes move from MoS₂ to PtSe₂ direction and produce net photocurrent. In contrast, under dark condition (with same reverse bias) less current is observed due to the barrier at the

Chapter 5: 2D PtSe₂ heterostructures for photodetector study

heterojunction which inhibit in separation of the charge carriers. However, in forward bias condition (positive bias to PtSe₂) electrons can easily move under dark and under illumination from MoS₂ to PtSe₂ side owing to absence of any appropriate barrier height at the junction and hence dark current and photocurrent are almost same

5.4 Conclusion

In summary, in this work we report a large area $PtSe_2/MoS_2$ heterostructure fabrication using PMMA assisted wet transfer method. A comparative study of $PtSe_2$ and $PtSe_2/MoS_2$ photodetector was carried out where heterostructure performed better in terms of enhanced in detectivity and decrease of dark current value (10^3 order). Moreover, the $PtSe_2/MoS_2$ device shows high performance with a wide range of detection abilities covering visible to NIR (400-1200 nm) spectral range. A high responsivity of 17.9 AW-1 and specific detectivity of 9.8×10^{12} Jones at -5V bias corroborated its high performance. The $PtSe_2/MoS_2$ device demonstrates an ultra-fast response with a rise time (t_r) of $103~\mu s$ and fall time (t_r) of $117~\mu s$. A detailed carrier transport mechanism is also proposed to understand the $PtSe_2/MoS_2$ photodetector working. Thus, this work gives direction to grow large area, ultra-fast heterostructure materials for next-generation photodetector applications.

References

- 1. Wang, Y., et al., Monolayer PtSe2, a New Semiconducting Transition-Metal-Dichalcogenide, Epitaxially Grown by Direct Selenization of Pt. Nano Letters, 2015. **15**(6): p. 4013-4018.
- 2. Huang, Z., W. Zhang, and W. Zhang Computational Search for Two-Dimensional MX2 Semiconductors with Possible High Electron Mobility at Room Temperature. Materials, 2016. **9**, DOI: 10.3390/ma9090716.
- 3. Zhang, W., et al., Two-dimensional semiconductors with possible high room temperature mobility. Nano Research, 2014. 7(12): p. 1731-1737.
- 4. Zhao, Y., et al., *High-Electron-Mobility and Air-Stable 2D Layered PtSe2 FETs*. Advanced Materials, 2017. **29**(5): p. 1604230.
- 5. Wang, X., et al., A Self-Powered Photodetector Based on Graphene Enhanced WSe2/PtSe2 Heterodiode with Fast Speed and Broadband Response. Advanced Optical Materials, 2024. **12**(18): p. 2400052.
- 6. Zhang, X., et al., Dark Current Mechanisms and Suppression Strategies for Infrared Photodetectors Based on Two-Dimensional Materials. Laser & Photonics Reviews, 2024. **18**(5): p. 2300936.
- 7. Pham, P.V., et al., 2D Heterostructures for Ubiquitous Electronics and Optoelectronics: Principles, Opportunities, and Challenges. Chemical Reviews, 2022. **122**(6): p. 6514-6613.
- 8. Bassi, G., et al., 2D–3D heterostructure of PtS2-x/Ga2O3 and their band alignment studies for high performance and broadband photodetector. Nanotechnology, 2024. **35**(32): p. 325706.
- 9. Bassi, G., R. Wadhwa, and M. Kumar, *Broadband and High-Performance Photodetector Fabricated Using Large Area and Transfer-Free 2D–2D PtS2/MoS2 Heterostructure*. Advanced Optical Materials, 2024. **12**(7): p. 2301899.
- 10. Wang, H., et al., *Two-dimensional heterostructures: fabrication, characterization, and application.* Nanoscale, 2014. **6**(21): p. 12250-12272.
- 11. Ganatra, R. and Q. Zhang, Few-Layer MoS2: A Promising Layered Semiconductor. ACS Nano, 2014. **8**(5): p. 4074-4099.
- 12. Venkata Subbaiah, Y.P., K.J. Saji, and A. Tiwari, *Atomically Thin MoS2: A Versatile Nongraphene 2D Material*. Advanced Functional Materials, 2016. **26**(13): p. 2046-2069.
- 13. Wadhwa, R., A.V. Agrawal, and M. Kumar, *A strategic review of recent progress, prospects and challenges of MoS2-based photodetectors*. Journal of Physics D: Applied Physics, 2022. **55**(6): p. 063002.
- 14. Gui, T., et al., *In-situ fabrication of PtSe2/MoS2 van der Waals heterojunction for self-powered and broadband photodetector.* Materials & Design, 2024. **238**: p. 112722.
- 15. Li, H. and Z. Yang *Highly Responsive and Self-Powered Photodetector Based on PtSe2/MoS2 Heterostructure*. Molecules, 2024. **29**, DOI: 10.3390/molecules29112553.
- 16. Wang, B., et al., *High-performance broadband photodetector based on PtSe2/MoS2 heterojunction from visible to near-infrared region*. Science China Information Sciences, 2024. **67**(3): p. 132401.
- 17. Wadhwa, R., et al., Wafer-scale controlled growth of MoS2 by magnetron sputtering: from in-plane to inter-connected vertically-aligned flakes. Journal of Physics: Condensed Matter, 2023. **35**(12): p. 124002.
- 18. Wu, D., et al., *Highly sensitive solar-blind deep ultraviolet photodetector based on graphene/PtSe2/β-Ga2O3 2D/3D Schottky junction with ultrafast speed.* Nano Research, 2021. **14**(6): p. 1973-1979.

- 19. Jakhar, A., et al., Optically Pumped Broadband Terahertz Modulator Based on Nanostructured PtSe2 Thin Films. Advanced Optical Materials, 2020. 8(7): p. 1901714.
- 20. O'Brien, M., et al., Raman characterization of platinum diselenide thin films. 2D Materials, 2016. **3**(2): p. 021004.
- 21. Chakraborty, B., et al., Symmetry-dependent phonon renormalization in monolayer MoS\${} {2}\$ transistor. Physical Review B, 2012. **85**(16): p. 161403.
- 22. Mitra, S., et al., *Tailoring phonon modes of few-layered MoS2 by in-plane electric field.* npj 2D Materials and Applications, 2020. **4**(1): p. 6.
- 23. Zeng, L., et al., *Ultrafast and sensitive photodetector based on a PtSe2/silicon nanowire array heterojunction with a multiband spectral response from 200 to 1550 nm.* NPG Asia Materials, 2018. **10**(4): p. 352-362.
- 24. Wu, D., et al., Design of 2D Layered PtSe2 Heterojunction for the High-Performance, Room-Temperature, Broadband, Infrared Photodetector. ACS Photonics, 2018. **5**(9): p. 3820-3827.
- 25. Wang, L., et al., *A high-performance near-infrared light photovoltaic detector based on a multilayered PtSe2/Ge heterojunction.* Journal of Materials Chemistry C, 2019. **7**(17): p. 5019-5027.
- 26. Kim, H.-S., et al., Broadband and ultrafast photodetector based on PtSe2 synthesized on hBN using molecular beam epitaxy. Applied Surface Science, 2023. 638: p. 158103.
- 27. Bassi, G., et al., Controlled and tunable growth of ambient stable 2D PtS2 thin film and its high-performance broadband photodetectors. Journal of Alloys and Compounds, 2023. 955: p. 170233.
- 28. Wadhwa, R., et al., Fast response and high-performance UV-C to NIR broadband photodetector based on MoS2/a-Ga2O3 heterostructures and impact of band-alignment and charge carrier dynamics. Applied Surface Science, 2023. 632: p. 157597.
- 29. Bao, J., et al., *Photoinduced oxygen release and persistent photoconductivity in ZnO nanowires*. Nanoscale Research Letters, 2011. **6**(1): p. 404.
- 30. Che, M., et al., *High-Efficiency Self-Powered Broadband Photodetector Based on PtSe2/MoSe2 Heterojunction*. ACS Photonics, 2024. **11**(4): p. 1693-1702.
- 31. Kwak, D.-H., et al., *High performance hybrid graphene–CsPbBr3–xIx perovskite nanocrystal photodetector.* RSC Advances, 2016. **6**(69): p. 65252-65256.
- 32. Zhang, Z.-X., et al., *Ultrafast, Self-Driven, and Air-Stable Photodetectors Based on Multilayer PtSe2/Perovskite Heterojunctions*. The Journal of Physical Chemistry Letters, 2018. **9**(6): p. 1185-1194.
- 33. Lu, Y., et al., Construction of PtSe2/Ge heterostructure-based short-wavelength infrared photodetector array for image sensing and optical communication applications. Nanoscale, 2021. **13**(16): p. 7606-7612.
- 34. Li, J., et al., *Edge and Point-Defect Induced Electronic and Magnetic Properties in Monolayer PtSe2*. Advanced Functional Materials, 2022. **32**(18): p. 2110428.
- 35. Avsar, A., et al., *Defect induced, layer-modulated magnetism in ultrathin metallic PtSe2*. Nature Nanotechnology, 2019. **14**(7): p. 674-678.
- 36. Hong, J., et al., *Exploring atomic defects in molybdenum disulphide monolayers*. Nature Communications, 2015. **6**(1): p. 6293.
- 37. Yuan, J., et al., Wafer-Scale Fabrication of Two-Dimensional PtS2/PtSe2 Heterojunctions for Efficient and Broad band Photodetection. ACS Applied Materials & Interfaces, 2018. 10(47): p. 40614-40622.
- 38. Zeng, L.-H., et al., Fast, Self-Driven, Air-Stable, and Broadband Photodetector Based on Vertically Aligned PtSe2/GaAs Heterojunction. Advanced Functional Materials, 2018. **28**(16): p. 1705970.

Chapter 5: 2D PtSe₂ heterostructures for photodetector study

- 39. Ma, M., et al., Multilayered PtSe2/pyramid-Si heterostructure array with light confinement effect for high-performance photodetection, image sensing and light trajectory tracking applications. Journal of Materials Chemistry C, 2021. 9(8): p. 2823-2832.
- 40. Xie, C., et al., *High-performance broadband heterojunction photodetectors based on multilayered PtSe2 directly grown on a Si substrate*. Nanoscale, 2018. **10**(32): p. 15285-15293.
- 41. Gong, K., et al., *High detectivity and fast response avalanche photodetector based on GaSe/PtSe2 p–n junction.* Materials & Design, 2023. **228**: p. 111848.
- 42. Song, Y., et al., *High-Performance Photodetector Based on the ReSe2/PtSe2 van der Waals Heterojunction.* ACS Applied Electronic Materials, 2023. **5**(5): p. 2748-2757.
- 43. Zhou, K., et al., *Broadband photodetector based on 2D layered PtSe2 / silicon heterojunction at room-temperature*. Physica E: Low-dimensional Systems and Nanostructures, 2020. **123**: p. 1141

Chapter 6: Summary and Scope for Future Studies

This chapter provides a summary of all work done in the thesis and future goals to be achieved. The thesis focused on PtX₂ (X=S, Se) heterostructure fabrication and their high-performance broadband photodetector study. The controlled and large area growth of PtS₂ is achieved on various substrates by thermally assisted conversion (TAC) method by optimizing the growth parameters such as Pt film thickness, sulfur amount, and gas flow rate. Moreover, in present thesis work various PtX₂ heterostructure (PtS₂/MoS₂, PtS_{2-x}/Ga₂O₃, PtSe₂/MoS₂) based broadband photodetectors fabrication and their in-depth band alignment study is also carried out. To reveal what is happening at the interface, a detailed carrier transport mechanism of the photodetector working is thoroughly explained.

6.1 Summary

6.1.1 Large area and controlled growth of PtS2 on various substrates

This chapter discussed the controlled and tunable growth of PtS₂ on various substates by optimizing the growth parameters and studying their photodetector performance. The main highlights of the chapter are mentioned below-

- A large area and controlled growth of PtS₂ is achieved by optimizing the growth parameters such as Pt film thickness, sulfur amount and gas flow rate.
- PtS to PtS₂ transition can be done by reducing the Pt thickness, increasing sulfur amount and using moderate gas flow rate.
- The Raman, XPS and AFM characterizations were performed to analyze the PtS₂ film.
- The growth of PtS₂ is highly reproducible and able to grow on various substrates such as SiO₂/Si, Si, sapphire and flexible mica.
- A growth mechanism is proposed to understand the effect of critical growth parameters.
- A high-performance broadband (400-1100 nm) PtS₂ based photodetector was fabricated on SiO₂/Si substrate with high responsivity of 31.38AW⁻¹ at low bias of 1V.

6.1.2 Large area 2D PtS₂ heterostructure for broadband photodetection

In this chapter, large area PtS₂ heterostructure (PtS₂/MoS₂ and PtS_{2-x}/Ga₂O₃) fabrication and their broadband photodetector study are explored. Moreover, a detailed interface study including their band alignment and carrier transport mechanism is also carried out. The key findings of the chapter are mentioned below.

6.1.2.1 PtS₂/MoS₂ heterostructure

- A large area PtS₂/MoS₂ heterostructure was fabricated by directly growing PtS₂ film over MoS₂ coated substrate using TAC method.
- Type-I band alignment is confirmed between the PtS₂ and MoS₂ by Kraut rule and XPS results.
- Raman, PL, AFM, XPS, and FESEM characterization are used to characterize the grown film quality.
- The PtS₂/MoS₂ photodetector shows a broad response (400-1200 nm) and much enhanced in responsivity (97 times) and detectivity (33 times) as compared with bare MoS₂.
- A carrier transport mechanism is proposed to illustrate the working of PtS₂/MoS₂ photodetector device under different external biasing.

6.1.2.2 PtS_{2-x}/Ga₂O₃ heterostructure

- A large area PtS_{2-x}/Ga₂O₃ heterostructure was fabricated by wet transfer of PtS_{2-x} film over Ga₂O₃ film grown substrate.
- The film quality was characterized by Raman, AFM, XRD, XPS and UPS characterizations.
- The XPS and UPS results confirmed a type-I band alignment between the PtS_{2-x} and Ga₂O₃ interface.
- The PtS_{2-x}/Ga₂O₃ photodetector gives a broad response covering UV-C to NIR region (250-1100 nm), whereas bare Ga₂O₃ detection is limited to UV region only.
- PtS_{2-x}/Ga₂O₃ heterostructure exhibits high ambient stability and shows stable response after six months also.
- The heterostructure device demonstrates maximum responsivity of 38.7 AW⁻¹ under 1100 nm (NIR) wavelength with fast milli second response.

6.1.3 2D PtSe₂ heterostructure for photodetector study

This chapter explains the PtSe₂/MoS₂ heterostructure fabrication and its broadband photodetector performance. The fabricated PtSe₂/MoS₂ heterostructure shows a broad response covering visible to NIR (400-1200 nm) region. Moreover, an ultrafast microsecond response is achieved in the heterostructure device.

• The PtSe₂ and MoS₂ films were grown by TAC and sputtering method, respectively.

- The PtSe₂/MoS₂ heterostructure was fabricated by wet transfer of PtSe₂ film over MoS₂ coated substrate.
- Compared to bare $PtSe_2$, the $PtSe_2/MoS_2$ heterostructure exhibits better device performance with ~10³ order reduction in dark current and increase in detectivity value.
- The PtSe₂/MoS₂ photodetector shows broad detection capability covering visible to NIR (400-1200 nm) region with maximum responsivity of 17.9 AW⁻¹ and detectivity of 9.8×10¹² Jones under 900 (NIR) illumination.
- The PtSe₂/MoS₂ photodetector device demonstrates an ultrafast response with rise/fall time of 103 μ s/117 μ s.
- A carrier transport mechanism is proposed at the heterointerface to illustrate the working of PtSe₂/MoS₂ photodetector.

6.2 Scope for future studies

The present thesis work has made significant contributions to the scientific field by establishing new and promising results. However, there are still some research gaps or opportunities which can be explored as future targets.

- 1. For commercializing 2D materials, it is essential to do their wafer scale growth. Although recent advancements in graphene and MoS₂ growth method made much progress in it. However, in the case of PtS₂, it is still lacking. During the wafer scale growth, controlled thickness with high quality and uniformity are major challenges.
- 2. The electronic properties of the materials highly rely on their band gap. In 2D materials their band gap can be tuned with thickness value. Therefore, there is also requirement of facile and cost-effective approach to achieve controllable thickness on the large area. For the 2D PtX₂ (X=S, Se) there are only limited reports which demonstrate a controllable thickness growth. Moreover, as per our literature so far there is no concreate experiment report which claims the large area monolayer growth of PtS₂.
- 3. The fabrication of flexible and wearable devices has become a highlighted research area owing to their potential applications in a variety of fields such as healthcare and wearable electronics. For PtX₂, it is a broad scope to fabricate flexible photodetector devices which can be achieved by choosing a novel fabrication technique.
- 4. The role of plasmonic nanoparticles on PtX₂ film for enhanced absorption and broadband photodetector have the high scope for future studies.

Chapter 6: Summary and Scope for Future Study

- 5. So far, doping in the PtS₂ film is not probe experimentally. Doping can be utilized to change the carrier concentration, polarity shifting and homo-junction formation. These modulations can be used to enhance the device preformation.
- 6. Calculate the band alignment of the heterostructure using TCAD (Technology Computer Aided Design) software.

Conferences/Workshop Attended

- 1. <u>Gaurav Bassi</u> and Mukesh Kumar, **Poster presentation**, Control growth of platinum disulfide for broadband photodetector, International Union of Materials Research Society-International Conference in Asia (IUMRS-ICA) 2022, December 19-23, 2022, IIT Jodhpur, India
- 2. <u>Gaurav Bassi</u> and Mukesh Kumar, **Oral presentation**, Controlled growth of PtS₂ thin film on various substrates and its high-performance broadband photodetector, Anusandhan 1.0 Research Fair-2023, IIT Mandi, HP, India.
- 3. <u>Gaurav Bassi</u> and Mukesh Kumar, **Oral presentation**, Tunable controlled growth of PtS and PtS₂ and its broadband photodetector, International Conference on Materials for Energy and Sustainable Development (MESD) 2023, October 27-29, JNU-New Delhi, India
- 4. <u>Gaurav Bassi</u> and Mukesh Kumar, **Poster presentation**, Controlled growth of PtS₂ thin film on various substrates with high performance broadband photodetector, Materials Research Society of India (MRSI) 2023, IIT-BHU-Varanasi, UP, India
- 5. <u>Gaurav Bassi</u> and Mukesh Kumar, Poster presentation, Large area-controlled growth of PtS₂ thin film on various substrates and its application as a broadband photodetector, Recent Progress in Graphene and 2D Materials Research (RPGR) 2023, LaLiT Ashok Bangalore, India
- **6.** <u>Gaurav Bassi</u> and Mukesh Kumar, **Poster presentation**, High performance broadband photodetector based on 2D–3D PtS_{2-x}/Ga₂O₃ heterostructure and their band alignment study, International Symposium on Semiconductor Materials and Devices (ISSMD) 2024, University of Kashmir, India
- 7. <u>Gaurav Bassi</u> and Mukesh Kumar, Poster presentation, Large area and high-performance broadband photodetector based on PtS₂/MoS₂ heterostructure, European Material research society (E-MRS) 2024 Fall Meeting, Warsaw, Poland.
- **8.** <u>Gaurav Bassi</u> and Mukesh Kumar, Poster presentation, Large area growth of 2D-2D PtS₂/MoS₂ heterostructure and its broadband photodetector study, 2024 Material Research Society (MRS) Fall meeting & Exhibit, Boston, USA
- **9. Workshop** on Nano Technology and its Applications, April 26-30, 2021, RGNIYD, Tamil Nadu with Collaboration with NIT Jalandhar, NIT Tiruchirappalli, JNU New Delhi.
- **10.** INUP-i2i, 3Rd User Awareness **Workshop** on Fabrication & Characterization Facility for Nanotechnology, September 2-3, 2022, IIT Delhi.
- **11. Workshop** on Characterization and testing of Components Laser Materials Processing including surface Engineering and Additive Manufacturing, March 18-26. IIT Kharagpur.

Curriculum Vitae

Mr. Gauray Bassi

PhD Research Scholar Department of Physics Indian Institute of Technology Ropar Rupnagar-140001, Punjab, India

Email: gaurav.19phz0005@iitrpr.ac.in, gauravbassi1995@gmail.com

Google scholar: https://scholar.google.com/citations?user=18EPt-UAAAAJ&hl=en

Research Gate: https://www.researchgate.net/profile/Gaurav-Bassi

Research Interest

• 2D Materials and heterostructures

- Characterization of thin film
- Synthesis and characterization of MoS₂, PtS₂ and PtSe₂
- Photodetectors fabrication and testing
- Wet transfer method for heterostructure fabrication

Education

Doctor of Philosophy | Physics

31 Dec 2019 - June 2025

Dissertation: Fabrication of Large area two-dimensional PtX₂ (X=S, Se) Heterostructures

for Broadband Photodetector Studies.

Indian Institute of Technology Ropar, India

Performance/CGPA: 8.6

Master of Science | Physics (2015-2017)

SGGS Khalsa College Mahilpur, Hoshiarpur, Punjab, India Percentage: 68.4

Bachelor of Science | Physics, Chemistry, Mathematics (2012-2015)

Sikh National College Banga, SBS Nagar, Punjab, India Percentage: 68.75

Research Expertise

- Expertise in thin film grown of MoS₂, PtS₂, PtSe₂, Ga₂O₃ materials and hand on expertise on sputtering and Chemical vapor deposition (CVD) methods.
- Photodetector device fabrication and testing
- Large area heterostructure fabrication by direct method and PMMA assisted Wet transfer method.
- Transmission electron microscope (TEM) sample preparation for thin film using PMMA assisted wet transfer method.
- Characterization tools known: XRD, XPS, UPS, TEM, Raman, FESEM, AFM, SEM, Optical microscope, Hall measurement, Raman, Photoluminescence (PL) and UV-Vis-NIR spectroscopy.
- Data analysis Software Known: MS Office, Origin, XPS Peak fit, Avantage, Gwyddion, ImageJ

Awards and distinction

- Best Poster in European-Material Research Society (E-MRS) Fall meeting-2024 held at Warsaw Institute of Technology, Warsaw, Poland.
- Best Oral presentation in Materials for Energy and Sustainable Development (MESD)-2023 International conference held at JNU, New Delhi
- Qualified GATE (Graduate Aptitude test in Engineering) Physics exam four times (2017, 2018, 2019, 2020)
- Qualified CSIR (Council of Scientific and industrial Research) National Eligibility test 2018

Teaching Experience

Assistant professor of Physics at Guru Nanak college, Sukhchainana Sahib, Phagwara, Punjab, India (Jan 2019- 30 Dec 2019)

Teaching Assistant at IIT Ropar

•	July 2023 – Dec 2023	TA for PH102 – Physics for Engineering (Lab Course)
•	Jan 2023- Jun 2023	TA for PH425 – Condense matter Physics (Theory Course)
•	Jul 2022 – Dec 2022	TA for PH102 – Physics for Engineering (Lab Course)
•	Feb 2022–Jun 2022	TA for PH101 – Physics for Engineering (Theory Course)

• March 2021–Jan 2022 TA for GE101–Technology Museum Lab (Lab Course)

Leadership Quality

Guided three M.Sc. Student for their thesis project.